Spaceborne Microwave Radiometry:

Calibration, Intercalibration, and Science Applications

by

John Xun Yang

A dissertation submitted in partial fulfillment
of the requirements for the degree of
Doctor of Philosophy
(Atmospheric, Oceanic and Space Sciences)
in The University of Michigan
2016

Doctoral Committee:

Associate Research Scientist Darren S. McKague, Co-Chair
Professor Christopher S. Ruf, Co-Chair
Associate Professor Derek J. Posselt
Professor Leung Tsang

DEDICATION

To my Mom and Dad,
Mrs Tianqiong Huang and Mr Chengmei Yang,
Who love and support me through my life and shape what I am

ACKNOWLEDGEMENTS

Grateful thanks to my advisors, Dr. Darren McKague and Dr. Christopher Ruf, without whom the thesis would not have been possible. They give critical support, advice, and critique to my research. They guide my through office meeting, lab engineering, and field experiment. I enjoy the group environment where I can implement my own ideas, get encouraged when I succeed, and get support when I mess up. I enjoy the feeling of being attacked and pushed by their brilliant ideas, as well as fighting back my bullets with smart or silly answers. I enjoy the group breakfast and dinner. They offer me a variety of opportunities on research and social network. Their training and mentoring not only make me an expert in my field but also shape me toward a bright scientist and integral person as them.

I thank my committee members, Dr. Derek Posselt and Dr. Leung Tsang. They offer useful suggestions to my research and spend much effort to polish my thesis. They help me understand a much broader picture of research, inform me opportunities, and help plan my career.

I thank the NASA GPM XCAL team. As a member of them, I learned a lot by interacting with them. The team members I would like to thank include but not limited to Dr. Tom Wilheit, Dr. Wesley Berg, Dr. Linwood Jones, Dr. Erich Stocker, Dr. Chris Kummerow, Dr. David Draper, Dr. James Wang, Dr. Jim Shiue, Dr. Spencer Farrar, Dr. Hamideh Ebrahimi, and Ms. Ruirao Cheng.

I thank the SPRL engineers who have helped me out in building up the benchtop radiometer for CYGNSS. Mr. Bruce Block has supported me through the

project. His professional skills and knowledge helped me out when I got lost in complicated engineering. Dr. Roger De Roo fixed the cable problem which I would otherwise have not figured out. Mr. Ryan Miller and Michael Long helped the soldering and wiring. Dr. Jon Van Noord offered me liquid nitrogen.

My labmates are terrific. They are smart and ready to help whenever I get stuck. I will forever memorize the experience with them about chasing the satellite, doing field experiment across states at blizzard midnight, engineering in the basement, struggling for assignments before the next-day deadline, and hanging out for fun. Thanks to Dr. Rachael Kroodsma, Amada Mims, David Chen, Marry Morris, David Austerberry, Deepak Singh, and Manjunath Ganesh.

Thanks to my colleagues and friends in the department and university. They support the tedious but critical things such as IT, registration, and reimbursement, as done by Sandra Pytlinski, Bryan White, and Barb Lupri. They have been with me working on a number of rewarding classes and projects. They offer me opportunities to step into local food, place of interest, culture, and society. They took me to church chorus, museums, lase tagging, karaoke, bars, etc. They engage me in running, rowing, softball, swimming, field camping, and travelling. They make me appreciate the life and universe.

I am grateful to my families who encouraged me to start the journey at Michigan. My Mom and Dad always back me up. My cousin and her husband, Dr. Shujuan Huang and Dr. Xi Yun have been with me for years with endless support. It is in Ann Arbor, Michigan, where I met this charming girl, Fei He, and has since married with her. Fei has supported me through my study, work, and life. As a wolverine football fan, engaging Fei in my life is like making a perfect touch-down to me. Go blue!

TABLE OF CONTENTS

LIST OF FIGURES

LIST OF TABLES

ABSTRACT

Spaceborne microwave radiometry is the backbone for assimilation into numerical weather forecasts and provides important information for Earth and environment science. The extensive radiometric data must go through the process of calibration and intercalibration prior to science application. This work deals with the entire process by providing systematic methods and addressing critical challenges. These methods have been applied to NASA and JAXA's Global Precipitation Measurement (GPM) mission and many other radiometers to make important contributions and to solve long-standing issues with coastal science applications.

Specifically, it addresses four important challenges: 1) improving cold calibration with scan dependent characterization; 2) reducing the uncertainty of warm calibration; 3) deriving calibration dependence across the full range of brightness temperatures with both cold and warm calibration; and 4) investigating calibration variability and dependence on geophysical parameters. A critical challenge in science applications of radiometer data is that coastal science products from radiometers have previously been largely unavailable due to land

contamination. We therefore develop methods to correct for land contamination and derive coastal science products. This thesis addresses these challenges by developing their solutions and then applying them to the GPM mission and its radiometer constellation.

A systematic calibration framework has been developed with both cold and warm calibration tie points to cover the full dynamic range of radiometer-measured brightness temperature (TB). First, an improved method for cold calibration is developed. This method produces reliable scan dependent information that was not available previously. By diagnosing the scan dependent calibration, instrument performance can be assessed and scan dependent errors can be identified and corrected. Second, warm calibration often suffers from large uncertainties. We develop methods for warm calibration with significantly reduced uncertainty. Warm calibration is expanded beyond previously utilized sites in the Amazon rainforest to include worldwide inland boreal and temperate forests, as well as forests in coastal and island regions. Techniques for mitigating land heterogeneity are also developed. By using the new warm-calibration method, the uncertainty in warm calibration is greatly reduced. Scan dependent information is also extracted. Third, by combining improved cold and warm calibration methods, we are able to diagnose calibration dependencies on TB and develop intercalibration parameters for the GPM constellation. When combining cold and warm calibration to the

GPM Microwave Imager (GMI), a calibration issue with TB dependence is found and resolved. The TB dependent calibration parameters are derived and applied to the GPM constellation.

We investigate a problem that is of fundamental importance to calibration, that is, calibration variability and its dependence on geophysical parameters. A series of analysis techniques is developed to conduct this investigation. It is found that GMI calibration using the improved cold technique has a pronounced temporal and spatial variability and depends on geophysical parameters. A 40-day cycle is discovered at all channels in the calibration data. It is then found that this periodicity is related to the spatial variation of geophysical parameters that can vary periodically with the shifting of calibration locations. Additionally, calibration shows a nonlinear and non-monotonic dependence on geophysical parameters. The dependence can result in large discrepancies between model and observation not only with high values of geophysical parameters (e.g., high water vapor) but also at calm weather conditions with low values of geophysical parameters (e.g., low water vapor); the latter has historically been considered a more reliable condition for calibration. These results reveal calibration variability and nonlinearity and point out directions for solving the issues.

While calibrated and intercalibrated data have provided extensive information, the coastal data tend to be wasted due to land contamination. We develop

algorithms that can handle land contamination. Land contamination signals are estimated, and then removed, using a representative antenna pattern convolved with a high-resolution land–water mask. This method has been applied in the Great Lakes and validated with simulated data and buoy measurements. This method can be combined with our work on calibration, that is, the intercalibrated constellation and climatological data can be used with this algorithm for coastal studies.

CHAPTER 1
Introduction

1.1 Remote Sensing from Spaceborne Microwave Radiometry

1.1.1 Spaceborne Radiometry for Meteorology

Weather satellites are the backbone in current global numerical weather prediction (NWP) systems and will play an important role in meteorology and climate research (Joo et al. 2013; Kelly and Thépaut 2007; Lorenc and Marriott 2014; Otkin 2010). Among various instruments onboard weather satellites, microwave radiometry is the dominant contributor of satellite observations to NWP systems. Observations are assimilated into NWP systems to reduce errors in forecasts. Satellite data account for 64% error reduction in short-range global forecasts, while surface-based observations contribute the remaining 36%, according to the evaluation of forecast sensitivity to observations in the UK Met Office global NWP system (Figure 1.1) (Joo et al. 2013). When differentiating the impact of different satellite platforms, microwave radiometry accounts for 43% of this error reduction, followed by 35% from infrared sounding, 10% from optical

imagers, 5% from scatterometers, and 4% from Global Positioning System (GPS) radio occultation (GPSRO) (Joo et al. 2013).

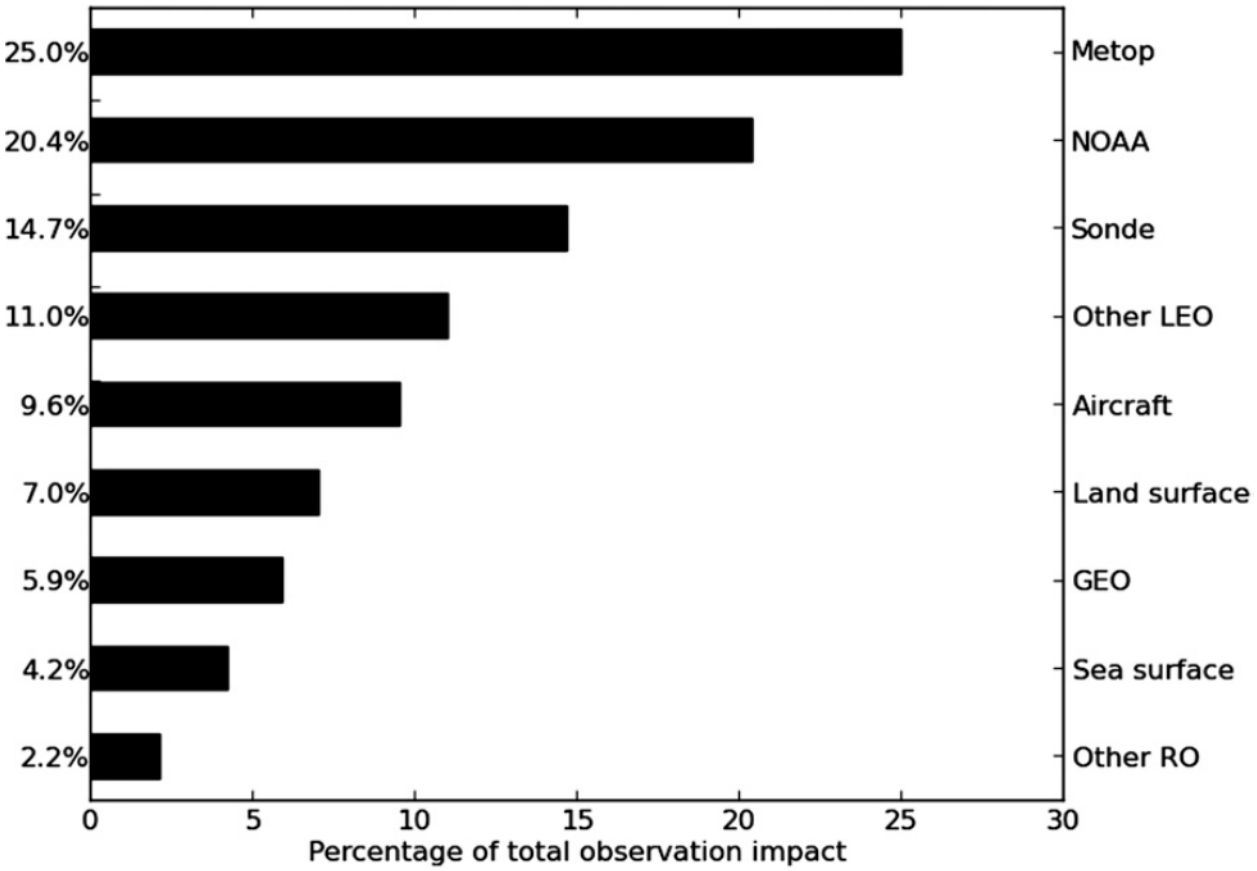

Figure 1.1: Comparison of the impact of different observations on NWP system. The satellite contribution dominates, contributing 64% of the error reduction, with the remaining 36% from surface-based observation. Among satellite platforms, microwave radiometry contributes the most with 43%. Courtesy of Joo et al. (2013).

Spaceborne microwave radiometry provides a wide variety of meteorological and Earth environmental information (Ulaby and Long 2014). It can sound atmospheric profiles such as temperature, humidity, and cloud liquid water; it measures oceanic near-surface and surface parameters such as sea surface

temperature, sea surface salinity, oceanic emissivity, and near-surface wind speed and direction; it measures soil moisture, vegetation canopy, land emissivity, etc. These data have been widely used in NWP systems to improve weather forecasts. Additionally, radiometer data have been used beyond the field of meteorology to study Earth environmental science, global climate change, and are used extensively in geographic information systems. (Hallikainen et al. 1988; Ulaby and Long 2014; Wentz et al. 2007).

Spaceborne microwave radiometry has the advantage of obtaining unique information content that cannot be provided by other sensors. While visible and infrared sensors cannot penetrate clouds and precipitation, electromagnetic waves at microwave wavelengths are much longer, at a scale from millimeters to centimeters, allowing all-weather observations. For targets that interact with visible, infrared and microwave radiation, the interaction with microwaves often yields additional information. For instance, microwave radiometry can measure oceanic surface wind, because oceanic emissivity at microwave frequencies is sensitive to wind as well as to ocean surface temperature. However, visible and infrared measurements do not respond to wind.

Microwave radiometry is a relatively new technology (~80 year history), compared to other remote sensing methods like photography (~200 years) (Ulaby and Long 2014). However, the past decades have seen a rapid development and

application of microwave radiometry in meteorology. In the 1930s, ground-based microwave radiometers were built to measure ground targets. The first weather satellite is generally considered as the Television Infrared Observation Satellite Program (TIROS) with its first spacecraft launched on 1 April 1960. It paved the way for the Nimbus program. The first scanning microwave radiometer, the Electrically Scanned Microwave Radiometer (ESMR), was onboard Nimbus 5 launched on 11 December 1972. These pioneering programs proved the utility of weather satellites and more spacecraft have since been launched. The number of operational weather and environmental satellites on orbit in 2015 is 104 according to the World Meteorological Organization (WMO) (World Meteorological Organization 2015). Satellite measurements have become indispensable for weather observations and forecasts.

Nowadays, satellite microwave radiometers have developed into a big family. The total power radiometer measures the power of received radiance and is one of the most important ones with reliability and long lifetime. Most spaceborne radiometers are total power radiometers and all GPM constellation radiometers are total power radiometers. In general, a total power radiometer does mechanic-scanning, either conically scanning with constant Earth Incidence Angle (EIA) or cross-track scanning with EIA varying. A more common classification is imager and sounder. The imager looks at surface through transparent channels and is used

to measure geophysical parameters such oceanic wind, SST, precipitation, and land emissivity. A sounder profiles the atmosphere through sounding frequencies with strong atmospheric absorption and emission. It has been widely used to measure temperature and humidity profiles as well as high-altitude precipitation (Njoku 2014).

1.1.2 Global Precipitation Measurement (GPM) Mission

Precipitation is one of the most important natural phenomena affecting human lives and is critical to the economic and scientific communities. It directly affects the availability of freshwater and is associated with severe events such as hurricane, blizzards, floods and droughts. Satellites extend precipitation observation from the limited ground-based network to a full global scale. Among satellite payloads, microwave radiometry is essential to measuring precipitation. Visible and infrared sensors are used to estimate rainfall in an indirect way inferred from cloud cover and cloud-top radiance (Adler and Negri 1988; Griffith et al. 1978). Microwave measurements contains direct information about the rain (Ulbrich 1983). Satellite rain products are mainly derived from microwave radiometers (Hou et al. 2013; Kummerow and Giglio 1994). Historically, the retrieval of rain using satellite radiometry dates back to ESMR on Nimbus 5 launched in 1972 (Allison et al. 1974; T. Wilheit 1994; Wilheit et al. 1977). Later, radiometers with multiple

polarizations and additional frequencies were introduced to measure precipitation, such as Scanning Multi-channel Microwave Radiometer (SMMR) (Prabhakara et al. 1986), Special Sensor Microwave/Imager (SSM/I) (Wentz and Spencer 1998), and Advanced Microwave Sounding Unit (AMSU) (Ferraro et al. 2000). The first satellite dedicated to precipitation measurement was the Tropical Rainfall Measuring Mission (TRMM), launched on 27 November 1997 (Kummerow et al. 1998; Simpson et al. 1988). TRMM has active (Precipitation Radar, PR) and passive (TRMM Microwave Imager, TMI) microwave instruments to measure precipitation. It provided invaluable precipitation products through its mission that ended on 15 April 2015.

Based on the success of TRMM, the Global Precipitation Measurement (GPM) Mission is an ongoing project using a satellite constellation to measure global precipitation. Lead by National Aeronautics and Space Administration (NASA) and Japanese Aerospace Exploration Agency (JAXA), this mission uses a constellation consisting of around 15 spacecraft with 12 of them already on orbit and the others to be launched later (Hou et al. 2013). These satellites include the GPM core observatory, Global Change Observation Mission (GCOM, W-1), Defense Meteorological Satellite Program (DMSP, F17-F20), Indian Space Research Organisation (ISRO) and French Centre National d'Etudes Spatiales (CNES) Megha-Tropiques satellite (M-T), European Space Agency (ESA)

Meteorological Operational satellite programme (Metop, A-C), National Oceanic and Atmospheric Administration polar-orbiting satellites (NOAA, 18-19), National Polar-orbiting Operational Environmental Satellite System (NPOESS) Preparatory Project (NPP), and the NOAA-NASA Joint Polar Satellite System (JPSS). Figure 1.2 shows the schedule for the GPM constellation. All satellites carry microwave radiometers as key instruments for precipitation measurement.

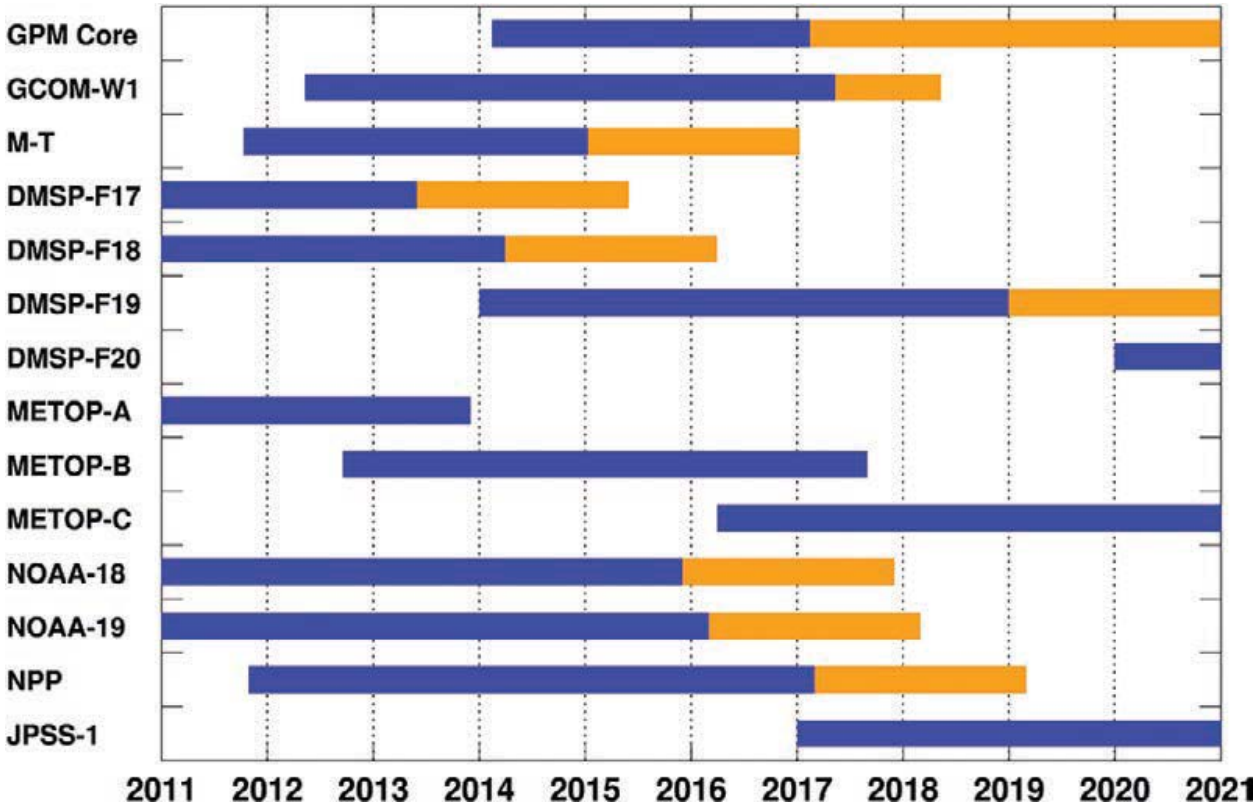

Figure 1.2: The radiometer mission phases of GPM constellation, with blue and yellow for primary and extended phases respectively. Courtesy of Hou et al. (2013)

The GPM core observatory was launched on April 2015 (Draper et al. 2015b; Hou et al. 2013). The spacecraft orbit has a 65° inclination with a mean altitude of

407 km and its conical-scanning radiometer extends observation to latitudes of ±68°. The GPM core observatory covers a larger range of latitudes than TRMM, which observed over ±40°. Its non-sun-synchronous orbit allows frequent Earth sampling that can capture the diurnal variability of precipitation. Together with the other GPM satellites, the GPM constellation provides a short revisit time with a revisit time under an hour for more than 60% of the globe and under three hours for more than 80% of the globe

The GPM core observatory carries the GPM Microwave Imager (GMI) and a dual-frequency radar (DPR) (Draper et al. 2015b). The radar provides complementary precipitation profile information to GMI. GMI is a conical-scanning radiometer with 13 channels ranging from 10 to 190 GHz. The 10.65, 18.7, 36.64, 89 and 166 GHz have both V and H polarization channels, and 23.8, 183.31±3 and 183.31±7 have V polarization only. EIAs are about 52.8° from 10.65 to 89 GHz, and 49.19° from 166 to 183.31 GHz. It is the reference radiometer to which all other GPM constellation radiometers are intercalibrated.

It is critical for the GPM mission to calibrate GMI and intercalibrate GPM constellation radiometers. The hardware performance needs to be diagnosed through calibration; different radiometers need to be reconciled through intercalibration. The group at University of Michigan is a member of the Intersatellite Radiometer Calibration Working Group (XCAL) team within GPM

that is responsible for GMI calibration and constellation intercalibration (http://www.gpm-x-cal.info/). Since the launch and operation of GMI, a number of calibration investigations have been developed and applied. The calibration effort is reflected in the evolution of the level 1C product, which provides the intercalibrated TBs for GPM. With the development of different calibration corrections, level 1C products have evolved through twelve versions, i.e., 01A-01C, 02A-C, 03A-03C, ITE010, ITE020, ITE030. The Michigan group has contributed to improved GPM calibration (Yang et al. 2014). We developed reliable warm-end calibration and improved cold-end calibration and applied them both to the GPM constellation.

1.1.3 Principles of Radiometer Remote Sensing

Remote sensing through spaceborne microwave radiometry is based on the measurement of Earth microwave emission. All objects with temperature above absolute zero emit radiation due to thermal motion. The ideal blackbody radiation emission can be described as:

$$B(\nu) = \frac{2h\nu^3}{c^2(e^{h\nu/kT} - 1)} \tag{1.1}$$

where B is the radiation, h is the Planck's constant, ν is the frequency of radiation, k is the Boltzmann's constant, c is the speed of light, and T is the absolute

temperature. At microwave wavelengths, where $h\nu \ll kT$, the above equation can be simplified as

$$B(\nu) = \frac{2kT\nu^2}{c^2} \tag{1.2}$$

This is called the Rayleigh-Jeans approximation. It states that the Earth's microwave radiation is linearly proportional to the absolute temperature of the object.

A real object is generally not an idealized blackbody but a gray body, i.e., the emitted radiation is less than that predicted from blackbody radiation. The emissivity of a gray body is defined the ratio of actual emission B_{gray} to blackbody emission B_{bb}, or

$$\varepsilon = \frac{B_{gray}}{B_{bb}} \tag{1.3}$$

Emissivity is dependent on frequency, polarization, and direction. The brightness temperature, TB, is defined as

$$TB = \varepsilon T \tag{1.4}$$

It is convenient to use TB in microwave remote sensing, since TB has a direct physical dependence on emissivity and temperature.

When an electromagnetic wave propagates through the atmosphere, it typically encounters absorption and scattering. Scattering in the microwave is small except in the case of precipitation. Assume that the atmosphere is plane-parallel without multiple scattering. The observed radiance at the top of the atmosphere (TOA) for a satellite radiometer can be written in terms of TB as follows:

$$\mathrm{TB} = \varepsilon T_s \exp(-\tau \sec\theta) + \mathrm{TB}_{\mathrm{up}} + (1-\varepsilon)\exp(-\tau \sec\theta)\mathrm{TB}_{\mathrm{dn}} + (1-\varepsilon)\mathrm{TB}_{\cos}\exp(-2\tau \sec\theta) \quad (1.5)$$

where T_s is the surface temperature, ε is the surface emissivity. τ is the vertically intergated atmospheric optical depth, θ is the EIA, $\mathrm{TB}_{\mathrm{up}}$ and $\mathrm{TB}_{\mathrm{dn}}$ are atmospheric upwelling and downwelling emission respectively, and $\mathrm{TB}_{\cos}$ is the cosmic background brightness. The optical depth is written as

$$\tau = \int_{z=0}^{z=TOA} \alpha(z)dz \quad (1.6)$$

where z is the height above the ground and α is the extinction coefficient. The atmospheric upwelling and downwelling emission are

$$\begin{aligned} \mathrm{TB}_{\mathrm{up}} &= \int_0^{TOA} T(z)\alpha(z)\sec\theta \exp(-\int_{z'}^{TOA} \sec\theta\alpha(z')dz')dz \\ \mathrm{TB}_{\mathrm{dn}} &= \int_{TOA}^{0} T(z)\alpha(z)\sec\theta \exp(-\int_{TOA}^{z} \sec\theta\alpha(z')dz')dz \end{aligned} \quad (1.7)$$

The atmospheric transmissivity can be defined as

$$\Gamma = \exp(-\tau \sec\theta) \quad (1.8)$$

The above equations of radiative transfer have important implications for remote sensing. If the optical depth is near zero (transmissivity near 1), the TB at TOA is mostly from surface emission; if the optical depth is large (transmissivity near 0), satellite radiometers barely see surface or low-level emission. Figure 1.3 shows the atmospheric transmissivity as a function of frequency in the microwave and millimeter wave range for clear-sky conditions. The strong absorption features due to oxygen and water vapor determine the selection of sounding and image channels.

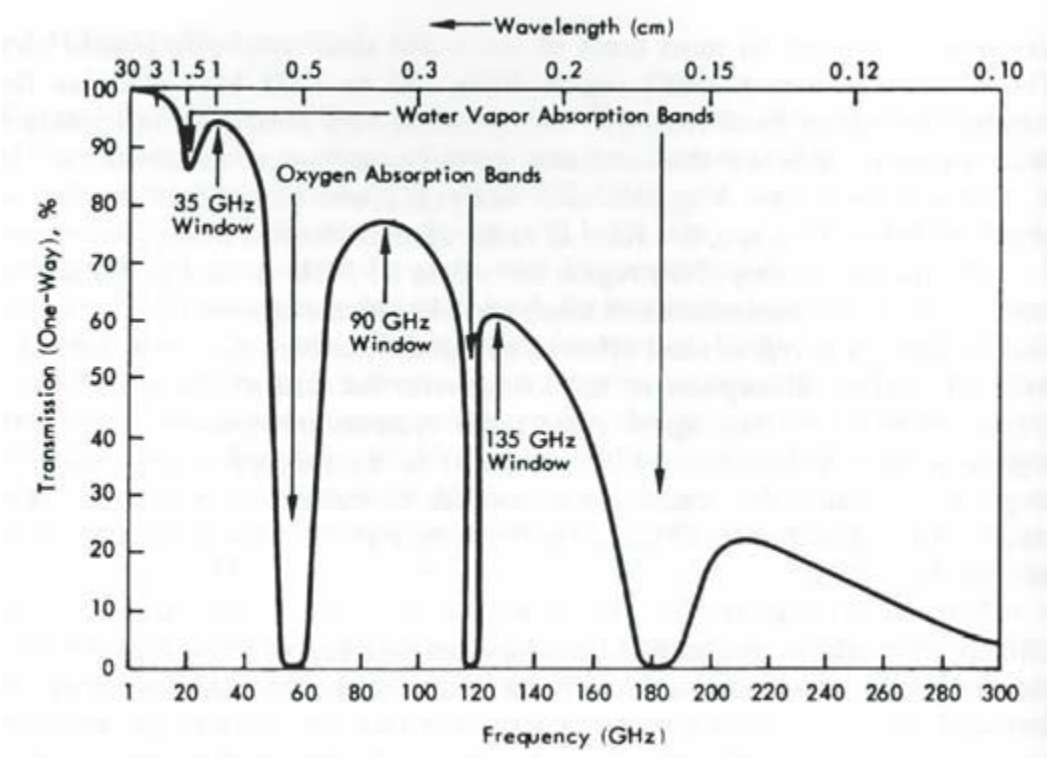

Figure 1.3: The atmospheric transmissivity of nadir view under clear-sky conditions. Courtesy of Ulaby and Long 2014.

Another important concept is atmospheric weighting function. The TB_{up} in Equation (1.7) can be rewritten as

$$TB_{up} = \int_{z=0}^{z=TOA} T(z)W(z)dz \tag{1.9}$$

where W(z) is the weighting function defined as

$$W(z) = \frac{d\Gamma}{dz} = \alpha(z)\sec\theta \exp(-\int_{z'}^{TOA} \sec\theta\alpha(z')dz') \tag{2.0}$$

The weighting function indicates that the atmospheric upwelling radiance is a weighted summation of emission from all atmospheric layers at temperature $T(z)$. Keep in mind the weighting function can also be written as a function of humidity. By adjusting the weighting function through the dependence of atmospheric extinction α on frequency in the vicinity of strong absorption features (e.g., the oxygen and water vapor absorption bands in Figure 1.3), satellite radiometers can detect different layers of the atmosphere. For instance, satellite sounders use channels with different weighting functions to probe atmospheric temperature and humidity at different heights from troposphere to stratosphere. Figure 1.4 shows the weighting function of the AMSU instrument (A-B). It can be shown that the weighting function in a clear atmosphere is maximum at the height where τ=1 (Liou 2002), but the actual height is higher due to multiple scattering.

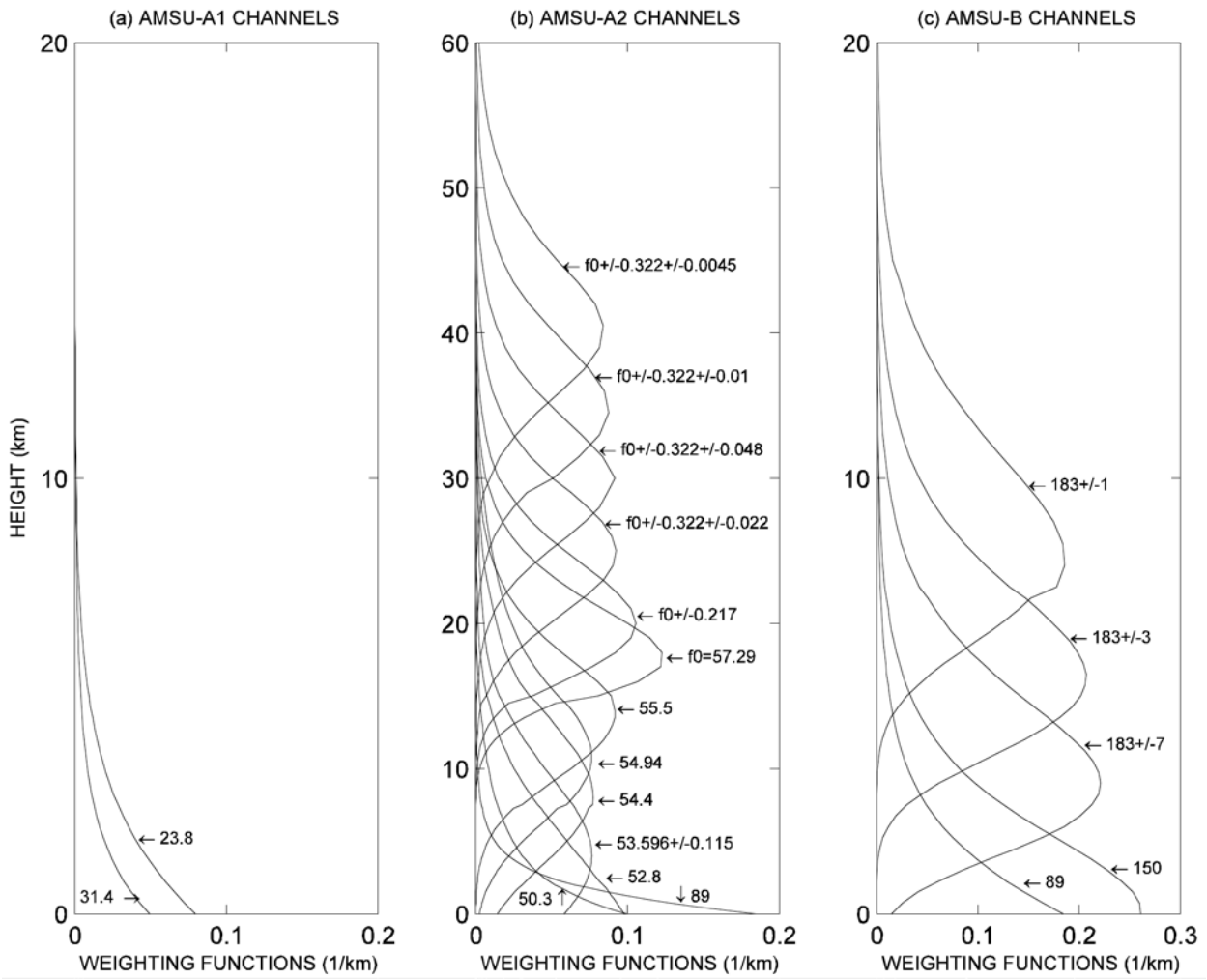

Figure 1.4: The weighting functions of AMSU for nadir view of clear-sky conditions. It is the basis for probing the atmospheric temperature (middle) and water vapor (right) at different heights. Window channels (left) can observe surface properties. Courtesy of (Aires and Roca 1998).

1.2 Radiometer Calibration

1.2.1 Why Calibration

For an individual spaceborne radiometer, calibration is the process of transforming the measured radiation to Earth-scene TB through a series of successive and consistent procedures with hardware and software. The incident

radiation at the radiometer antenna is a small signal that needs to be amplified and transformed into antenna temperature (TA). TA is a weighted summation through the whole antenna field of view (FOV) including the main lobe, side lobes, and back lobe. Appropriate processes are executed to derive the Earth scene TB corresponding to the main lobe. For specific channels, TA often corresponds to a specific polarization state through hardware (e.g., an orthomode transducer), however calibration is still needed to remove cross-polarization contamination. The process for converting TA to TB is called antenna pattern correction (APC). APC algorithms are dependent on a number of measurements and modeling with empirical parameterization. It is not unusual that radiometers have various hardware or software related issues, which need to be corrected through calibration. Additionally, calibration and intercalibration are indispensable processes for constellations of radiometers, since instrument differences among different radiometers (e.g., differences in center frequency, bandwidth, and Earth incidence angle) should be reconciled.

From the perspective of data structure, calibration is the base level data processing that is of fundamental importance to the development of higher level products. The products from satellites are developed in a bottom-up way from instrument base to final scientific products. The GPM mission structures data into four levels in addition to the level-0 data (Hou et al. 2013). The level-0 data are the

raw instrument data received by the ground data center from the satellite; level-1 data contain calibrated brightness temperatures from each individual radiometer, with ancillary information such as geolocation and time; level-2 data are the retrieved precipitation data from individual satellites at the native spatial and temporal resolution of the instruments (e.g., rain rate); level-3 data contain merged precipitation data from the constellation as well as products that are processed to time and spatial scales not directly linked to the original observations (e.g., latent heat and combined precipitation estimates from radiometer and radar); and level-4 are assimilated precipitation data from satellite observations and modeling. Table 1.1 presents details of the GPM data structure. Calibration produces the level-1 data from level-0 data. The level-1 data have three subsets: level 1A, antenna temperature data with geolocation, time, and ancillary information, level 1B, radiometrically corrected and calibrated main-beam brightness temperature data, and level 1C, intercalibrated data. Calibration errors in the level-1 data should be minimized, which should otherwise affect subsequent higher-level data including the final scientific products. For GPM, it is expected that TB errors are less than 1 K (Wilheit et al. 2015; Wilheit 2013).

Level	Sub-Level	Description
Level 0	Level 0 GMI	Raw instrument data

Level 1	Level 1A GMI	Reconstructed data with ancillary information, including radiometric and geometric calibration coefficients
	Level 1B GMI	Geolocated and radiometrically calibrated data including brightness temperature
	Level 1C GMI	Intercalibrated data
	Level 1C, partner radiometers	Intercalibrated constellation data using GMI as the reference
Level 2	Level 2 GMI	Retrieved precipitation data using additional Radar data
	Level 2 combined GMI/DPR	Combined retrieval data using GMI and DPR
	Level 2 partner radiometer	Retrieval data from the other constellation radiometers, based on intercalibrated level 1 data
Level 3	product	Resampled and gridded (0.25°×0.25°) precipitation data using the whole constellation
Level 4	product	Precipitation forecast and analysis with model assimilation

Table 1.1: The GMI related data structures in GPM mission (Hou et al. 2013). Calibration works on producing reliable Level 1 data from Level 0.

Radiometer calibration is closely related to the hardware. The input radiation to the front-end of a radiometer needs to be amplified by a factor of 10^{12}-10^{14} through a series of amplifiers. A radiometer needs to be carefully designed and built. Its performance can be significantly undermined by a number of factors such as unstable environmental temperature control, circuit impendence mismatch, standing waves in the circuit, etc. The error budget for antenna temperature can be written as (Ulaby and Long 2014):

$$\Delta T_A = T_{sys}[\frac{1}{\Delta \nu \tau} + (\frac{\Delta G}{G})^2]^{1/2} \tag{2.1}$$

where T_A is the antenna temperature, T_r is receiver temperature, and T_{sys} is system temperature in the form of $T_{sys} = T_A + T_r$, $\Delta \nu$ is the bandpass width, τ is the integration time, ΔG is the fluctuation of gain. The first term, $1/\Delta \nu \tau$, describes the impact of bandpass width and integration time. A wider bandpass and longer integration time will reduce noise. The second term is the error from gain fluctuations. This term becomes dominant when $\frac{1}{\Delta \nu \tau} \ll (\frac{\Delta G}{G})^2$, which is often the case when measuring very small input signal such as with radio astronomy and with early radiometers, which generally suffered from unstable gain. Figure 1.5 shows the circuit of a simple benchtop L-band radiometer developed at the University of Michigan (UM) (Yang 2015).

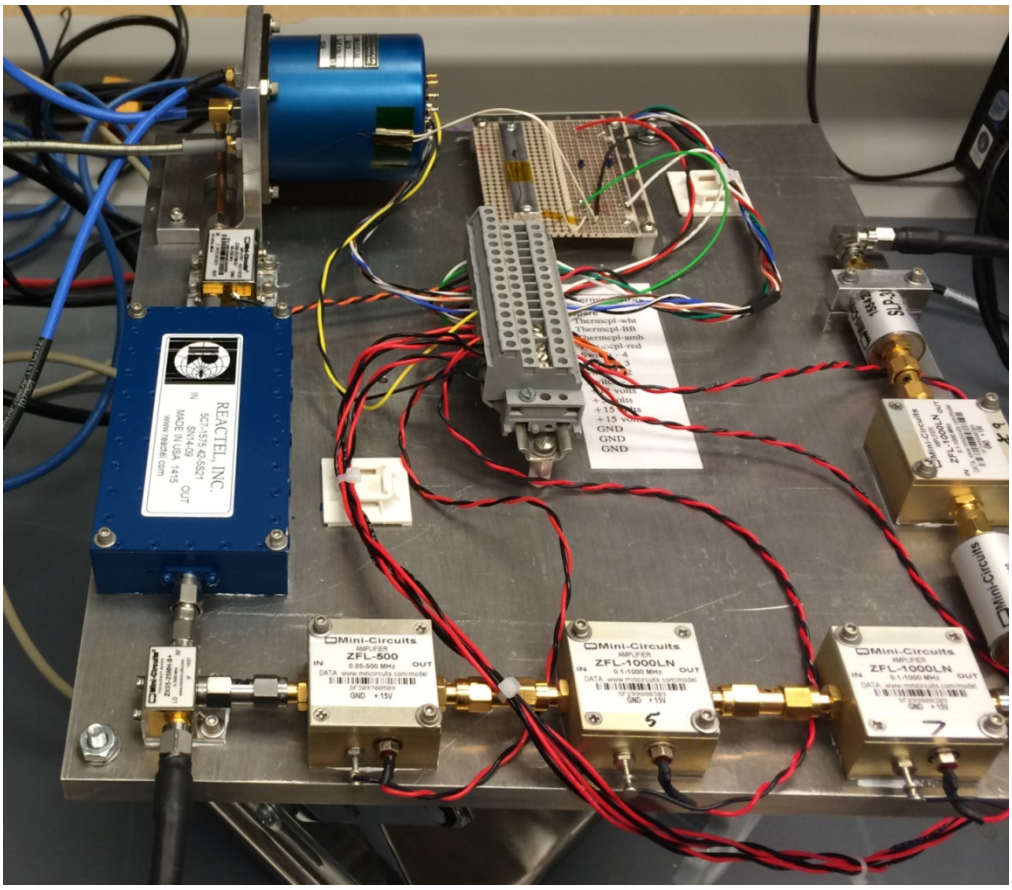

Figure 1.5: An L-band radiometer developed at the University of Michigan (Yang 2015). The circuit consists of a SP4T switch and a series of amplifiers and filters. By employing a number of amplifiers, the total gain of this radiometer is 112.35 dB. That is, the input signal is amplified by a factor of ~10^{11}. The input signal is negligible compared to electronic noise and therefore careful calibration is necessary.

A spaceborne radiometer is integrated to the spacecraft and has more complicated challenges. Figure 1.6 shows the GMI structure. The GMI instrument consists of seven major subsystems: main reflector, reflector deployment assembly, receiver subsystem, spin mechanism assembly, instrument support subsystem, the calibration subsystem (cold sky reflector, hot load and hot load tray), and instrument controller assembly. In operation mode, the GMI main reflector rotates

at 32 rpm to collect microwave radiances from Earth scenes (an azimuthal sector of 152° per 360° spinning), cold cosmic sky, and onboard hot load, where the latter two provide cold and warm references for calibration.

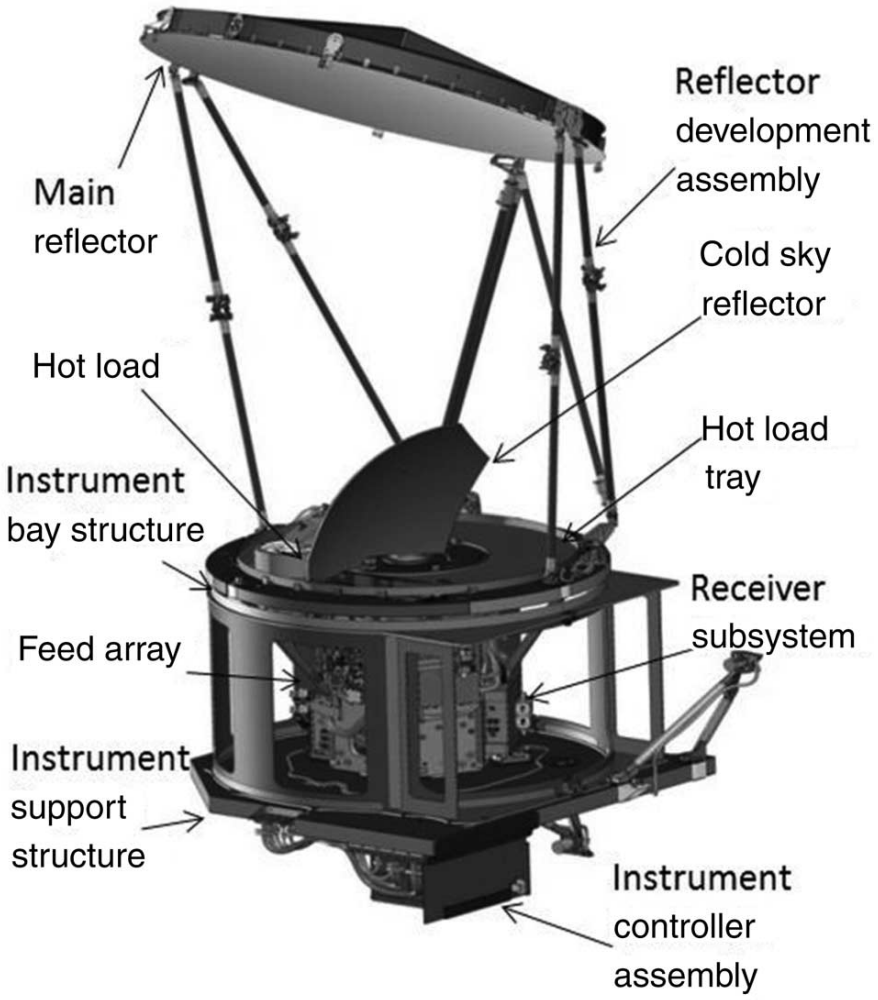

Figure 1.6: The GPM Microwave Imager, courtesy of Draper et al. (2015b). It is a conical-scanning total power radiometer. The onboard system uses the cold cosmic sky and an internal blackbody warm-load to calibrate the radiometer as it scans.

A number of instrument issues can happen on orbit. A radiometer can drift on orbit due to the extreme space environment (Ruf 2000). The onboard radiometer can be affected, for example, by the spacecraft itself due to obstruction of the

antenna field of view (FOV) (McKague et al. 2011). Other payloads onboard the spacecraft can interfere with the radiometer, resulting in observation anomalies (Wentz et al. 2001; Yang et al. 2015b). The onboard calibration system can have issues, e.g., the internal blackbody target used as the warm calibration can be affected by solar intrusion (Kunkee et al. 2008). A reflector is commonly used for conical-scanning radiometers such as GMI. However, the reflector could be emissive and add error to the observed radiance as antenna physical temperature changes with the orbit (Biswas et al. 2010; Gopalan et al. 2009; Wentz et al. 2001). As the radiometer spins, scan-dependent anomalies can occur because of antenna beam blockage and other instrumental effects (Draper 2014a; Wentz et al. 2001; Yang et al. 2015a). When converting TA into Earth scene TB through the APC, errors can occur since the APC contains parameters that are empirically derived and tuned (Wentz et al. 2001).

In general, the complete calibration process consists of three stages: prelaunch calibration, onboard calibration, and inflight vicarious calibration. Prelaunch calibration is conducted on the ground when the radiometer has not been integrated into the spacecraft. The onboard calibration system generally uses two point calibration. The cold sky with 2.7 K cosmic radiation background is used as the cold reference point, while an internal warm blackbody (~270 K) is used as the warm reference.

While the first two calibrations cannot be adjusted after launch, the third method, inflight vicarious calibration, is flexible and commonly used in post-launch calibration. In this method, vicarious targets are used as calibration references for relative or absolute calibration. The word “vicarious” refers to calibration not dependent on an onboard calibration system. By using a radiative transfer model (RTM) with ancillary data about the geophysical state, the TB at TOA can be simulated and compared with satellite observations. In this way, the performance of a spaceborne radiometer can be examined. The same approach can be applied to multiple radiometers, and the relative bias can be calculated between different radiometers and then removed for the constellation. This process is called intercalibration. Intercalibration is a special case of calibration, where a target radiometer can be calibrated with respect to a reference radiometer. Another useful way for diagnosing radiometer inflight performance is to flip the spacecraft so that the radiometer is pointing to deep space rather than Earth. Cold space provides a uniform 2.7 K background that helps diagnose hardware performance. However, this practice requires careful spacecraft control. Deep space calibration can still be considered as a kind of vicarious calibration, where cold space is used as the vicarious target.

1.2.2 Review of Calibration Methods

Inflight vicarious calibration can be divided into two basic categories, ocean and land calibration. The ocean has lower emissivity than the land. TBs over the ocean are therefore generally colder than those over land. For instance, GMI channel 10.65H has typical oceanic scenes of 80 K but is 270 K over land. Combining ocean and land calibration covers the TB range of Earth scenes. Empirical corrections can be derived to account for calibration dependence on TB. The two types of calibration are often referred to as cold-end and warm-end calibration. This classification is particularly useful for imager channels, for which weighting functions peak on the ground and are therefore sensitive to surface emission. The weighting functions of sounding channels peak at specific altitudes and are relatively insensitive to surface emission. A few special vicarious targets have also been used other than ocean and land (Chander et al. 2013; Rüdiger et al. 2014).

Over the ocean, a number of calibration methods have been developed. Most of them are based on using RTM with ancillary analysis or reanalysis data representing geophysical states to simulate TBs at TOA. The ocean emissivity is relatively well understood and a number of emissivity models have been developed. Under clear-sky conditions, the radiative transfer can be accurately modeled. For instance, Geer et al. (2010) simulated the TB for TMI using ancillary data from the European Centre for Medium−Range Weather Forecast (ECMWF). They found

that there is orbit-dependent temporal variability in the difference between observation and simulation, which was eventually confirmed by others as the emissive reflector whose temperature varied with the orbit (Biswas et al. 2010; Wentz et al. 2001). By implementing oceanic calibration for multiple radiometers, intercalibration can be done to obtain relative biases of different radiometers that accounts for instrument differences in frequency, EIA, and bandwidth. Geophysical differences between scenes viewed by two instruments can be reduced by collocating the FOVs of the instruments to the same area and time (the collocation method). A number of radiometers have been calibrated using the oceanic collocation method (McKague et al. 2011; Sapiano et al. 2013; Wentz et al. 2001; Wilheit et al. 2015; Wilheit 2013; Yang et al. 2015a, 2015b; Yang et al. 2011). In addition to the RTM based method, some other methods for oceanic calibration have been developed. Ruf (2000) found that the ocean emission can have a naturally occurring minimum TB that can be used as a stable reference point toward absolute calibration. He then developed a statistical method to derive the minimum TBs for calibration.

Since oceanic scenes provide only the cold part of the full dynamic TB range, calibration over warm land is a necessary complement. However, calibration over land is much more difficult. Land scenes are generally heterogeneous, with different land types. Even in a limited terrestrial region, with the same surface type,

TBs can have large variations. The variability of soil moisture, for example, results in significant changes in land emissivity. Land scenes also have a large diurnal and seasonal variability. It is difficult to characterize the dependence of land emissivity on polarization, frequency, and EIA.

Among different land types, forests have been found as useful vicarious calibration sites (Biswas et al. 2013; Brown and Ruf 2005; McKague et al. 2011; Mo 2005). The branches and leaves of dense forests form an optically thick canopy, hiding the ground that is more difficult to model. An optically thick forest canopy has near-blackbody properties of high emissivity and a small dependence on polarization and EIA. Brown and Ruf (2005) identified two areas of water-free Amazon rainforests and developed an empirical model to characterize the diurnal and seasonal changes of TBs using SSM/I data. These two areas have since been used as the warm calibration site in a number of studies. McKague et al. (2011) combined both warm Amazon and cold ocean scenes to examine edge-of-scan FOV obstructions for WindSat. Biswas et al. (2013) used the Amazon rainforest as one of their calibrations sites for intercalibration between TMI and WindSat. Mo (2005) studied TBs over the Amazon rainforest using the cross-track scanning radiometer AMSU-A. These studies demonstrate the value of the Amazon rainforest as a reliable warm scene calibration site.

1.2.3 Calibration Challenges

Despite significant achievements in calibration, there are challenges to be addressed. The four major challenges are: improving cold calibration with scan dependence characterization, developing reliable warm calibration, examining calibration dependence on TB, and investigating calibration variability and dependence on model parameterization.

Cold-end calibration can still benefit from improvement - particularly the characterization of the calibration dependence on scan position. When intercalibrating radiometers using the collocation method, the calibration dependence on scan position provides important information. The radiometer's FOV can be blocked by the spacecraft, resulting in large errors near the edge of scan (McKague et al. 2011; Yang et al. 2015a). The radiometer can be affected by sources of interference onboard the same spacecraft, resulting in scan dependent errors (Draper et al. 2015b; Wentz et al. 2001). The attitude of the spacecraft affects observations by altering EIAs across the scan, resulting in a change of observed TB as a function of scan position (Berg et al. 2012). These scan dependent biases can vary as a function of TB (Yang et al. 2015b). Accurate characterization of scan dependent performance helps diagnose and correct these issues. However, analyzing the data as a function of scan position reduces the

amount of data that may be averaged per calibration point by 1/N, where N is the number of scan positions. This increases the noise from random fluctuations by the square root of N, making it more difficult to determine scan dependent performance. Techniques are needed to derive reliable scan dependent information in cold-end calibration.

There are two major limitations in current warm-end calibration. First, the amount usable data is very limited. Compared to the amount of data from the ocean, the Amazon rainforest provides very little data for statistical analyses or for continuous monitoring. The situation is even worse for intercalibration, where different radiometers with different orbits need to simultaneously overpass the same region, causing further reduction in data availability. Second, reliable scan-dependent calibration information is not available. This is due not only to the limited data availability but also to problems with surface heterogeneity. Forests are not as homogeneous as the ocean, which increases the cross-track variability in TBs. Further investigation is needed to handle the problem of heterogeneity.

Calibration has a dependence on TB and the development of a TB dependent calibration correction is necessary. However, developing a proper TB dependent correction is still problematic. One big barrier is due to the warm-end calibration. Characterizing TB dependence requires at least two-end calibration, cold and warm, to cover the dynamic range of TB. Cold-end calibration has been relatively well

developed, but reliable warm-end calibration is still unavailable. As discussed in above paragraphs, warm-end calibration has large uncertainty due to sparse data and insufficient calibration techniques. The large errors at the warm-end will propagate into empirically derived corrections for radiometer calibration and intercalibration. Warm calibration is especially important for missions like GPM, since TBs from precipitating scenes are considerably warmer than those for clear-sky oceanic scenes.

The calibration variability and dependence on model parameterization have not been carefully investigated. Calibration has temporal and spatial variability that needs to be addressed, and this variability is affected by models used in calibration. For constellation calibration, RTMs and data representing geophysical fields are generally used (Berg et al. 2012; McKague et al. 2011; Sapiano et al. 2013; Wilheit 2013). RTMs consist of parameterized modules such as atmospheric absorption and surface emissivity that always have some level of uncertainty associated with them. The geophysical data are often from numerical weather prediction analysis or reanalysis fields. There are always errors in these data since they cannot perfectly represent the real geophysical conditions (Bengtsson et al. 2004; Dee et al. 2011). These errors in RTM and reanalysis data affect calibration. For instance, the observed radiance from a radiometer is a function of geophysical parameters such as water vapor. The water vapor profile in reanalysis data may have a bias with

respect to the actual profile, and this bias will propagate into simulations and therefore into final calibration results. Additionally, the temporal and spatial variability of water vapor will result accordingly in variability of calibration and in particular of collocation based intercalibration. These challenges have not been investigated previously. As a first step, we need to examine whether calibration variability exists, how it behaves temporally and spatially, how it is related to geophysical parameters, and what the primary and secondary factors are in causing said variability. By addressing these questions, we can move toward understanding and mitigating calibration variability and the effects of model parameterizations.

1.3 Science Applications

Calibrated radiometer data and corresponding derived products have been used in a number of fields in weather and Earth environmental science. In weather research, retrievals have been developed for precipitation, cloud liquid water, profiles of temperature and humidity, oceanic surface wind speed, ice cover, etc. In Earth environmental science, data have been used to study soil moisture, vegetation canopy, lake and river ice, etc.

It is always important to maximize the use of radiometer data. However, in coastal ocean areas or inland lakes and rivers, products are often omitted. For example, Figure 1.7 shows SSM/I-derived wind speeds from standard products of

the NOAA Center for Satellite Application and Research (STAR; http://manati.star.nesdis.noaa.gov), where coastal regions, including the Great Lakes, show no retrievals. These limitations also exist in the SSM/I water vapor and rain-rate products. The lack of retrieval products is due to the relatively large footprint of SSM/I radiometers that covers both land and water within a coastal FOV. The additional land signals make retrievals over water using standard open-ocean algorithms invalid. This phenomenon is often referred to as land contamination.

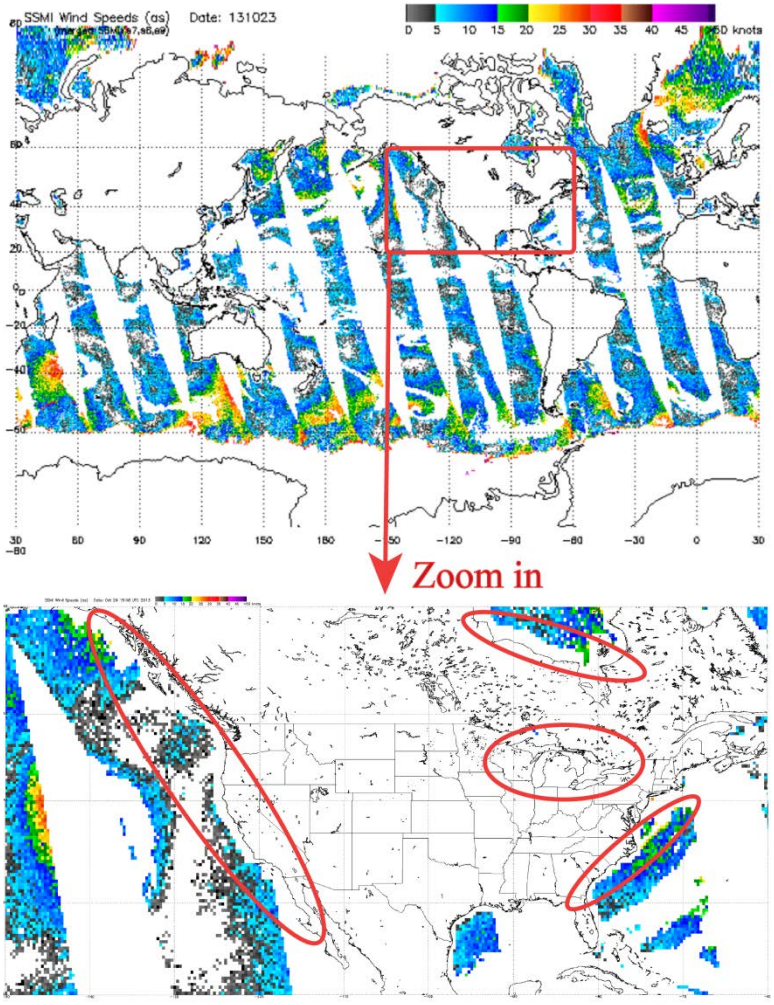

Figure 1.7: Map of SSM/I derived wind speeds globally (upper) and over North America (lower) as produced by NOAA/STAR (http://manati.star.nesdis.noaa.gov).

The circled regions, such as the Great Lakes and water areas within 100 km of coasts, illustrate the lack of retrieval products due to land contamination.

To further illustrate the land contamination problem, Figure 1.8 shows an example of the TB observed by SSM/I over the Great Lakes. Coastal areas of all lakes are contaminated: in particular, the SSM/I footprint extends across all of Lake Ontario, so that all of the lake data are contaminated. Because of land contamination, coastal data have to be discarded without applying any retrieval. However, coastal data contain important information on various physical parameters. For example, the series of SSM/I instruments have documented more than two decades of historical data that could provide useful climatological information about coastal regions.

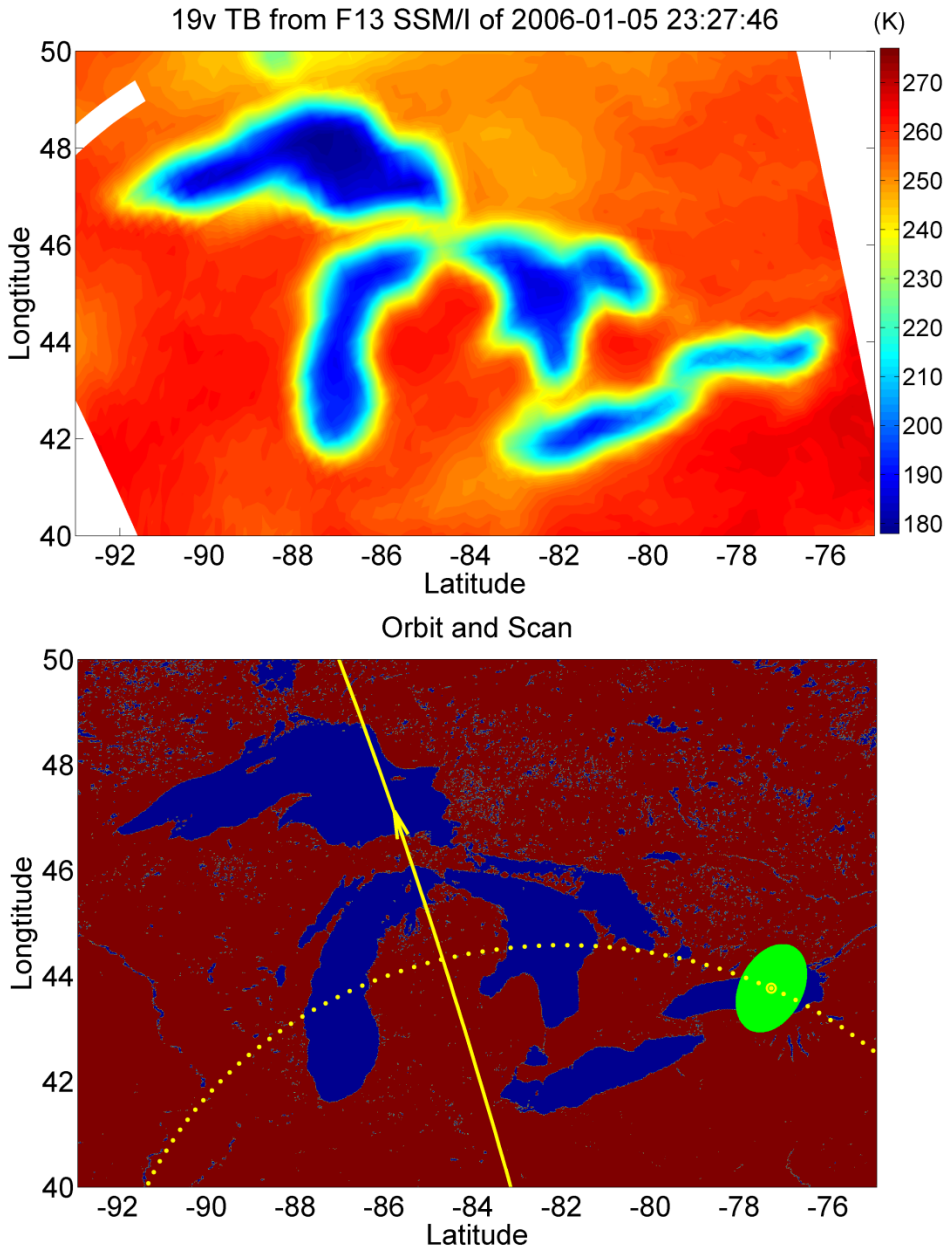

Figure 1.8: An example of land contamination over the Great Lakes (upper) and the corresponding SSM/I scan geometry (lower). In the upper panel, over-water TBs close to coastlines (shaded yellow) are higher than that at the center of the lakes (shaded blue) due to land contamination. For example, all of Lake Ontario is contaminated since the SSM/I footprint is larger than the width of Lake Ontario. In the lower panel, the solid line is the spacecraft ground track, the dotted line identifies the center of each SSM/I sample in a single azimuthal scan, and the green ellipse is a single antenna footprint for the 19V channel (3 times 3 dB beamwidth with 99% on-Earth radiance).

In the past, approaches for correcting land contamination have been reported by other researchers. The main strategy involves two steps toward extrapolating coastal information: first, various techniques have been proposed to remove the land signal from the total signal; next, existing over-ocean algorithms are applied to the corrected data to do retrievals. For example, correction methods were investigated and data after correction were used for retrieving water vapor in the Baltic Sea (Bennartz 1999), wind speed near Britain (Bellerby et al. 1998), coastal wet path delay (Desportes et al. 2007), and sea ice concentration (Maass and Kaleschke 2010). This two-step strategy is physically clear and straightforward, corrections are based on measured data and do not need additional simulation from an RTM, and existing over-ocean algorithms for retrieving physical parameters do not need to change.

Although previous approaches have shown promising results, many issues still need to be addressed. First, reported corrections often show significant inconsistencies. For example, the corrected TBs should be of comparable magnitude in the same region; however, variations between the highest and lowest TBs are at times larger than 20K (Bennartz 1999), which suggests the need to further improve the correction method. Second, our analysis indicates that the difference in corrected TBs can be larger than 10K between different approaches (Bellerby et al. 1998; Bennartz 1999; Desportes et al. 2007), indicating the

necessity to validate those approaches and to reconcile their differences. Third, error sources affecting correction have not been completely considered. For example, spacecraft navigation errors directly affect the estimation of land signals; however, such errors were ignored or assumed to be static previously, and this would produce significant errors in the corrected data. Furthermore, the antenna pattern was typically approximated using a Gaussian pattern (Bennartz 1999; Desportes et al. 2007; Drusch et al. 1999; Maass and Kaleschke 2010). Our analysis found that this is a poor approximation due in part to the absence of sidelobes. In coastal regions, using an inappropriate antenna pattern can result in larger errors than in the open ocean, since TBs are quite different between land and water. Last, the quality of corrected data was not well validated—both removing land-contaminated TBs and retrieval algorithm tuning were often implemented to improve the quality of products near land. When only showing the retrieval products, it is unclear from which the improvements come. In general, there should be two validations. The first is for the corrected TB, which can be compared with simulated TBs over water using the RTM. This validation is important because the quality of corrected TBs is the most important aspect of the correction method; however, it was not presented in previous studies (Bellerby et al. 1998; Bennartz 1999; Desportes et al. 2007; Maass and Kaleschke 2010). A second validation should confirm the retrieved physical parameters from the corrected data with

independent observations (Bennartz 1999; Desportes et al. 2007; Maass and Kaleschke 2010). It is insufficient to solely implement the second validation, because retrieval algorithms are often tuned to match observations in order to compensate for TB errors.

1.4 Thesis Overview

This work concerns spaceborne radiometer calibration, intercalibration, and science applications. It addresses four important challenges in radiometer calibration and one challenge in science applications. The four challenges in radiometer calibration are: improving cold calibration by characterizing scan dependence, developing a more robust warm calibration method, examining the calibration dependence on TB, and investigating calibration variability and dependence on model parameterization. The challenge in science applications of radiometer data is that coastal data are previously unusable and discarded due to land contamination. Methods are developed to answer these challenges. Calibration methods are developed and applied to radiometers within the GPM constellation. Algorithms for removing coastal land contamination are developed. These methods consist of a systematic frame to calibrate and intercalibrate radiometers, and to conduct scientific studies in coastal regions.

Chapter 1 gives the background introduction for this study. The motivation of this study is specified. That is, new methods are needed to address the five important challenges in radiometer calibration and science applications.

Chapter 2 presents an improved method for cold-end calibration. This method produces reliable scan dependent information that was not available previously. In this method, the calibration dependence on spatial and temporal criteria is examined. It is found that spatial resolution for collocation significantly affects intercalibration while temporal resolution does not. The optimal choice for collocation is presented. This method also allows examination of the TB dependence of calibration and intercalibration within a range of cold scenes.

Chapter 3 presents methods for warm-end calibration. While previous warm-end calibration methods resulted in large uncertainties, this method is able to produce relatively precise warm-end calibration. Warm scene calibration is expanded beyond previously utilized sites in the Amazon rainforest to include worldwide inland boreal and temperate forests, as well as forests in coastal and island regions. Techniques for mitigating land heterogeneity are also developed. By using this method, the uncertainty in warm-end calibration is greatly reduced. Scan dependent information can be extracted, which was not previously available due to noise. The data for warm-end calibration are increased by a factor of ~30

compared to previous methods, allowing a near-continuous monitoring of radiometer performance, e.g., with a temporal resolution of almost once per day.

Chapter 4 shows the results of combining cold and warm calibration to diagnose calibration dependence on TB and to develop intercalibration parameters for a radiometer constellation. Combining the newly developed cold and warm calibration method, the full TB-range calibration is obtained. This method is applied to GMI and calibration issues with TB dependence are found and resolved. The TB dependent intercalibration parameters are derived and applied to the GPM constellation.

Chapter 5 tackles the fundamental problem of calibration variability and dependence on model parameterization. A series of analysis techniques are used to examine calibration and intercalibration variability. It is found that calibration has pronounced temporal and spatial variability and depends on geophysical parameters. A 40-day cycle is discovered for all GMI channels in calibration in terms of both calibration and intercalibration. This signal is related to the spatial variation of geophysical parameters that vary periodically with the shifting of calibration locations. Additionally, calibration shows a nonlinear and non-monotonic dependence on geophysical parameters. The nonlinearity and non-monotonic properties come from model parameterization and can result in large

discrepancies between model and observation and calibration. Improper sampling will result in calibration biases due to temporal and spatial variability.

In Chapter 6, the calibrated and intercalibrated data are used for science applications in coastal regions. Methods for removing land contamination signals have been developed to use previously discarded coastal data for scientific study such as surface wind speed retrievals. The land contamination signals are estimated, and then removed, using a representative antenna pattern convolved with a high-resolution land–water mask. This method is demonstrated using SSM/I data over the Great Lakes and validated with simulated data and buoy measurements. This method can be applied to any microwave radiometer in coastal regions for various retrieval purposes.

Chapter 7 summarizes results from these studies and highlights directions for future research.

CHAPTER 2
Cold-End Calibration

2.1 Introduction

Clear-sky ocean observations are the most common on-Earth reference for assessing space borne microwave radiometer calibration. They provide relatively cold, homogeneous scenes for which models are readily available. Calibration from these data can be applied to a single radiometer, or multiple radiometers for intercalibration. Geophysical fields (e.g., sea surface temperature, wind speed, humidity, etc.) are input to a radiative transfer model (RTM) to simulate TBs that a radiometer observes. The difference between observation and simulation can be used to diagnose radiometer performance. Oceanic calibration can be used for the intercalibration of multiple radiometers to account for instrument differences in frequency, EIA, and bandwidth. Geophysical differences between scenes viewed by two instruments can be reduced by collocating FOVs of the instruments to the same area and time. A number of radiometers have been calibrated using the

oceanic collocation method (McKague et al. 2011; Sapiano et al. 2013; Wentz et al. 2001; Wilheit et al. 2015; Wilheit 2013; Yang et al. 2011).

Cold-end calibration still needs to be refined, in particular, to characterize the calibration dependence on scan position. A number of hardware and software errors are scan dependent such as FOV blockage (McKague et al. 2011; Yang et al. 2015a), on-board interference (Draper et al. 2015b; Wentz et al. 2001), spacecraft attitude errors (Berg et al. 2012), and APC issues (Yang et al. 2015a). Characterizing scan dependent calibration can help correct these. However, scan dependent information is often unavailable or noisy in previous studies. Surface heterogeneity results in noise. In addition, the data available for each scan position will be reduced by a factor of N, where N is the number of scan positions, relative to assessing calibration over all scan positions. For instance, N is 246 for on-Earth scenes of GMI. At each scan position, the available data are therefore reduced by orders of magnitude, making calibration vulnerable to noise. Techniques are needed to derive reliable scan dependent information in cold-end calibration. We present possible solutions in this chapter.

2.2 Methodology

The flowchart of oceanic calibration is shown in Figure 2.1. This method can be used to calibrate an individual radiometer or to intercalibrate multiple

radiometers. When intercalibrating radiometers, it is convenient to define the reference and target radiometers (Wilheit et al. 2015; Wilheit 2013). The reference radiometer serves as the transfer standard for the constellation radiometers, while a target radiometer will be calibrated to the reference radiometer. For the GPM mission, GMI is the reference radiometer to which the other radiometers are intercalibrated.

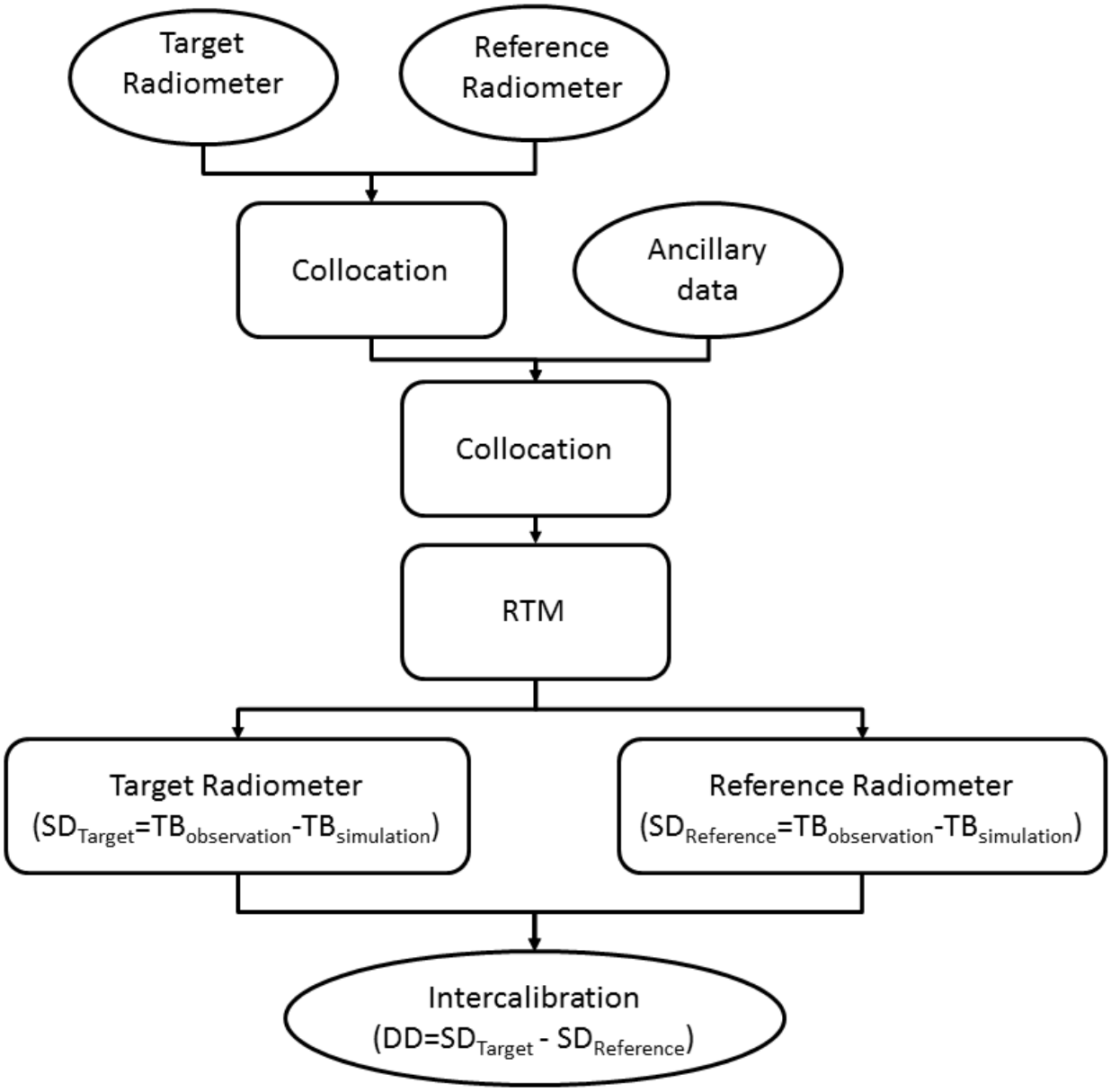

Figure 2.1: Flowchart for computing cold-end calibration single differences (SDs) and intercalibration double differences (DDs). The flowchart can be applied to an individual radiometer or to a target and reference radiometer for intercalibration.

Within this processing flow, the first collocation is implemented to pull out collocated FOVs from the reference and target radiometers. This step can be skipped when calibrating an individual radiometer. The Earth is divided into

subgrids in latitude and longitude. Collocation is satisfied when there are FOVs from both instruments falling into a subgrid box within a specific time window. For instance, a 1°×1° grid resolution and 1-hour time window (time difference is smaller than 1-hour) are often used in previous studies (Biswas et al. 2013; Sapiano et al. 2013; Wilheit 2013). For multiple FOVs from a given radiometer falling within a subgrid box, the corresponding parameters (e.g., TBs) are averaged. Figure 2.2 shows an example of collocation between GMI and TMI from March 2014 to March 2015 with 0.1°×0.1° grid resolution and 1-hour time window (Yang et al. 2015a). Figure 2.3 shows the corresponding TB map of GMI 10.65 H.

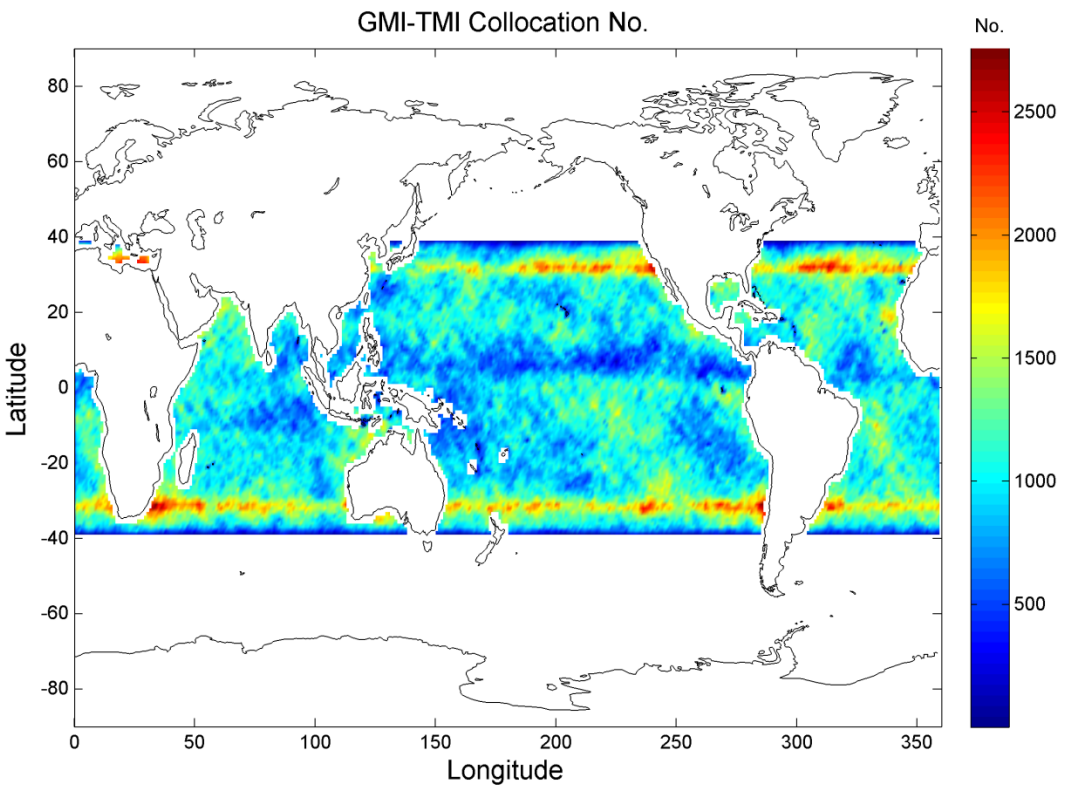

Figure 2.2: A collocation example, showing the number of collocations between GMI and TMI for a 0.1°×0.1° grid from March 2014 to March 2015. GMI and TMI orbits are not sun-synchronous. TMI has a lower orbital inclination that limits the latitudinal boundary [-40°,40°] with more frequent collocations near the boundary.

After the collocated data between the reference and target radiometers are produced, a second collocation is conducted with ancillary data that provide geophysical fields such as sea surface temperature, surface wind speed, atmospheric humidity, and temperature profile. The second collocation assigns these geophysical fields to the observed data. We use the National Centers for Environmental Prediction (NCEP) Final (FNL) Tropospheric Analyses data. NCEP FNL data have a 1°×1° horizontal resolution and 27 vertical layers (NOAA 2000).

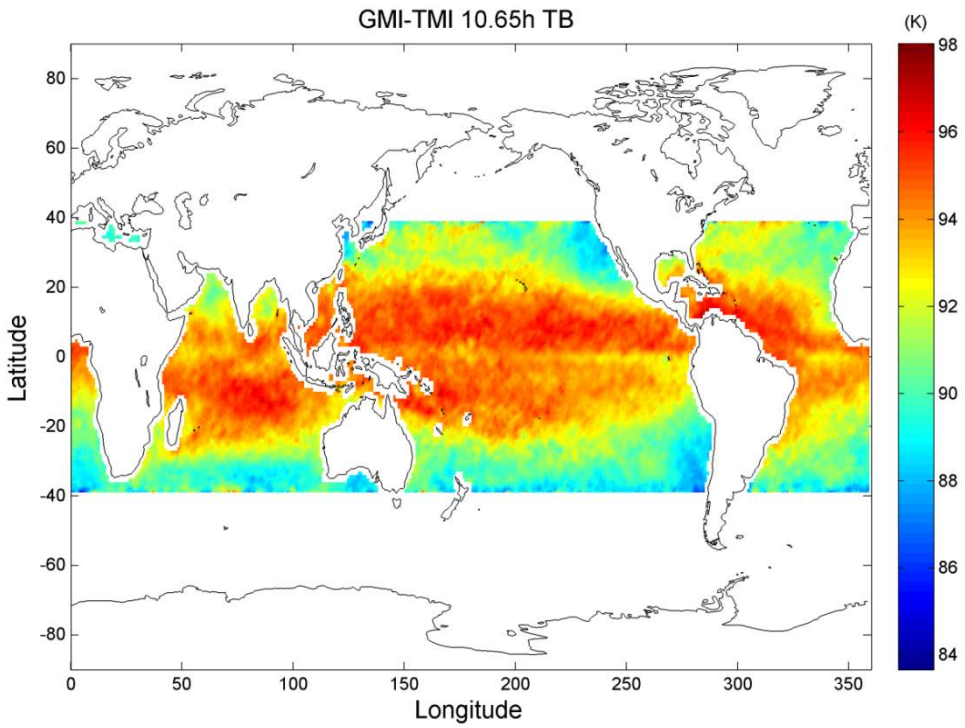

Figure 2.3: The TB map at 10.65H corresponding to GMI-TMI collocation from March 2014 to March 2015.

A RTM is used to simulate TBs from the ancillary data corresponding to the observed TBs. The simulation can be done for an individual radiometer or for both reference and target radiometers. The RTM is a one dimensional plane-parallel (Yang et al. 2014) model developed at the University of Michigan. It is based on modules for atmospheric absorption (Liebe et al. 1991; Liebe et al. 1992; Rosenkranz 1993, 1998) and surface emissivity (Elsaesser 2006; Hollinger 1971; Stogryn 1972; Wilheit 1979) from previous research. The reanalysis fields are interpolated vertically to a 250m resolution for the RTM. The RTM is coded with MATLAB in a highly vectorized way to facilitate parallel simulations for many

(hundreds of thousands) FOVs with multiple frequencies and EIAs. This vectorization results in negligible changes to final simulation outputs while increasing the speed of the RTM by a factor of ~2500.

Rain and heavy clouds cannot be accurately modeled and are removed using a rain filter (Stogryn et al. 1994) before simulation. The rain filters are:

$$\begin{aligned} &TB_{37V} - TB_{37H} > 50K \\ &TB_{19V} < TB_{37V} \\ &TB_{19H} < 185K \\ &TB_{37H} < 210K \end{aligned} \tag{2.1}$$

The effect of applying the filter is shows in Figure 2.4. The GMI data on March 1st, 2015 are shown. The above filter is applied and results are shown for TB at 18.7 H. It is seen that the filter effectively screens out meteorological phenomena such as clouds and a cyclone vortex. In calibration, the oceanic clear-sky data are generally used to reduce simulation uncertainty (McKague et al. 2011; Sapiano et al. 2013; Wentz et al. 2001; Wilheit 2013; Yang et al. 2011).

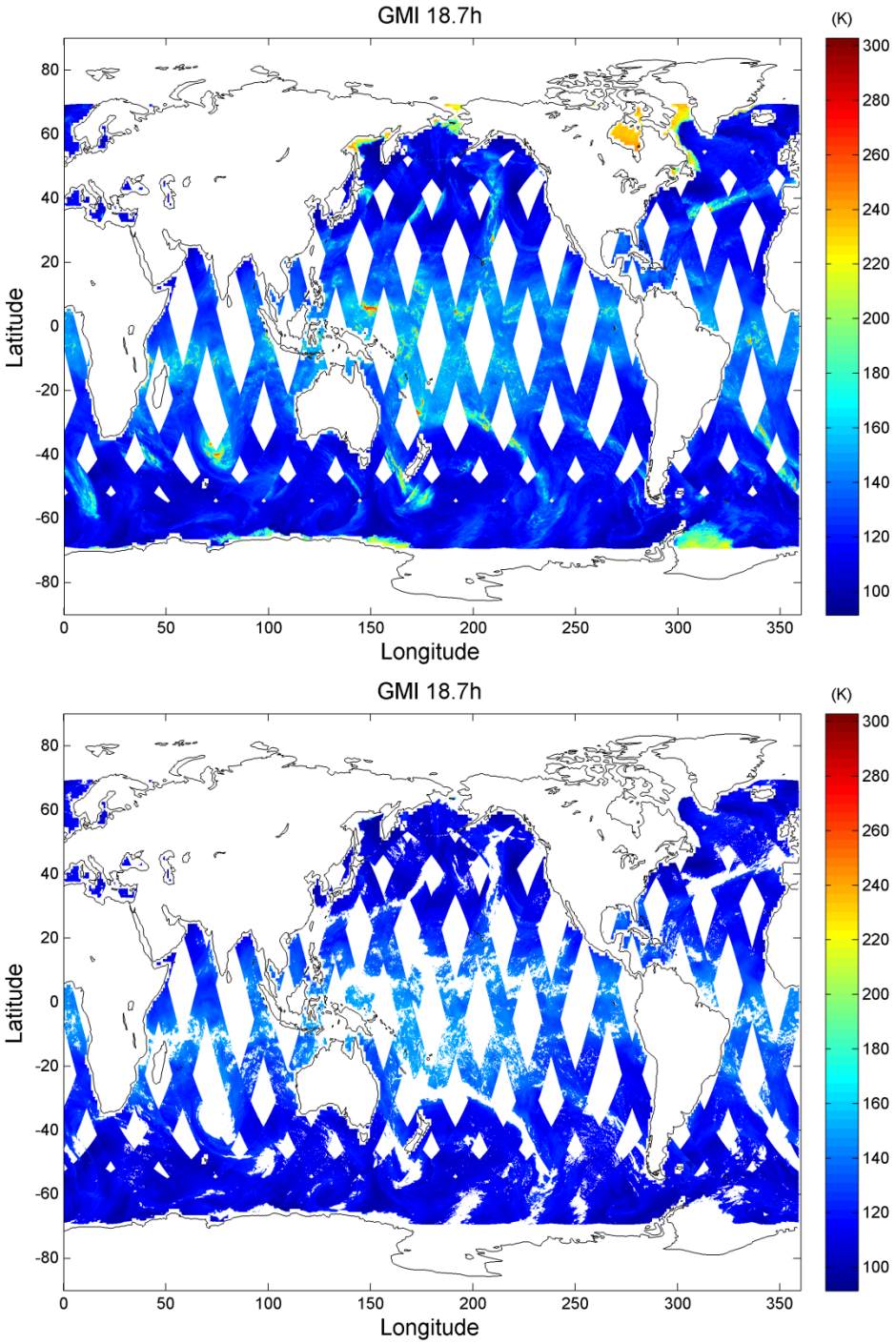

Figure 2.4: Screening out rain and heavy clouds that affect calibration on March 1st, 2015. The upper and bottom panels show before and after applying the filter. Weather patterns like convection (as shown in warm TB at 18.7 H) are effectively screened out.

After implementing the RTM simulations, the difference between the reference and target radiometers can be computed and analyzed. The single difference (SD), observed minus simulated TB, is computed for each individual radiometer. The double difference (DD), i.e., subtracting the single difference for reference radiometer from that for the target radiometer, is the relative bias of the target to the reference radiometer that accounts for radiometer difference in frequency, EIA, and bandwidth (McKague et al. 2011; Wilheit 2013) via the RTM. The DD is written as:

$$\mathrm{DD} = (\mathrm{TB}_{\mathrm{tar}} - \mathrm{TB}_{\mathrm{tar,sim}}) - (\mathrm{TB}_{\mathrm{ref}} - \mathrm{TB}_{\mathrm{ref,sim}}) \tag{2.2}$$

These results are averaged as a function of scan position to examine the scan dependent performance. A number of subsequent analyses can be conducted to assess intercalibration performance.

Some quality control filters are used to screen out extreme cases due to possible precipitation and heavy clouds. A filter is used to control scene homogeneity, regarding the fact that precipitation is often heterogeneous. The filter screens out subgrids with large TB standard deviations and is applied before the RTM simulation.

$$\begin{aligned} \sigma(TB) < 3K,\ f \le 22GHz \\ \sigma(TB) < 5K,\ f > 22GHz \end{aligned} \tag{2.3}$$

The filters for quality control after simulation are:

$$\begin{aligned} \left|SD_{tar}\right| &< 10K \\ \left|SD_{ref}\right| &< 10K \\ \left|DD\right| &< 10K \end{aligned} \tag{2.4}$$

where SD_{tar} is the single difference of the target radiometer, SD_{ref} is for the reference radiometer, and DD is the double difference. These filters screen out cases with major discrepancies between simulations and observations.

In our method, the oceanic cold calibration has several differences from previous methods. The primary difference is that we use collocation criteria different from previous methods. The collocation grid resolution is 0.1°×0.1° with 1-hour time windows. In previous studies, a 1°×1° grid resolution and 1-hour time window (time difference is smaller than 1-hour) are often used (Biswas et al. 2013; Sapiano et al. 2013; Wilheit 2013). This small difference is found to have a significant impact and we will discuss this in the next section. The second difference is the filters used for quality control. The filters affect sampling and results, particularly for samples of small size.

2.3 Scan Dependence

The scan dependent calibration is important for assessing radiometer performance. Given known scan dependent performance (e.g., from pre-launch

characterization), it is also an effective metric for examining the performance of calibration method (Yang et al. 2015a). We find that the collocation criteria have significant impact on scan dependent calibration. We examine a number of space and time collocation criteria. A set of six different collocation grids are examined with 0.01°, 0.05°, 0.1°, 0.5°, 1°, and 2° grid resolution. A set of six different time windows are examined with 0.1, 0.5, 1, 2, 3, and 6 hour matchup windows. In total, 36 different combinations were used as input to the calibration process described in the method flowchart in Figure 2.1.

The collocation grid is found to affect intercalibration significantly. Figure 2.5 shows the comparison of scan dependent performance between grid resolutions of 1° and 0.1°. In previous studies, the collocation criteria were with a 1° grid and 1-hour time window (Biswas et al. 2013; Sapiano et al. 2013; Wilheit 2013). However, it is shown that scan dependent features are much better captured using resolution collocation of 0.1°. The DDs should be consistent from scan position to scan position for a radiometer with proper scan bias corrections, i.e., the scan position dependent DDs should be flat. However, a number of scan dependent anomalies are seen in Figure 2.5. Channel 10.65V tilts up on the right side of the scan, ~1 K higher than the left side. A short period (~5 scan position) oscillation with a peak-to-peak amplitude of ~0.1 K is also seen. This signal is also present in the other channels. Channel 10.65H shows the most significant scan dependent

anomalies, where scan position dependent DDs show fairly significant variability, decreasing from scan positions 0 to 50, increasing from 50 to 80, and increasing again from 180 to 221. Channels 18.7V, 18.7H, 23.8V, and 36.64V show drops in the middle of the scan. Channels 36.64H, 89V, and 89H have the 0.1-K peak-to-peak oscillation and drop slightly at the edge of scan.

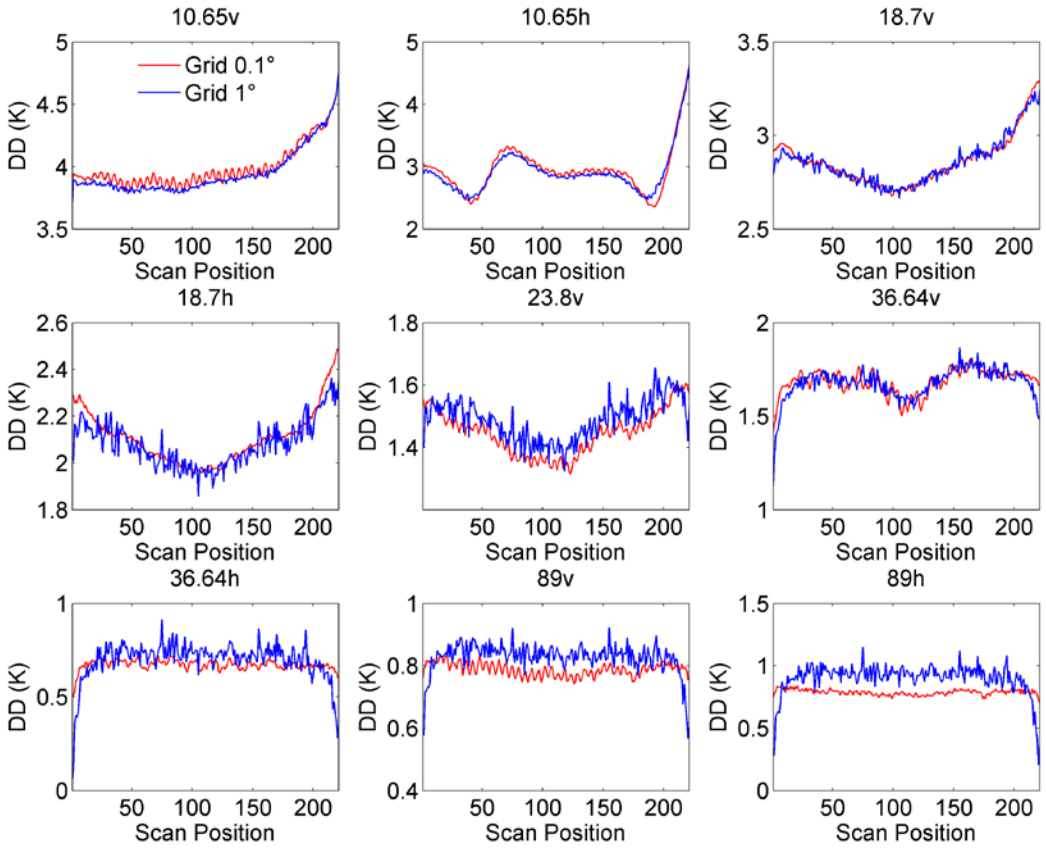

Figure 2.5: Double differences of GMI to TMI as a function of GMI scan position for grid resolutions of 0.1° (red) and 1° (blue). The 0.1° grid is able to resolve more fine scale variability than the 1° grid while the 1° grid shows an unrealistic edge-of-scan drop for 23, 36 and 89 GHz channels.

These scan dependent anomalies have been seen using different methods in prelaunch data, post-launch deep space maneuver analysis, vicarious cold-end calibration, and vicarious warm-end calibration (Draper et al. 2015b; Wilheit et al. 2015). Magnetic interference is the cause of the low amplitude, small period oscillations and the anomalies in middle scan positions. When mechanical scanning is conducted, interference from the onboard magnetic fields results in the longer period variability in 10.65H as well as the short-period, small amplitude oscillations in all channels (Draper et al. 2015b). Variability in the Earth's magnetic field over the spacecraft orbit also induces a magnetic anomaly but with an overall longer period and weaker amplitude (Draper et al. 2015b). Antenna FOV blockage is the source of the observed edge-of-scan biases (Draper et al. 2015b).

Using a 1° grid resolution, as shown in blue lines in Figure 2.5, produces noisy and even unrealistic scan dependent features. The 0.1K peak-to-peak oscillation cannot be resolved at all channels. Unrealistically large drops (amplitudes as high as 0.8 K) relative to other analyses as well as the analysis above at the edge of scan are produced at channels 36.64V, 36.64H, 89V, and 89H. Overall shifting is noticed in some channels (23.8V, 89V&H), resulting in a change in the mean DD across all scan positions relative to the analysis above. These unrealistic features are due to scene heterogeneity and sampling, as discussed in the next section.

Figure 2.6 shows the results with a grid resolution of 0.01° and compares it with 0.1°. The 0.01° case produces noisier results than 0.1°. Beyond some point set by the FOV spacing of the reference radiometer, decreasing the collocation grid spacing reduces the number of boxes with collocations, which results in noisy scan dependent features and hinders diagnosing scan dependent performance. Coarser grids (as with the greater than 0.1° resolution grids in Figure 2.5) may increase the number of observations averaged within a grid box, but for homogenous clear-sky observations the advantage gained by averaging multiple observations from a single radiometer for a given scene is relatively small. For heterogeneous scenes, averaging multiple observations introduces pixels with possible cloud and rain that are difficult to simulate. On the other hand, using a coarser grid reduces the number of grid boxes with collocations for a given scan position to be averaged over the span of the dataset, which in turn provides fewer collocations over which to reduce random variability from day to day.

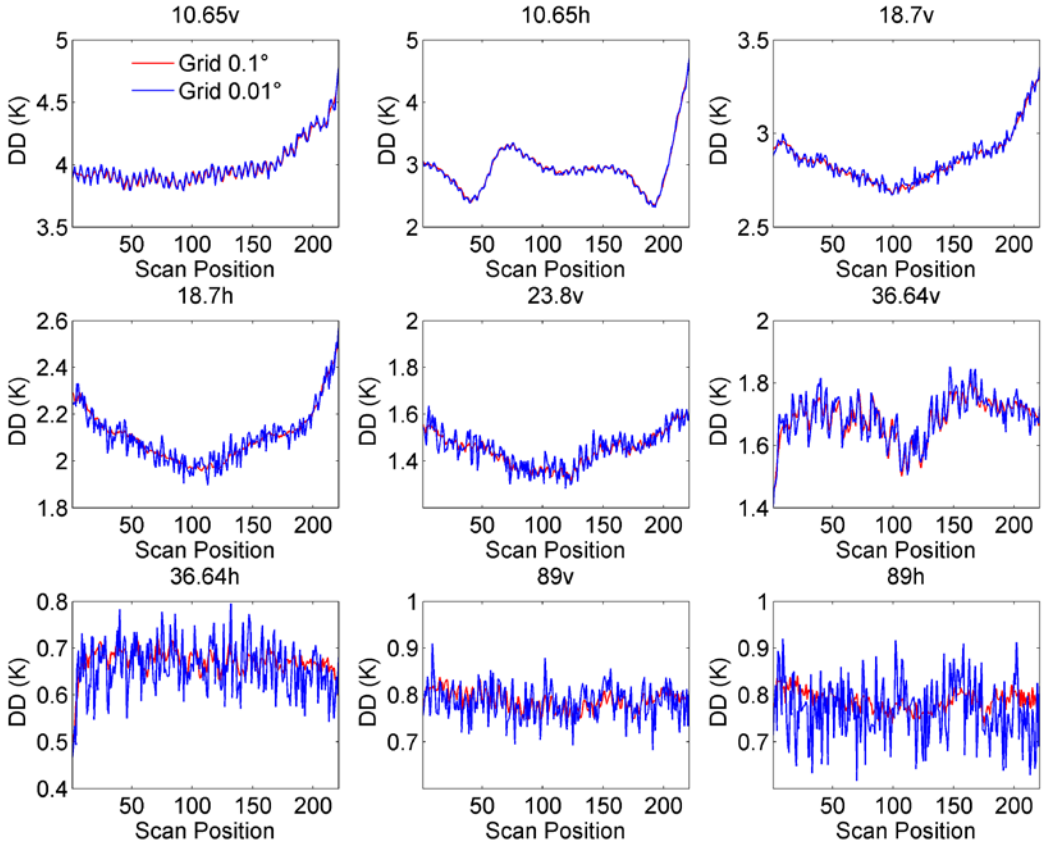

Figure 2.6: Double differences for TMI and GMI as a function of GMI scan position for grid resolutions of 0.1° (red) and 0.01° (blue). The 0.1° grid is able to resolve more fine scale variability than the 0.01° grid for channels above 10 GHz.

In addition to varying the collocation spacing, the time window was also varied. Figure 2.7 shows the comparison of scan dependent DD between 1-hour and 0.1-hour time windows (both with 0.1° grid). There is no significant difference between the two time windows for all channels. Both collocation criteria show realistic scan dependent features as described above. Figure 2.8 shows the comparison between 1-hour and 6-hour windows, and again there is a negligible

difference. In fact, all 36 test cases indicate that the time window selected has no significant impact on calibration.

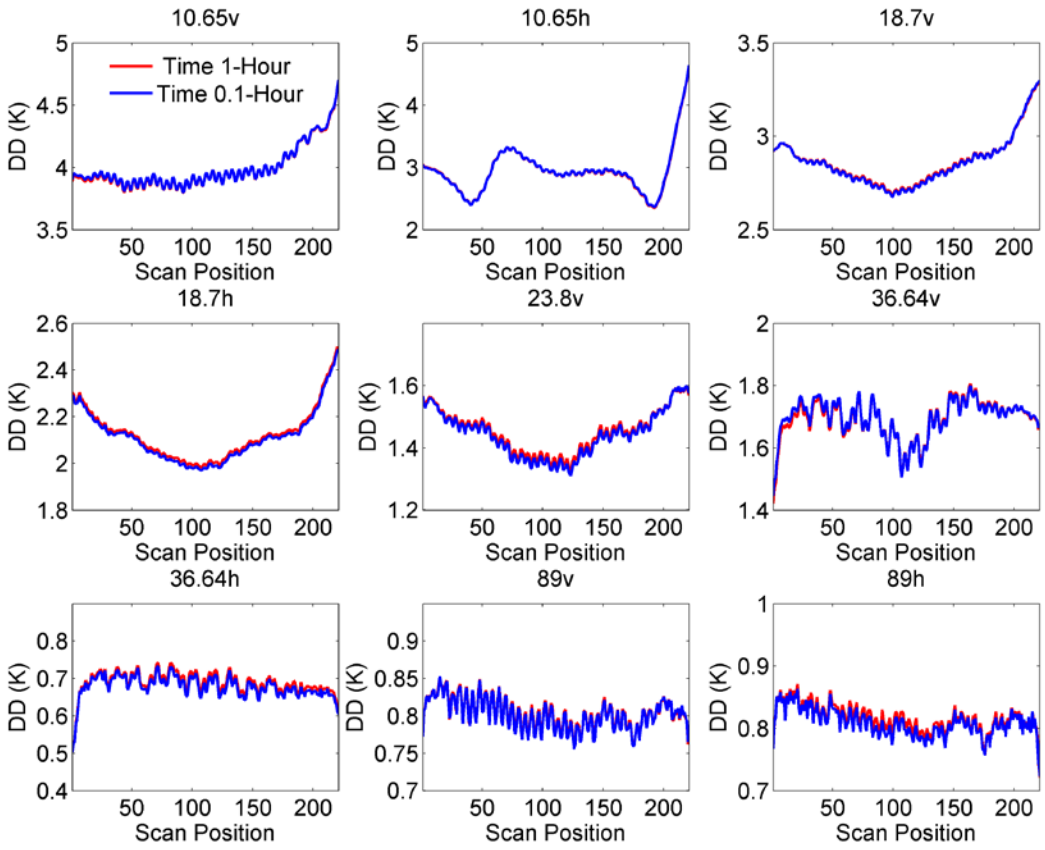

Figure 2.7: Double differences for GMI and TMI as a function of GMI scan position with a 1-hour (red) and a 0.1-hour (blue) time window. Varying the time window over this range has little impact on performance.

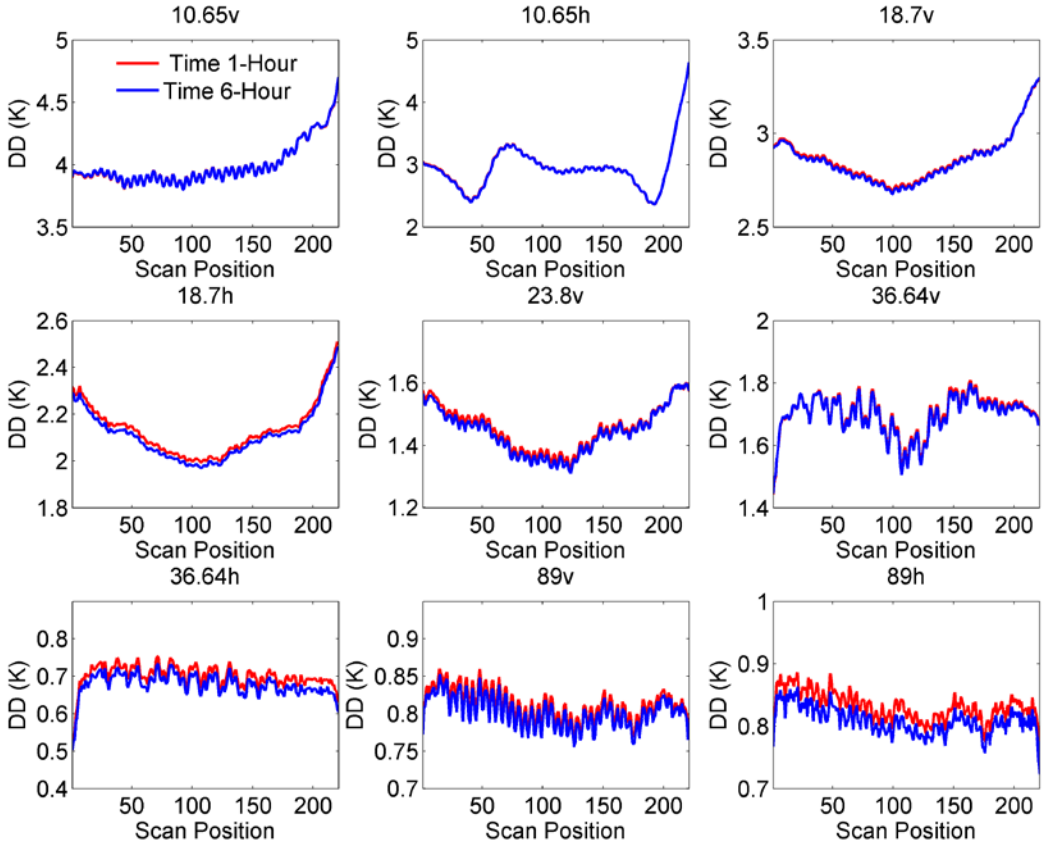

Figure 2.8: Double differences for GMI and TMI as a function of GMI scan position with a 1-hour (red) and a 6-hour (blue) time window. Varying the time window over this range has little impact on performance.

Table 2.1 shows the impact of varying spatial grid size (top) and time window (bottom) on the mean DD across all scan positions and on the number of grid boxes with collocations. The number of boxes with collocations is greatest for 0.1° grid spacing. For example, 0.1° resolution has ~50 times more boxes with collations than 1°, reducing the variability in the scan position dependent intercalibration. The mean DD changes with grid spacing, but the change is small (of the order of 0.01 K) except for the 89H channel (~0.1 K), which is still a

relatively modest shift. By comparison, the time window has a much smaller impact on both the number of boxes with collocations and the mean DD. It should be pointed out that the optimal collocation grid spacing will depend on reference radiometer FOV spacing as noted above.

	Grid (degree, with 1-hour time windows)					
	0.01	0.05	0.1	0.5	1	2
No. Collocation	1076374	24839026	38888798	2522072	793208	247278
10v	3.99	3.99	3.96	3.94	3.95	3.94
10h	2.94	2.92	2.93	2.93	2.94	2.89
19v	2.86	2.86	2.83	2.84	2.85	2.86
19h	2.11	2.11	2.09	2.07	2.08	2.09
22v	1.45	1.44	1.42	1.46	1.48	1.45
37v	1.70	1.69	1.69	1.68	1.68	1.66
37h	0.67	0.67	0.68	0.69	0.70	0.68
89v	0.80	0.80	0.80	0.82	0.84	0.81
89h	0.80	0.79	0.81	0.88	0.91	0.87
	Time (hour, with 0.1° grid)					
	0.1	0.5	1	2	3	6
No. Collocation	40751456	37612792	38888798	37392999	38343671	38353381
10v	3.96	3.96	3.96	3.95	3.96	3.96
10h	2.93	2.93	2.93	2.93	2.93	2.94
19v	2.83	2.84	2.83	2.82	2.83	2.84
19h	2.10	2.10	2.09	2.08	2.10	2.11
22v	1.44	1.44	1.42	1.42	1.43	1.44
37v	1.69	1.69	1.69	1.67	1.69	1.70
37h	0.69	0.68	0.68	0.69	0.68	0.70
89v	0.80	0.80	0.80	0.80	0.80	0.81
89h	0.81	0.80	0.81	0.82	0.81	0.83

Table 2.1: Impact of grid resolution (top) with a 1-hour window, and time window (bottom) with a 0.1° grid on double difference and the number of grid boxes with collocations. The maximum boxes with collocations are with a grid resolution of 0.1°.

2.4 TB Dependence

Calibration dependence on TB is often examined by combining cold and warm calibration. The cold-end has a relative narrow range of TBs compared to combining both cold and warm ends. However, it would be useful to examine the dependence on either end. We use a simple statistical method to examine the TB dependence at cold-end and apply it to examine scan dependence.

Figure 2.9 shows the scan position dependent DD with different TBs. The histogram of observed TBs is used to divide TBs into two sets, cold and warm, where the 50 percentile TB is the boundary. For instance, the boundary point for channel 10.65V is 173.3 K, where the cold and warm TBs below and above this value contain half of total samples, respectively. Accordingly, the DDs are divided into two sets and then averaged as a function of scan position. The value of averaged TBs is given in the legend for each channel.

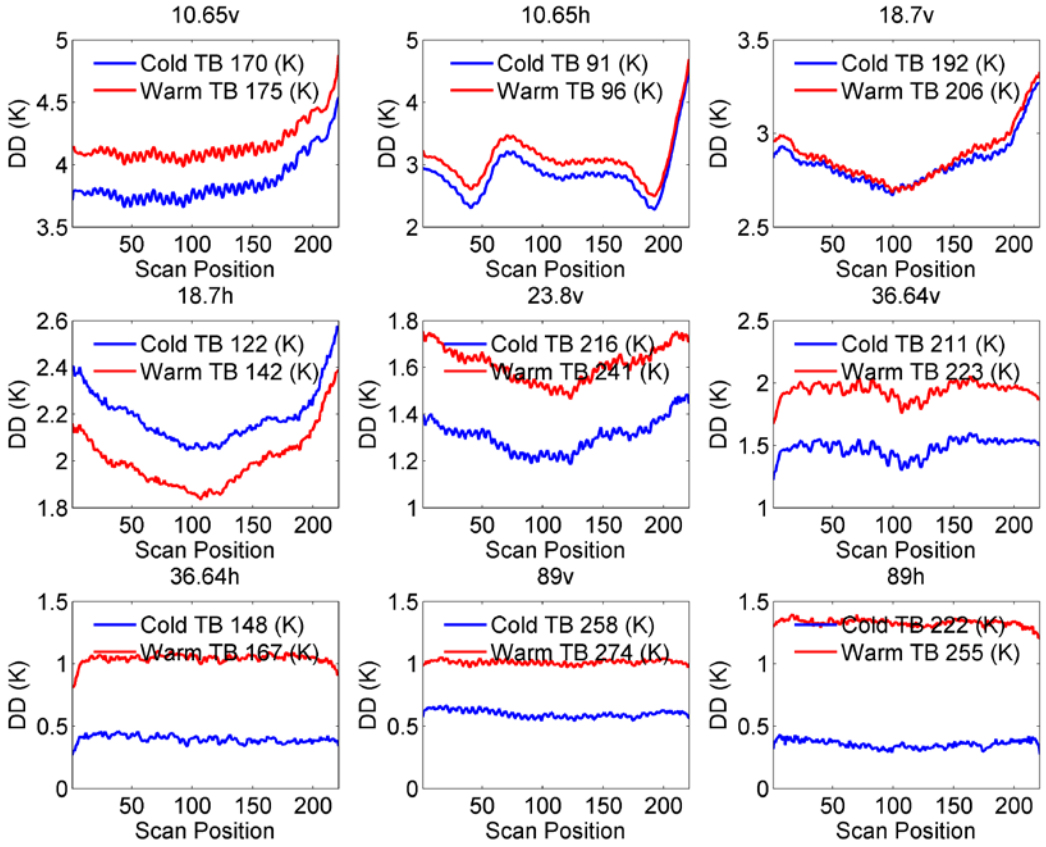

Figure 2.9: Clear-sky over ocean double differences for TMI and GMI as a function of GMI scan position for cold (blue) and warm (red) TBs (mean TBs for each dataset indicated in legend). The mean DDs shift between the cold and warm observations, but the magnitude of the scan position dependent magnetic anomalies does not vary with TB.

The scan dependent DD show clear dependence on TB. Negative dependence is found, i.e., DD is smaller with higher TB, for 18.7H. The other channels show positive TB dependence, i.e., DD increases with TB. The magnitude of this TB dependence varies with channel. Table 2.2 presents the average value across all scan positions. The change of DDs per 10K TB is calculated. Channel 19V has a DD slope of -0.09 K per 10 K TB change. The other channels have positive DD-

TB relationship, where the channels 10V and 89 have the largest change of 0.58 K per 10 K TB change. These results show clear calibration dependence on TB. However, the cold-end calibration has a narrow TB range. To cover the full TB range, warm-end calibration is necessary. This is addressed in Chapter 3.

	DD (K)		TB (K)		ΔDD
	Cold	Warm	Cold	Warm	0.58
10v	3.86	4.16	170.03	175.24	0.47
10h	2.85	3.08	91.41	96.33	0.02
19v	2.84	2.88	192.16	206.15	-0.09
19h	2.19	2.00	121.52	142.42	0.12
22v	1.31	1.61	215.77	241.06	0.39
37v	1.48	1.94	211.08	222.71	0.34
37h	0.40	1.04	148.22	167.30	0.25
89v	0.60	1.01	257.77	274.15	0.29
89h	0.36	1.33	222.47	255.48	0.58

Table 2.2: The TB dependence at cold-end calibration. The mean DDs and TBs are listed with respect to Figure 2.6. The ΔDD corresponds to the change of DDs per 10K TB.

As shown in Figure 2.9, intercalibration (mean DD) is a function of TB. However, the amplitude of the scan dependent magnetic anomalies (short period oscillation, variability in middle of scan) shows no dependence on TB. For example, the bump-shape anomaly at 10H keeps the same amplitude of ~1K, although the DDs shift up with warmer TBs. This indicates that these TB anomalies are additive rather than multiplicative. Therefore, these anomalies can be removed by simply subtracting a constant correction term without considering TB dependence.

2.5 GPM Intercalibration

Figure 2.10: Time series of GMI-TMI daily-mean double difference. The upper panel shows the daily-mean DDs and the lower panel shows the variability with mean DDs removed.

The daily-mean DDs of GMI-TMI are shown in Figure 2.10. The intercalibration indicates that GMI and TMI performance are quite stable. For most channels, the peak-to-peak variation is within 1 K. Channels 18.7 and 23.8 GHz have larger variability. This is due to the geophysical variations such as water vapor and wind speed, which affect calibration through the simulations. We will discuss this further in Chapter 5.

	AMSR2	SSMIS-F16	SSMIS-F17	SSMIS-F18	SSMIS-F19	TMI	WindSat
10v	-3.4	NA	NA	NA	NA	2.3	1.2
10h	-2.9	NA	NA	NA	NA	1.9	0.6
19v	-4.0	-0.3	-0.2	-0.4	-0.6	-0.5	-0.7
19h	-2.0	0.4	0.4	0.1	-2.0	0.1	-2.0
22v	-3.3	0.5	0.6	0.4	-1.5	0.3	-0.9
37v	-2.0	1.5	1.6	1.5	0.0	1.8	-1.5
37h	-3.6	0.8	0.5	0.5	-2.2	0.8	-1.6
89v	-0.5/-0.4	0.5	0.7	0.8	1.4	1.0	NA
89h	-1.1/-0.8	0.8	0.7	0.9	0.1	1.0	NA

Table 2.3: GPM constellation intercalibration (GMI as reference radiometer) at cold end. The value of DDs is shown.

	AMSR2	SSMIS-F16	SSMIS-F17	SSMIS-F18	SSMIS-F19	TMI	WindSat
	Cold	Cold	Cold	Cold	Cold	Cold	Cold
10v	167.0	166.7	167.1	167.4	166.5	170.7	166.8
10h	90.4	90.5	90.7	90.8	90.2	92.4	90.6
19v	189.0	188.0	188.9	189.5	188.0	195.1	188.5
19h	120.8	119.7	121.0	121.7	119.6	128.7	120.4
22v	214.7	212.4	214.4	215.5	212.8	226.1	213.4
37v	212.2	211.7	212.4	212.8	211.7	216.3	212.2
37h	150.6	150.2	151.2	151.8	149.9	156.4	151.1
89v	256.6	254.9	256.5	257.3	255.2	265.4	255.9
89h	221.7	219.3	222.2	223.7	219.5	237.2	221.4

Table 2.4: GMI reference TBs at which the DDs in Table 2.3 were computed.

The cold-end calibration has been applied to the GPM constellation. Tables 2.3 and 2.4 show the table of intercalibration offsets for the GPM constellation relative

to GMI. This table contains intercalibration DDs for windows channels of all available GPM radiometers. Some channels have no intercalibration because those radiometers have fewer channels than GMI. For example, the SSMISs do not have 10 GHz channels and WindSat does not have any 89 GHz channels. These intercalibration numbers are consistent with the other X-CAL teams, as shown in Chapter 4.

The intercalibration table indicates that relative biases are present and depend on the specific instrument. Even for similar instrument like the SSMIS instruments onboard the F16-F19 satellites, DDs vary from instrument to instrument. SSMIS-F19 stands out compared to F16-F18. This could be the fact that F19 was recently launched in 2014 with fewer data than the other SSMIS instruments. AMSR2 and WindSat are overall colder than GMI. SSMIS and TMI are generally warmer than GMI, except some channels and SSMIS-F19. The intercalibration table provides the relative biases between radiometers and will be used to provide constellation data that are consistent from instrument to instrument so that inter-instrument biases don’t propagate into constellation-wide precipitation estimates.

2.6 Conclusions

We develop methods for oceanic cold-end calibration. Characterizing scan dependent performance was used as a metric to assess various criteria that affect

calibration. The impact of collocation criteria, including grid resolution and time window, is investigated. Optimizing these criteria reduces heterogeneity and maximizes sampling, allowing accurate characterization of scan dependent performance. The grid resolution significantly affects intercalibration. The previously used 1° grid does not produce reliable scan dependent calibration. Using a finer grid reduces the impact of scene heterogeneity on collocation and increases the number of averged grids for each scan position. On the other hand, using a grid resolution beyond this optimal point does not improve scan dependent calibration but rather reduces the number of grid boxes for a given scan position. For GMI, we found that a 0.1° grid performs best. The choice of time window has a relatively insignificant impact on intercalibration.

The GMI scan dependent magnetic anomaly and edge-of-scan biases are revealed. This improved method provides reliable scan dependent information. Channel 10H has a significant anomaly with a bump in the middle of scan and edge-of-scan biases. Channels 18.7V, 18.7H, 23.8V, and 36.64V show slight drops in the middle of the scan. Channels 36.64H, 89V, and 89H have the 0.1-K peak-to-peak oscillation and a slight drop at the edge of scan. These scan dependent anomalies have been confirmed using different methods in prelaunch data, post-launch deep space maneuver analysis, vicarious cold-end calibration, and vicarious warm-end calibration. Magnetic interference is the cause of the low amplitude,

small period oscillations and the anomalies in middle scan positions. Antenna FOV blockage is the source of he observed edge-of-scan biases.

The scan dependent DDs for GMI and TMI show a clear dependence on TB. Most channels show a positive TB dependence, where DD increases with TB. Channel 18.7H has negative DD-TB dependence. The magnitude of DD-TB dependence is pronounced. For instance, DD changes 0.58K per 10K TB for channels 10V and 89. Since cold-end calibration does not cover the full Earth-scene TB range, warm-end calibration is necessary. The amplitude of GMI scan dependent magnetic anomalies shows no dependence on TB. Therefore, they can be removed by simply subtracting an empirically derived term from the cold-end analysis.

An intercalibration table is produced for GPM constellation windows channels. This table presents the relative biases of all other radiometers with respect to GMI. The biases can be several Kelvins and vary significant from channel to channel and radiometer to radiometer. Even for the same instrument design like SSMIS, F16-F19 can have different relative biases. Intercalibration is therefore necessary to reconcile instrument differences for the level-1 products (TAs, TBs). Together with warm-end calibration, intercalibration tables have been applied to the GPM constellation to produce the intercalibrated level 1C products that are used to develop level 2 and 3 science products.

CHAPTER 3
Warm-End Calibration

3.1 Introduction

Warm-end calibration is an important part of inflight calibration. Earth scene TBs have a roughly bi-modal probability distribution. Figure 3.1 show the TB histogram at 10.65H of GMI in March 2015. The cold-TB from the ocean and warm-TB from land dominate the distribution, and cryosphere and coastal transition regions provide a smaller percentage of intermediate TBs. TB-dependent calibration errors can come from scan-dependent interference, APC errors, uncorrected radiometer non-linearity, and simulation errors (Yang et al. 2015a). Current vicarious cold calibration uses clear-sky ocean scenes that cover a limited part of the full TB dynamic range (Berg et al. 2012; Draper et al. 2015b; Kroodsma et al. 2012; Wentz et al. 2001; Wilheit 2013). For example, the 10 GHz horizontal polarization TBs of a conical-scanning radiometer typically ranges from 80 to 290 K, while the clear-sky ocean TBs ranges from 80 to 100 K. As a result, empirical

corrections derived from cold scenes alone may not work well for a warm scene (Yang et al. 2015a). For missions like GPM, warm end calibration is especially important because precipitating scenes are considerably warmer than clear-sky ocean scenes at lower microwave frequencies where scattering from ice is not significant. Thus, both cold and warm-end calibration is necessary.

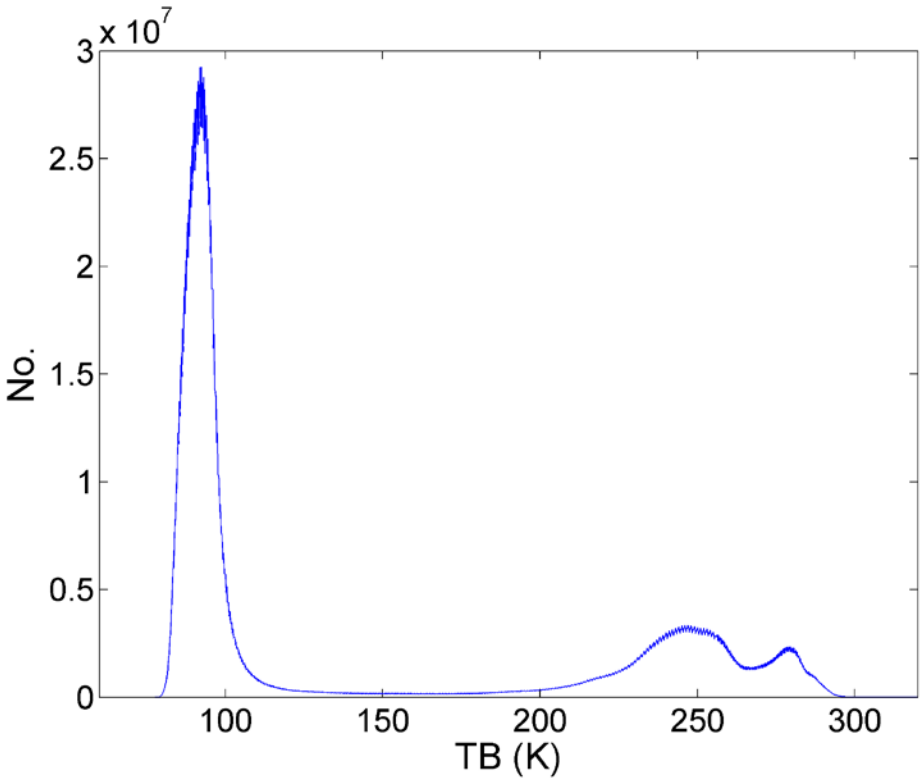

Figure 3.1: The bi-modal distribution of TB at 10.65H of GMI in March 2015. The peak at cold TB corresponds to ~80 K with ~260 K at warm TB.

Modeling warm scene emission is more difficult than cold scenes. It is more difficult to characterize the dependence of land emissivity on polarization, frequency and EIA. Land scenes are also much more heterogeneous than the ocean. As a result, warm-end calibration has to-date provided only limited utility and has

been unable to provide the continuous radiometer monitoring necessary to reliably resolve scan-dependent calibration anomalies at warm TBs. Among the few warm calibration efforts, forests have been used most often (Biswas et al. 2013; Brown and Ruf 2005; McKague et al. 2011; Mo 2005). The branches and leaves of dense forests form an optically thick canopy, hiding the ground that is more difficult to model. An optically thick forest canopy has near-blackbody properties of high emissivity and a small dependence on polarization and EIA.

There are two major challenges in warm-end calibration. First, calibration sites are very few, limiting the amount of data available for a statistically significant analysis of warm-end performance. The two Amazon rainforest areas (latitude ranges [-10°, -5°] and [-5°,-1°], and longitude ranges of [-74°,-65°] and [-59°, -53°]) identified by Brown and Ruf (2005) are typically the only ones used for warm-end calibration. The orbit revisit time over the two areas is several days for an individual spacecraft or a few weeks for collocation of multiple radiometers. The contamination of heavy clouds and precipitation further reduces the volume of usable data. As a result, intercalibration is limited to roughly once every few months. More importantly, warm-end calibration has large uncertainties relative to cold-end calibration. This is due not only to the limited data availability but also to problems of surface heterogeneity. Forests are not as homogeneous as the ocean, which increases the noise in cross-track TBs. Furthermore, the models for forest

emission are less well developed, often depending upon empirical relationships (e.g., Brown and Ruf 2005) with larger uncertainties than their ocean model counterparts. As a result, useful scan dependent information is not available at the warm-end, and mean calibration parameters across all scan position still show large uncertainties. For all these reasons, improved methods are needed to handle the problem of heterogeneity and data availability.

3.2 Methodology

In our improved warm-end calibration, forest calibration sites are determined using a filter of polarization differences:

$$\begin{aligned} TB_V - TB_H &\le 3 \text{ K}, f < 22 \text{ GHz} \\ TB_V - TB_H &\le 2.5 \text{ K}, f >= 22 \text{ GHz} \end{aligned} \tag{3.1}$$

where TB_V and TB_H are TBs at V and H polarization respectively, and f is frequency. Figure 3.2 shows a map of GMI polarization difference compared to a forest map derived from the Phased Array type L-band Synthetic Aperture Radar (PALSAR) measurements. The PALSAR plot shows the annual forest distribution in 2009, provided by JAXA as an Advanced Land Observing Satellite (ALOS) product (Shimada et al. 2011). There is a pronounced similarity between the GMI polarization difference and forest distribution, indicating the potential suitability of these forests as calibration sites in our method.

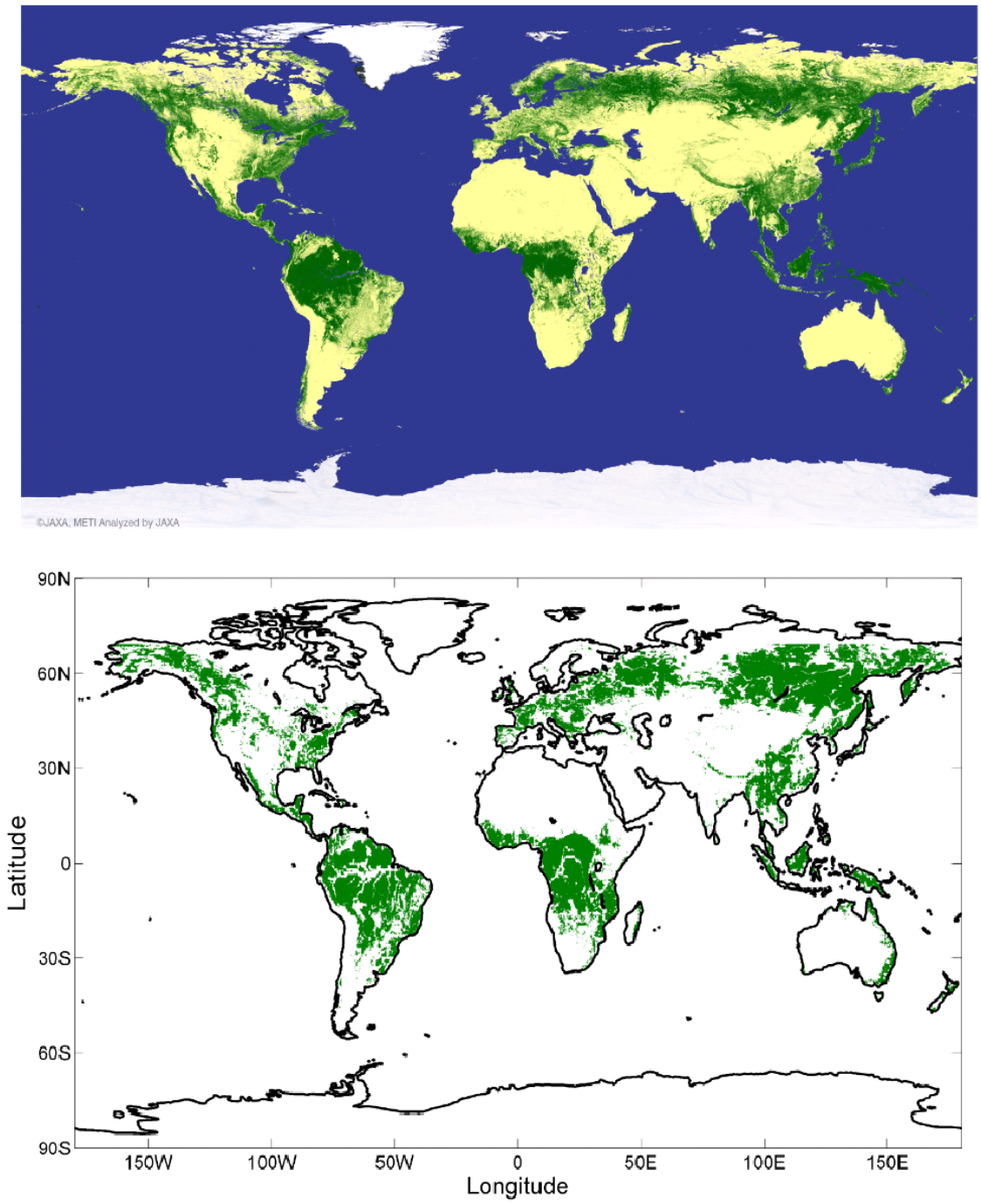

Figure 3.2: The forest distribution from PALSAR (top) and the distribution of vicarious calibration sites from GMI polarization difference (bottom) using the polarization difference filter in Equation 3.1. The determined sites correspond well to forests.

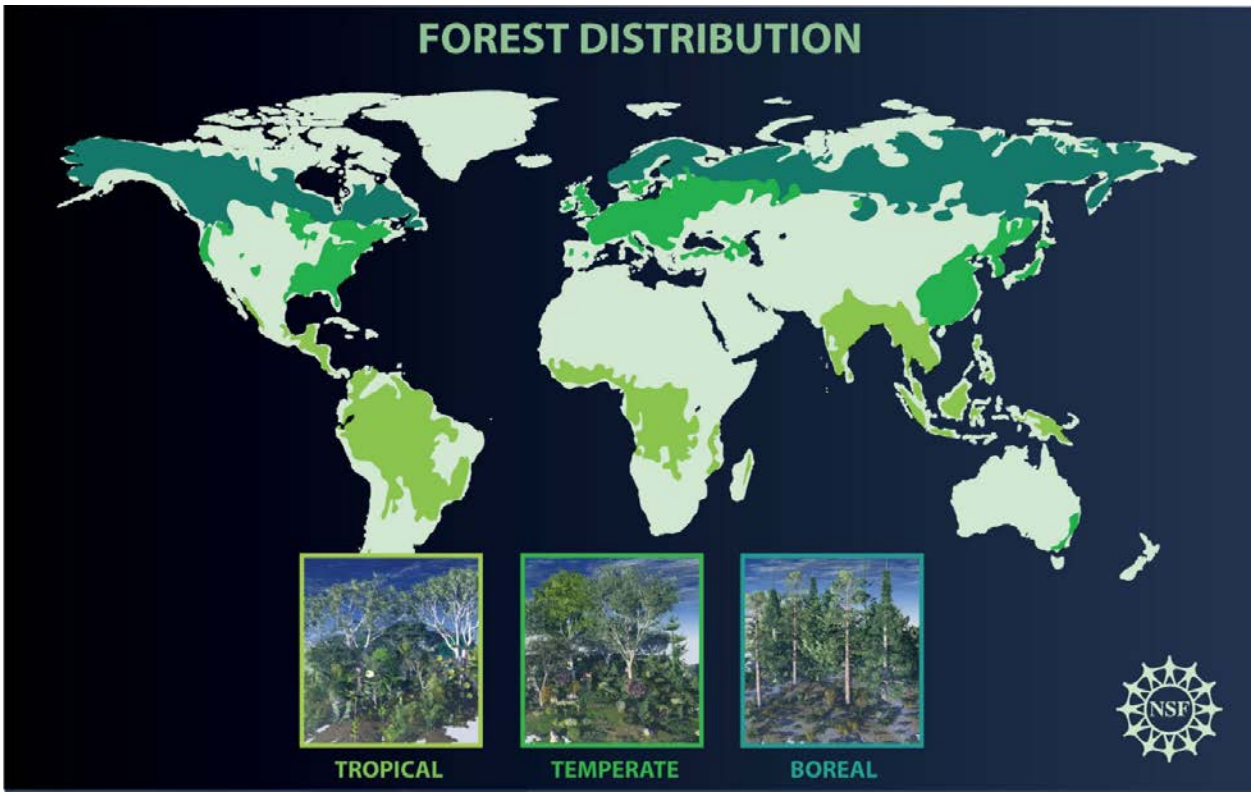

Figure 3.3: Forest distributions of boreal, temperate, and tropical species (http://www.ucar.edu/news/features/forests/).

These calibration sites extend the distribution from the previously used two Amazon rainforest areas to a much wider range. Figure 3.3 shows the distribution of worldwide forest, including three different general classifications: boreal, temperate, and tropical forests (http://www.ucar.edu/news/features/forests/). The figure verifies that these calibration sites can have different forest types other than tropical rainforest. We will use these maps to define a group of calibration regions and validate them.

A model for effective canopy emissivity is used (McKague et al. 2011)

$$\varepsilon = a \times (f - 10.7)^2 + b \tag{3.2}$$

where f is the frequency in GHz, and a and b are constants to be determined; the parameter a is constrained to be negative. In this model, canopy emissivity increases at low frequency until 10.7 GHz because lower frequency radiance is able to penetrate the forest canopy from the lower emissivity surface below, while higher frequency radiance scatters more, obscuring the surface and decreasing the effective emissivity (Ferrazzoli and Guerriero 1996; Macelloni et al. 2001; McKague et al. 2011). The two parameters, a and b, can be determined empirically using multiple channels. For instance, the five channels of GMI from 19 to 37 GHz can be used to determine the two unknowns. This emissivity model does not account for angular dependence, since both model and observation show that dense forests have only a small emissivity dependence on incidence angle (Macelloni et al. 2001; Mo 2005). Macelloni et al. (Macelloni et al. 2001) compared airborne measurements with simulation, showing that forest emissivity is relatively flat as a function of incidence angle. Mo (Mo 2005) showed that observed TBs from the cross-track radiometer AMSU-A over Amazon rainforest have little angular dependence. The impact of angular dependence is further reduced when intercalibrating conical scanning radiometers, which often have EIAs varying over only a few degrees such as WindSat (50°-55°) and GMI (50°-53°).

The above equations can be combined with a RTM to retrieve the surface emissivity using data from a reference radiometer. Then surface emissivity can be used in the RTM to simulate TBs for both reference and target radiometers, respectively. The double difference can be calculated after simulation.

A few filters are used on the observations for data quality control. An effective filter for screening precipitation is found to be

$$TB_{19V} - TB_{37V} \leq 10K \tag{3.3}$$

Greater scattering from precipitation at the higher frequency results in a decrease in the higher frequency radiance and therefore an increase in the difference between TB 19V and 37V (Brown and Ruf 2005). Filters for the single and double differences are used to screen out data with anomalous observed or simulated TBs

$$\begin{aligned} &(TB_{ref} - TB_{ref,sim}) \leq 3K \\ &(TB_{tar} - TB_{tar,sim}) \leq 8K \\ &DD \leq 8K \end{aligned} \tag{3.4}$$

TB range filters are used to screen out extreme high or low TBs, which can result from the presence of ice (cold TBs) or radio frequency interference (warm TBs):

$$\begin{aligned} &260K \leq TB_{ref} \leq 320K \\ &260K \leq TB_{tar} \leq 320K \end{aligned} \tag{3.5}$$

A filter for retrieved surface emissivity removes poor quality retrievals:

$$0.7 \le \varepsilon \le 1 \tag{3.6}$$

Sufficiently dense forests have emissivity values above 0.9 (Macelloni et al. 2001). Non-physical retrieved emissivities above unity or below the lower bound can be caused by inaccurate representation of atmospheric emission derived from ancillary data such as NCEP FNL data.

We demonstrate this method by intercalibrating GMI and WindSat and then apply it to all GPM constellation radiometers. WindSat is a conical-scanning polarimetric microwave radiometer aboard the Coriolis satellite launched on Jan. 6, 2003 (Gaiser et al. 2004). It has 22 channels at five frequencies. The 10.7, 18.7 and 37 GHz are fully polarimetric, each frequency including vertical (V), horizontal (H), +45°, -45°, left-hand circular and right-hand circular polarizations. The 6.8 and 23.8 channels are dual polarized (V and H only). WindSat's EIA ranges from 50° to 55°. WindSat has been well calibrated and has shown satisfying performance since its operation (Gaiser et al. 2004; Jones et al. 2006; Ruf et al. 2006).

3.3 Scan Dependence

GMI scan dependent performance is examined at the warm end. Figure 3.4 shows the GMI-WindSat DD as a function of GMI scan position for each channel. The red lines are from our method, while the blue lines show results using the

previous method that uses a 1° grid for collocation and is refers to as COL-1 (Biswas et al. 2013). The most significant along-scan anomaly is noted at 10.65H, where the DD first decreases from scan positions 0 to 50, then increases from 50 to 80, and tilts up again from 180 to 198 with a slightly drop from 198 to 221. A similar feature but with a smaller amplitude is also found at 10.65V. Noticeable tilts on the right side of scan position are seen at 18.7V and 18.7H. The edge-of-scan drop on the left side is noticed at 36.64V and 36.64H. The absolute value of DDs indicates that GMI has positive biases from 10.65 to 23.8 GHz and negative biases at 36.64 GHz. The old method produces such noisy scan dependent calibration that it cannot be used to infer any scan dependent hardware performance.

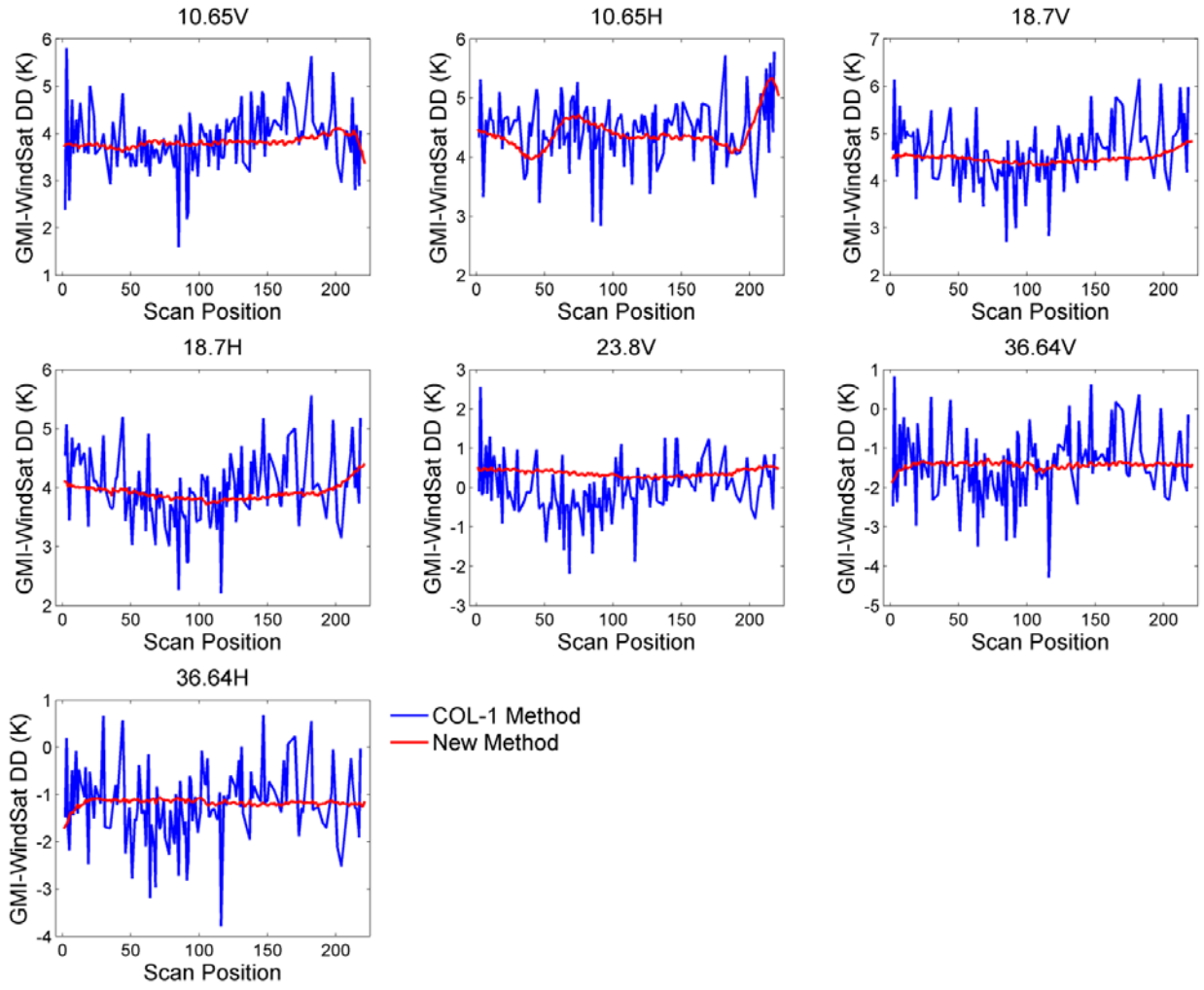

Figure 3.4: The GMI-WindSat along-scan double differences using the warm scene calibration method. The red lines are from our method that reveals the along-scan information: the magnetic anomalies from scan position 50 to 100 at 10.65 V- and H-pol, and the edge-of-scan anomalies at different channels. The blue lines are from previous "COL-1" method that has large fluctuations with indistinguishable along-scan signals.

These scan dependent anomalies are consistent with cold-end analyses as well as with different calibration teams using methods such as prelaunch data, vicarious cold-end calibration, and deep space maneuver (Draper 2014a; Draper et al. 2015b; GPM Intersatellite Calibration Working Group (XCAL) 2015). Magnetic

interference is identified as the main cause of the feature observed around scan position 50 for 10.65H (Draper et al. 2015b; Yang et al. 2015a). The edge-of-scan biases are due to antenna FOV blockage (Draper et al. 2015b). These anomalies and biases, particularly the 10.65H magnetic feature, are useful tracers. They should be detected in different calibration sites. They can also be used to examine and improve the APC and along-scan corrections.

The importance of using extended worldwide forests rather than limited Amazon areas is illustrated in Figure 3.5. Figure 3.5 shows the results using the same method but with different areas. The red lines are from using worldwide forest sites, and the blue lines are from using only the two Amazon rainforest areas (Brown and Ruf 2005). The method is the same, but the sample sizes are different. It turns out that using limited Amazon areas produces unrealistic scan dependent features relative to what is seen in the worldwide data and in the cold end analysis.

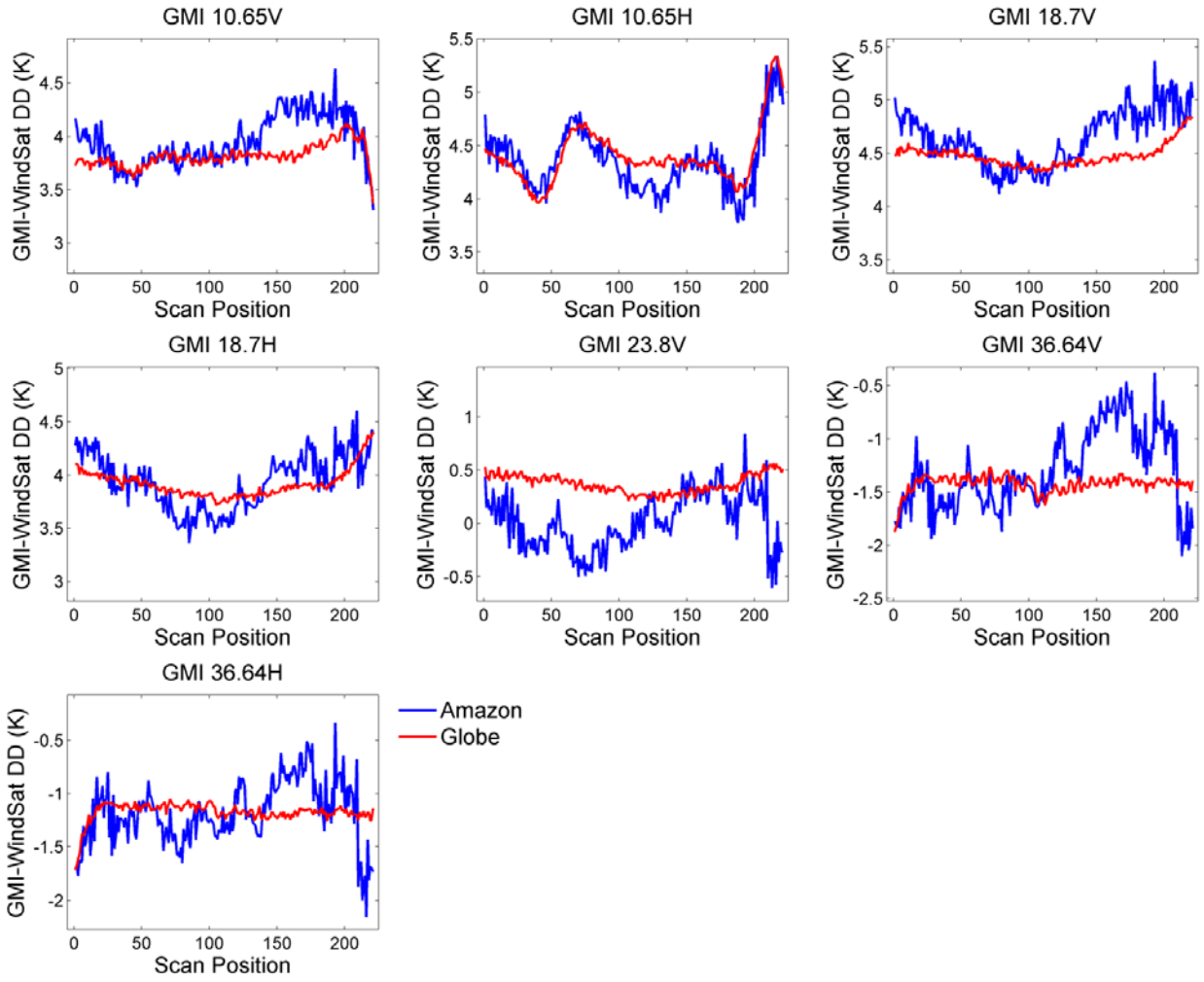

Figure 3.5: Comparison of GMI scan-dependent bias detection for warm TBs derived from double differences using only Amazon rainforest sites (blue) and global sites (red). Much larger fluctuations result from using only Amazon rainforest sites because of their limited sample size.

We implement a rigorous examination of collocation criteria, grid resolutions and time windows. The grid resolution is found to significantly affect calibration. A set of grids are used, including 2°×2°, 1°×1°, 0.5°×0.5°, 0.25°×0.25°, 0.1°×0.1° and 0.05°×0.05°. The time difference is kept the same at one hour. Figure 3.6 shows an example of an along-scan DD comparison between 1°×1° and 0.1°×0.1°

grids. The 1°×1° grid is very noisy, while the 0.1°×0.1° grid significantly reduces the noise so that along-scan features are discerned. Figure 3.7 shows the comparison of 0.1°×0.1° to a finer resolution 0.05°×0.05°. The 0.05°×0.05° grid is noisier because of the decrease in number of collocated data points in each grid box.

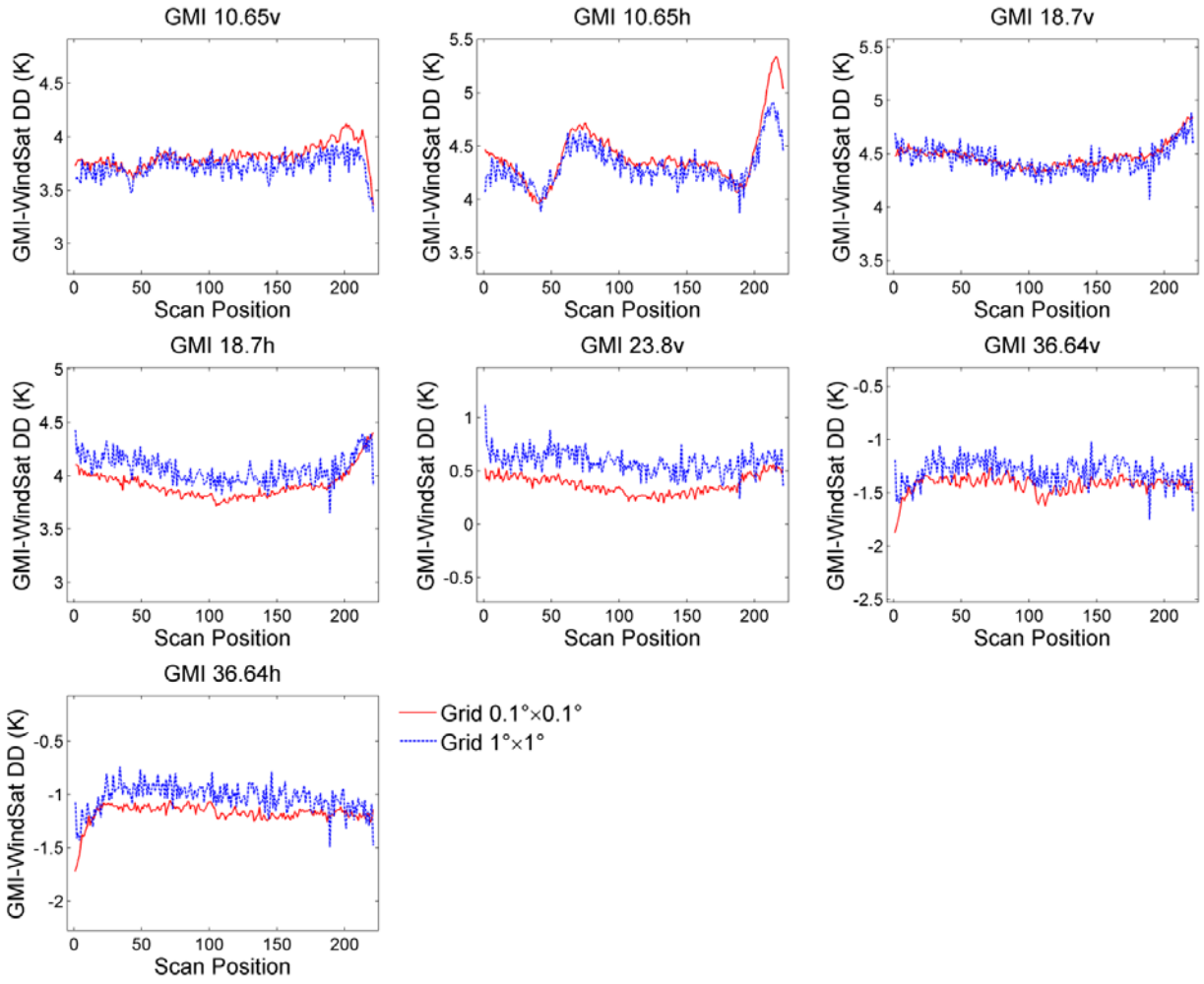

Figure 3.6: The impact of grid resolution on along-scan calibration, 1°×1° (blue) versus 0.1°×0.1° (red). Both use identified global forest sites with 1-hour intercalibration time difference. The absolute double difference and degree of fluctuation change with grid resolution. Using 0.1°×0.1° grid gives more accurate double differences and best resolves the along-scan information. The reduction of

fluctuation improves the statistical properties of the ensemble across all scan positions as well as the ensemble mean. The new warm-end ensemble mean double difference is also better aligned with cold-end results in terms of better improved linear regression from cold and warm results.

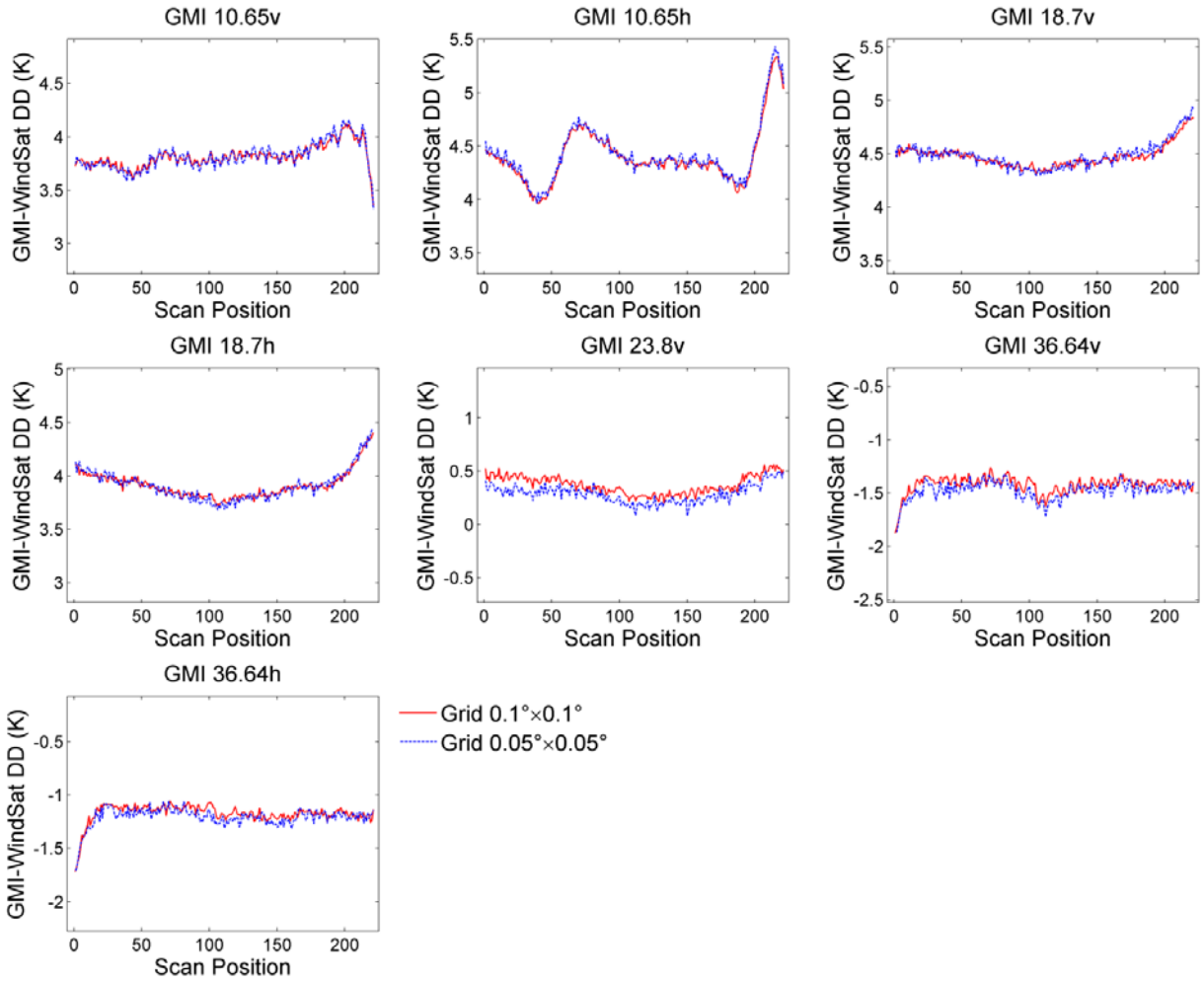

Figure 3.7: The same as Figure 3.5, but for 0.1°×0.1° versus 0.05°×0.05°, where the 0.1°×0.1° grid is better. For instance, the ripple signal at 10.65 V&H with 0.1 K amplitude is clear with 0.1° grid.

Figure 3.8 shows the 10.65H along-scan DDs at each grid resolution given above. Using the 0.1°×0.1° grid produces the best results such as maximizing the sample size and best discerning along-scan anomalies. It should be noted that the 0.1°×0.1° grid is not a universal optimum. The choice of an optimal grid resolution

can depend on radiometer specifications such as footprint size and scanning interval distance. It should also be noted that the actual size of a grid box is a function of latitude, i.e., smaller at higher latitude, since we use uniformly divided grids in the unit of degrees latitude and longitude.

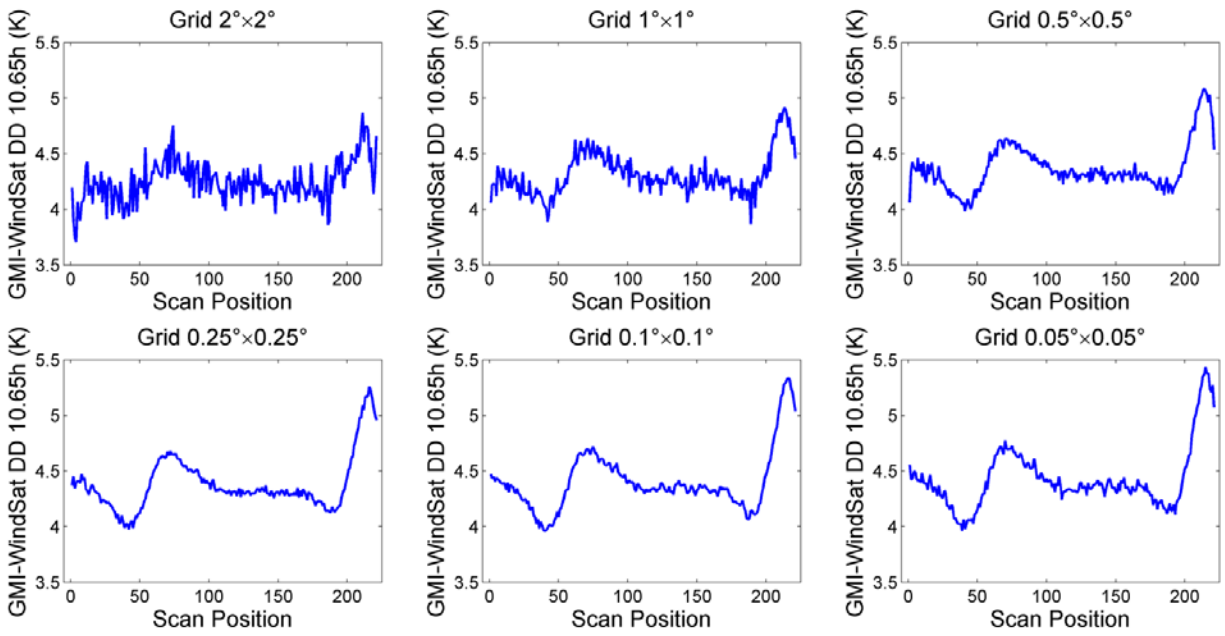

Figure 3.8: The 10.65H anomalies detected with different grid resolutions, 2°×2°, 1°×1°, 0.5°×0.5°, 0.25°×0.25°, 0.1°×0.1° and 0.05°×0.05°, where grid 0.1°×0.1° is the best (they all use identified global forest sites with 1-hour intercalibration time difference). The identified global forest sites are used and the intercalibration time difference is one hour.

Table 3.1 presents DDs and the number of collocations (collocated grid boxes) for different grid resolutions. The DDs change gradually with grid resolution at all channels. The 23.8V DD decreases from 0.58 K with 2°×2° to 0.29 K with 0.05°×0.05°. The number of collocations increases when grid resolution decreases from 2°×2° to 0.1°×0.1°, then decreases with smaller grid resolution. It should be

noted that the number of collocations are defined as the number of collocated grid boxes, and the collocated TBs has been averaged at each grid box (if there are multiple TBs at each grid box) before applying intercalibration methods. The number of collocations first increases with finer grid because of an increase in the number of grid boxes, then decreases with extremely fine grids due to strict constrains for collocation since the distance between two FOVs from reference and target radiometers has a distribution that tails off toward small distance and has a minimum greater than zero.

	Grid0.05	Grid0.1	Grid0.25	Grid0.5	Grid1	Grid2
No. Col.	195673	433662	210451	74424	27160	10362
10v	3.82	3.81	3.80	3.78	3.73	3.65
10h	4.44	4.40	4.38	4.38	4.33	4.27
19v	4.48	4.46	4.44	4.45	4.44	4.42
19h	3.91	3.90	3.96	4.04	4.06	4.05
23v	0.29	0.36	0.52	0.57	0.58	0.58
37v	-1.48	-1.42	-1.33	-1.30	-1.31	-1.32
37h	-1.21	-1.17	-1.08	-1.03	-1.03	-1.05

Table 3.1: The impact of grid resolutions on double differences and the corresponding number of collocations. Using the 0.1°×0.1° grid has the maximum number of collocations. The absolute value of double differences shifts with grid resolutions.

Grid resolution affects calibration in two ways. A coarse grid resolution is vulnerable to land heterogeneity. Finer grid resolutions better constrain the collocation of FOVs to the same scenes. Additionally, fine grid resolution results in more subgrid boxes containing collocations. Recall that the observations from all collocations within a given subgrid box for a given instrument are averaged to

form one valid data point for the given 1 hour time frame. So with more subgrid boxes with collocations, the sample size is increased and fluctuations are reduced. It should be noted that grid resolutions cannot be arbitrarily small, since there is always some distance between different FOVs. Too fine a grid resolution does not mitigate scene heterogeneity but reduces the number of subgrid boxes with collocations.

We also examined the impact of time differences on calibration. They have an insignificant impact on the along-scan and average DDs. For example, changing the time difference from 60 minutes to 30 minutes does not produce a noticeable effect.

3.4 Regional Difference

We examine the site-to-site differences in the boreal, temperate, and tropic forest areas. As shown in Figure 3.9, nine sub-regions are defined. They represent boreal, temperate, and tropical regions, including 1) Alaska (boreal), 2) West Russia (boreal), 3) East Russia (boreal), 4) Europe (temperate), 5) East Asia (temperate), 6) USA (temperate), 7) South America (tropical), 8) Africa (tropical), and 9) Southeast Asia (tropical).

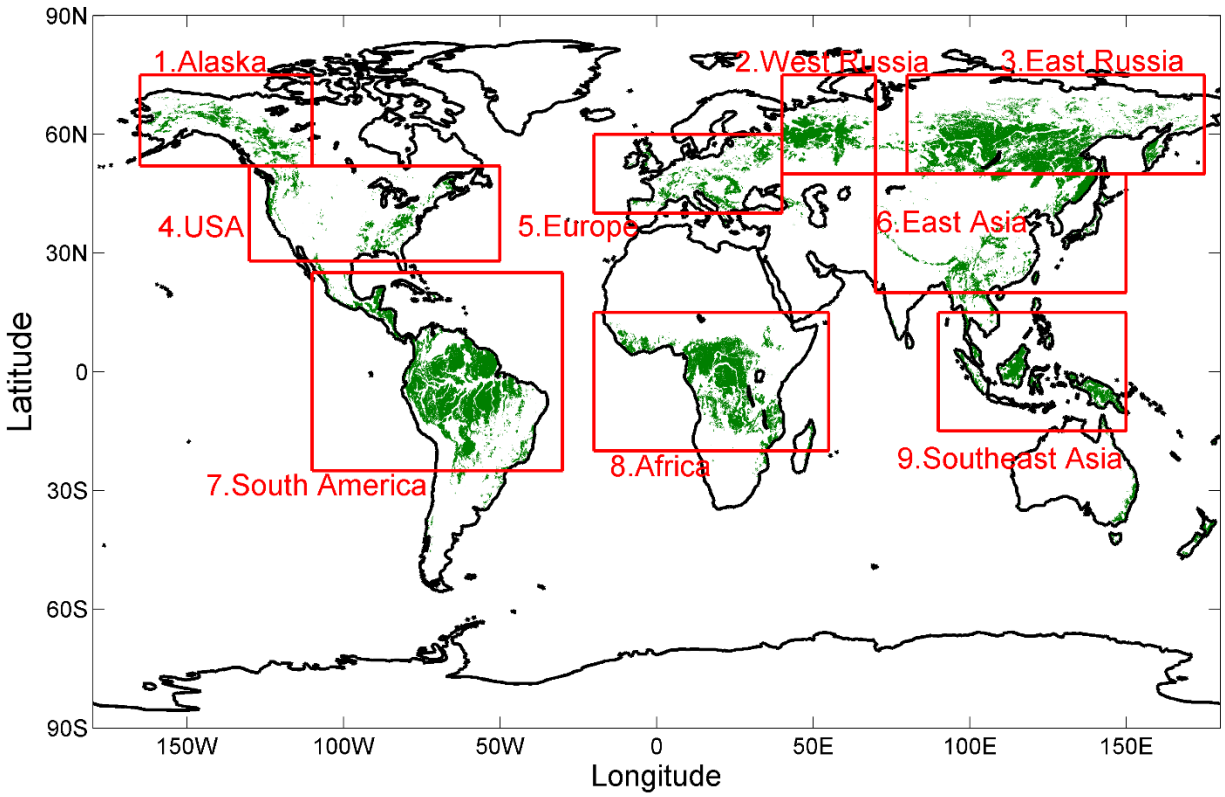

Figure 3.9: The distribution of collocated calibration sites (green color) between GMI and WindSat. Nine sub-regions are defined for comparison: 1. Alaska, 2. West Russia, 3. East Russia, 4. USA, 5. Europe, 6. East Asia, 7. South America, 8. Africa, and 9. Southeast Asia. Regions 1 to 3 are boreal forests, 4 to 6 are temperate forests, and 7 to 9 are tropical forests.

Figure 3.10 shows the DDs as a function of scan position for the 10.65H channel for each of the nine regions. These regions all show the magnetic anomalies and edge-of-scan biases. Fluctuations on top of the signal seen for data from all regions above, which vary region by region, mainly due to the number of samples, are considered in the next section. The inland boreal and temperate regions as well as coastal and island regions show results consistent with the other

regions. Like 10.65H, the other channels also have consistent results among the nine regions.

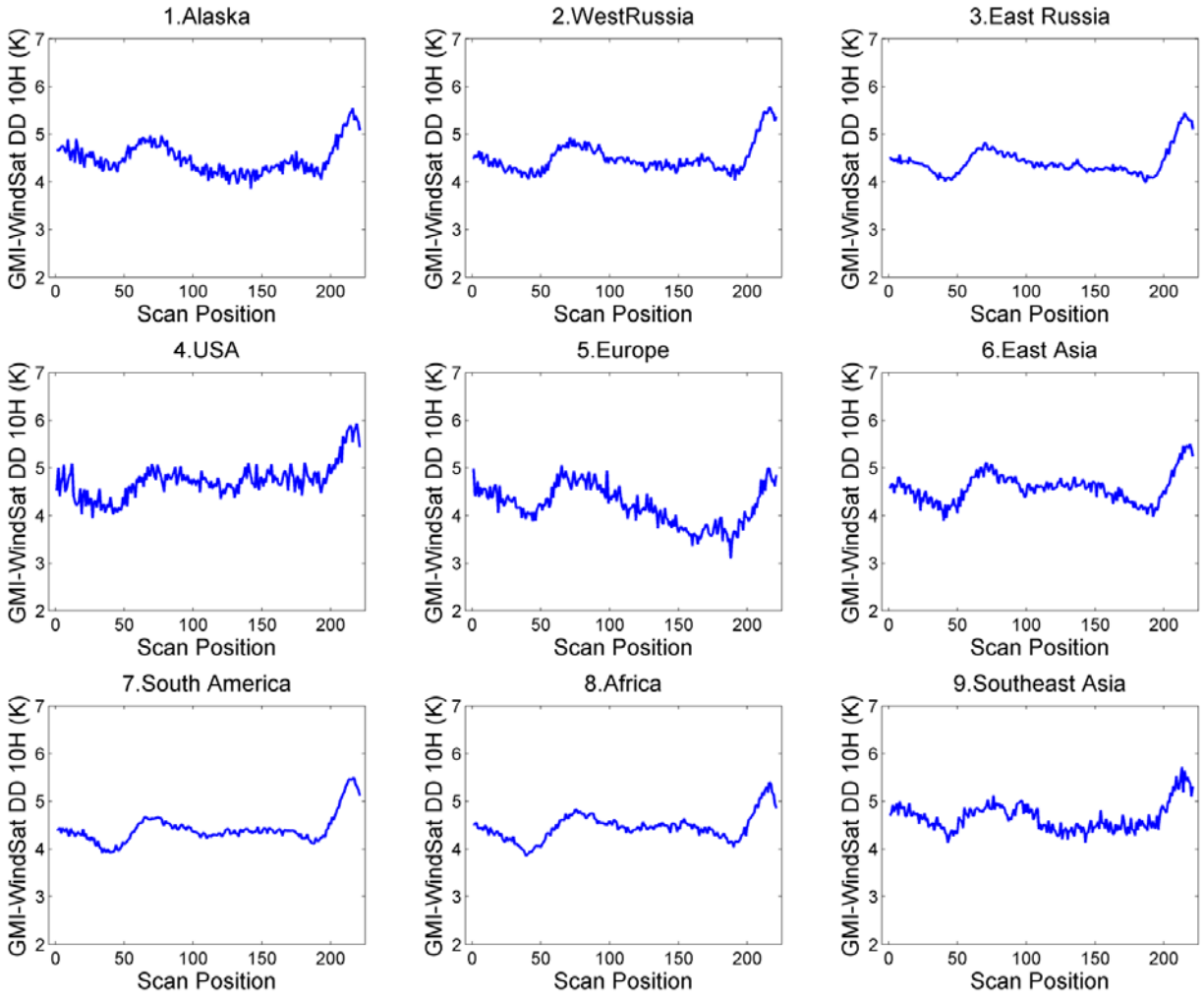

Figure 3.10: The along-scan double differences at 10.65H for the nine regions. The anomalies are reproduced in all regions with differences in fluctuation due to the number of samples.

Figure 3.11 shows the sample size in boreal, temperate, and tropical forest. The three forest species contribute 42.64%, 14.02%, and 43.34% of the data, respectively. The change in sample size between worldwide and Amazon areas is

also shown. The total number of data points from this extended method is 433662, which is 30 times more than that from the Amazon rainforest (14430). The number of available days also increases from 17 to 164, out of a total of 181 possible days. Because of the order of magnitude increase, we are now able to monitor the near-daily GMI calibration status.

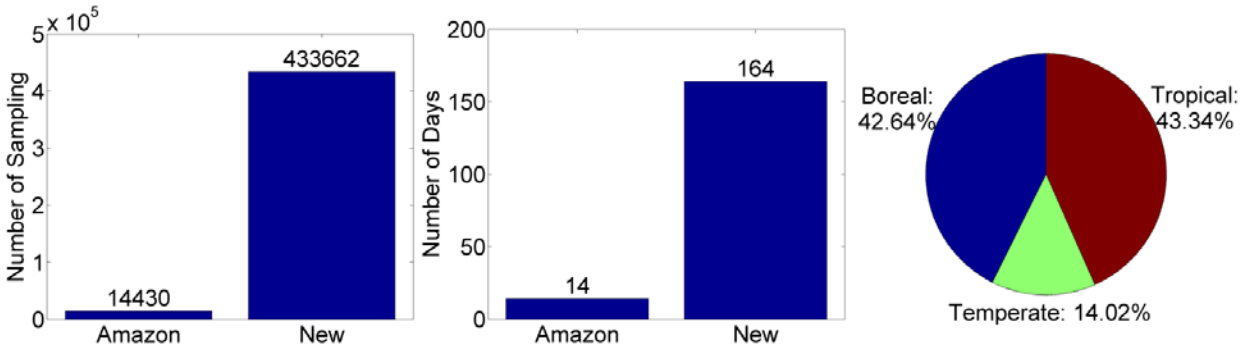

Figure 3.11: The global forest vicarious warm calibration sites significantly increases the number of data in terms of total number (left) and number of days (middle), compared to the Amazon rainforest. The percentages of boreal, temperate, and tropical regions are also shown (right).

Figure 3.12 shows the histogram of TBs in each region. Boreal sites have more cold TBs close to 260 K than tropical regions. Note a filter has been used to limit the lower range of TBs to 260 K. These cold TBs extend the range of warm-end calibration toward this lower boundary. This wider TB range is valuable to examine the dependence of warm calibration on TB.

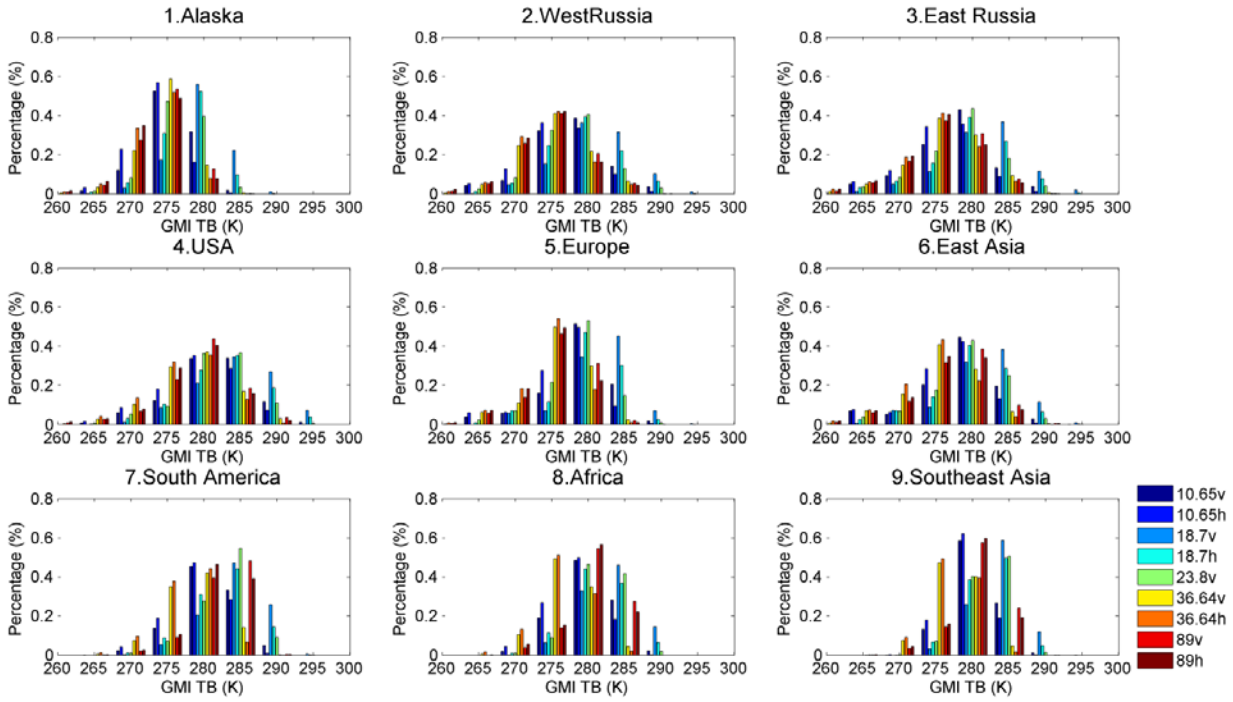

Figure 3.12: TB histograms from different regions. Boreal and temperate regions provide more cold TBs and extend the TB range for warm-end calibration.

The intercalibration table of different regions is shown in Tables 3.2 (DDs) and 3.3 (TBs). The DDs are overall consistent from region to region. But regional calibration differences are noted, which are most significant for the water vapor channels. As shown in Table 3.2, the DDs at 23.8V channel are 0.7, 0.8, and 0.7 K in high-latitude boreal sites, Alaska, West and East Russia, respectively. Middle-latitude temperate sites have closer numbers, e.g., 0.5 K in USA, Europe and East Asia. However, tropical sites show very small DDs of <0.1 K in South America, Africa and Southeast Asia. A small but noticeable difference is seen at 37V that is affected by water vapor. Reanalysis data like NCEP FNL have known uncertainties and extensive studies have been performed to evaluate them (Bengtsson et al. 2007;

Kleist et al. 2009). For example, the observed latitudinal difference can result from either overestimation or underestimation of water vapor, from biases in the vertical placement of the water vapor, or from inexact diurnal variations. The clear latitudinal dependence implies that using limited sites such as tropical Amazon rainforests could bias the results.

	Global	Alaska	West Russia	East Russia	USA	Europe	East Asia	South America	Africa	SE Asia
No. Col.	433662	20230	44548	115661	11432	19389	28494	109688	58785	14899
10v	3.8	3.8	3.9	3.8	4.0	3.6	3.9	3.8	3.8	3.8
10h	4.4	4.3	4.4	4.3	4.6	4.1	4.5	4.4	4.4	4.6
19v	4.5	4.3	4.5	4.4	4.5	4.3	4.4	4.5	4.6	4.6
19h	3.9	3.9	3.9	3.8	4.1	4.0	3.8	3.9	4.0	3.9
23v	0.4	0.7	0.8	0.7	0.5	0.5	0.5	0.0	0.0	0.0
37v	-1.4	-1.4	-1.3	-1.3	-1.3	-1.4	-1.4	-1.6	-1.5	-1.6
37h	-1.2	-1.1	-1.1	-1.1	-1.0	-1.0	-1.1	-1.3	-1.2	-1.2

Table 3.2: The global and regional mean double differences as well as number of collocations between GMI and WindSat.

	Global	Alaska	West Russia	East Russia	USA	Europe	East Asia	South America	Africa	SE Asia
10v	281.9	278.5	280.6	280.6	284.2	281.7	281.2	283.8	282.9	283.4
10h	280.5	276.8	279.1	279.0	282.7	280.1	279.9	282.6	281.6	282.5
19v	285.3	282.5	284.0	284.5	287.5	284.6	284.4	287.1	286.0	286.4
19h	283.7	280.8	282.4	282.8	285.8	282.8	282.8	285.6	284.4	285.1
23v	282.9	279.2	280.5	281.3	284.4	281.2	281.9	285.6	284.4	284.7
37v	279.0	276.8	277.5	278.6	280.7	278.0	278.0	280.6	279.2	279.7
37h	278.0	275.6	276.6	277.5	279.5	276.7	277.0	279.9	278.4	279.2

Table 3.3: The global and regional mean TBs of GMI corresponding to Table 3.2.

3.5 Seasonal Variation

Figure 3.13 shows the daily mean DDs. GMI and WindSat show stable temporal performance at the warm end. The peak-to-peak difference is around 1K.

There is no noticeable drifting. The Amazon only results are also shown with the dot markers. Using Amazon region results in limited data with only a few days, making it difficult to assess GMI stability during the mission commissioning phase (GMI launched in March of 2014.

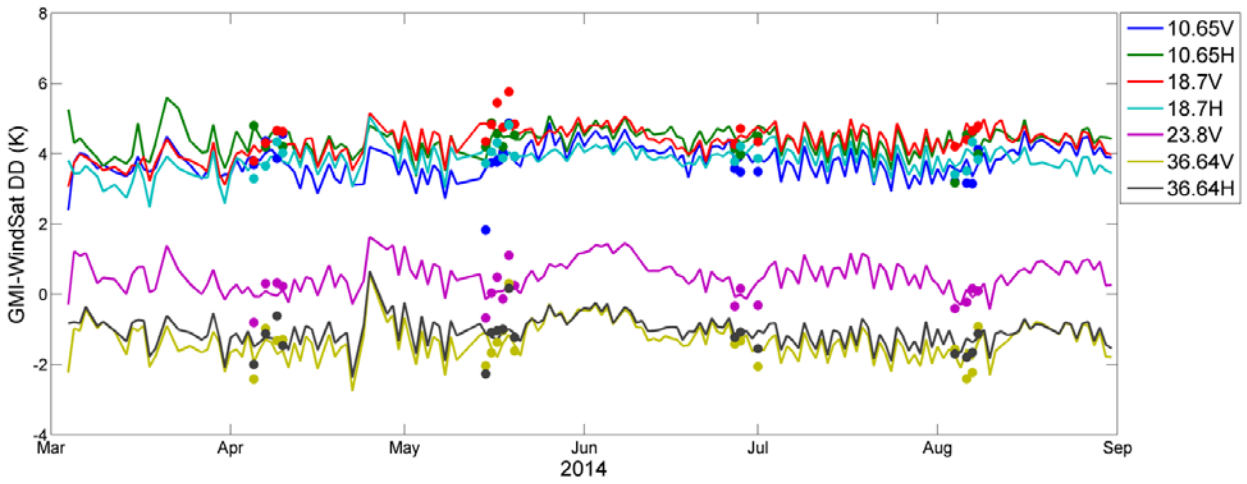

Figure 3.13: GMI daily mean double differences with respect to WindSat from March to August, 2014. The solid lines are from using the extended method (164 days available out of total 181 days), while solid circles are from the Amazon rainforest alone (17 days). The GMI performance is stable without noticeable drifting.

We observe a seasonal change within the calibration sites. Figure 3.14 shows the distribution of available GMI-WindSat calibration sites in the northern hemisphere seasons, March-April and July-August, respectively. A clear seasonal contrast is present. The contrast results from the summer green-up of boreal forest sites in the northern hemisphere through Alaska, Europe and Russia, which almost disappears in winter. Temperate and tropical sites also have noticeable changes.

Since the southern hemisphere has opposite seasons, green-up occurs in southern Africa and Australia from March to April (winter in the northern hemisphere).

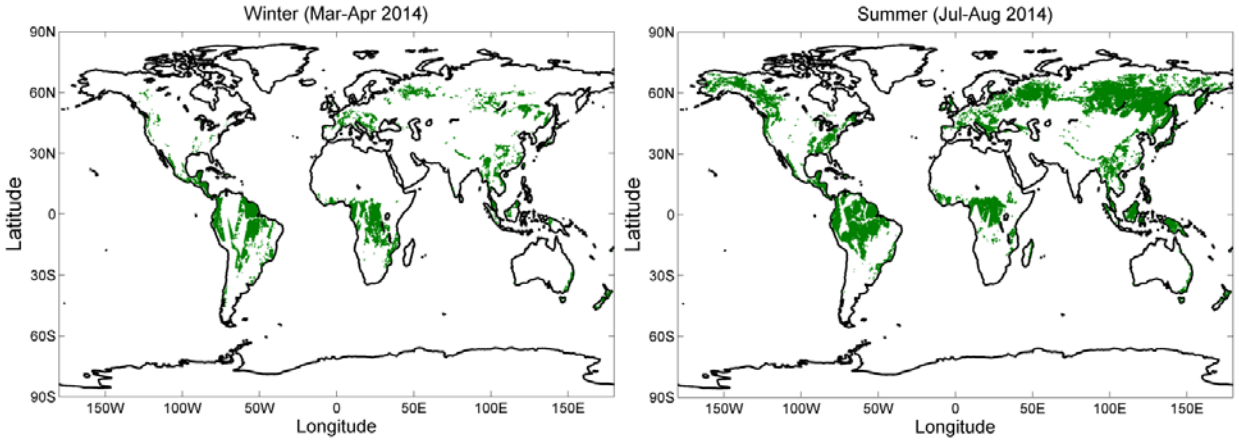

Figure 3.14: The seasonal change in vicarious calibration sites, increasing in summer and decreasing in winter.

To verify this seasonal change, Figure 3.15 shows the Normalized Difference Vegetation Index (NDVI) from MODIS in winter and summer of 2014, respectively. NDVI is a measurement of vegetation canopies based on chlorophyll induced differences in near infrared and visible signatures (Huete et al. 2002). The NDVI maps show a similar seasonal change of vegetation canopies.

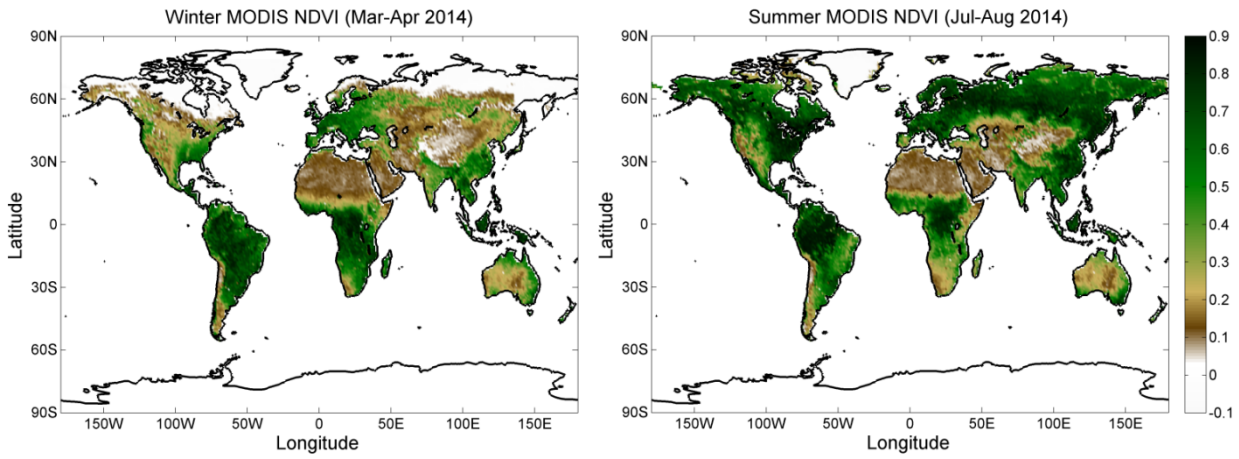

Figure 3.15: MODIS NDVI in winter and summer respectively, verifying that there is a seasonal change in vegetation canopies.

These seasonal differences are further quantitatively illustrated in Tables 3.4 and 3.5. The available data increase from winter to summer, particularly for the northern hemisphere boreal sites. In winter, the number of collocations are 93, 1966, and 2278 in Alaska, West and East Russia, respectively, while they are 16307, 29104, and 82676 in summer. Regional differences still exist for the water vapor channels, both in winter and summer. Consequently, the 23.8V channel has a seasonal difference of 0.5 K between winter and summer.

	Global	Alaska	West Russia	East Russia	USA	Europe	East Asia	South America	Africa	SE Asia
No. Col.	53006	93	1966	2278	459	2315	3893	23512	14712	985
10v	3.9	3.4	3.5	3.6	4.0	3.2	3.7	4.0	3.9	3.9
10h	4.5	4.1	4.1	4.3	4.5	3.7	4.6	4.5	4.5	4.5
19v	4.2	4.0	3.9	4.2	4.2	4.0	4.0	4.3	4.2	4.0
19h	3.7	3.7	3.5	3.9	4.0	3.9	3.6	3.7	3.7	3.6
23v	0.0	0.8	0.5	0.6	0.7	0.4	0.2	0.0	-0.2	-0.2
37v	-1.6	-1.2	-1.3	-1.1	-1.0	-1.5	-1.7	-1.6	-1.8	-1.7
37h	-1.3	-1.1	-1.0	-0.7	-0.6	-1.0	-1.2	-1.4	-1.5	-1.4

Table 3.4: GMI, WindSat mean double differences by region in winter (March-April, 2014).

	Global	Alaska	West Russia	East Russia	USA	Europe	East Asia	South America	Africa	SE Asia
No. Col.	218626	16307	29104	82676	7146	10424	14590	34498	15364	4993
10v	3.7	3.7	3.8	3.8	3.9	3.4	3.8	3.7	3.7	3.6
10h	4.3	4.3	4.3	4.3	4.6	4.0	4.6	4.3	4.3	4.5
19v	4.5	4.3	4.4	4.4	4.6	4.4	4.5	4.6	4.8	4.6
19h	3.9	3.9	3.9	3.9	4.1	4.0	3.9	3.9	4.0	3.8
23v	0.5	0.6	0.7	0.7	0.5	0.5	0.5	-0.1	0.2	-0.2
37v	-1.5	-1.5	-1.5	-1.4	-1.4	-1.6	-1.6	-1.7	-1.4	-1.9
37h	-1.2	-1.2	-1.2	-1.2	-1.0	-1.2	-1.2	-1.4	-1.2	-1.5

Table 3.5: GMI, WindSat mean double differences by region in summer (July-August, 2014).

The observed seasonal changes result from several causes. In temperate regions, the deciduous trees defoliate in winter, exposing the ground beneath the canopy. Since ground emission generally has a large polarization difference, our algorithm will automatically filter out those sites. In boreal regions, trees are generally evergreen coniferous species. They also shed needles, but in a slower process. Furthermore, boreal sites have snow in winter, which increases the polarization difference and are also filtered out by our algorithm.

The observed seasonal change has two implications. The available data would be very limited if calibration were based on fixed local regions, as used in the past. Seasonal shifting will cause a change in the amount of usable data, limited as it is, in any specific region. Furthermore, the water vapor channels will be affected by

the seasonal change, since the seasonal change is related to regional differences as is the distribution of water vapor as discussed above.

3.6 GPM Intercalibration

The warm-end calibration has been applied to the GPM constellation. Tables 3.6 and 3.7 show the table of intercalibraiton DDs and TBs, respectively. A number of channels have absolute DDs larger than 1K. A relative bias larger than 1K between radiometers is not negligible and should be corrected through intercalibration to build up consistent constellation data. SSMIS series F16-F18 are consistent, but F19 shows different DDs at every channel. Given the fact F19 has only a few month's data, more data from F19 are necessary to accurately characterize its performance.

The DDs at the warm end are different from those at the cold-end. AMSR2 has DDs of -3.4, -2.9, -4.0, -2.0, -3.3, -2.0, -3.6 from 10V to 37H respectively at the cold end, with warm-end DDs of -0.2, -0.1, 0.1, 0.4, -0.8, -0.5, -0.5. The different between cold and warm ends are as large as 4K. This highlights the importance of conducting both cold and warm calibration. The correction for intercalibrating constellation radiometers should consider TB dependence over the full TB range. We will present these results in the next chapter.

	AMSR2	SSMIS-F16	SSMIS-F17	SSMIS-F18	SSMIS-F19	TMI	WindSat

10v	-0.2	NA	NA	NA	NA	2.5	1.3
10h	-0.1	NA	NA	NA	NA	2.7	1.6
19v	0.1	1.7	1.8	0.9	0.4	0.2	-0.4
19h	0.4	3.0	3.1	1.4	-0.3	0.1	-0.6
22v	-0.8	1.8	2.1	1.6	-0.8	1.4	-0.8
37v	-0.5	2.1	2.9	2.0	-0.2	1.9	-1.0
37h	-0.5	2.6	2.7	1.4	-1.1	1.7	-0.8
89v	0.5	1.6	1.1	1.3	1.6	1.4	NA
89h	0.8	2.8	1.9	1.8	0.5	2.0	NA

Table 3.6: GPM constellation DDs (GMI as reference radiometer) at warm end.

	AMSR2	SSMIS-F16	SSMIS-F17	SSMIS-F18	SSMIS-F19	TMI	WindSat
10v	279.1	279.4	280.1	278.3	278	282	277.1
10h	277.4	278	278.6	276.6	276.2	280.5	275.4
19v	280.2	280.7	281.2	279.7	279.1	282.9	278.4
19h	278.9	279.6	280.1	278.3	277.6	281.6	277
22v	280.8	281.6	282.3	280.5	280.1	283.9	279.1
37v	278.8	279.4	279.7	278.3	277.3	281.1	276.9
37h	277.8	278.6	278.9	277.3	276.2	280.3	275.9
89v	279.2	280.6	281.3	279.2	278.4	282.9	277.7
89h	278.6	280	280.8	278.5	277.6	282.4	276.9

Table 3.7: Corresponding GMI TBs for the DDs shown in Table 3.6.

3.7 Conclusions

We find that boreal, temperate, and tropical forests are all useful vicarious sites for warm-end calibration. These sites can all be used for high quality calibration. The introduction of boreal, temperate, coastal, and island sites significantly expands the calibration sites, allowing for near-global coverage. The addition of these new regions increases the available data by a factor of ~30 compared to using the Amazon rainforest alone, providing near-daily calibration for GMI in this study.

The warm-end TB range is extended to include colder TBs because of the inclusion of boreal and temperate forests. These calibration sites have a noteworthy seasonal change, a green-up in summer and reduction in winter. The winter reduction is due to tree defoliation and snow contamination. Our method is able to automatically filter out contaminated sites.

Our method is able to reproduce reliable scan-dependent biases. This method reveals the along-scan magnetic interference and edge-of-scan biases that are present with GMI observations at warm brightness temperatures. It discerns extremely small signals, e.g., a scan dependent calibration ripple with a peak-to-peak amplitude of 0.1 K in GMI. This technique is able to diagnose issues with and improve calibration including scan bias corrections and the APC algorithm.

By using these worldwide calibration sites, regional differences are found, which are significant for water vapor channels and have a strong latitudinal dependence. Specifically, high and middle latitude regions, including boreal and temperate sites, yield similar calibration, which is different from tropical sites. The root cause is still under investigation. However, the clear presence of these differences implies that using limited sites, such as the Amazon rainforest alone, could result in latitudinal dependent calibration biases.

The warm-end calibration has been used to intercalibrate the GPM constellation. Most GPM radiometers have biases relative to GMI that are larger than 1K, which is not negligible and should be corrected through intercalibration. Warm-end and cold-end intercalibration biases can differ by as much as 4 K. A complete and thorough approach to calibration should consider its dependence on TB and should cover the full dynamic range of possible TB values.

CHAPTER 4

Combining Cold and Warm Calibration to Cover the Full TB Dynamic Range

4.1 Introduction

Combining cold and warm calibration allows the examination of calibration dependence on TB and development of intercalibration corrections for a radiometer constellation. In general, different radiometers have differences that are TB dependent. Either cold or warm calibration is limited to a narrow range of TBs, which cannot provide the information for the full TB range. Combining cold and warm calibration supports full-range TB calibration. A radiometer can exhibit calibration errors that vary with respect to TB due to hardware or improper calibration corrections such as APC errors. The errors may scale linearly with TB or they may be a result of instrument nonlinearity. A reliable two-point calibration is necessary to detect TB-dependent errors, and additional (three- or four-point)

calibration references may be required to adequately characterize nonlinearities (Draper et al. 2015a).

The XCAL team is responsible for GPM calibration and intercalibraton. An important task is to deliver the intercalibration table to the GPM ground data center – the Precipitation Processing System (PPS). This table consists of relative offsets of each member of the constellation with respect to the reference radiometer, GMI, at specific TB tie points, between which the offsets are linearly interpolated. PPS applies this intercalibration table to the GPM constellation TBs so that data are reconciled starting at level 1 and so that science data at levels 2 and 3 will be consistent from radiometer to radiometer. The XCAL team includes groups from Colorado State University (CSU), Texas A&M University, University of Central Florida (UCF), NASA GSFC, Earth System Science Interdisciplinary Center (ESSIC) at University of Maryland (UMD), and University of Michigan (UM). Radiometer specialists from Ball Aerospace and Technology Corporation (BATC) and Remote Sensing Systems (RSS) also engage in calibration. The first delivery table was sent to PPS and applied to GPM data in August, 2015.

The cold and warm calibration methods have been independently developed at UM as presented in previous chapters. We extend and improve the current state-of-the-art in radiometer calibration. The calibration results by UM make important contributions to GPM calibration. In particular, our warm-end calibration allows

accurate scan-dependent information as a function of TB and makes warm-end calibration reliable for two-point intercalibration. We discovered a GMI calibration issue that is TB dependent and resolved this issue so that the latest GMI data have been corrected.

4.2 Methodology

The cold and warm calibrations are separately applied to GPM constellation radiometers. The GPM core observatory GMI is of critical importance and is particularly investigated. The results are then combined using developed analysis tools. We seek to understand how calibration parameters such as intercalibraton biases are dependent on TB. The dependence is characterized and calibration corrections are developed for the GPM constellation. In addition to the average calibration parameters, the scan dependent calibration is investigated in different TB ranges. This can reveal phenomena that cannot be found in the parameters averaged across all scan positions.

The intercalibration table is produced. We compare our results with the other XCAL teams. The calibration methods are different. For instance, the vicarious coldest-TB method uses a statistical technique to derive a cold reference point for calibration. This method does not require matching FOVs between two radiometers for intercalibration (Kroodsma et al. 2012). On the other-hand, there are multiple

match-up intercalibration methods, including one at UM, but each has unique elements in the way data are processed and TBs are simulated. Results from different match-up methods can therefore have slightly different TB ranges, allowing for the examination of TB dependence of the calibration offsets. If there is a significant difference between methods within the same TB range, the teams discuss and further analyze the methods to find the root cause. The delivery table to PPS is compiled using independent results from all teams. Significant outliers are identified empirically and removed before producing the delivery table.

4.3 Identification and Resolution of a TB Dependent Calibration Issue with GMI

We used the combined cold and warm methods to identify and resolve a calibration issue with GMI. This issue is found in GMI data level 1C 3B (V03B). The V03B data were the latest GMI data at the time of our calibration analysis. The V03B data cover the period from 3 Mar to 31 Aug 2014. These data have since been modified to account for the warm-scene issue analyzed here. In the original V03B data, a few corrections have already been applied, including corrections for the magnetic interference and edge-of-scan obstruction. These corrections, however, are mainly derived from prelaunch and cold-scene calibrations.

Figure 4.1 shows the GMI, WindSat double differences as a function of GMI azimuthal scan position for both cold and warm scenes. With cold scenes, the double difference is flat. Note that GMI has along-scan anomalies due to magnetic interference and edge-of-scan biases due to intrusions (Draper 2014b). Based on prelaunch and cold-scene calibration, corrections have been developed and applied to the V03B data used here (Draper 2014b). The previously used along-scan correction works well at the cold-scene where it was developed. However, noticeable edge-of-scan biases, particularly at the right side of scan, are found for warm scenes at channels 10.65V and 10.65H. The right-side tail at 10.65H goes up 1 K compared to the middle scan positions. A similar but small tail is noticeable at 10.65H. Higher frequency channels do not show such obvious edge-of-scan obstructions.

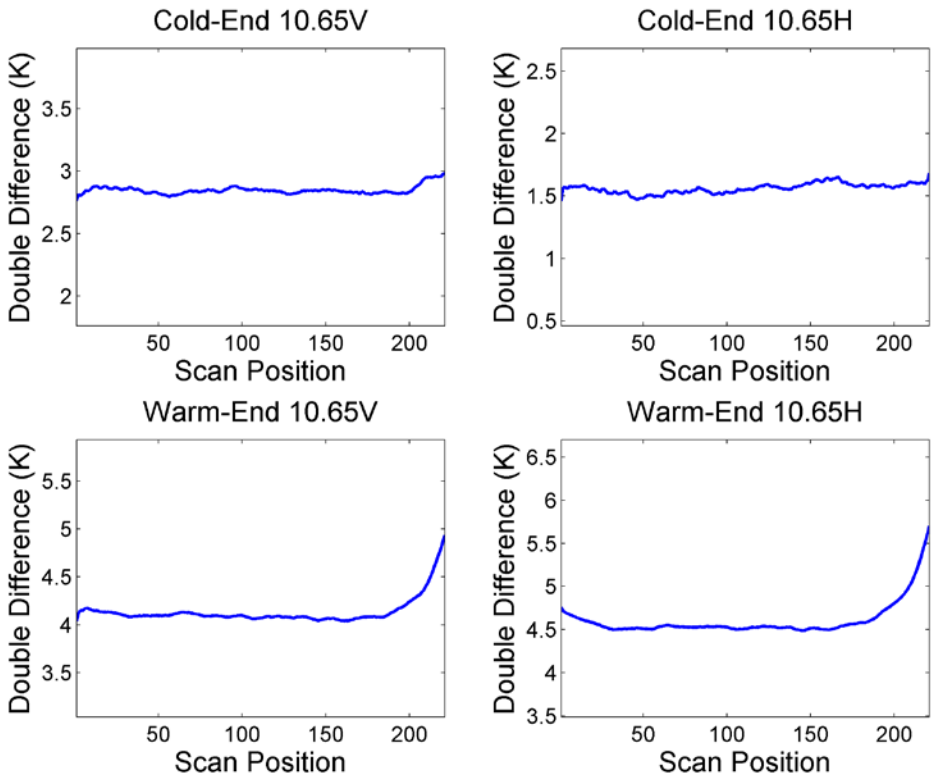

Figure 4.1: The double difference between GMI and WindSat from (upper) cold scenes and (lower) warm scenes. While the cold scene shows no residual along-scan anomalies, the warm-scene shows significant edge-of-scan blockage.

The along-scan bias at warm TBs results from the along-scan correction that was applied to the V03B data. The biases are related to the intrusion at edge-of-scan. The along-scan correction was intended to remove edge-of-scan anomalies based on cold-scene calibration. As a result, while it works for cold TBs over ocean, it causes an overcorrection for warm TBs over land.

More specifically, the expression for the original along-scan correction, quoted from the GMI Calibration Book, is given by (Draper 2014b)

$$T_{b-corr}(i) = T_b(i) - \Delta T_{const}(i) - (T_{\text{intr}} - T_b(i))\Delta t_{mult}(i) \tag{4.1}$$

where $T_{b-corr}(i)$ is the calibrated TB, $T_b(i)$ is the TB to be calibrated, $\Delta T_{const}(i)$ is the constant along-scan bias term attributed to spillover, T_{intr} is the temperature of the intrusion into the radiometer feedhorns at the edge-of-scan, and $\Delta t_{mult}(i)$ is a multiplicative bias term. The i term indicates the GMI scan position, meaning that corresponding parameters are scan-dependent.

The multiplicative term $\Delta t_{mult}(i)$ is the primary cause of the large positive bias at the edge-of-scan for warm TBs. Figure 4.2 shows the original $\Delta t_{mult}(i)$ as a function of scan position. Its tails are for correcting edge-of-scan biases. However, the original values of $\Delta t_{mult}(i)$ were derived using cold-scene TB over the ocean. These values work well for cold TBs but not for warm TBs.

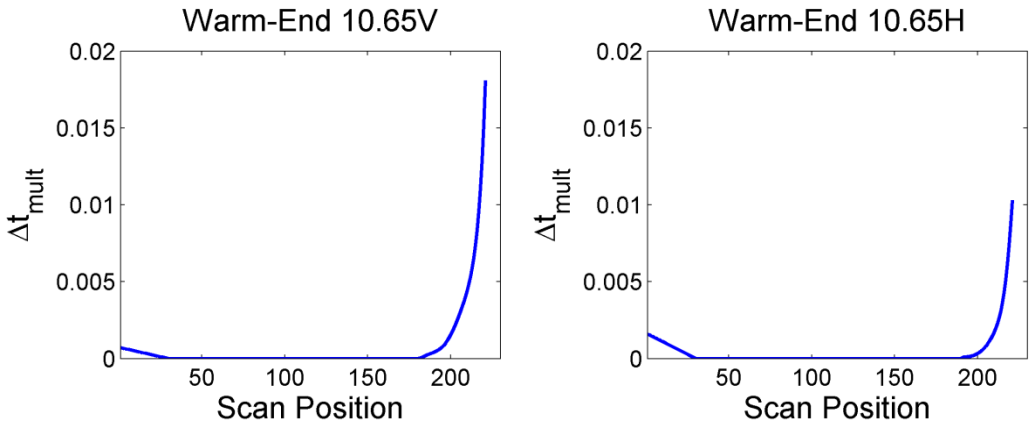

Figure 4.2: The original cold-scene derived parameter $\Delta t_{mult}(i)$ for along-scan corrections.

Figure 4.3 illustrates the impact of the old along-scan correction on cold and warm TBs, respectively. Assuming a flat along-scan TB with a typical cold value of 170 K for 10.65V and 90 K for 10.65H, respectively, the adjusted TBs with the along-scan correction are shown in green lines. The adjusted TBs have a downward tail on the right side. However, for warm TBs of 280 K, this correction results in very large upward tails. The cold-scene derived correction causes overcorrection in the warm-scene case.

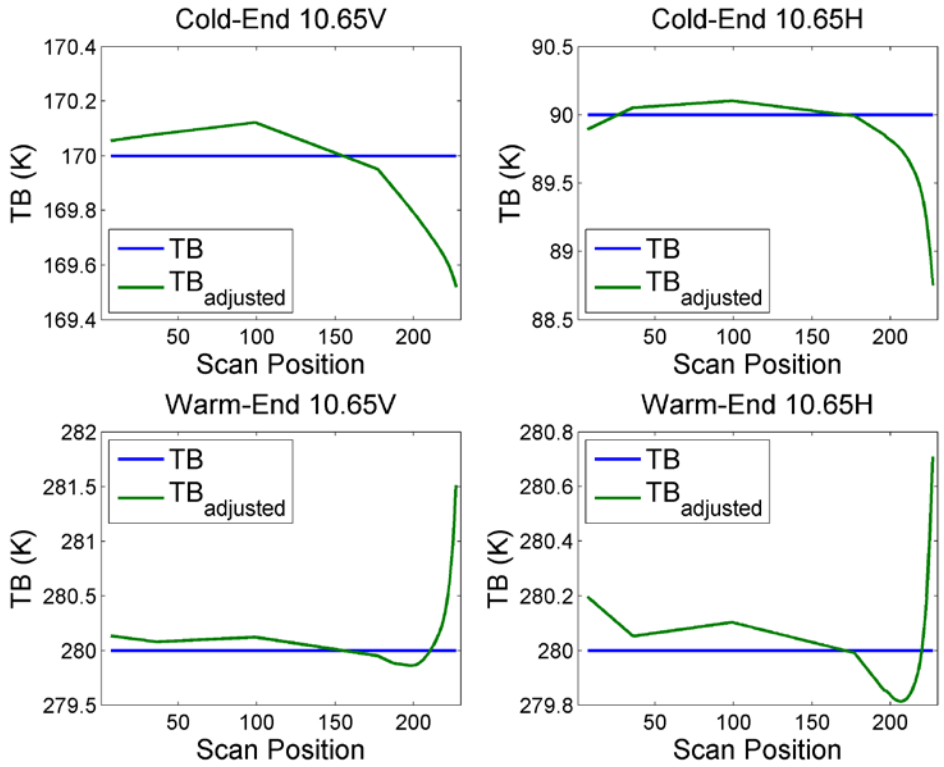

Figure 4.3: Impact of the original along-scan correction. At the cold-scene (upper), a negative term is added to TBs at the right edge of the scan. Using the same correction with warm-scene TBs (lower) results in a very large positive correction at the edges of scans.

To resolve this issue, warm-scene data are used. Figure 4.4 shows the along-scan antenna temperatures (TAs) over the African rainforests. TA data are used because, while they have been corrected for the GMI magnetic anomaly, biases at edge-of-scan still exist. In Figure 5, the downward tail on the right side of scan positions at 10.65V is obvious. For 10.65H, the right-side tail first goes up and then drops down slightly. Using the along-scan TA data, a new along-scan correction is derived to flatten TBs for warm scenes. This correction was provided to BATC. BATC is the manufacturer of GMI. BATC combined it with their cold scene correction to produce an improved version that covers the full dynamic range of expected TBs (Draper 2014b). This new along-scan correction is applied to TAs together with the other corrections (magnetic interference, spillover, etc.).

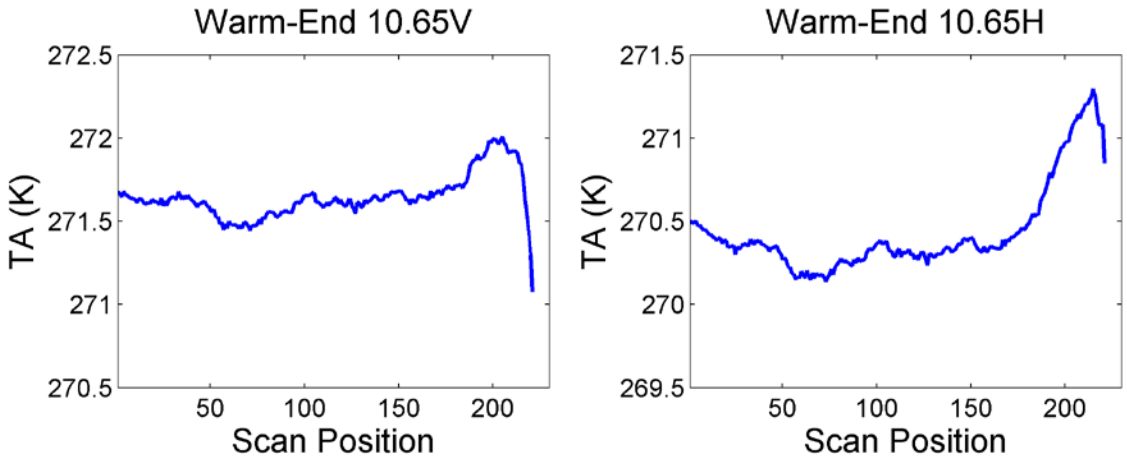

Figure 4.4: The GMI along-scan TAs for warm scenes. Although the TAs have been corrected for magnetic interference, the edge-of-scan biases still exist. A correction can be derived using the TA data.

Figure 4.5 shows the comparison of double differences with new and old along-scan corrections. The new correction accounts for warm-scene calibration in addition to cold-scene calibration. By taking into account the warm-scene calibration, the edge-of-scan biases are resolved.

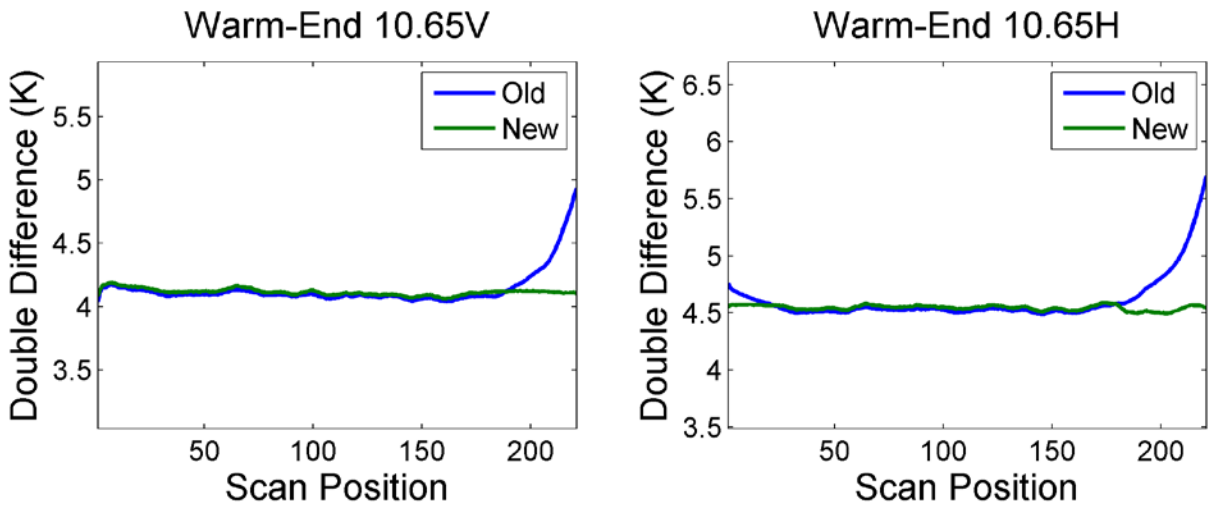

Figure 4.5: GMI and WindSat warm-scene double differences with the old and new along-scan corrections. The new one removes the along-scan biases.

4.4 Cold and Warm Calibration

We examine the calibration dependence on TB by combining cold and warm calibrations. The relationship of DD and TB is examined for GMI-TMI intercalibration in subsequent plots. These plots are derived from both cold and warm results. The plots show the 2D number density relationship between DD and TB. A linear regression is performed for each channel as shown in the red line. Note that a quality filter has been applied to screen out DDs with absolute value

larger than 10K, as described in the methodology part. This is a loose filter, since we want to keep as many data as possible.

At channels 10V&H, the cold and warm scenes show clear bimodal structure as shown in Figure 4.6. That is, cold TBs are around 80K and 170K with warm TBs of 280K for 10V and 10H, respectively. The linear regression shows an increasing trend of DD as a function of TB, which is about 2K-DD per 100K-TB. Although the linear regression does not appear to perfectly represent all the samples, this positive DD-TB trend is appreciable. There is some scatter in the DDs at both cold and warm ends. In particular, the warm-end scattering is relatively significant. This can result from the fact that low-frequency channels have larger FOVs than high frequency channels and are therefore vulnerable to surface heterogeneity. Overall, the linear regression represents the trend of the DD-TB relationship well.

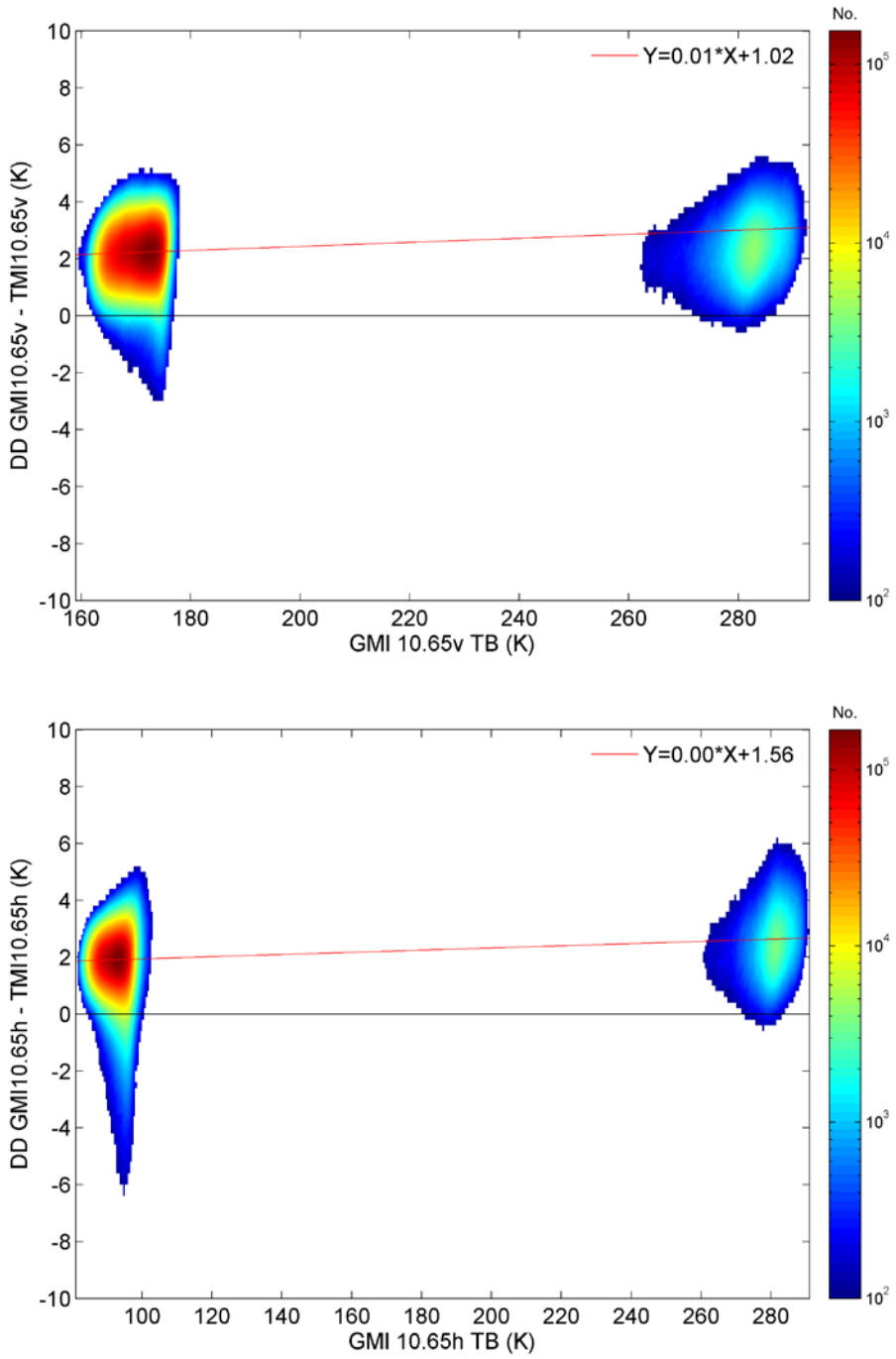

Figure 4.6: DD Vs TB for GMI-TMI at 10V and 10H respectively. A bimodal structure is seen.

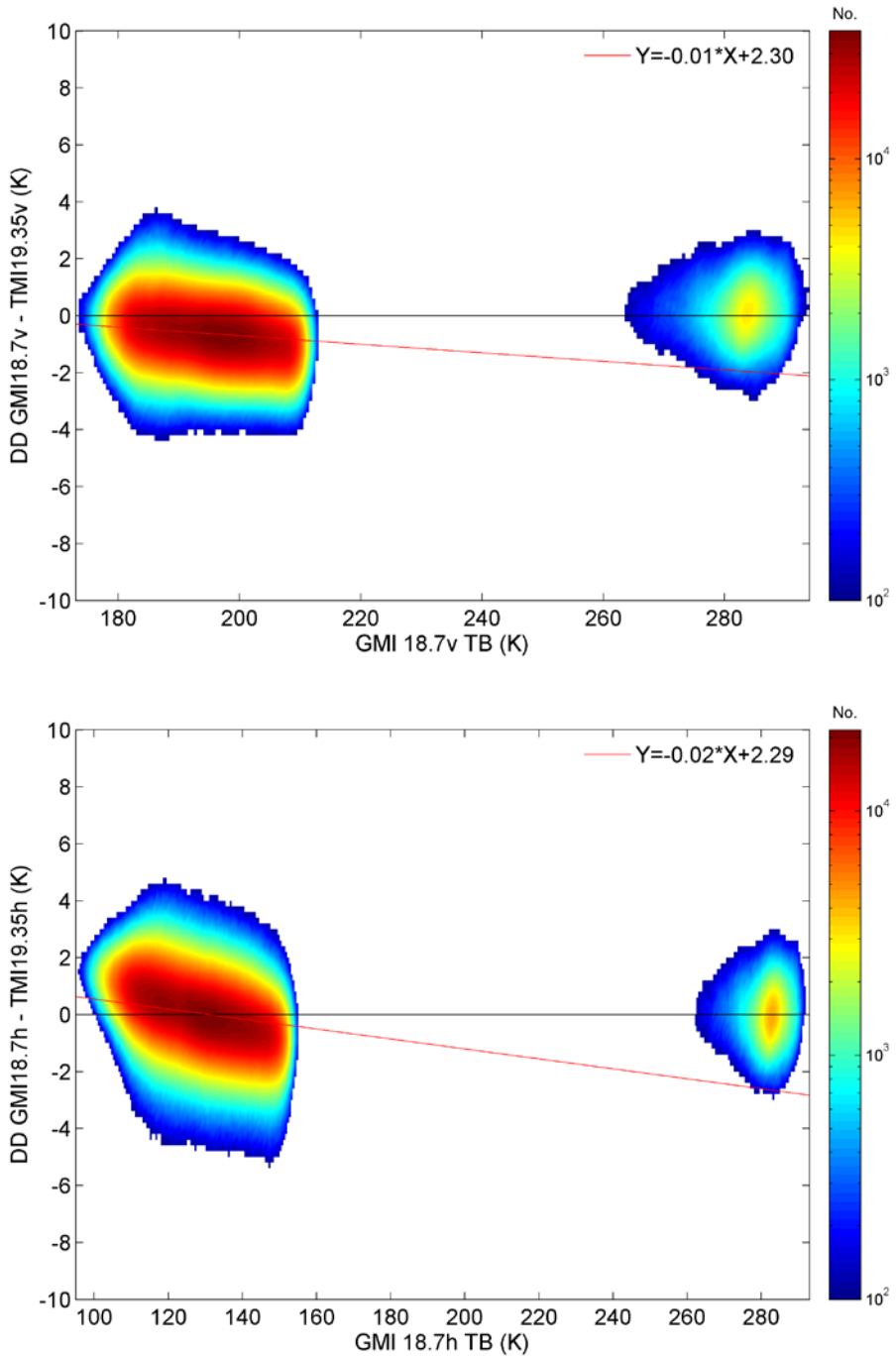

Figure 4.7: DD Vs TB at 19V and 19H, respectively. Although linear regression shows near-zero slope, cold-end DDs decrease with TB.

The 19V and 19H channels are shown in Figure 4.7. Like 10GHz channels, the bimodal TB distribution is significant, though with closer distance between

cold and warm ends. The warm-end scattering is reduced compared to 10GHz, since FOVs at 19 GHz are smaller. One very distinct feature is that the linear regression is close to zero. However, the cold-end shows clear decreasing trend with TB. In fact, the cold-end DD decreases with TB by 5K over a 100K change in TB at 19H. GMI and TMI have the same frequency at X-band (10.65 GHz), but differ at K-band with channels at 18.7 and 19.35 GHz respectively. The frequency difference is taken into account by the intercalibration method, but might have some residual difference due to factors like model parameterization. This is considered in greater detail in Chapter 5.

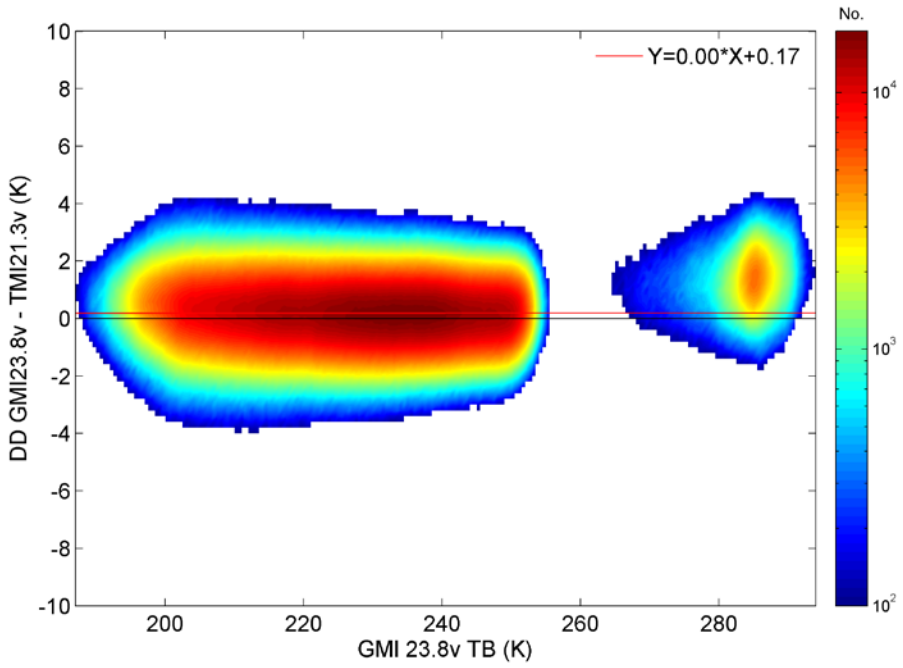

Figure 4.8: DD Vs TB at 22V.

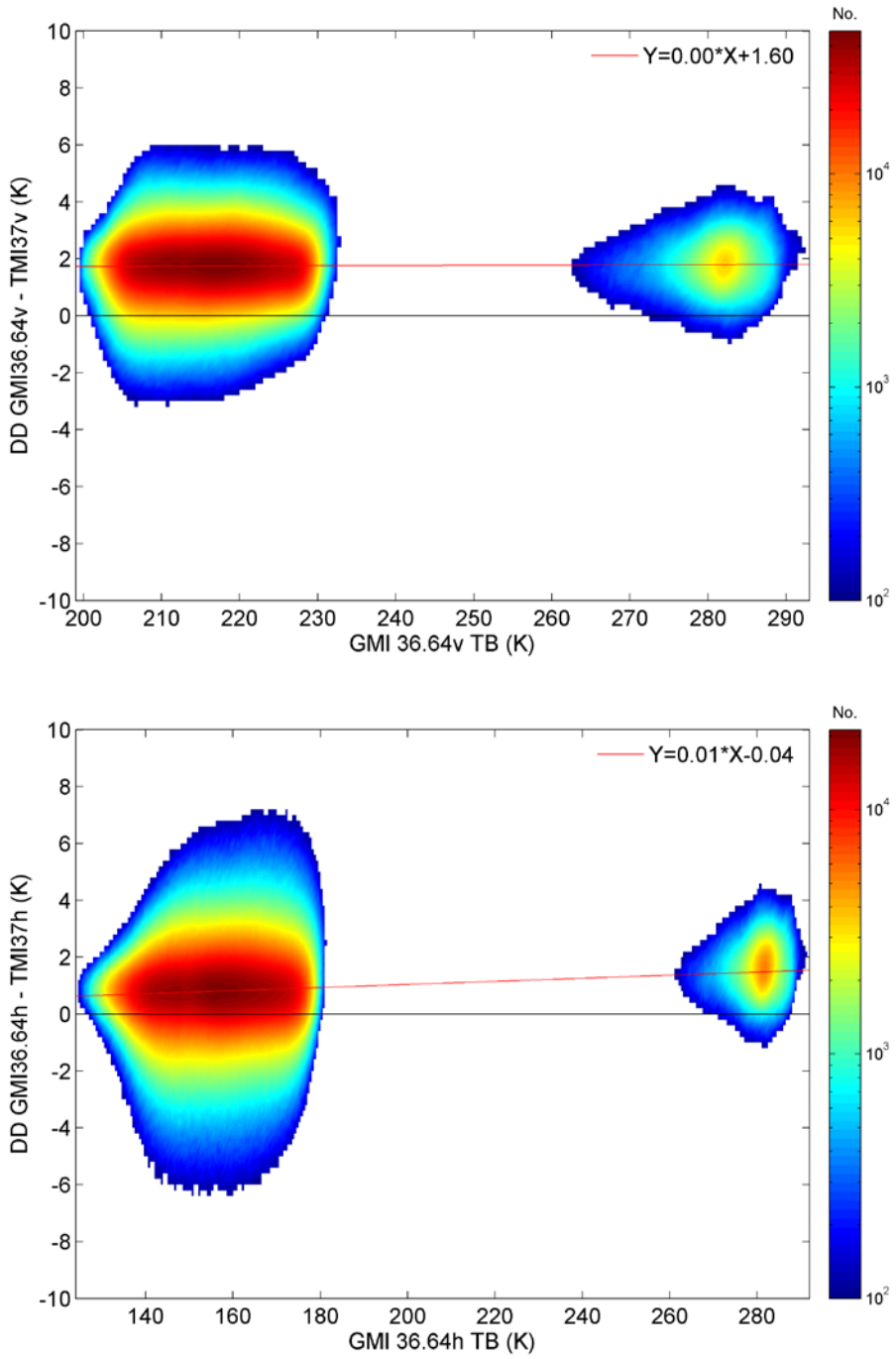

Figure 4.9: DD Vs TB at 37V and 37H, respectively.

Figure 4.8 shows the DD vs. TB behavior for the 22V channel. 22V is the water vapor channel and is very warm at the cold end. The cold and warm TBs

overlap, but the bimodal distribution of calibration TBs remains visible. It has positive slope with 2K-DD per 100K-TB. Channels 37V and 37H are shown in Figure 4.9. The cold and warm ends are well aligned using the linear regression. The slope is half that of 22V.

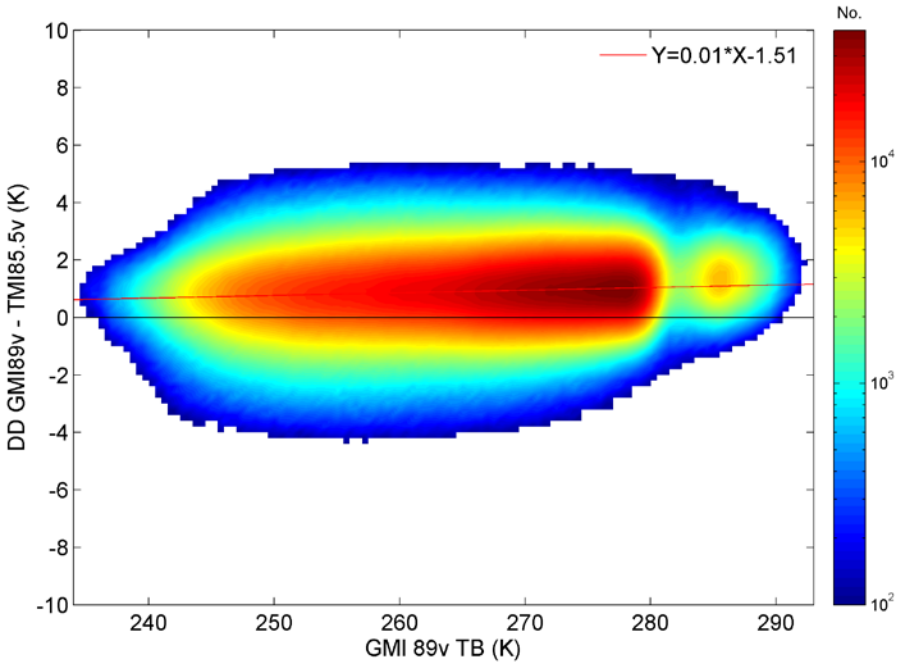

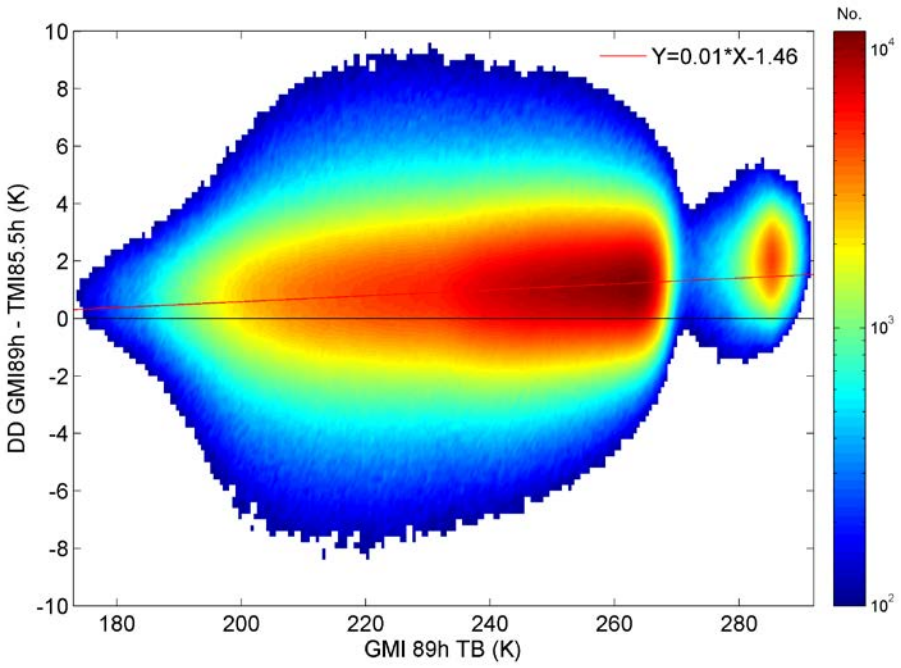

Figure 4.10: DD Vs TB at 89V and 89H, respectively.

Figure 4.10 presents results for 89V and 89H. The frequency is high enough that cold-end TBs merge with warm-end. The linear regression well represents a positive trend, where channel 89H has relatively large slope of 6K-DD per 100K-TB. Keep in mind that the range at 89H is small so that the linear regression is sensitive to any uncertainty that would affect intercalibration slope.

The procedure of cold-warm intercalibration has been applied to the entire GPM constellation. In this way, the intercalibration correction parameters are derived. The results together with the other teams' are shown in next section.

4.5 Intercalibration Delivery Table for GPM Constellation

We combine cold and warm calibrations and derive TB dependent intercalibration parameters for the full GPM constellation. The other XCAL teams also implement independent intercalibration. These results are shown in the following plots and tables. Figures 4.11-4.14 shows the examples of GMI-TMI intercalibraton.

Figure 4.11 shows the GMI-TMI intercalibraton at 10 GHz. The results of different XCAL teams are represented in different symbols and colors. These symbols are the averaged DDs and TBs at the cold and warm end. The results from different groups are overall consistent. It indicates that DD has a negative dependence on TB at this frequency. An outlier with larger deviation is noticeable at the cold end.

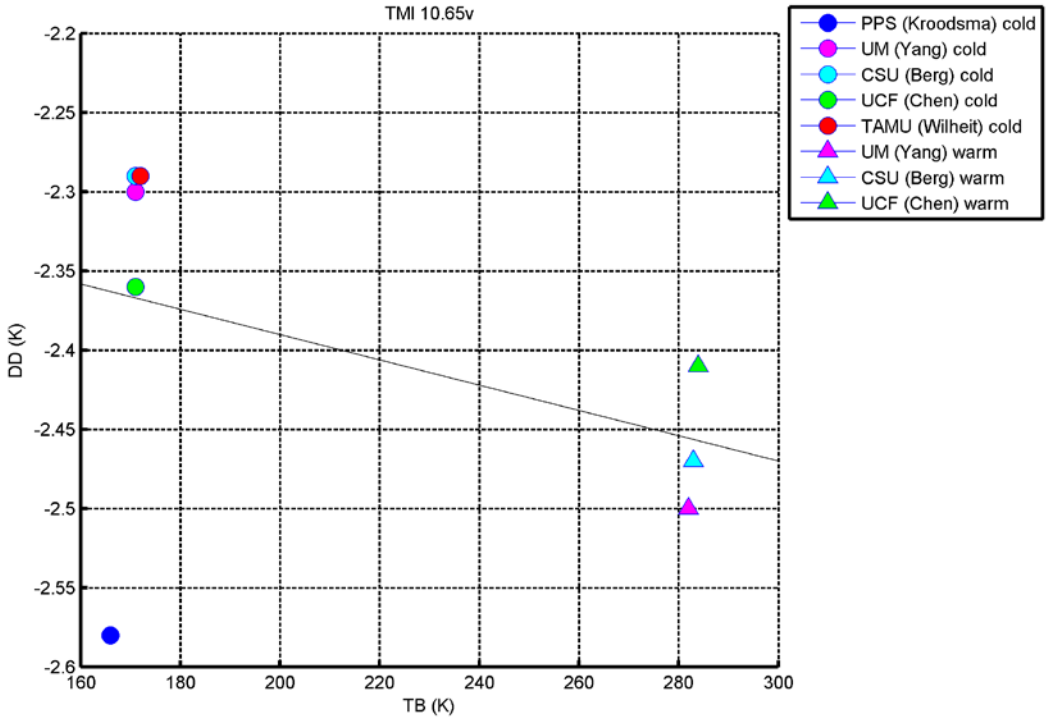

n

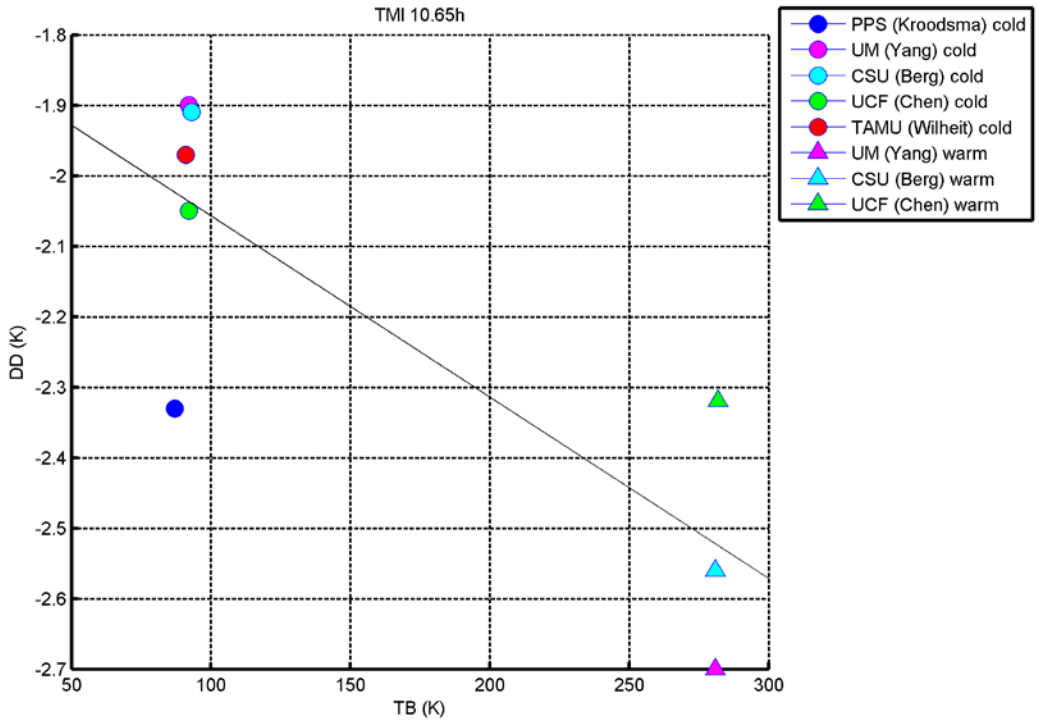

Figure 4.11: GMI-TMI cold-warm intercalibration at 10 GHz from XCAL teams.

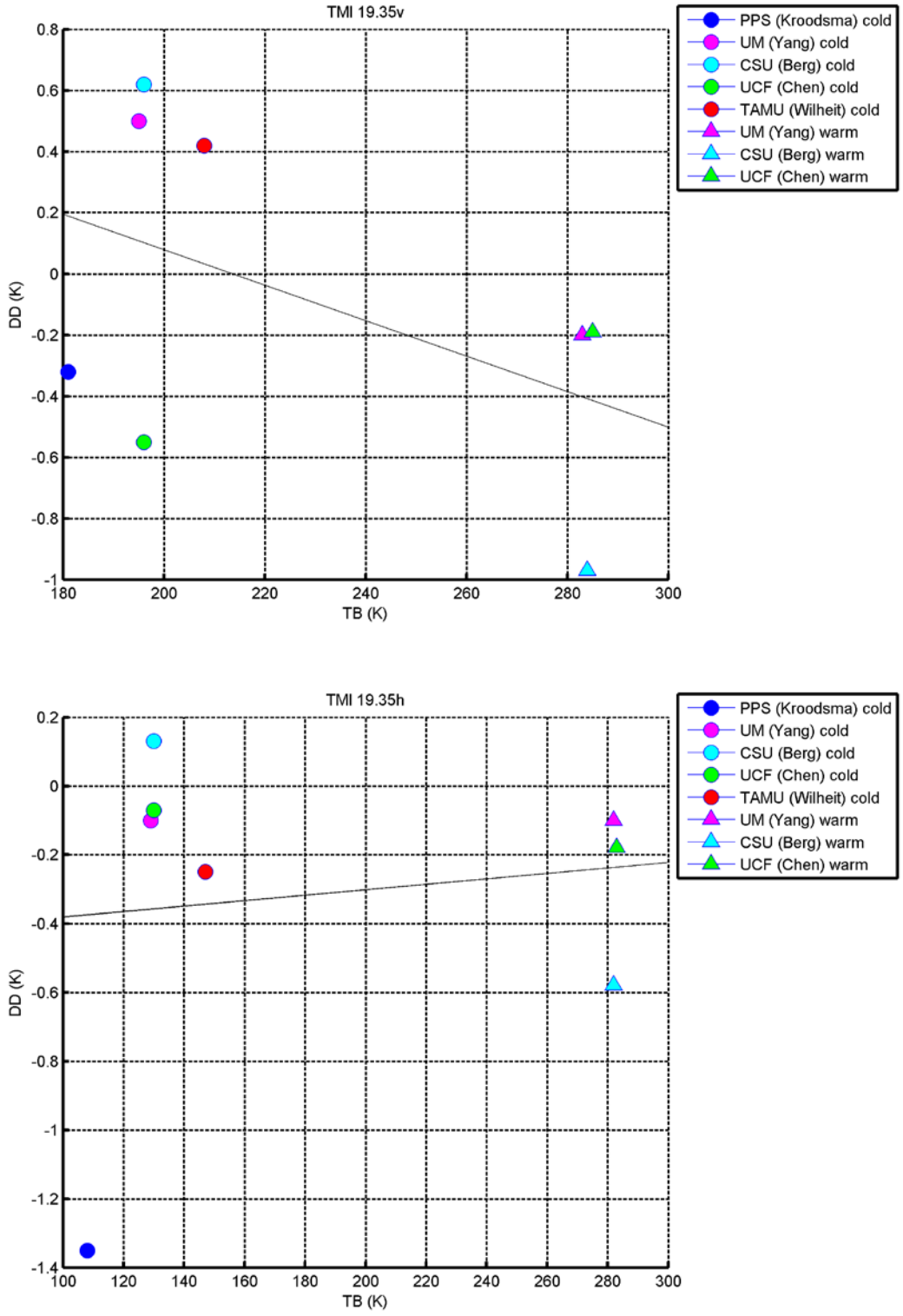

Figure 4.12: GMI-TMI cold-warm intercalibration at 19 GHz from XCAL teams.

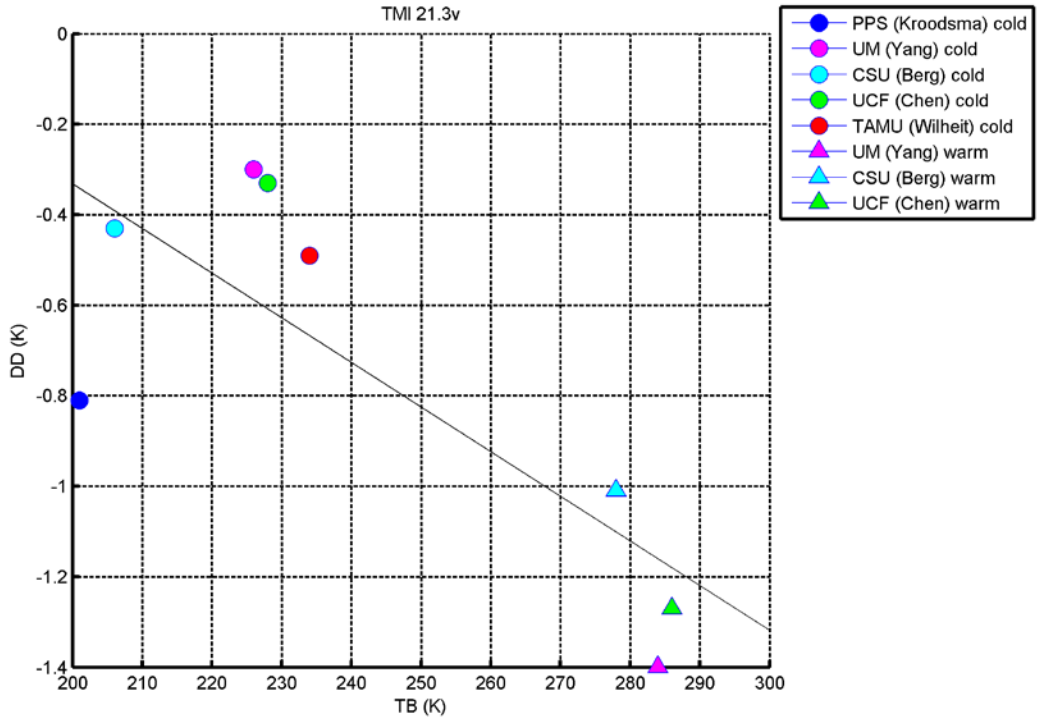

Figure 4.13: GMI-TMI cold-warm intercalibration at 22 GHz from XCAL teams.

Channels 19V and 19H are shown in Figure 4.12. The two channels have opposite TB dependence. The changes of DDs throughout the range of TB are -0.6 and 0.2 K at the two channels respectively. Channel 19H appears to have an outlier at cold end. Figure 4.13 present 22V. It has a pronounced negative TB dependence, i.e., the DDs drops as much as 1K through the range of TB.

Figure 4.14 shows channels 37V and 37H. Channel 37V has slightly positive TB dependence, with DDs increasing by 0.1K. Channel 37H has a negative TB dependence with a much larger magnitude of 1.3 K.

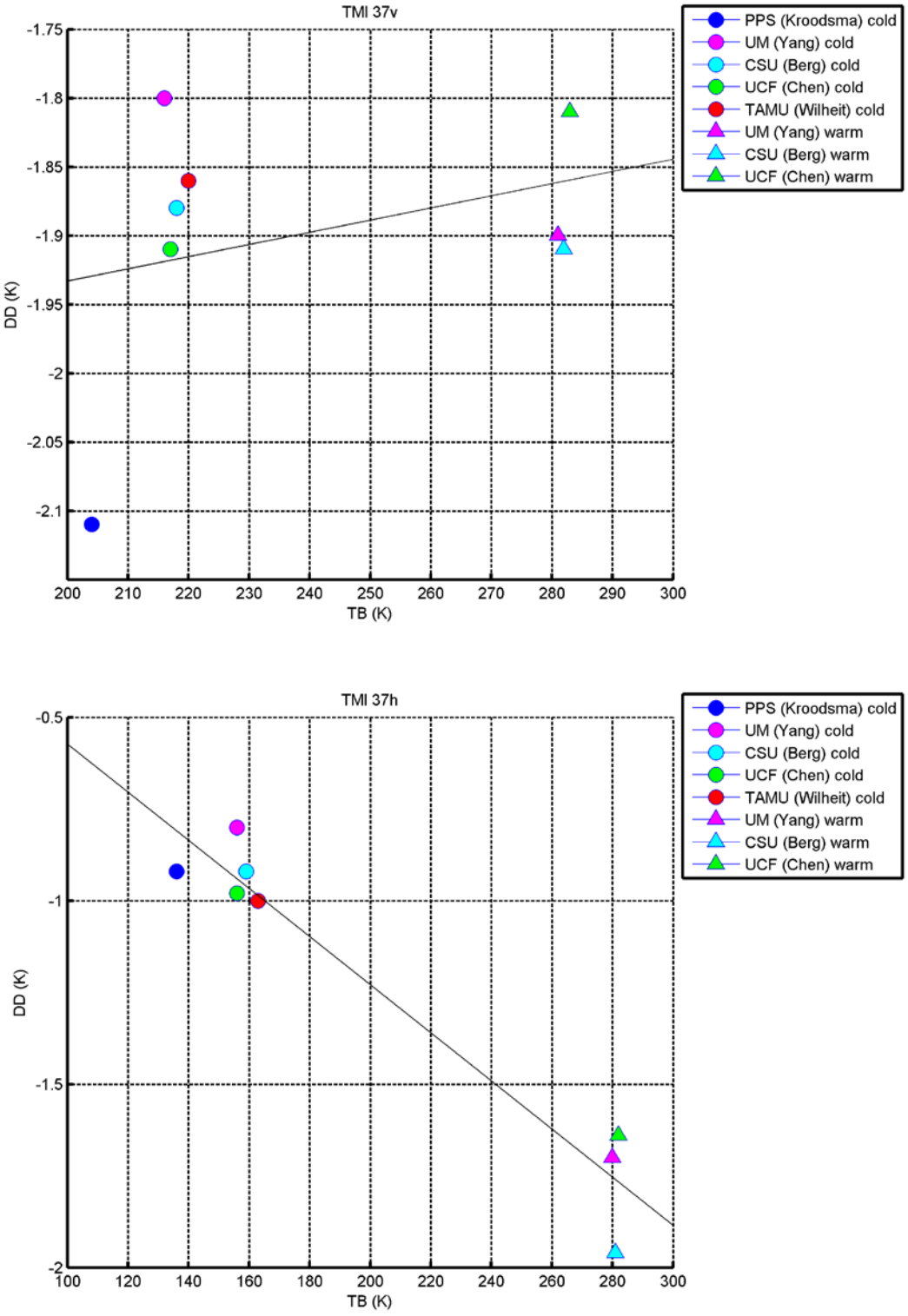

Figure 4.14: GMI-TMI cold-warm intercalibration at 37 GHz from XCAL teams.

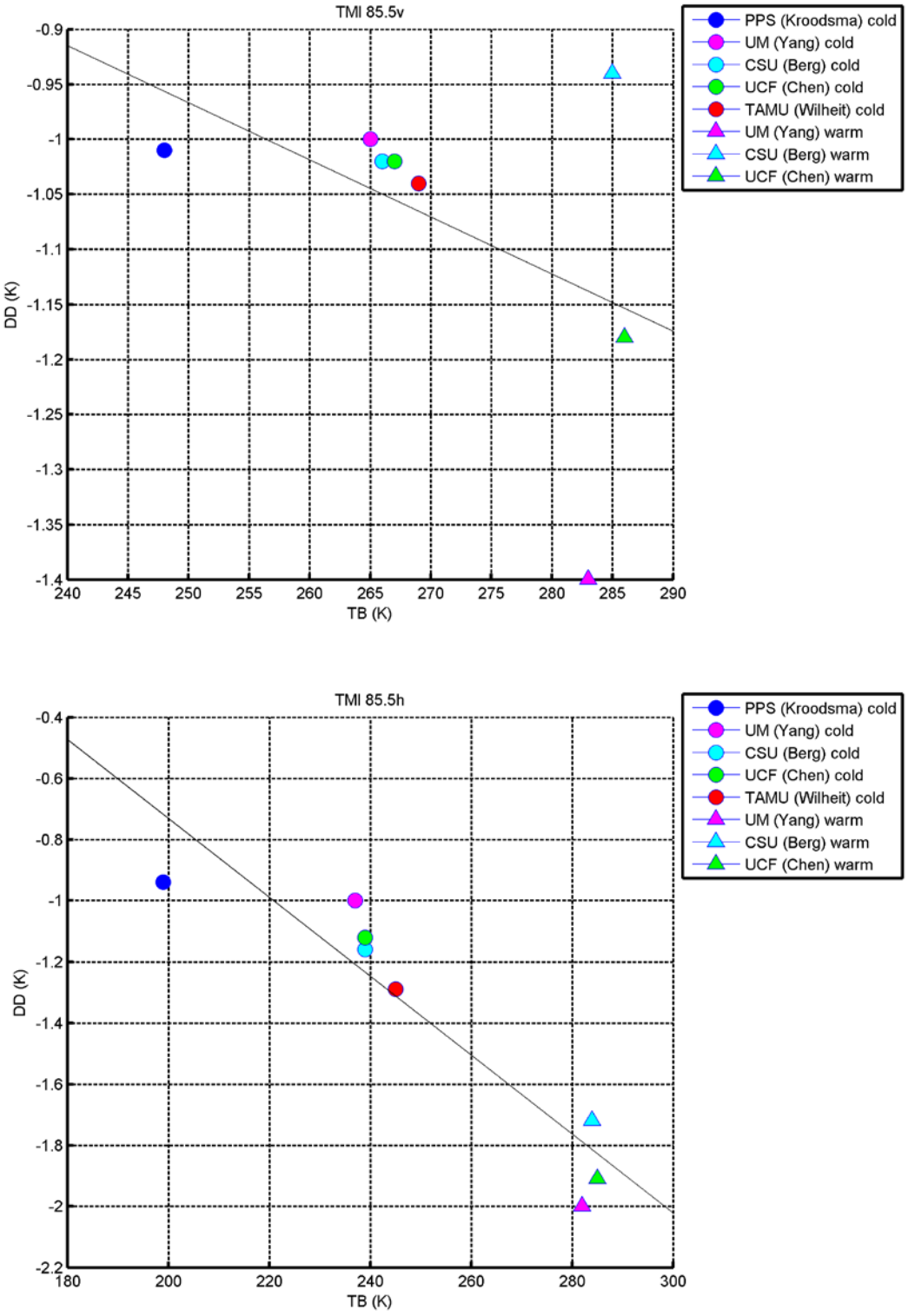

Figure 4.15: GMI-TMI cold-warm intercalibration at 89 GHz from XCAL teams.

Channels 85V and 85H are shown in Figure 4.15. Both channels have a negative dependence on TB. 85H has a larger DD variation of -1.5 K compared to -0.3 K at 89V.

		10V	10H	19V	19H	22V	37V	37H	89V (a&b)	89H (a&b)
AMSR2	TB1	158	83	174	99	188	201	130	235 235	177 177
	TB2	290	288	290	289	291	288	287	289 289	289 289
	DD1	-3.51	-2.98	-4.6	-2.49	-3.91	-2.38	-4.37	-0.76 -1.14	-2.24 -1.74
	DD2	0.25	0.26	0.62	0.86	-0.55	-0.1	-0.08	-0.02 -0.2	-0.11 -0.22
SSMIS F16	TB1	174	99	188	201	130	NA	NA	235	177
	TB2	285	283	286	283	282	NA	NA	286	285
	DD1	-0.38	0.29	0.56	1.69	0.67	NA	NA	0.29	0.16
	DD2	1.42	2.89	1.67	2.01	2.74	NA	NA	1.8	3.12
SSMIS F17	TB1	174	99	188	201	130	NA	NA	235	177
	TB2	284	282	285	282	281	NA	NA	285	285
	DD1	-0.23	0.41	0.64	1.6	0.53	NA	NA	0.61	0.01
	DD2	1.57	2.84	1.91	2.83	2.64	NA	NA	1.28	2.19
SSMIS F18	TB1	174	99	188	201	130	NA	NA	235	177
	TB2	284	282	285	282	281	NA	NA	285	285
	DD1	-0.37	0.28	0.56	1.68	0.73	NA	NA	0.67	0.76
	DD2	0.92	1.24	1.4	1.86	1.42	NA	NA	1.62	2.04
SSMIS F19	TB1	174	99	188	201	130	NA	NA	264	177
	TB2	284	282	285	280	279	NA	NA	264	282
	DD1	-0.64	-2.02	-1.64	0.09	-2.16	NA	NA	1.55	0.2
	DD2	0.55	-0.23	-0.09	-0.3	-1.13	NA	NA	1.55	0.37
TMI	TB1	166	87	181	129	201	204	136	271.13	199
	TB2	284	282	285	283	286	283	282	271.13	285
	DD1	2.36	2.02	-0.19	0.06	0.34	1.93	0.81	1.08	0.72
	DD2	2.46	2.53	0.41	0.29	1.18	1.86	1.77	1.08	1.83
WindSat	TB1	158	83	174	99	188	201	130	NA	NA
	TB2	284	282	285	283	286	283	282	NA	NA
	DD1	1.2	0.67	-0.62	-2.01	-0.88	-1.41	-1.53	NA	NA
	DD2	1.41	1.55	-0.4	-0.7	-1.06	-1.06	-0.92	NA	NA

Table 4.1: The delivery intercalibration to NASA PPS, compiled from results of XCAL teams.

Like GMI-TMI, the same method is applied to the rest of the GPM constellation. The results are shown in Table 4.1. AMSR2 has four independent channels at 89 GHz. The table is compiled as shown in GMI-TMI plots. That is, the linear regression is conducted using results from all groups with outliers removed. The range of TBs is taken from the actual coldest and warmest data among all groups, as represented by TB1 and TB2. The DDs (DD1 and DD2) correspond to the range of TBs and are calculated based on linear regression. Some radiometers have fewer channels than GMI and are marked as NA. PPS applies these relative offsets to GPM constellation, linearly interpolated the DDs shown above between their corresponding TBs. The dependence of DD on TB varies between the radiometers. These differences must be reconciled in building up solid level-1 data.

4.6 Conclusions

Calibration covering the full TB dynamic range has been implemented using the cold and warm calibration methods. This allows the examination of calibration dependence on TB that can be linear or nonlinear. The GPM constellation is intercalibrated. As a first-order approximation, linear behavior is found to reconcile different radiometers well. The GPM intercalibration table has been

developed using a linear-regression based method to reconcile radiometer differences. However, nonlinear dependence is noticed in some channels.

A first intercalibration table has been compiled by the XCAL teams and delivered to PPS and applied to the GPM constellation. During the process, UM made important contributions. The methods we develop establish a solid base for production of reliable calibration across the TB range. In particular, the warm-end calibration allows for reliable warm calibration and scan-dependence characterization. Useful signals such as along-scan anomalies can now be reliably detected, characterized, and corrected. This method has been adopted by other XCAL teams.

By combining the cold and warm-end methods, we find a TB dependent calibration issue with GMI and resolve this issue. The latest GMI data have been corrected specifically for the issue we identified. An along-scan anomaly is found in GMI warm TBs. The original along-scan correction was based on cold TBs alone that cannot properly correct biases for warm TBs. With both cold and warm-end information, new corrections for the full TB dynamic range are developed and the along-scan anomaly is resolved.

CHAPTER 5
Calibration Variability and Dependence on Geophysical Parameters

5.1 Introduction

It is important to characterize calibration variability and dependence on geophysical parameters, since they affect the results from our calibration tools. The time series of calibration analysis parameters always shows variability. Spatially, calibration is different depending on geographic regions. Improper temporal and spatial sampling will change the mean calibration and intercalibration. Therefore, it is necessary to characterize the variability both temporally and spatially and identify underlying root causes.

One major factor affecting calibration methods is the choice of models. For calibration, a RTM and data representing geophysical fields are necessary to account for radiometer differences in frequency, EIA, and bandwidth. The RTM has parameterized modules such as atmospheric absorption and surface emissivity

that cannot fully represent the truth. The geophysical analysis or reanalysis data are produced from models, observations, and data assimilation, which always have errors (Bengtsson et al. 2004; Dee et al. 2011). These errors in RTM and reanalysis data affect our calibration methods. A specific example is water vapor. The observed radiance is affected by water vapor, particularly for water vapor channels. Errors in the assumed water vapor profile will propagate into simulation and final calibration results. The temporal and spatial variability of water vapor will result accordingly in variability of vicarious calibration methods.

These challenges have not been investigated previously, at least when it comes to intercalibration. It is generally accepted that the process of double differencing will remove any sensitivity to model errors. We examine this assumption by using a series of systematic analysis tools. We examine how calibration variability behaves temporally and spatially, how it is related to geophysical parameters, and what primary and secondary factors contribute to the variability. We conduct the investigation over the ocean, since it is the most commonly used calibration target. We discover a number of original findings that help understand the variability and improve vicarious calibration.

5.2 Temporal Variability

5.2.1 2D Temporal Variability

An unexpected signal is discovered when examining the time series of GMI intercalibration. Figure 5.1 shows the calibration time series of single and double differences for GMI and WindSat as well as their corresponding power spectra. Although the time series show no obvious cyclic fluctuation, the power spectra reveal a clear signal with ~40 day period in both single and double differences. This 40-day signal is present in all channels and its amplitude is dependent on the specific channel. In general, H-polarization (H-pol) channels have stronger amplitude than V-pol; the water vapor channel 23.8V also has pronounced 40 day peak in its power spectrum. The results imply that the signal is related to a combination of water vapor and surface features. Some other signals with different periods are also noted, but with weaker amplitudes. In fact, we intercalibrated GMI with other radiometers such as TMI, SSMIS, and AMSR2 and also found this signal, but the exact spectral characteristics vary.

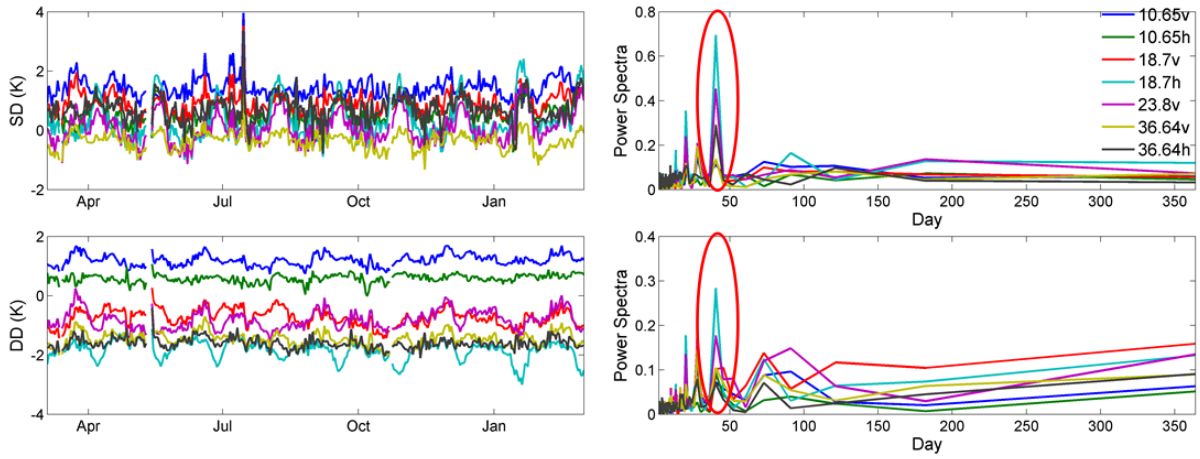

Figure 5.1: Time series (left) of single and double difference for GMI and WindSat and corresponding power spectra (right). A signal with a ~40-day period is found in both single and double difference at all channels, as shown in the power spectra.

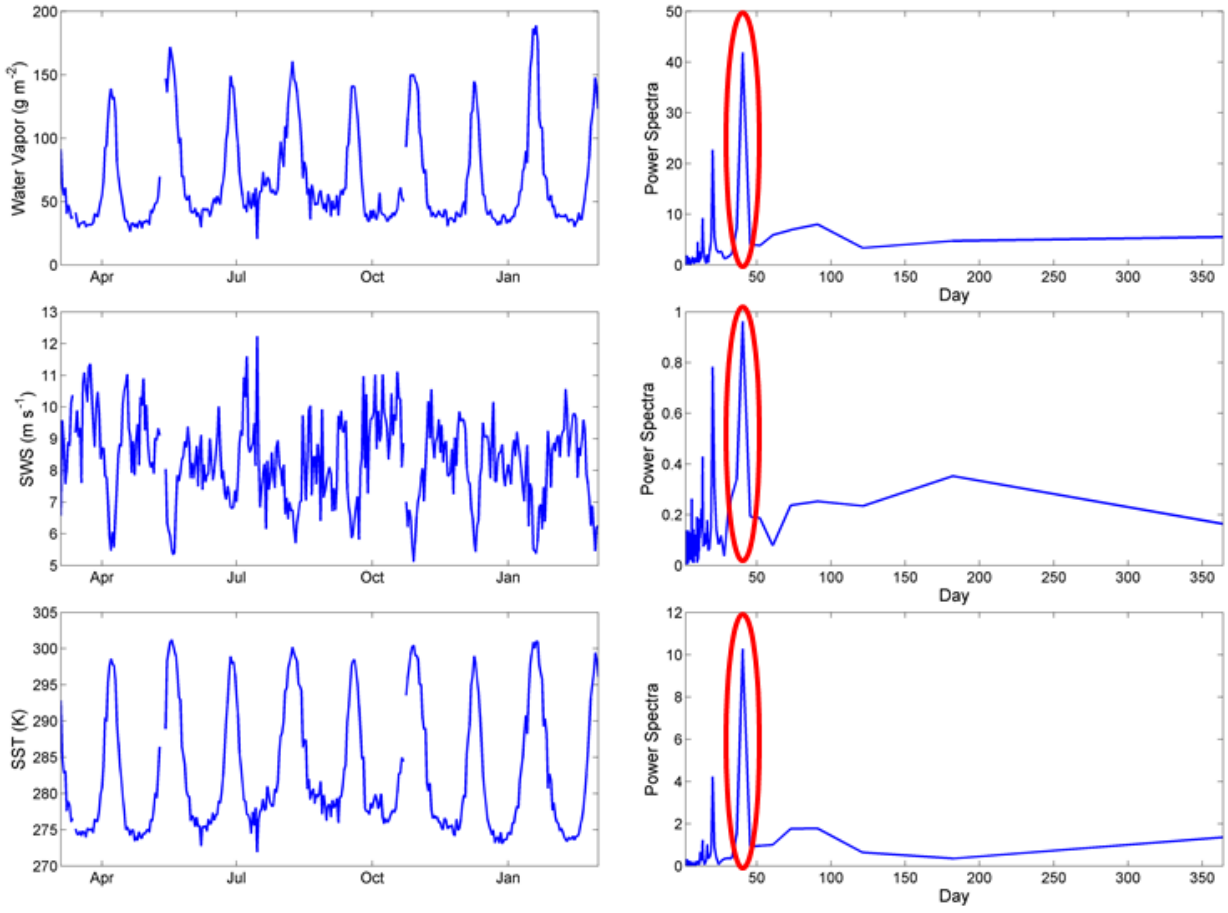

Figure 5.2: The same as Figure 5.1, but for geophysical parameters including water vapor, SWS, and SST. The 40-day signal is also found.

Corresponding parameters are examined to further investigate this signal. Over the ocean, there are three major geophysical parameters affecting calibration through observations and the RTM - water vapor, surface wind speed (SWS), and sea surface temperature (SST). Therefore, these three parameters are investigated in terms of integrated water vapor (g/m^2), SWS (m/s), and SST (Kelvins), which are drawn from the ancillary NCEP FNL data. Figure 5.2 shows the time series and power spectra for water vapor, SWS, and SST for the GMI, WindSat collocations. The three geophysical parameters all have this 40-day signal, where water vapor and SST have stronger signal amplitude than SWS. Another consideration is the observed TB, which depends on these geophysical parameters. Figure 3 shows the observed GMI TBs and corresponding power spectra. All channels have the 40-day signal, which is generally stronger in H-pol than V-pol. These results suggest a correlation between calibration variability and geophysical parameters. Further investigation is presented in the next section.

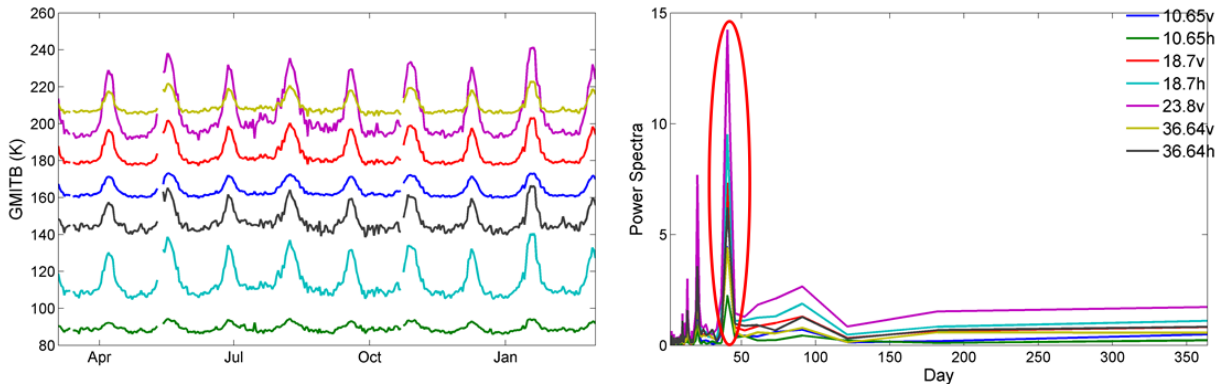

Figure 5.3: The same as Figure 5.1, but for TB. The 40-day signal is found.

5.2.2 3D Temporal Variability

A three dimensional (3D) analysis (parameter and time axes plus the third dimension shown with color) provides more insights that cannot be found from a two dimensional perspective. Figure 4 shows the histogram of the temporal variability of five parameters, including water vapor, SWS, SST, collocation latitude and longitude. Water vapor and SST have noticeable periodicity, with SWS less so. Furthermore, the latitude of collocation shows significant repeated oscillation, i.e., the collocation moves between high latitudes and the tropics. The collocation comes from a sunsynchronous polar-orbiting satellite (WindSat) and a non-sunsynchronous satellite (GMI). GMI's orbit has an inclination angle of 65° with an average 407-km altitude, while WindSat's are 98.7° and 830-km. A two dimensional (2D) Fourier transform is implemented as in Figure 5.5 and shows that this movement has a 40-day period, well correlated to the oscillation period of calibration variability and geophysical parameters. In fact, all the five parameters have the 40-day signal according to their 2D power spectra.

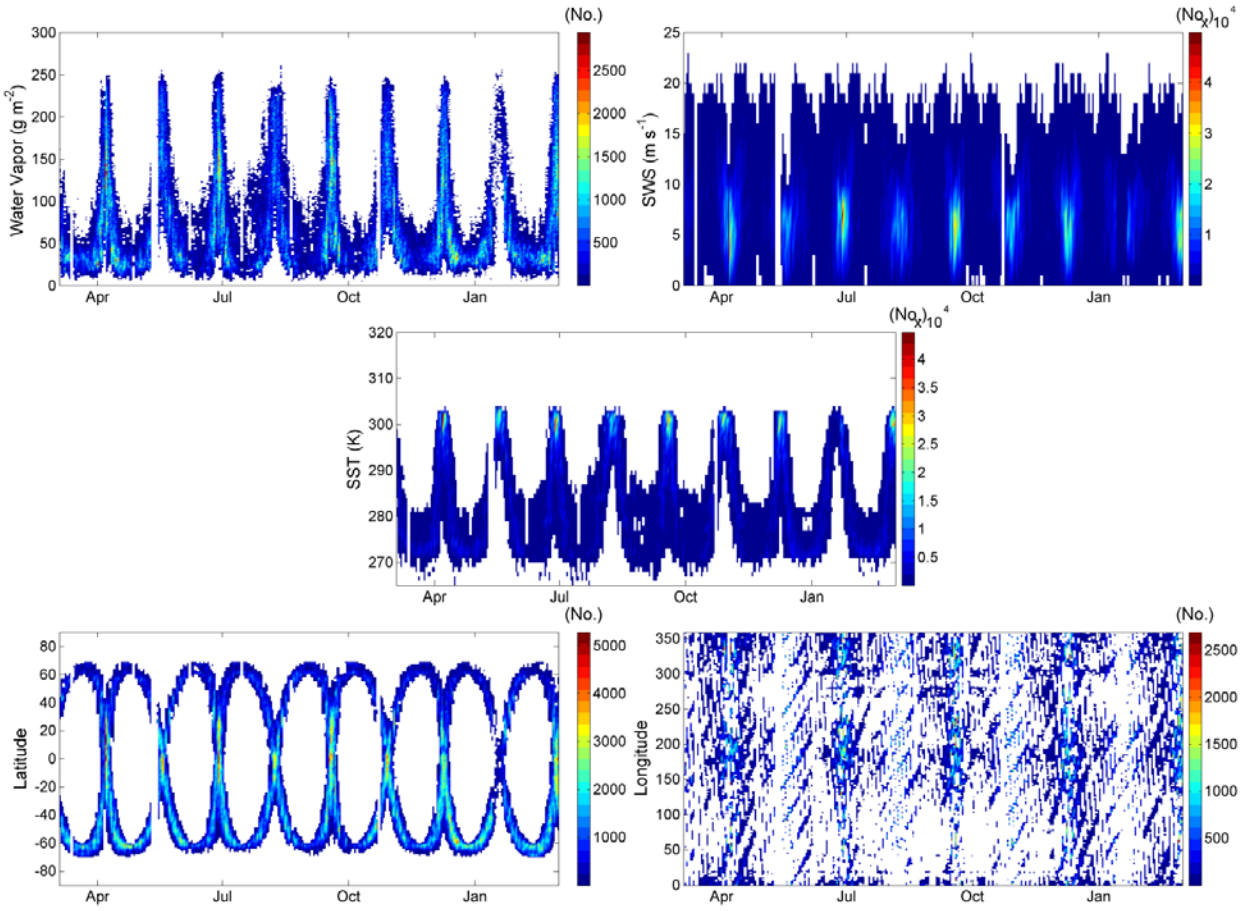

Figure 5.4: The temporal variability of a number of parameters, including water vapor, SWS, SST, and intercalibration locations (latitude and longitude).

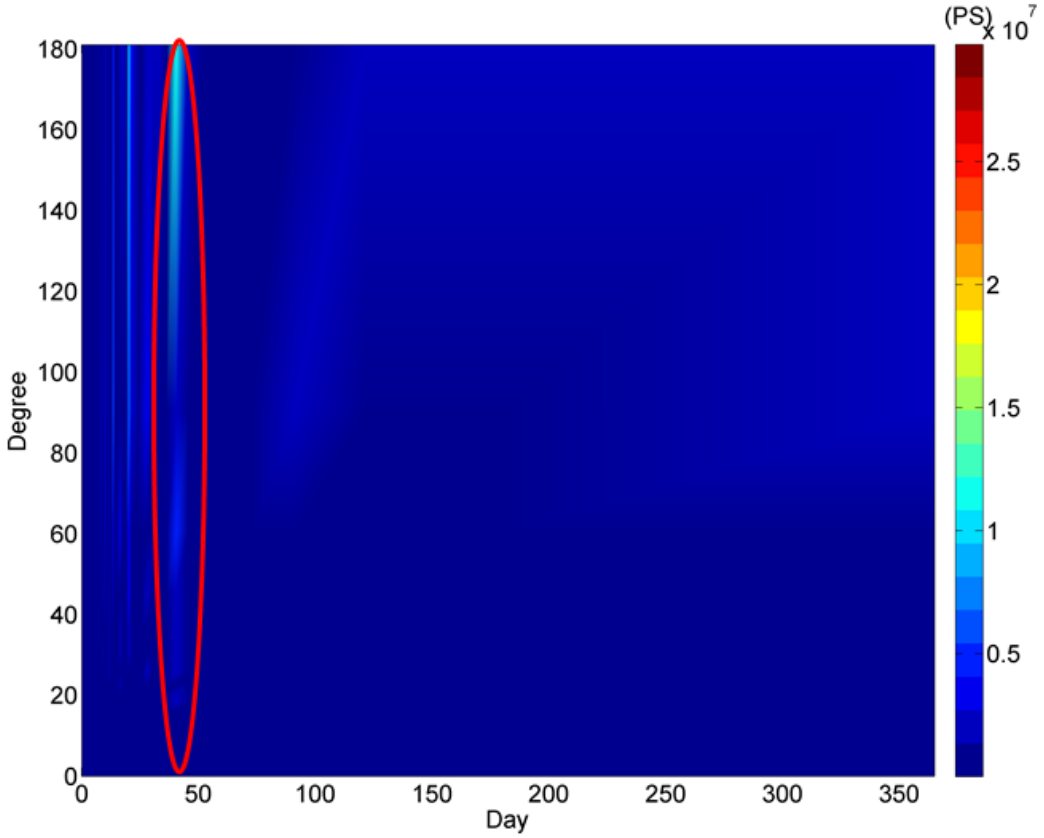

Figure 5.5: The power spectra of 2D Fourier transform for time series of latitudinal collocation as in Figure 5.4 (panel 4). The 40-day signal is seen.

The latitudinal oscillation affects geophysical parameters in the way that the tropics have higher water vapor and SST but lower SWS (spatial analysis is presented in Section 5.3). Accordingly, the variability of these geophysical parameters impacts calibration through observations and the RTM, resulting in the 40-day signal. On the other hand, the longitudinal oscillation also has the 40-day signal as found from a 2D Fourier analysis, though with weaker amplitude.

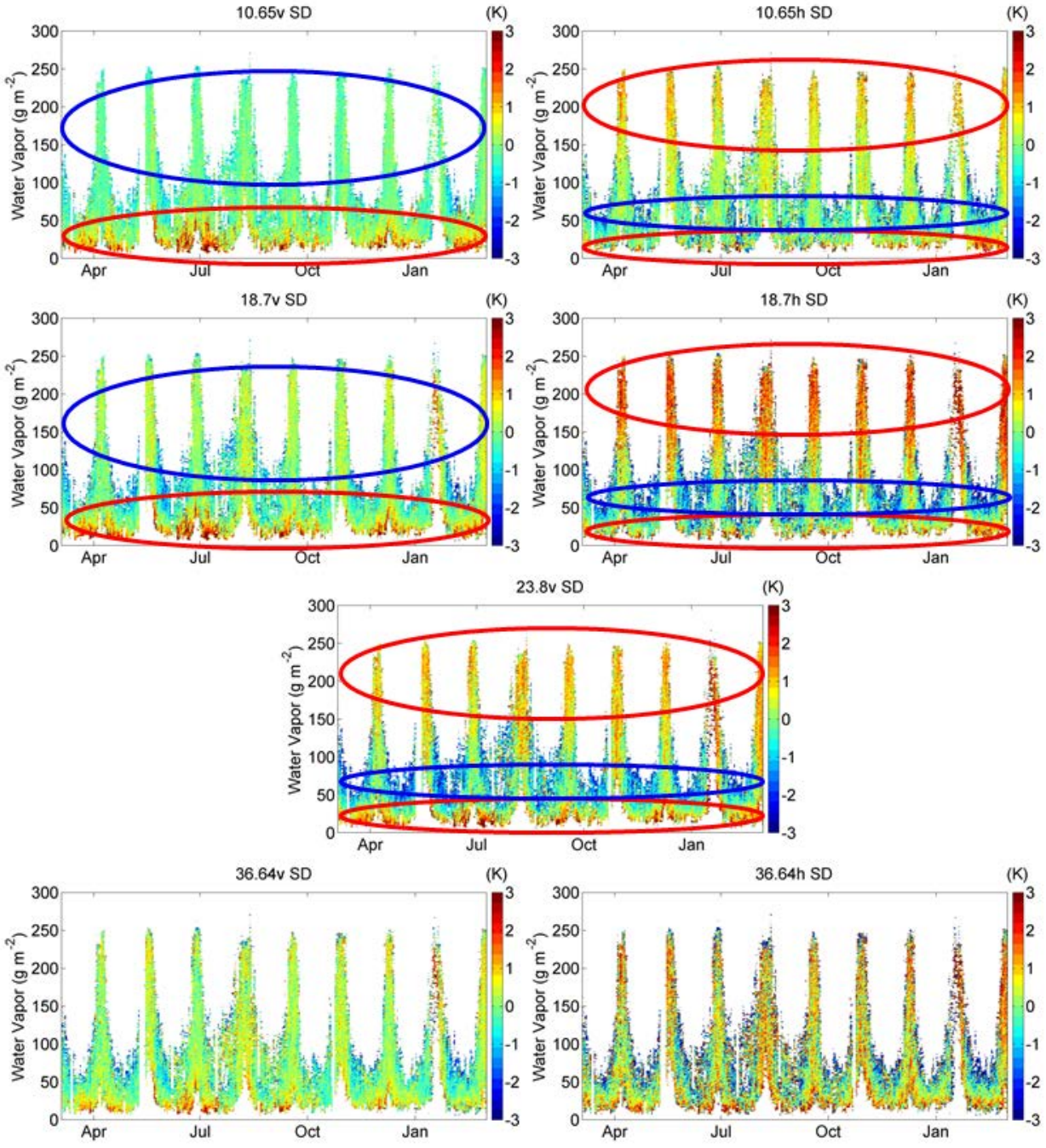

Figure 5.6: The temporal variability of water vapor dependent single difference. The positive and negative departures are highlighted, showing different types of dependence with different channels.

The dependence of the single difference on water vapor is examined from the 3D temporal variability perspective, as shown in Figure 5.6. The single difference is for GMI (WindSat shows similar results). The mean of the single difference is subtracted for each channel. The red and blues ellipses highlight the positive and negative departures, respectively. Three different types of dependence are found, depending on the channel. The first one is that the single difference does not show a significant dependence on water vapor. In channels 36.64V and 36.64H, the coded color for single difference is relatively uniformly distributed as water vapor changes over time. A second type is monotonic dependence, where single difference shows monotonic increase or decrease with the change of water vapor. In channels 10.65V and 18.7V, single difference is large with low water vapor, but becomes smaller with high water vapor. The third type is non-monotonic, where single difference is large with low water vapor below 30 g/m^2, small with moderate water vapor between 30 and 80 g/m^2, and large again with high water vapor from 80 to 250 g/m^2, as shown in channels 10.65H, 18.7H and 23.8V. In this non-monotonic type, the single difference is extremely large with very high water vapor beyond 150 g/m^2. The three types can mix with each other.

Figure 5.7 show the results for GMI/WindSat double differences. Overall, the dependence of the double difference on water vapor is reduced, compared to that of the single difference. However, pronounced variability remains at some

channels. In channels 18.7H and 23.8V, monotonic dependence is observed. That is, double differences decrease with water vapor. This is different from the single difference, where non-monotonic dependence is presented for the two channels. Temporal differences are found. For instance, channel 18.7V has noticeably larger double differences from March – July compared to later months.

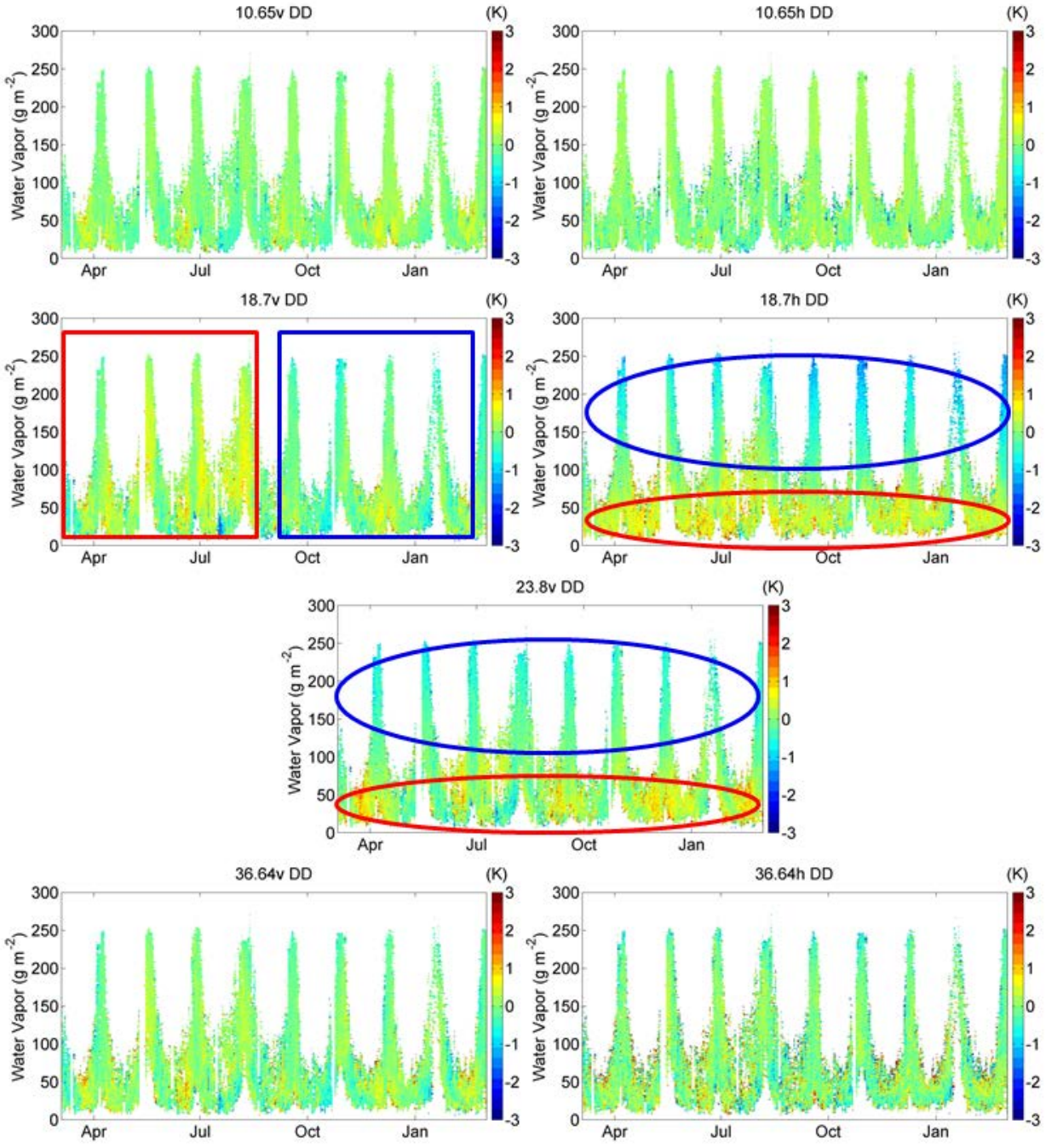

Figure 5.7: The same as Figure 5.6, but for double difference.

SWS has a pronounced impact on calibration in terms of both single and double difference. In Figure 5.8, single difference is found to have either monotonic increase or decrease with SWS, depending on the channel. For 10.65H,

18.7H and 36.64H, single difference monotonically increases with SWS; it decreases for 10.65V, 18.7V, 23.8V, 36.64V. Slightly non-monotonic dependence is noticed for 23.8V and 36.64V, where large single difference is observed with both very low (<5 m/s) and high (>15 m/s) SWS. Compared to water vapor, SWS demonstrates stronger impact on single difference. For example, average single differences at 18.7V are 2.5K and -1.5K for high (>15 m/s) and low (<10 m/s) SWS respectively, differing by as much as 4 K. Furthermore, the impact of SWS persists with locations crossing both tropical and high-latitude regions. Channel 10.65V, for instance, keeps a small and large single difference for high SWS (>15 m/s) and low SWS (<10 m/s), respectively. Moreover, the impact from other geophysical parameters such as water vapor is noticeable. For channels 18.7H to 37.H, the 40-day signal is noticeable, where single difference periodically increases with low SWS (<5 m/s). These channels are more affected by water vapor than channels like 10 GHz V and H. Therefore, when SWS is low, the impact of water vapor becomes pronounced.

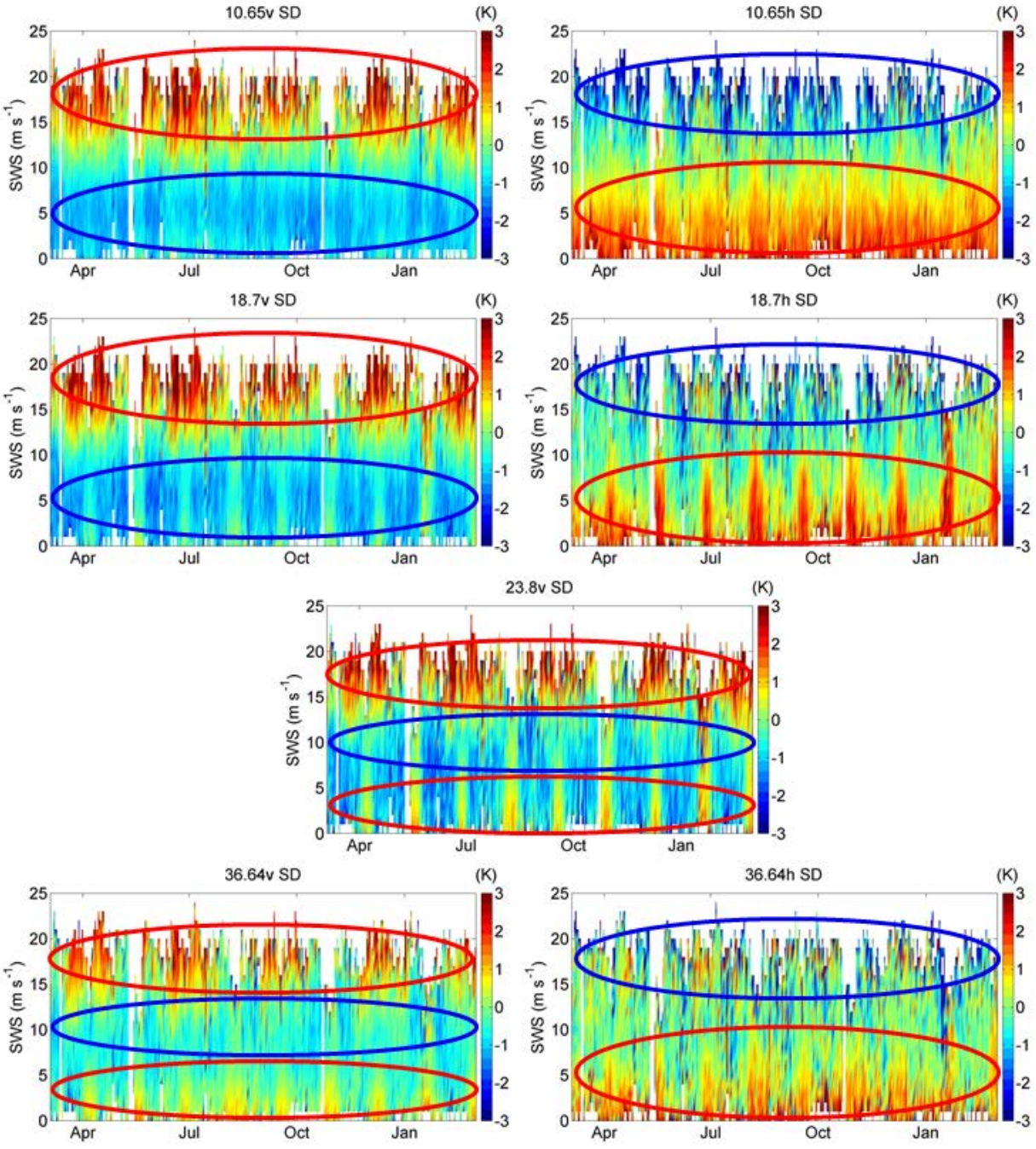

Figure 5.8: The temporal variability of SWS dependent single difference. Highlighted positive or negative departures show there are different dependences that vary by channel.

As in Figure 5.9, the double difference is affected by SWS, although not as strongly as the single difference. For SWS larger than 15 m/s, the double

difference becomes either very large (10.65V, 18.7H, 23.8V, 36.64V, 36.64H) or very small (18.7V). Channel 10.65H does not show much SWS impact. This SWS impact also persists in both tropical and high-latitude regions. Temporal variability is noticed, where 18.7H and 18.7V have larger double difference in the first five months than in later months. The impact of water vapor shows up in 23.8V as a 40-day oscillation.

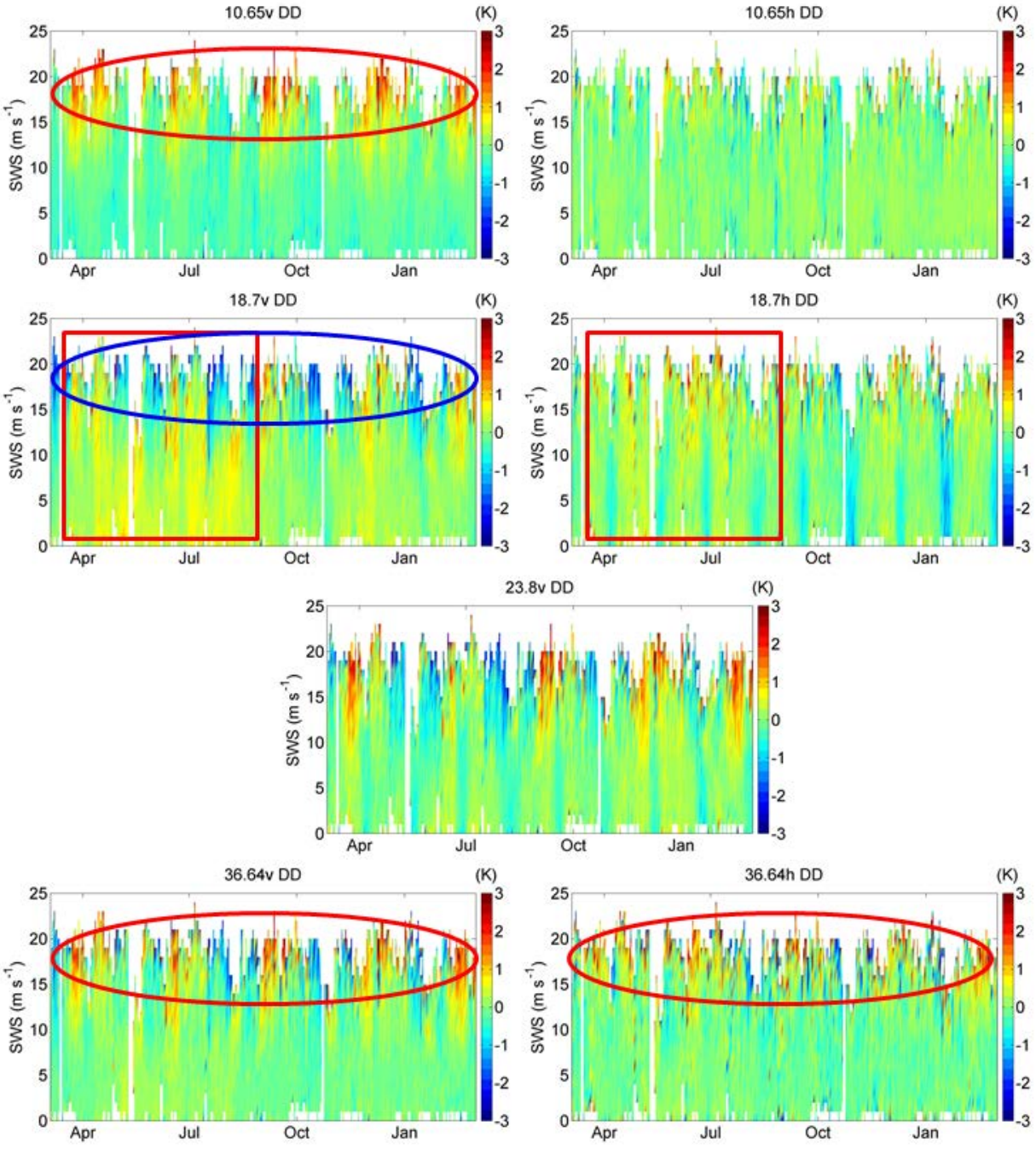

Figure 5.9: The same as Figure 5.8, but for double difference.

SST shows similar impact on calibration to water vapor, but with some differences worth noting. In Figures 5.10 and 5.11, the SST dependent temporal variability is shown for single and double difference, respectively. SST affects

calibration and shows monotonic or non-monotonic dependence similar to that of water vapor. Since SST and water vapor are correlated in terms of temporal and spatial variability their impact on calibration is also correlated. On the other hand, SST shows less impact on calibration than water vapor and SWS, as shown in the more uniformly distributed color. For instance, while low water vapor (<5 m/s) tends to correspond to high single difference, low SST (<277 K) does not show much difference relative to moderate SST (277-280 K)

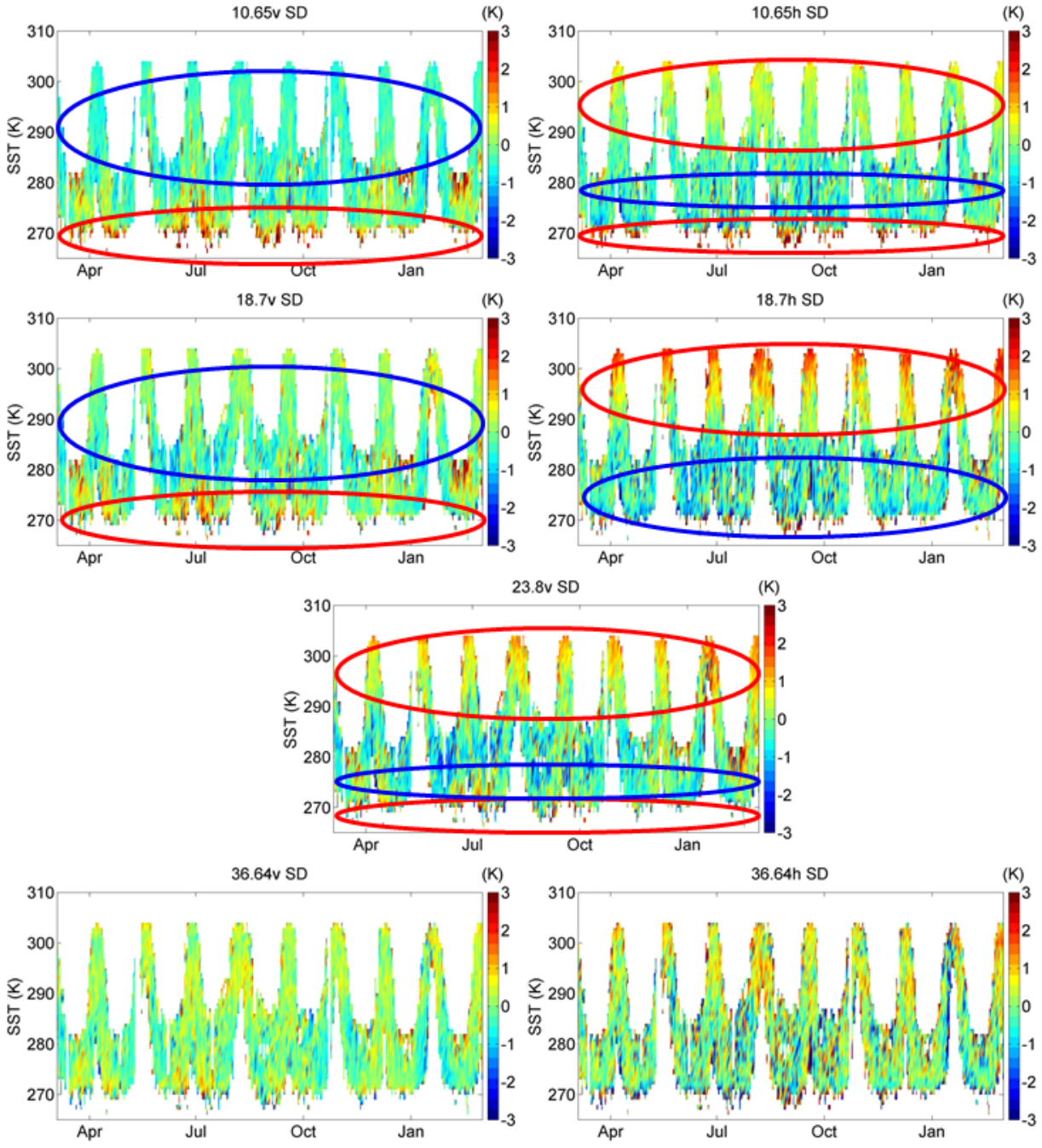

Figure 5.10: The temporal variability of SST dependent single difference. Highlighted positive or negative departures show different types of dependences with different channels.

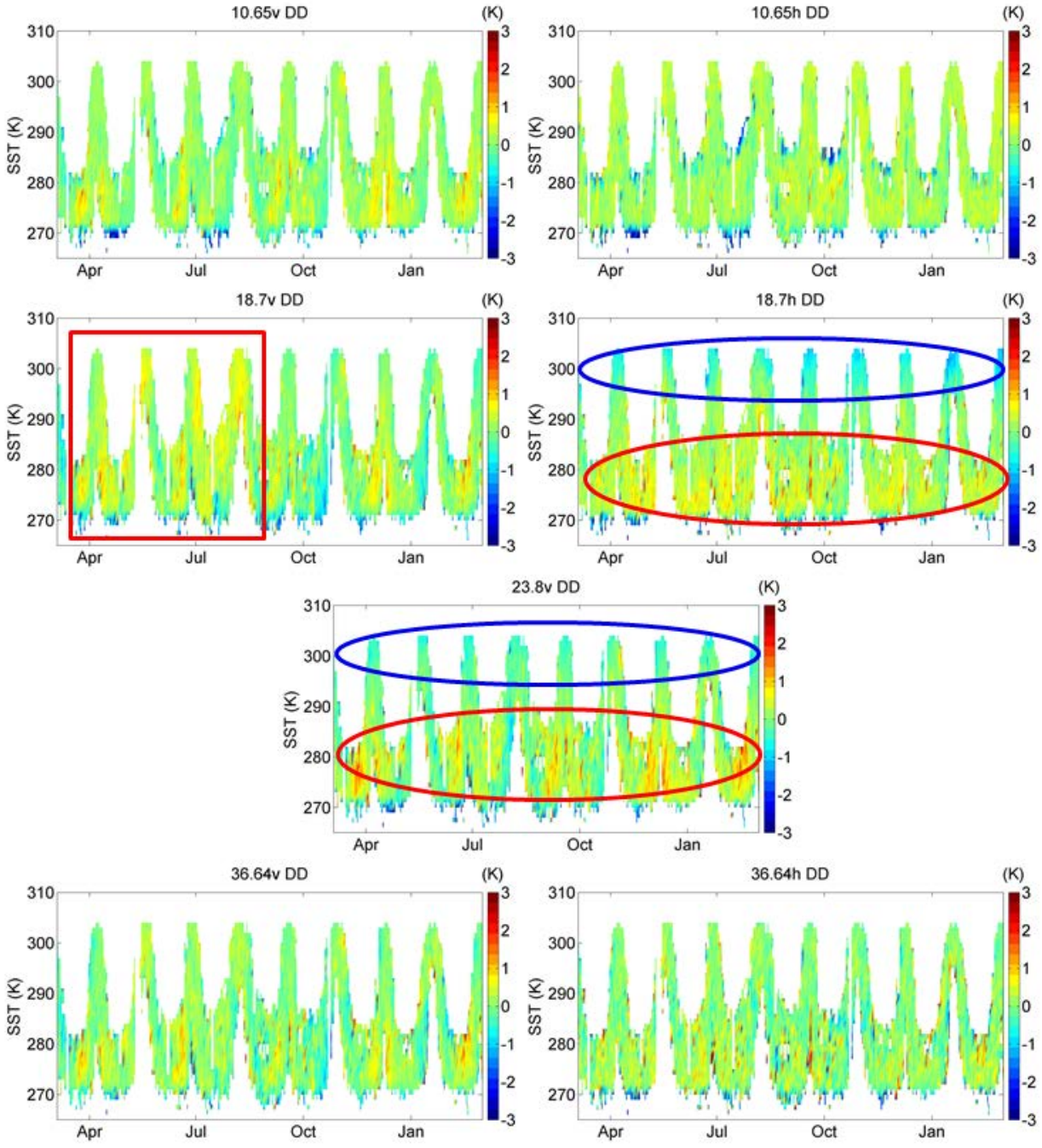

Figure 5.11: The same as Figure 5.10, but for double difference.

Calibration has a strong latitudinal dependence. Figures 5.12 and 5.13 show the latitudinal variability for single and double differences, respectively. Calibration location shows a latitudinal oscillation with a 40-day period. A

pronounced high single difference is observed in the tropics for channels 10.65H, 18.7H, and 23.8V. This verifies previous temporal variability analysis (Figure 5.6), where high water vapor results in a large single difference. For channels 10.65V, a high single difference is observed at high latitudes, agreeing with the SWS temporal analysis (Figure 5.8). The double difference is smaller in tropics than high latitude for 18.7H and 23.8V, opposite to that of single difference. Channel 18.7V has a larger double difference in the first five months, as confirmed in previous analysis.

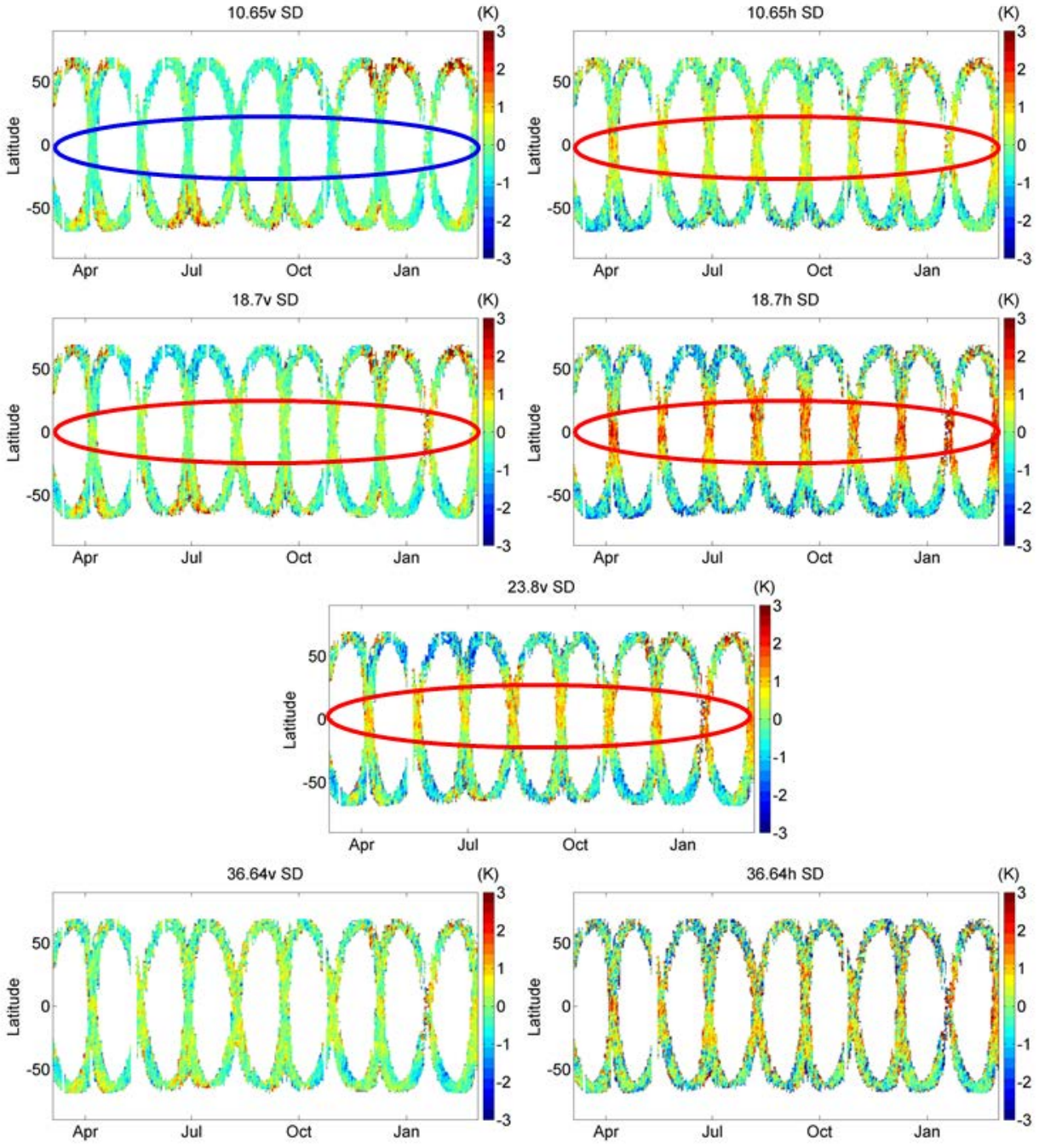

Figure 5.12: The temporal variability of latitude dependent single difference. Highlighted positive or negative departures show different dependences with different channels.

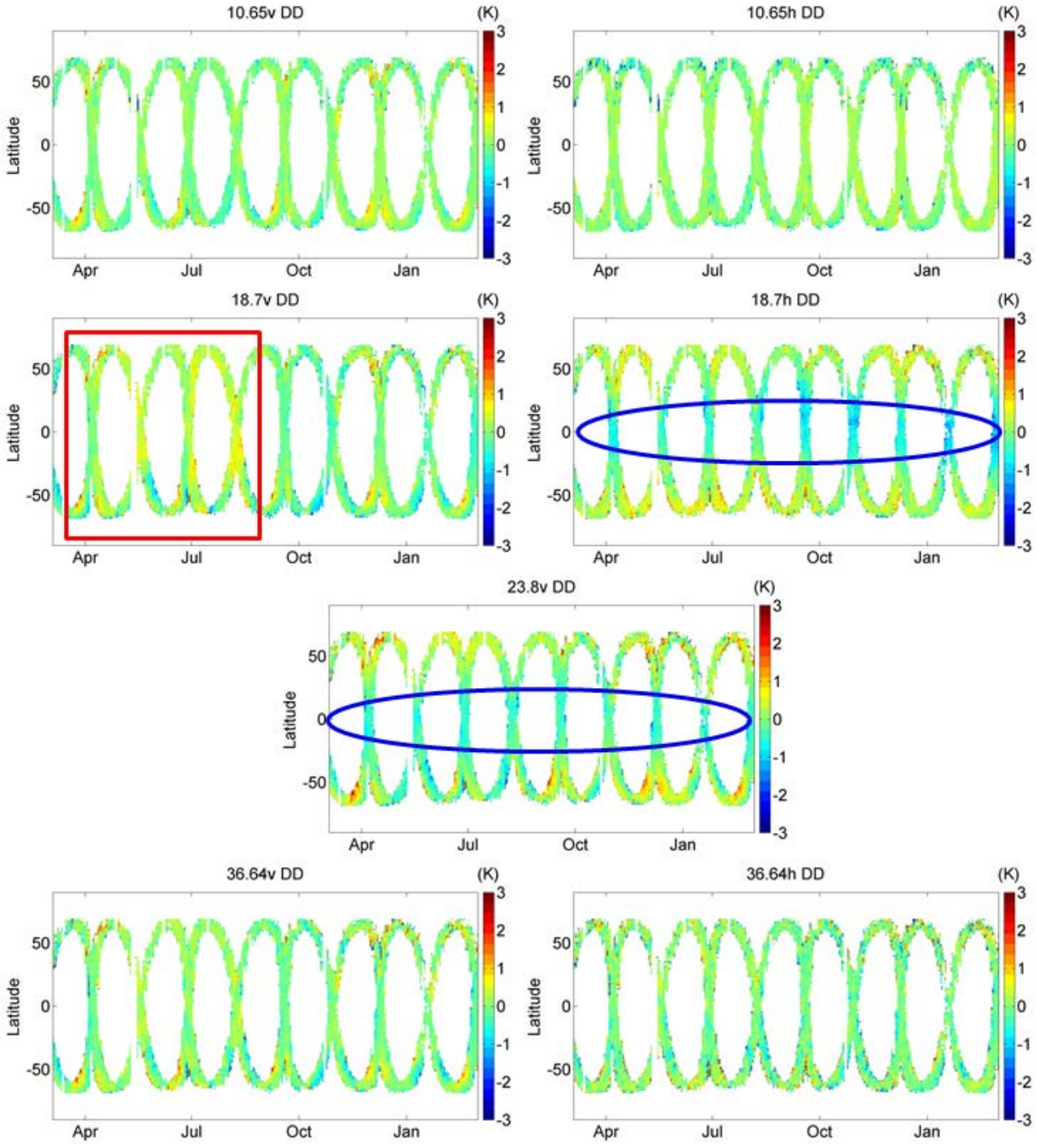

Figure 5.13: The same as Figure 5.12, but for double difference.

A longitudinal impact on calibration exists but is weaker than that of latitude, as shown in Figures 5.14 and 5.15. The calibration location shifts longitudinally. According to Fourier analysis, a 40-day signal is found. The previously found

18.7V temporal variability is noticed here, i.e., larger double difference in the first five months that later months. For channel 18.7H and 23.8V, locations with longitudinally high water vapor like the West Pacific show larger single difference than regions with low water vapor like the East Pacific.

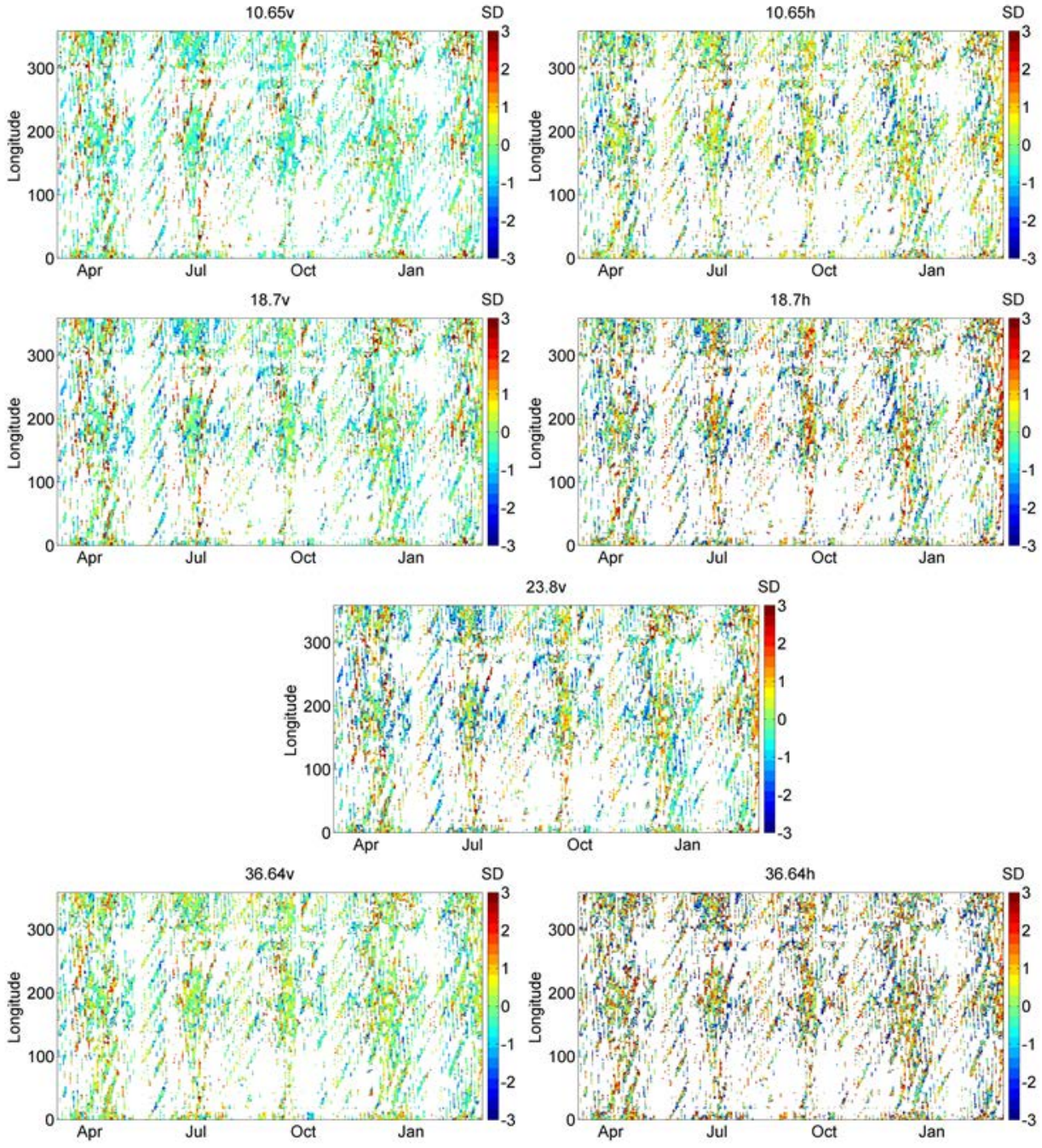

Figure 5.14: The temporal variability of longitude dependent single difference.

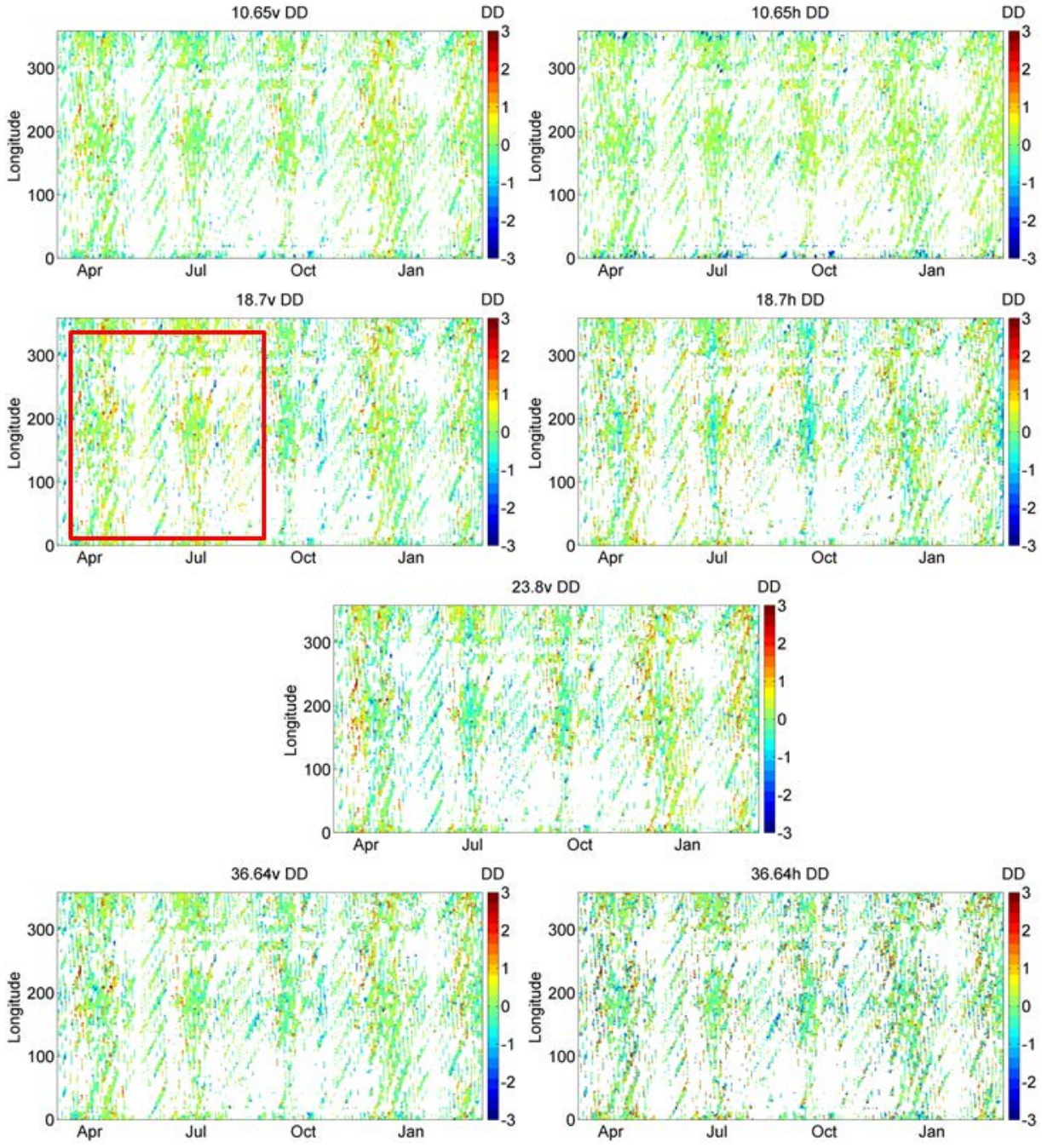

Figure 5.15: The same as Figure 5.14, but for double difference

5.3 Spatial Variability

Calibration's spatial variability provides complementary information to its temporal variability. Figure 5.16 shows the spatial distribution for collocation and

geophysical parameters. More collocations occur at high latitude (~±60º), since the GMI orbit places it in these latitudes more often over a given time period. Water vapor is abundant in the tropics. It also has longitudinal variability such that more water vapor is present in the West Pacific than in the East Pacific. Likewise, SST also shows regional differences, but with less variability than water vapor. SWS is higher in high latitude zones (~±50º) and is stronger in the southern hemisphere where land areas are small. Longitudinally, SWS is higher in the East Pacific than in the West Pacific (opposite to water vapor and SST).

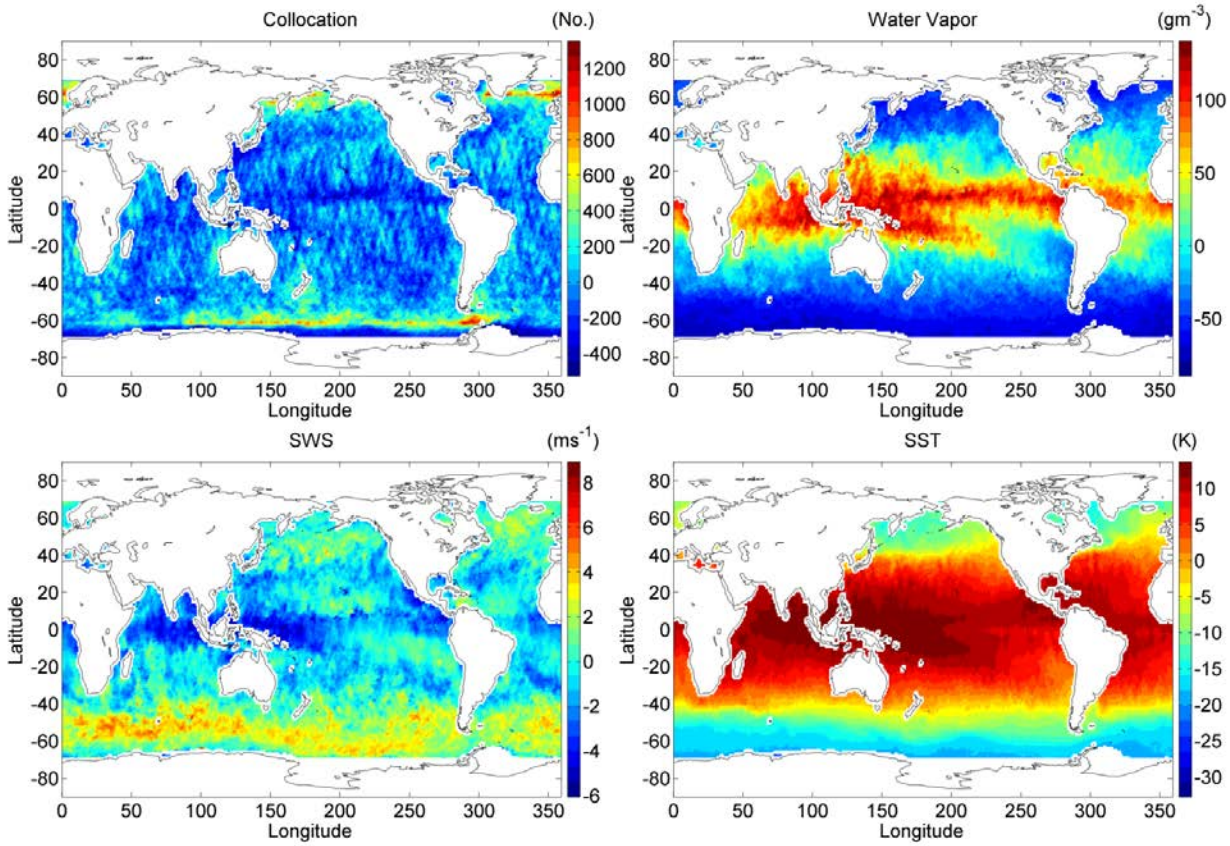

Figure 5.16: The maps of geophysical parameters and collocation number density, showing the regional variability.

The maps of mean TB at different channels are presented in Figure 5.17. These channels demonstrate different features. Channel 10.65V shows a spatial distribution in between those of water vapor and SST, while 10.65H is closer to the water vapor distribution. The other channels are similar to the water vapor distribution, indicating the dominant impact from water vapor. The impact from SWS should not be overlooked, since SWS has an opposite feature to water vapor.

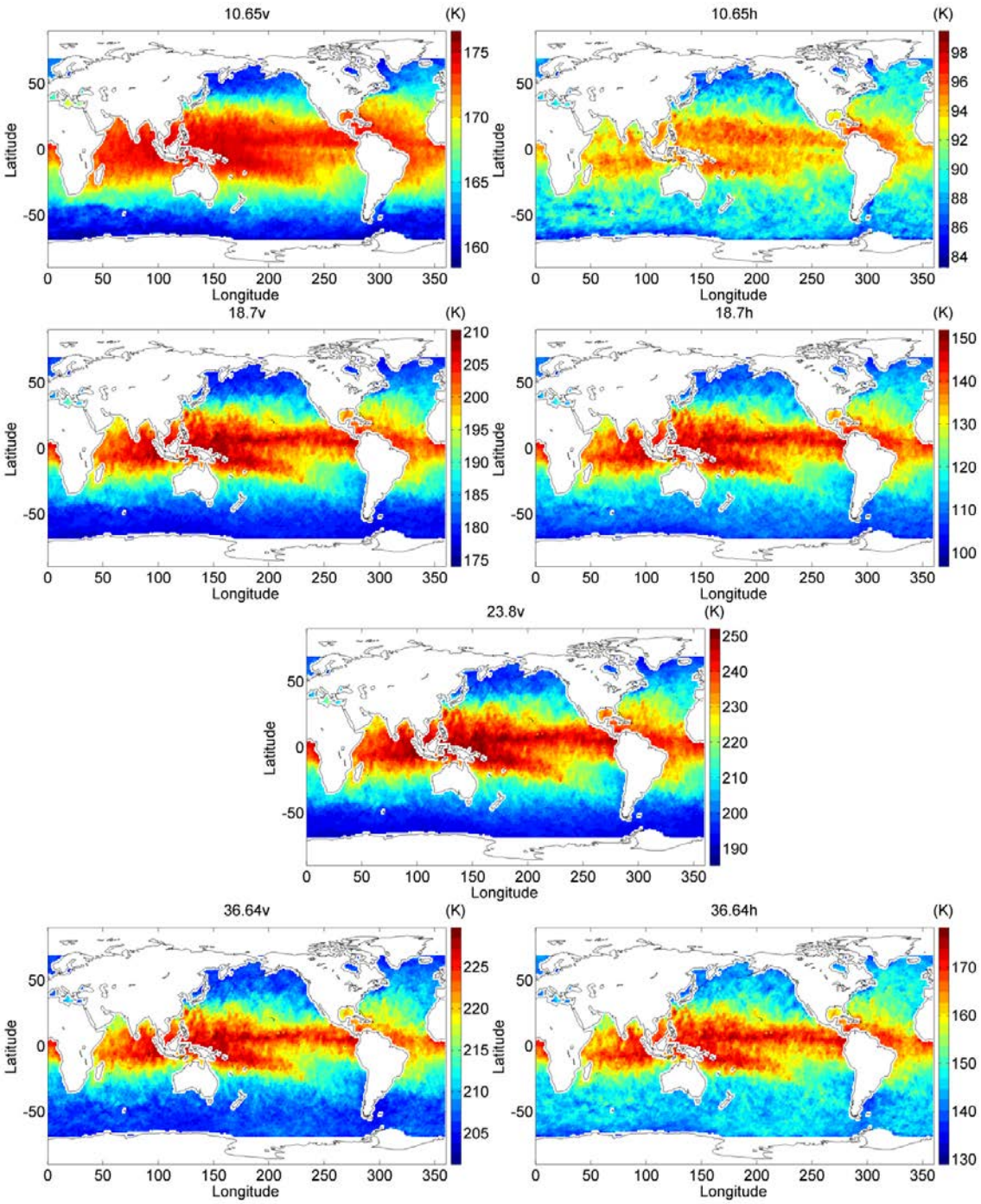

Figure 5.17: The maps of mean TB at different channels. Regional variability is present and dependent on channel.

The spatial distribution of single difference reveals pronounced calibration regional difference. In Figure 5.18, most channels show similarity to water vapor

distribution as well as SST. Except for channel 10.65V, single difference is noticeably larger in the tropics. It also has longitudinal variability, e.g., larger in the West Pacific than in the East Pacific. Channel 10.65V has a flipped latitudinal dependence, i.e., lower in tropics. In fact, 10.65V looks similar to the SWS distribution, e.g., large single difference corresponding to large wind speed in both northern and southern hemisphere zones (±50º). Channel 18.7V also shows larger single difference in high latitude zones (±50), indicating the impact of SWS.

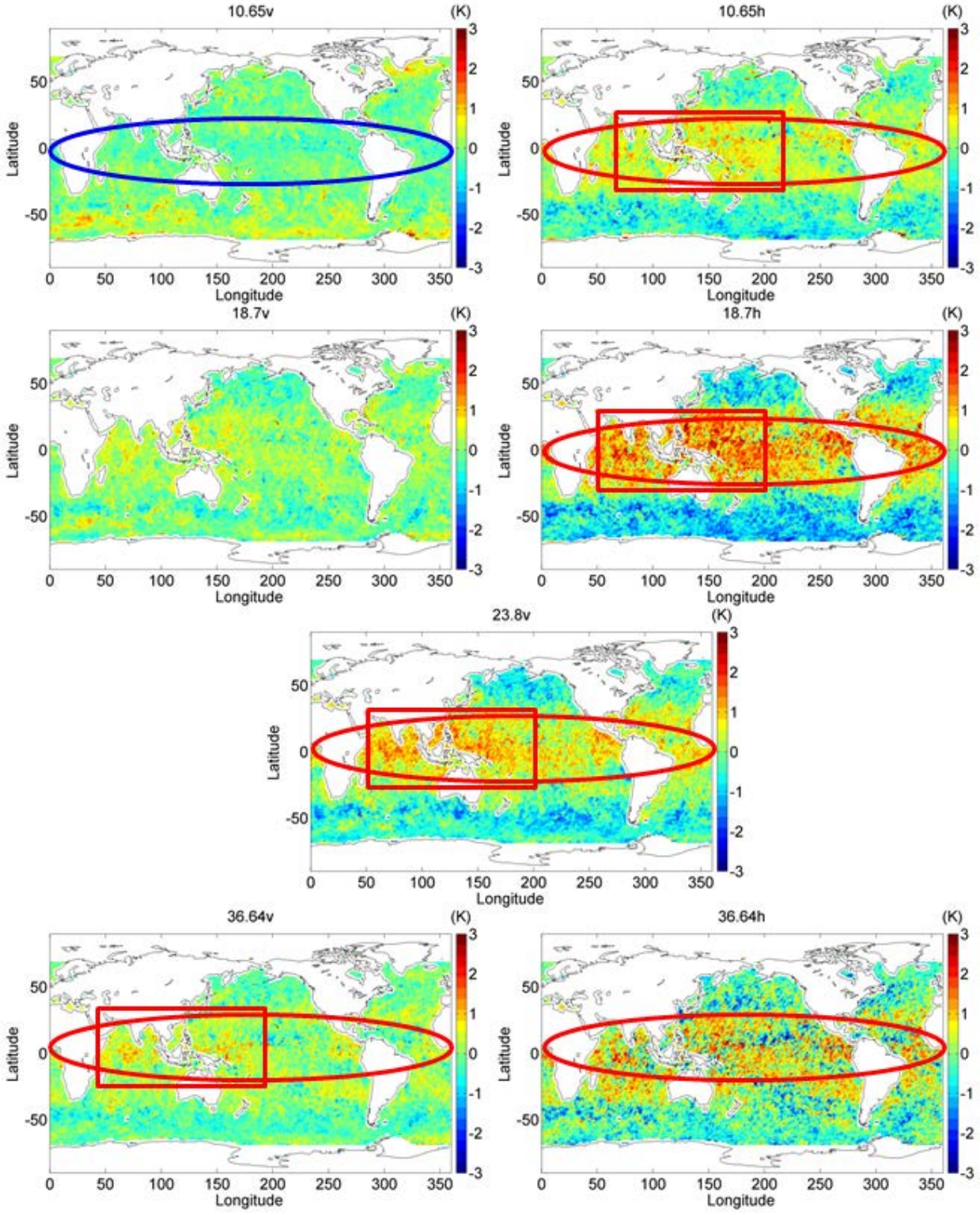

Figure 5.18: The maps of single difference. The positive and negative departures are highlighted and depend on channel.

Figure 5.19 shows the spatial distribution of double difference. Channels 18.7H and 23.8V have flipped patterns compared to that of single difference, i.e., tropical regions have smaller double difference than high latitudes. Longitudinally, the two channels also flip with colder double difference in the West Pacific than in the East Pacific. The other channels show less spatial variability, however, regional differences are still present. For instance, channel 10.65V still has patterns similar to SWS, where high latitude zones have larger double difference.

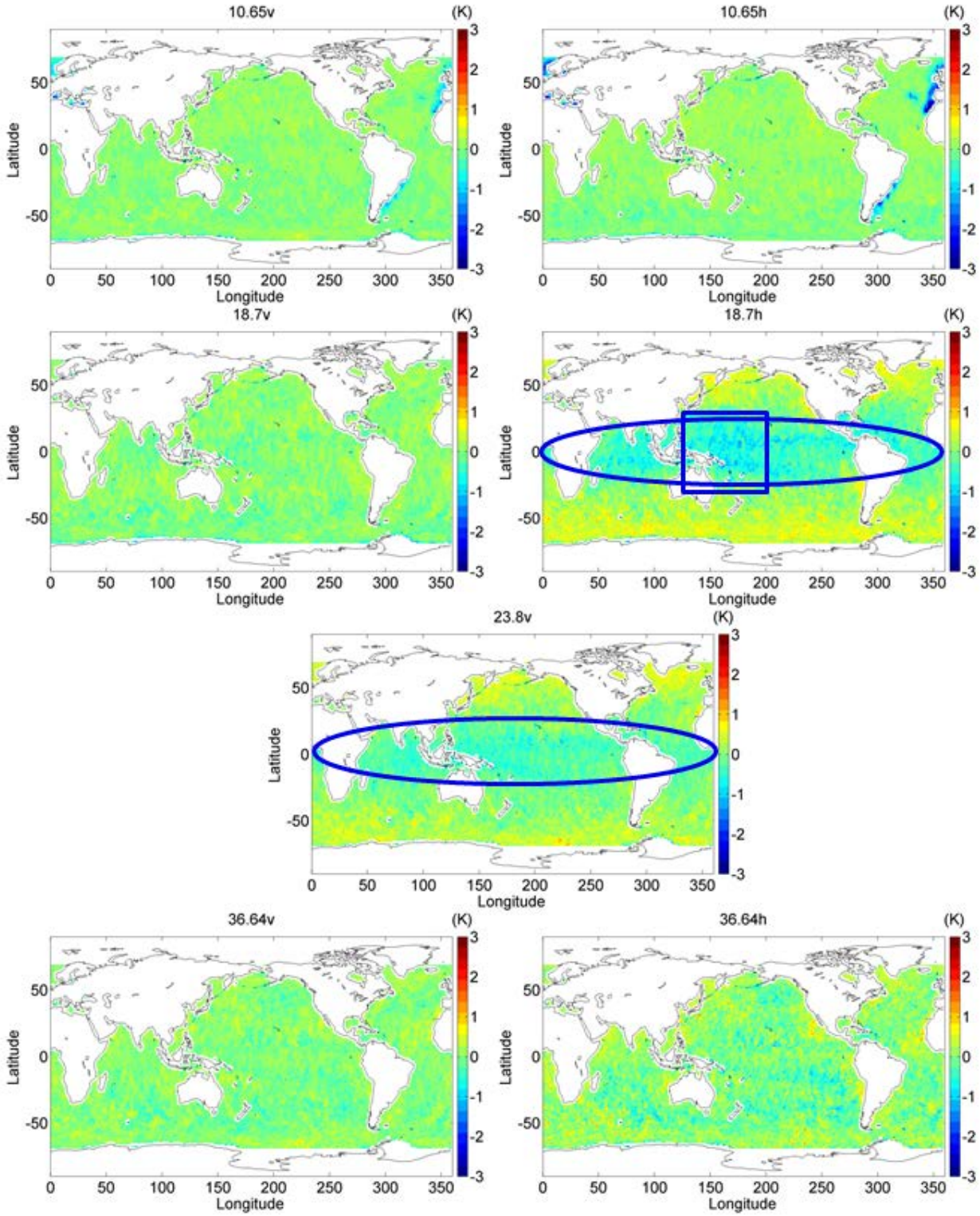

Figure 5.19: The same as Figure 5.18, but for double difference.

The calibration spatial variability confirms the calibration dependence on

geophysical parameters. Since the calibration location shifts latitudinally and longitudinally, the regional difference affects calibration and can result in temporal variability. One important implication is that calibration at any local region can have biases compared to the whole globe. Different sampling over the globe (e.g., the GMI/WindSat collocation sampling shown in Figure 5.16 relative to other satellite pairs or other time periods) can change results due to this variability.

5.4 Nonlinearity

The calibration dependence on geophysical parameters and TB is considered further to asses possible TB, parameter nonlinearity. Figures 5.20 and 5.21 show the polynomial regression and number density plots between water vapor and single difference. The dependence of single difference on water vapor can be represented through polynomial regression. Different degree of polynomial regressions have been tested, it is found that R-square of polynomial regressions converge starting from the fourth degree of polynomial regression, i.e., $y = \sum_{i=0}^{4} a_i x^i$. In addition to water vapor, the fourth degree polynomial is also adequate to fit the data of other parameters and is therefore applied hereafter. As shown in Figure 5.21, all channels show that modeling overall underestimates observation, particularly with high water vapor conditions. Nonlinearity is appreciated in all channels. A left-side tilt-up tail is present with low water vapor

(<40 g/m^2). A slight bump with middle-range water vapor (100-160 g/m^2) is appreciated, particularly at 23.8V. The single difference increases with high water vapor (>160 g/m^2). The nonlinearity and large discrepancy are issues that have not been cared in current calibration. It implies issues in model parameterization (e.g. surface emissivity and atmospheric absorption model) and the ancillary water vapor field that does not properly represent reality. Another implication is that clear-sky calibration with low water vapor has potential errors, although it is intensively used for calibration since cloudy and precipitation conditions are difficult to model.

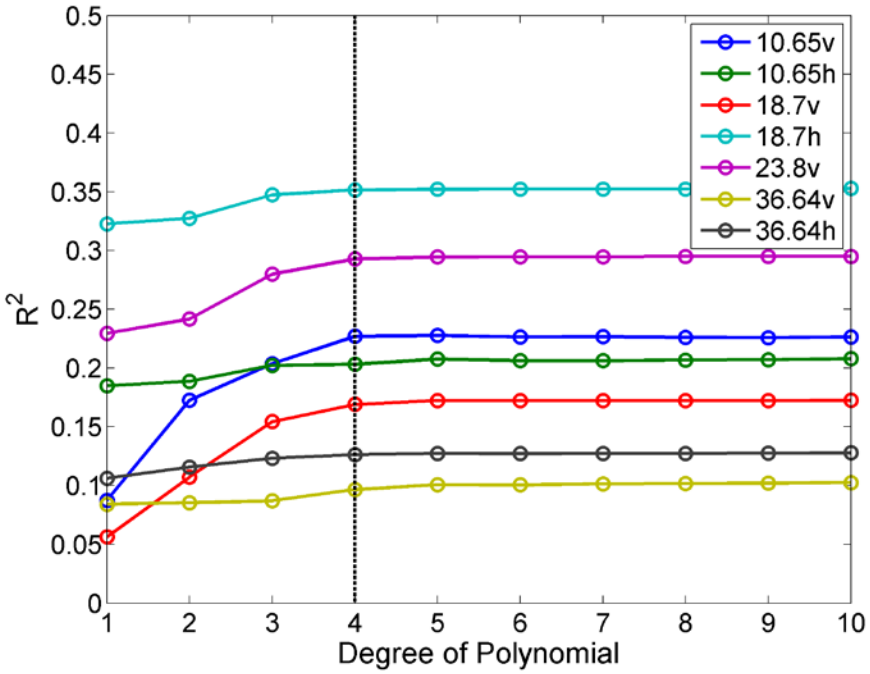

Figure 5.20: R-square of polynomial regressions for single difference and water vapor, which converges starting at the 4th degree of polynomials regression.

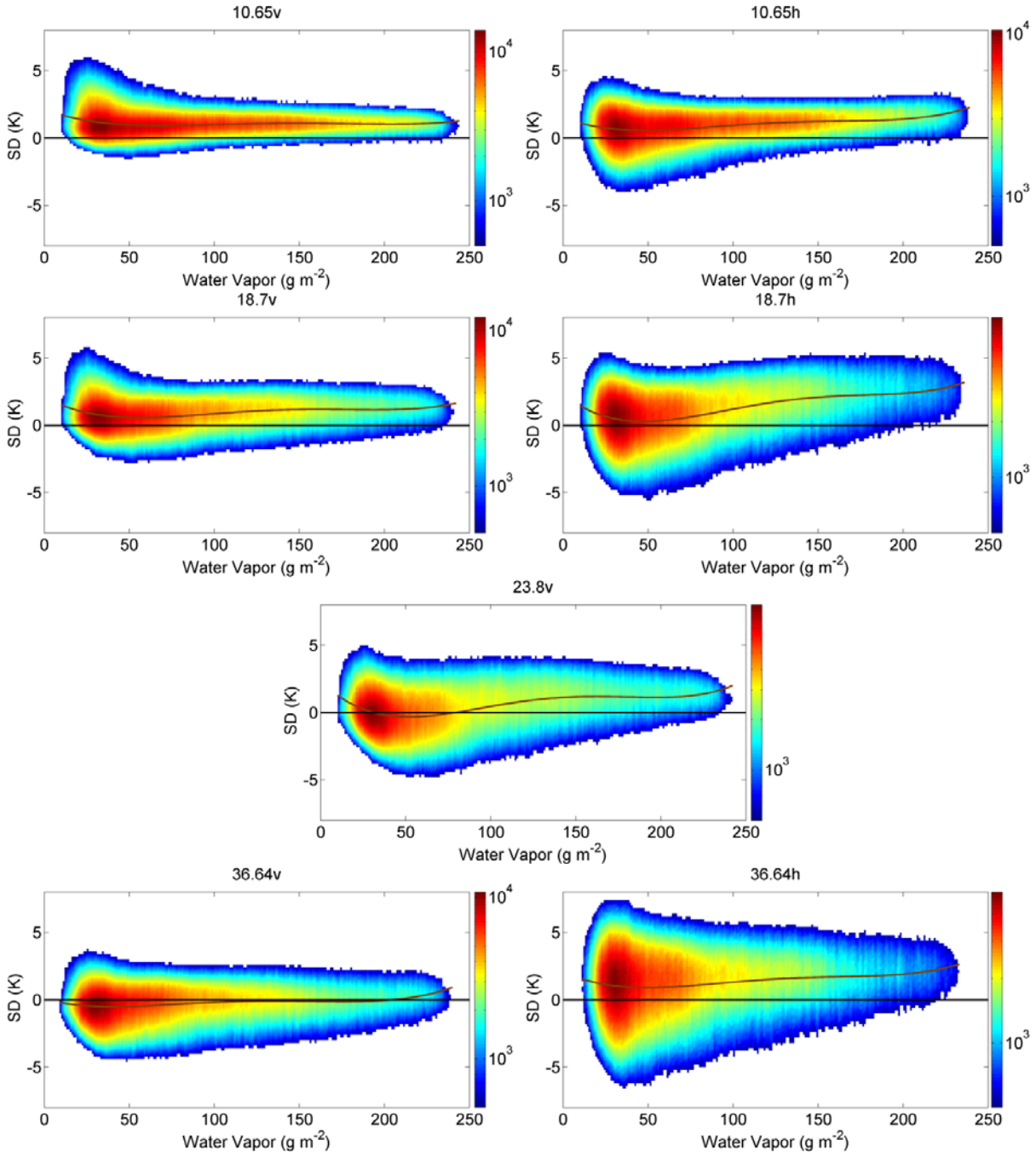

Figure 5.21: The dependence of single difference on water vapor. The brown lines are from polynomial regression of the fourth degree. Nonlinear and non-monotonic dependence is found. The discrepancies between model and observation not only present at high end, but also with low water vapor corresponding to calm weather conditions, which is commonly used for calibration and contains these potential errors.

Figure 5.22 shows the results for double difference. The overall nonlinearity is reduced compared to single difference. Residual nonlinearity is appreciated with low water vapor. The overall double difference dependence on water vapor becomes negative, contrasted to the positive dependence in single difference.

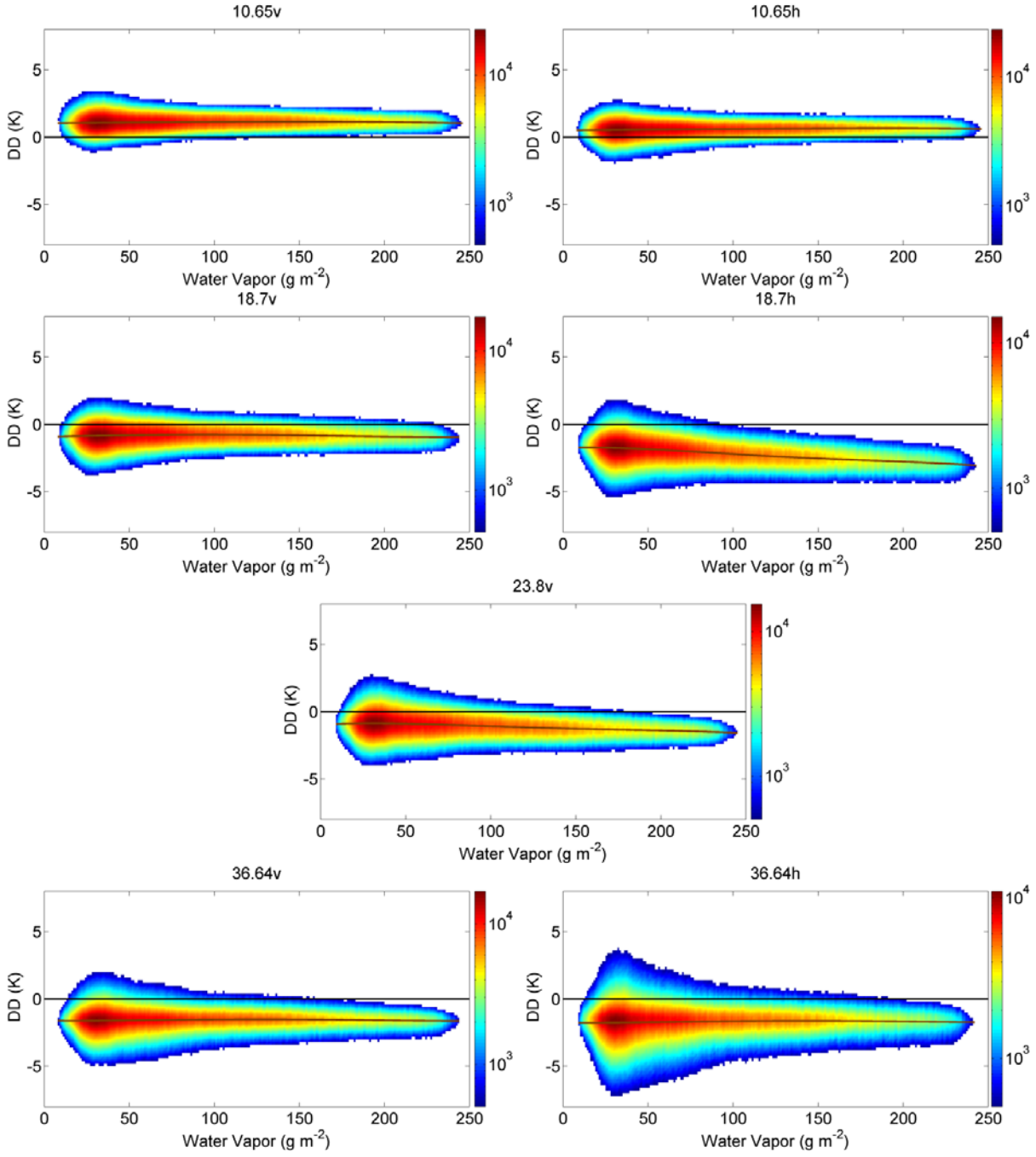

Figure 5.22: The same as Figure 5.21, but for double difference.

The dependence on SWS is studied. Figure 5.23 shows pronounced nonlinear and non-monotonic dependence. The H-pol channels such as 18.7H show a first order harmonic signal as illustrated by the polynomial regression. Overall, single

difference at H-pol shows a negative dependence on TB. The V-pol channels bends with SWS ~m/s and tilts up at both ends. A positive dependence on TB is observed. Figure 5.24 shows the results for double difference. The magnitude of nonlinearity is reduce but is still appreciable. The overall dependence flips from negative to positive for channels 18.7V&H, 23.8V, and 36.64H, compared to that of single difference. Wind speed is a major factor affecting calibration through parametrization in emissivity model. For window channels, the surface emission dominates. The emissivity dependence on TB and frequency is parameterized in model. Errors in parameterization can result in nonlinear and non-monotonic discrepancies as found here

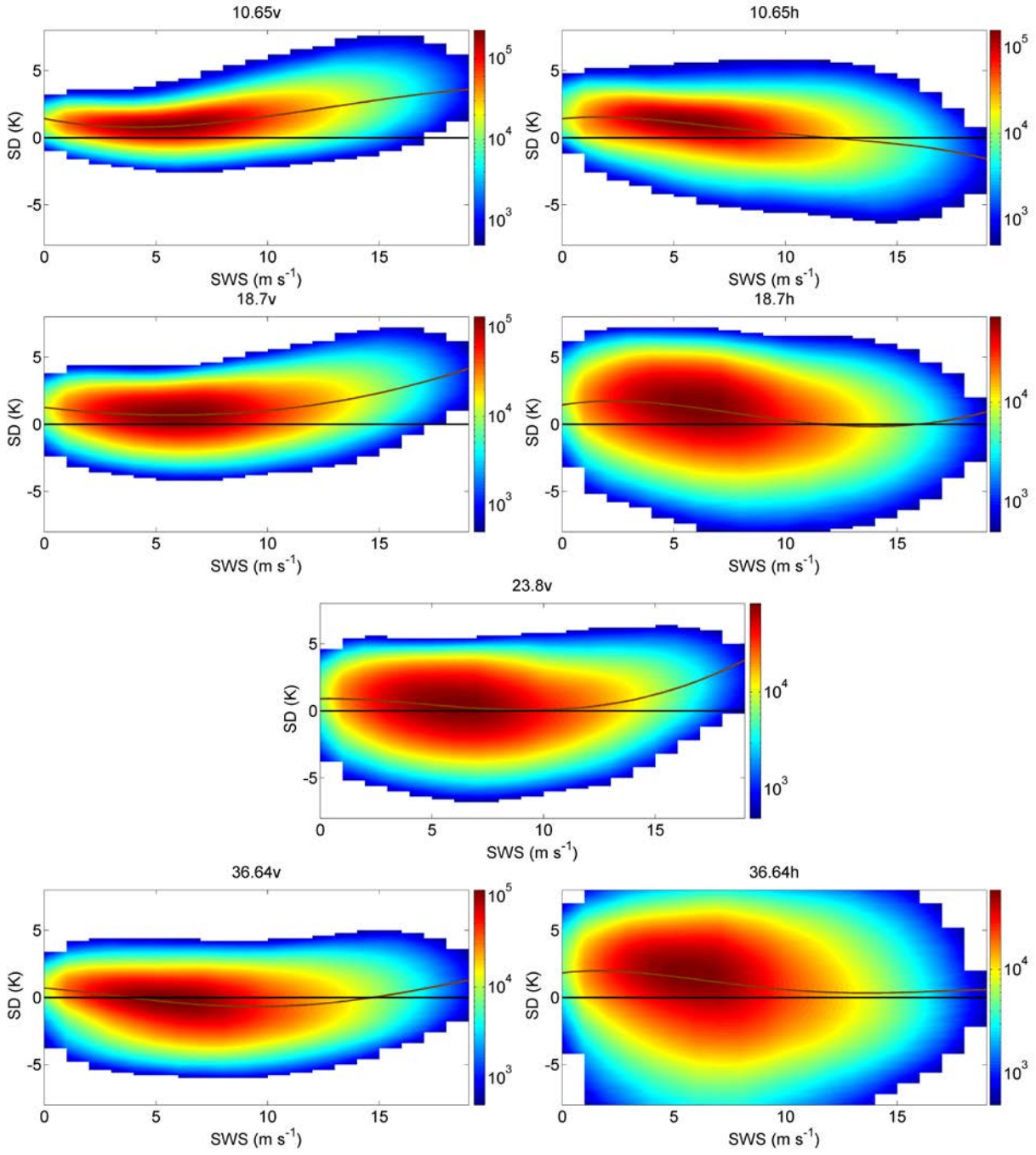

Figure 5.23: The dependence of single difference on SWS. Nonlinear and non-monotonic dependence can be found. The H-pol channels appear to have a first order harmonic signal, while v-pol channels tilts up at both ends.

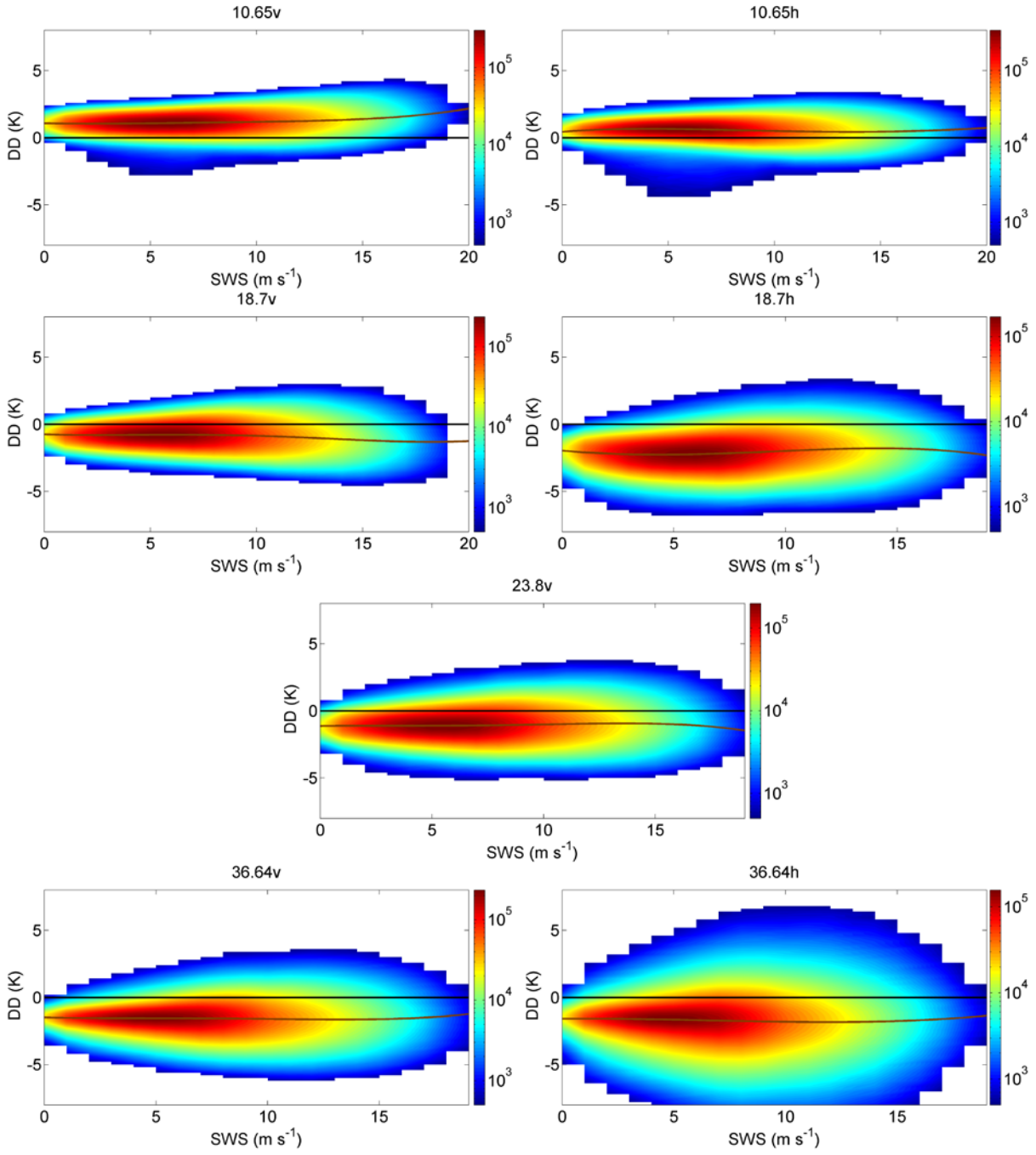

Figure 5.24: The same as Figure 5.23, but for double difference.

Figures 5.25 and 5.26 show the results for SST. SST appears to have two modes with a number of samples at cold (270-277ºC) and warm (300-305ºC) SSTs. The single difference tilts up at the warm mode of TBs. In channel 18.7H, single

difference increases much rapidly with SST larger than 285 K. A positive dependence is seen at all channels. The H-pols show more significant scattering than V-pols. For double difference, channels 18.7H and 23.8V show negative dependence, opposite to that of single difference.

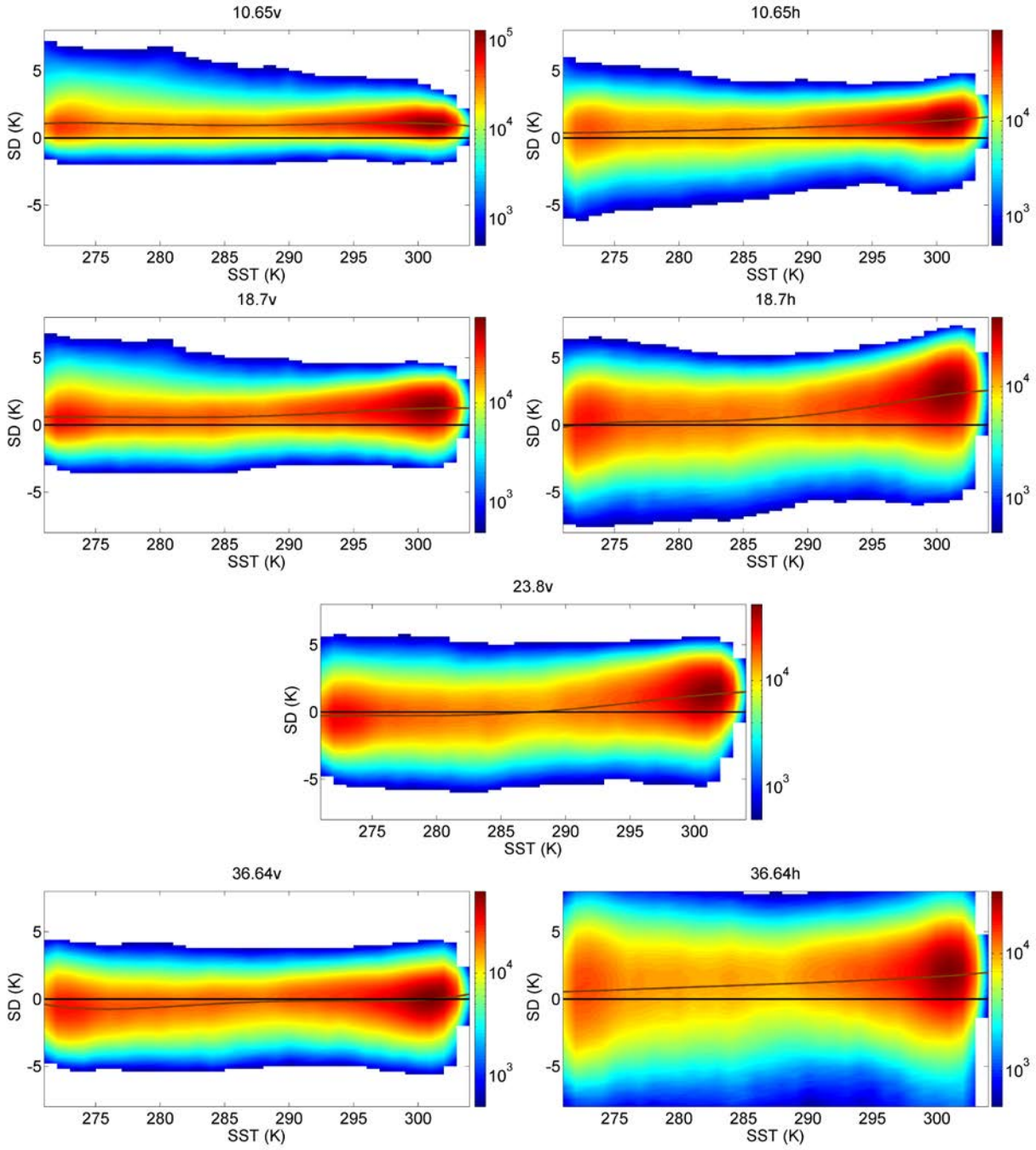

Figure 5.25: The dependence of single difference on SST.

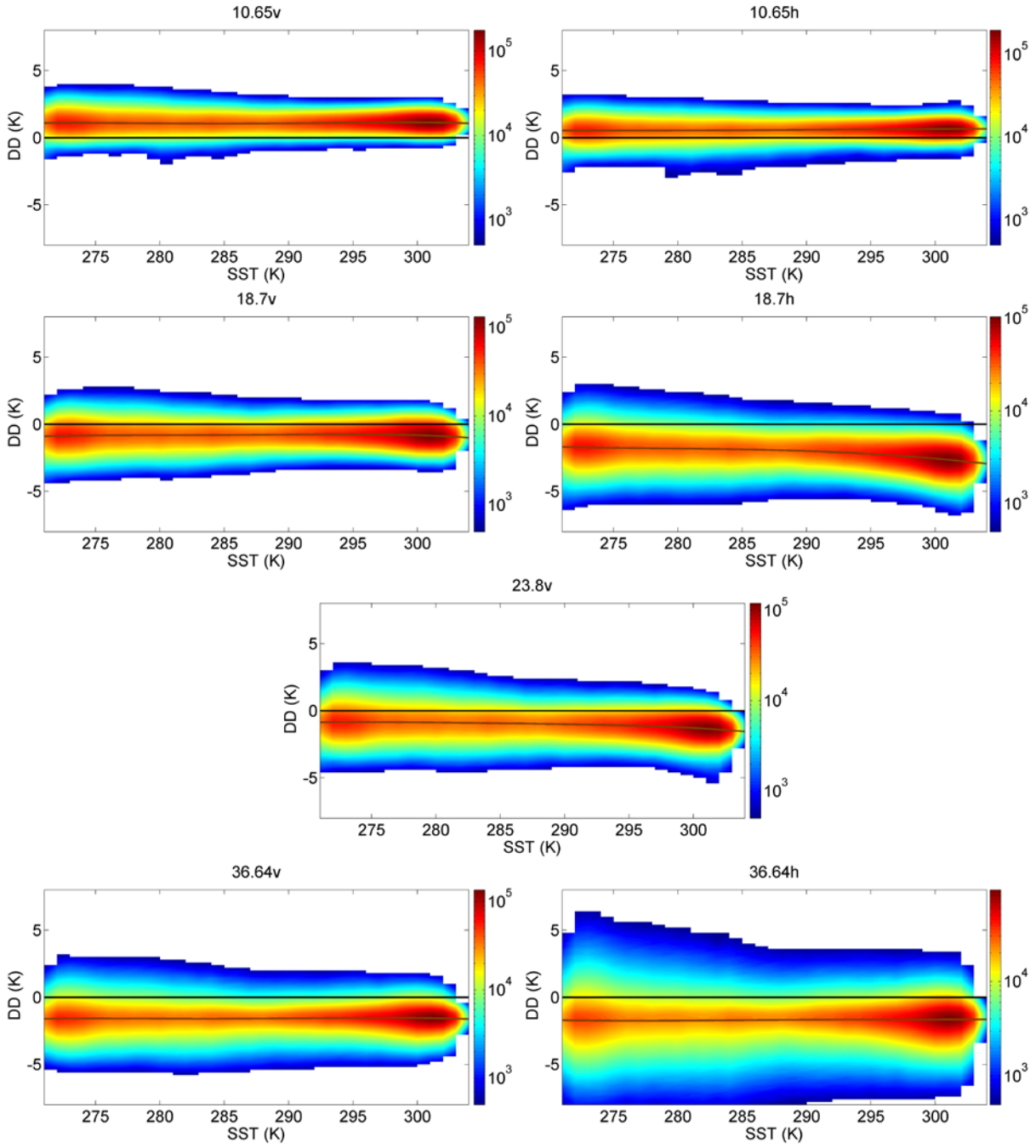

Figure 5.26: The same as Figure 5.25, but for double difference.

The calibration dependence on TB is examined in Figures 5.27 and 5.28. Since TB is a function of all three geophysical parameters, the TB dependence shows combined features from each individual parameter. For instance, channel 10.65V

has a bi-mode feature as with SST. The V-pol channels have tilt-up at low to moderate TBs, which represent the water vapor features. Channel 10.65H shows slightly harmonic feature like SWS. A positive dependence on TB is observed in single difference but becomes negative at some channels for double difference. Overall, the combination of all three geophysical parameters makes the calibration dependence on TB more complicated and more difficult to be removed.

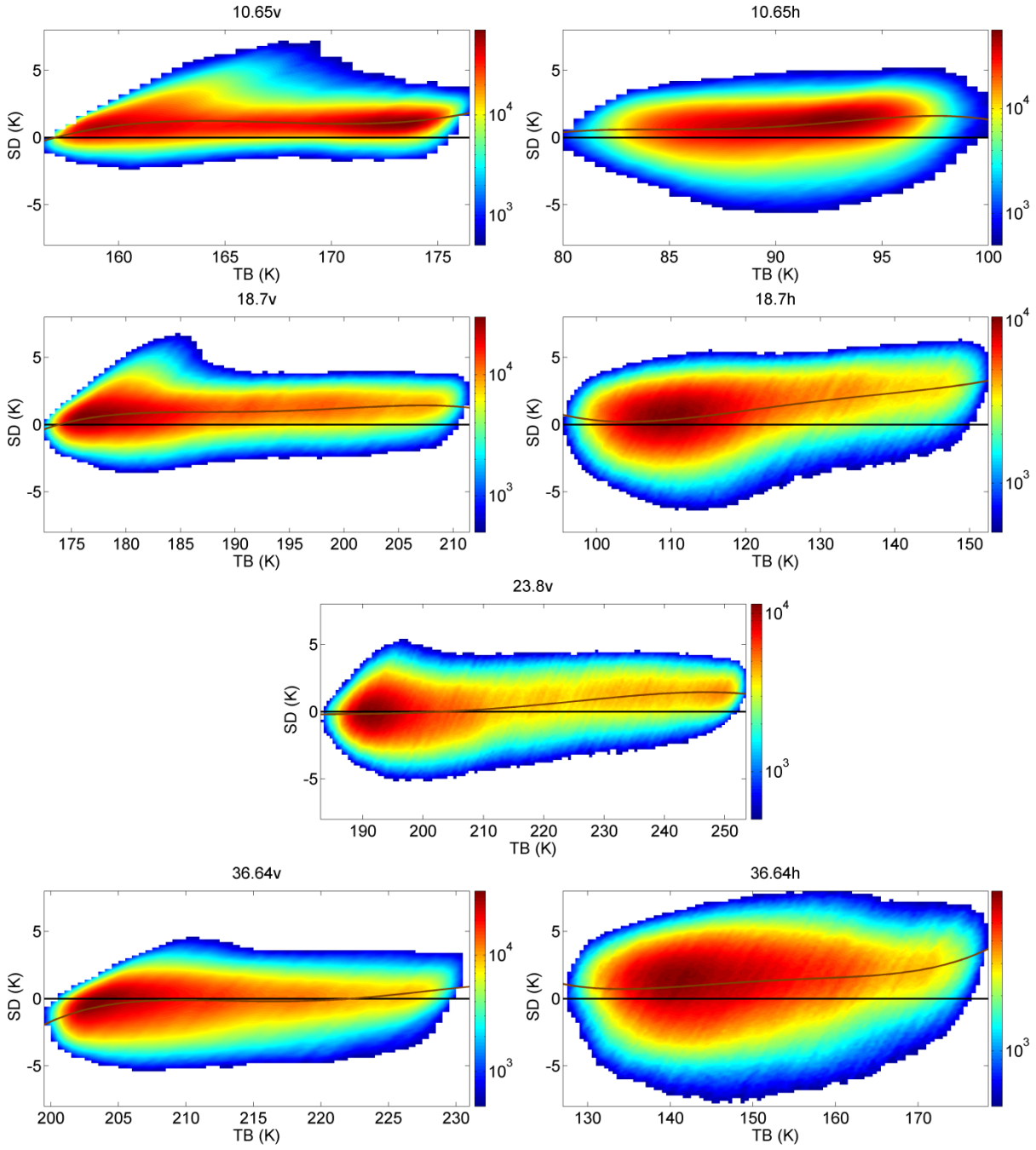

Figure 5.27: The single difference as a function of TB, where nonlinear dependence is found with specific channels.

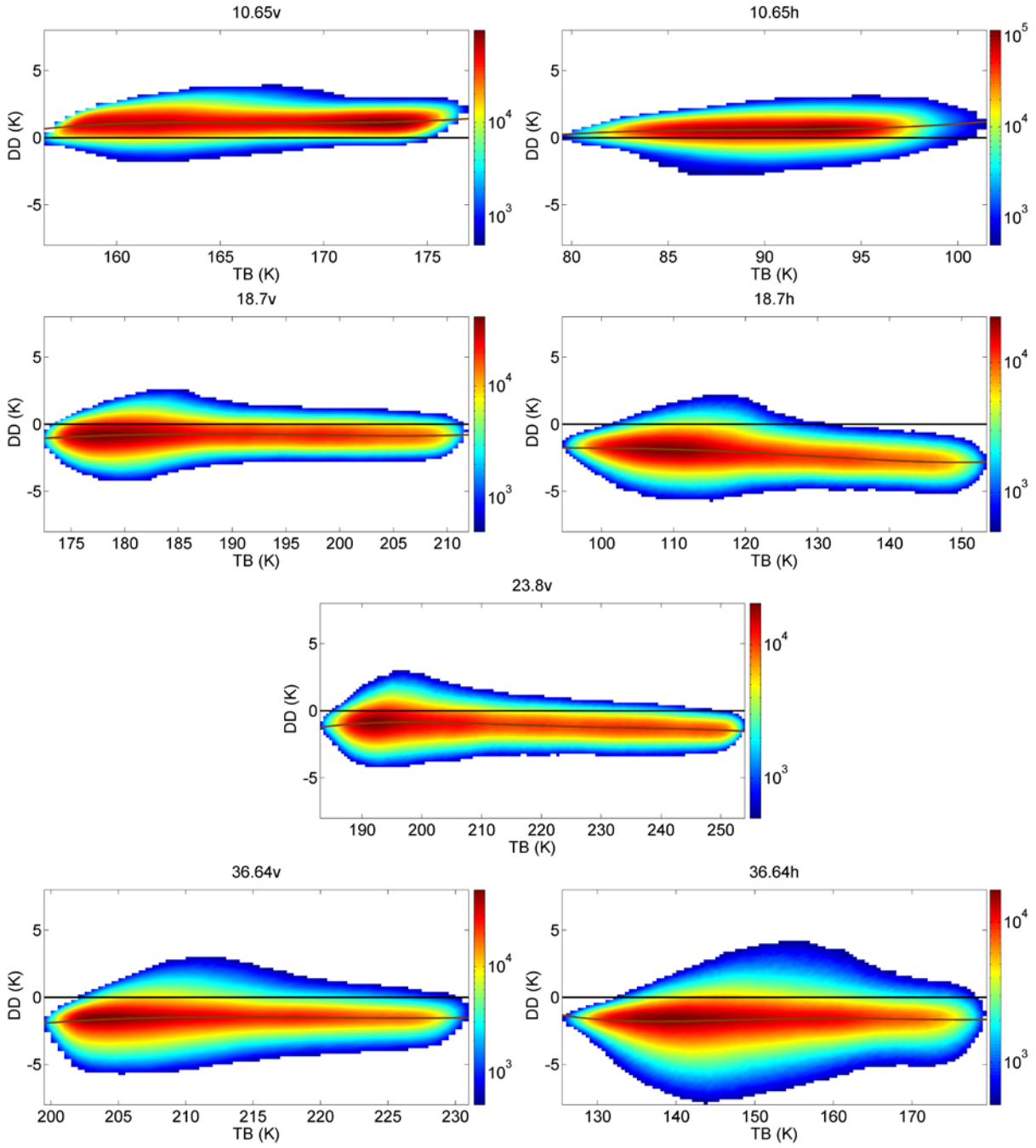

Figure 5.28: The same as Figure 5.27, but for double difference.

5.5 Conclusions

Intercalibration has pronounced temporal and spatial variability and depends

on geophysical parameters. A 40-day cycle is found at all channels for both single and double differences for collocations of GMI and WindSat. This periodic signal is related to the variation of geophysical parameters, which impact the observations and vary periodically with the shifting of calibration locations. A regional dependence is found, which corresponds to the spatial distribution of geophysical parameters that have different impacts on different channels. Although we only present the results using GMI and Windsat, we have studied other radiometers such as TMI, SSMIS, and AMSR2 and the same phenomena and conclusions are found.

Calibration shows nonlinear and non-monotonic dependence on geophysical parameters, depending on the channel. The dependence can result in discrepancies between model and observation not only with high values of geophysical parameters (e.g., high water vapor) but also for calm weather conditions (e.g., low water vapor), of which the latter are commonly used as vicarious calibration sites.

The models used in this study tend to underestimate TBs compared to observation, particularly at high values of geophysical parameters. Nonlinear discrepancies between model and observation are present with low water vapor. Model, observation nonlinearity is also present for wind speed and SST. The nonlinearity is reduced but not removed for double differences. Double differences can have opposite dependence on geophysical parameters compared to single differences for some channels. The dependence of single and double differences on

TB becomes more complex since TB incorporates the impact of all geophysical parameters.

The investigation implies that improper sampling can result in biases due to temporal and spatial variability. The nonlinearity and non-monotonic dependence implies possible issues in RTM parameterizations and ancillary geophysical fields. Our method can be used for diagnosing other radiometers in future studies, and these results should be considered for improving intercalibration.

CHAPTER 6
Science Applications in Coastal Areas

6.1 Introduction

The calibration and intercalibration efforts enable extended consistent data that can be used in Earth science. It is always important to maximize the use of these data. However, near coastlines or over lakes these data often cannot be used. This is due to the typically large footprint of spaceborne radiometers, which include a mixture of contributions from both land and water. The additional land signals invalidate retrievals over water using standard open-ocean algorithms. For example, current standard SSM/I products, including wind, water vapor and precipitation, are typically unavailable within about 100 km of any coastline. This phenomenon is often referred to as land contamination. Coastal data are particularly important since these areas typically have a large human population. It would be valuable to derive a method to remove this land contamination so we may expand the usefulness of the extensive intercalibrated data sets that are

available.

Although previous research proposed some methods for coastal areas (Bellerby et al. 1998; Bennartz 1999; Desportes et al. 2007; Maass and Kaleschke 2010), they are subject to large errors that make them impractical for reliable coastal science. In this study, we examine methods for correcting land contamination. Different techniques are studied. We develop methods that significantly reduce errors when removing land contamination. We demonstrate the method in the Great Lake regions using SSM/I. The corrected data are demonstrated using a wind retrieval algorithm and validated with surface buoy measurements. These results indicate our method effectively handles land contamination that helps fill the gap in current standard retrieval products.

6.2 Land Fraction Estimation

A flow chart describing the overall approach of the land contamination correction algorithm is shown in Figure 6.1. The algorithm consists of three parts: geolocation corrections, land fraction estimation with appropriate antenna patterns, and contamination removal. A dataset with accurate geolocation is necessary, from which the fraction of land contamination is calculated using a high resolution land-water mask convolved with a realistic antenna pattern. The land signal can then be removed using the correlation of multiple measurements around the FOV.

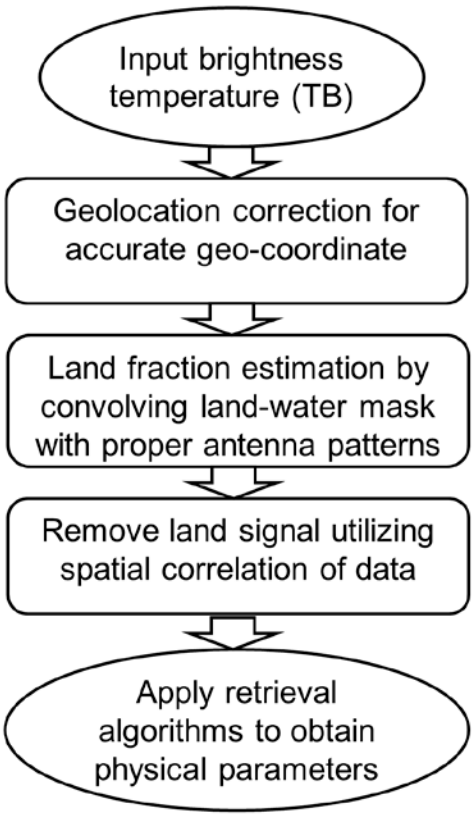

Figure 6.1: Flow chart of the land contamination correction algorithm. The correction consists of three parts: geolocation correction, land fraction estimation using appropriate antenna patterns and land contamination removal.

Land contamination correction refers to the process of removing the land signal from the measured TB. The measured TB can be written as

$$TB = f_{Land} TB_{Land} + (1 - f_{Land}) TB_{Water} \tag{6.1}$$

where TB_{Land} and TB_{Water} are the TBs of land and water, respectively. f_{Land} is computed as the convolution of the land mask and antenna pattern. f_{Land} can be written in the latitude and longitude *x*-*y* coordinate as

$$f_{Land}(x,y)=\frac{\iint A(x,y)M(x,y)dxdy}{\iint A(x,y)dxdy} \tag{6.2}$$

where $A(x,y)$ is the antenna pattern, $\mathrm{M(x,y)}$ is the land-water mask, which is 1 for land and 0 for water, and the limits of integration are defined by an ellipse having major and minor axes aligned with the v- and h-pol principal planes of the antenna pattern and extending out about 3 times the 3 dB beamwidth in each principal plane.

By rearranging (1), we have $TB_{Water}=(TB-f_{Land}TB_{Land})/(1-f_{Land})$, where the term $1/(1-f_{Land})$ becomes very large when f_{Land} gets close to 1 such that any small error in f_{Land} can result in large errors in $\mathrm{TB_{water}}$. Errors in f_{Land} relate to the geolocation displacement, inappropriate approximations of the antenna pattern, and the use of a land-water mask with too coarse a resolution. Inhomogeneity in the land and water TBs affects the correction as well. One way to improve homogeneity within the observations is to break the land and water areas up into sub-areas so that homogeneity is met within each sub-area. A simpler way is to treat water areas as homogeneous and to divide land areas into different types, such as forest, urban area, soil, etc, which however complicates the problem. We need to examine the homogeneity and its impact.

An illustration of the impact of land fraction error due to geolocation errors is shown in Figure 6.2. A geolocation displacement of 5 km is assumed and the

corresponding error impacting the land contamination correction is shown as a function of the land fraction. Quantitative details for calculating the error can be found in the following section. Qualitatively, the error comes from either over or under estimation of the land fraction, depending on whether the displacement is toward or away from the land. In either case, the error increases with the land fraction. For example the TB error exceeds 20 K at a land fraction of 0.5 for a 5 km displacement. The analysis indicates that a dataset of very high quality geolocation is important.

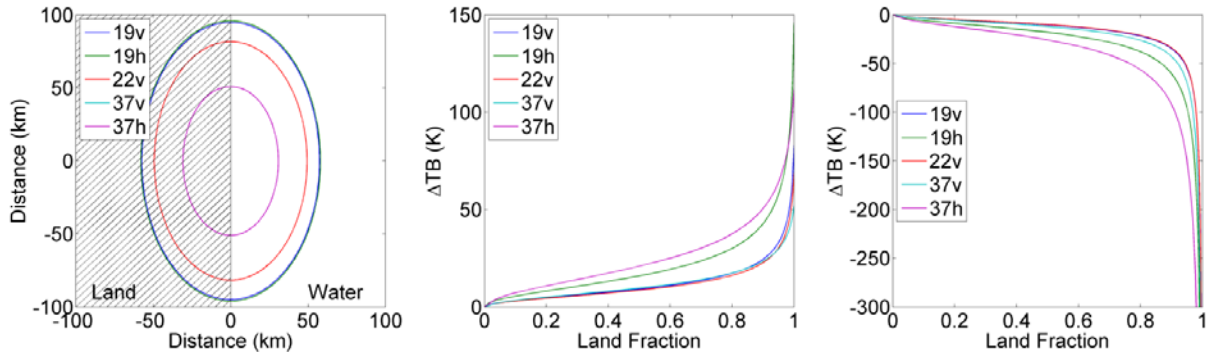

Figure 6.2: Analysis of TB error caused by geolocation displacement. Left panel shows the footprints at each channel using the approximate sizes of the SSM/I footprints. The 37v and 37h footprints overlap. TB_{Land} and TB_{Water} are from typical measured data and are assumed to be homogeneous. A 5 km displacement toward or away from land is assumed. Center and right panels show the error as a function of land fraction, with the center panel considering displacement away from land and the right panel considering displacement toward land. The TB error can be seen to increase significantly with land fraction, indicating that accurate geolocation is necessary before applying the correction.

Geolocation correction methods based on examining the coastline shift have been developed (Poe and Conway 1990). More recently, Berg et al. (2012) further

improve geolocation accuracy for SSM/I to uncertainties of less than 5 km and reduced EIA uncertainty from 0.5° to 0.1°. The 85h channel was used to examine coastline shift. It has the smallest footprint among SSM/I channels and has larger land-water contrast than 85v, since emissivity difference between land and water is larger for h-pol than v-pol. Ascending and descending orbits are compared to examine coastline shifts. The coasts of Australia and Japan can be used to check west-east and north-south shifts. In addition, 19v and 37v are used to examine spacecraft attitude and distinguish roll and yaw offsets, because v-pol is more sensitive to EIA change than h-pol. In this study, we use data with this geolocation correction from CSU (Berg et al. 2012).

6.3 Bessel Function-Approximated Antenna Pattern

An accurate antenna pattern is critical. It also affects the estimate of land fraction f_{Land}. In the past, a Gaussian-shaped antenna pattern was used because it is mathematically simple and shows a small difference from the actual antenna pattern within the 3dB beamwidth (Bennartz 1999; Desportes et al. 2007; Drusch et al. 1999; Maass and Kaleschke 2010). A Gaussian-shaped antenna pattern can be described by

$$A(x,y) = \exp[-4\ln(2)(\frac{x^2}{w_1^2} + \frac{y^2}{w_2^2})] \quad (6.3)$$

where w_1 and w_2 are the two 3dB beam widths, in the along-track (E plane) and cross-track (H plane) directions, respectively.

However, the real antenna pattern is not Gaussian shaped (Colton and Poe 1999; Hollinger et al. 1990). It has sidelobes that are not well represented by a Gaussian function. A typical land TB is about 280 K, so a 1% change at the footprint edge in computing land fraction can result in a 2.8 K difference. It is necessary to use a representative antenna pattern that properly models these sidelobes. The antenna pattern of parabolic reflectors , like those used on instruments such as SSM/I, can be better approximated using a Bessel function (Galindo-Israel and Mittra 1977; Hung and Mittra 1983; Mittra et al. 1979; Rahmatsamii and Galindoisrael 1980). Figure 6.3 shows the difference between Gaussian and Bessel shaped patterns. The two patterns show a relatively good match within the 3dB beamwidth, but the difference increases significantly outside of it. The power fractions show that the Gaussian pattern attributes more weight to sidelobes beyond 0.93 times the 3dB beam width. Consequently, the land contamination-corrected TB is colder because of overestimation of land signals in the sidelobes.

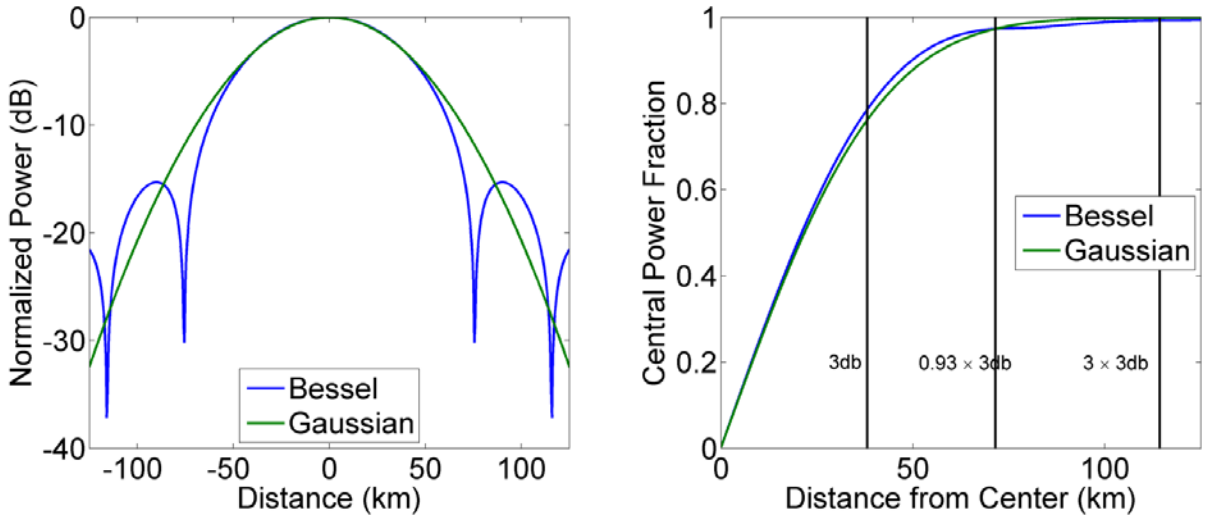

Figure 6.3: The antenna patterns and power fractions from Bessel and Gaussian modeling. The antenna patterns corresponds to the along-track principal plane of SSM/I at 19v. The patterns differ significantly in the sidelobes. Their central power fractions cross at about 70 km (0.93 times the half power beam width). At 3 times 3dB distance, the central power fraction is larger than 0.99 for Bessel modeling. The Gaussian pattern attributes more weight to signals from the sidelobes.

In Figure 6.4, the on-orbit estimated SSM/I antenna pattern is compared with Bessel and Gaussian function models. The estimated SSM/I antenna pattern is from (Hollinger et al. 1990), where they derive the antenna patterns at 37 GHz from coastline overpasses. We see the Hollinger et al.'s estimate of the along-track antenna patterns for V and H in blue lines. In contrast, modeled antenna patterns from Bessel and Gaussian functions are shown in red and green lines, respectively. The first panel shows that the Bessel function captures the approximate sidelobe locations, particularly for H-pol. The Gaussian antenna pattern model does not produce any sidelobes. The other two panels show the cumulative difference between SSM/I antenna pattern models and estimates (model minus estimate integrated over ground track distance) for h-pol and v-pol, respectively. This

difference is significantly smaller for the Bessel function than for the Gaussian. A few minor points are: a) Hollinger et al.'s antenna pattern estimates have uncertainties, having been derived from coastline overpasses; b) we show comparison for the along-track patterns, which correspond closely to the instrument instantaneous field of view (IFOV), while cross-track antenna patterns are more accurately represented by the effective field of view (EFOV) for which the IFOV needs to be convolved over the instrument integration time to take into account smearing as the FOV shifts cross-track. We will discuss this effect later.

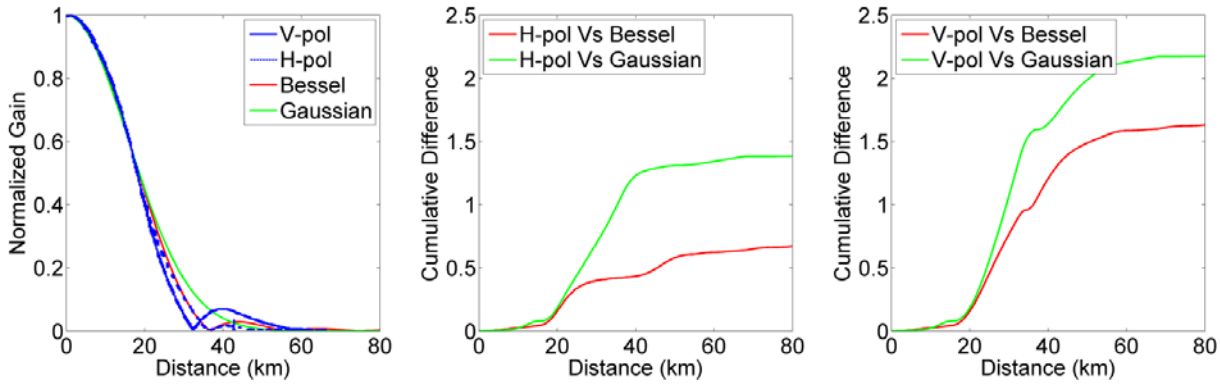

Figure 6.4: Comparison between measured and modeled SSM/I antenna patterns. a) The measured SSM/I antenna patterns at 37 GHz, V and H pols, are for the along-track direction derived from coastline overpasses (Hollinger et al. 1990). In contrast, modeled ones from Bessel and Gaussian are presented, respectively. b) The difference is obtained by subtracting measured h-pol from models and the cumulative difference is shown as a function of distance. c) Same as that in b), but for V-pol. Bessel reproduces sidelobes in the right location, particularly for h-pol and has smaller cumulative differences relative to the Hollinger et al. patterns than Gaussian.

The Bessel function-based antenna pattern can be described by

$$A(r) = 47.9985 \frac{J_3(r)}{r^3} \tag{6.4}$$

where $J_3(r)$ is a third order Bessel function of the first kind, $J_3(r) = \sum_{k=0}^{\infty} \frac{(-1)^k}{2^{2k+3} k! \Gamma(k+4)} r^{2k+3}$, and r is given by $r = \frac{1}{s} \sqrt{\frac{x^2}{w_1^2} + \frac{y^2}{w_2^2}}$, where s is a scale constant, $s = 0.5 / 3.2106$. The argument to the Bessel function is scaled so that its 3dB beamwidth in both principal planes matches that of the actual antenna pattern. In this study, we use the 3dB beam widths from the paper (Hollinger et al. 1990). For example, the 3dB beamwidths are 24.25 and 24.35 km at the cross-track direction for 37 V and H, respectively.

Another point about antenna patterns is distinguishing instaneous field of view (IFOV) from effective field of view (EFOV). Antenna patterns for IFOV were used in past studies (Drusch et al. 1999; Maass and Kaleschke 2010). However, the recorded TBs correspond to EFOVs. SSM/I integration times are 7.95 ms for 19, 22 and 37 GHz channels and 3.89 ms for 85 GHz channels, during which time the foot-prints move on the ground due to the cross-track scanning nature of the instrument about 25 km and 12.5 km, respectively. During the integration time, the IFOV moves to form the EFOV.

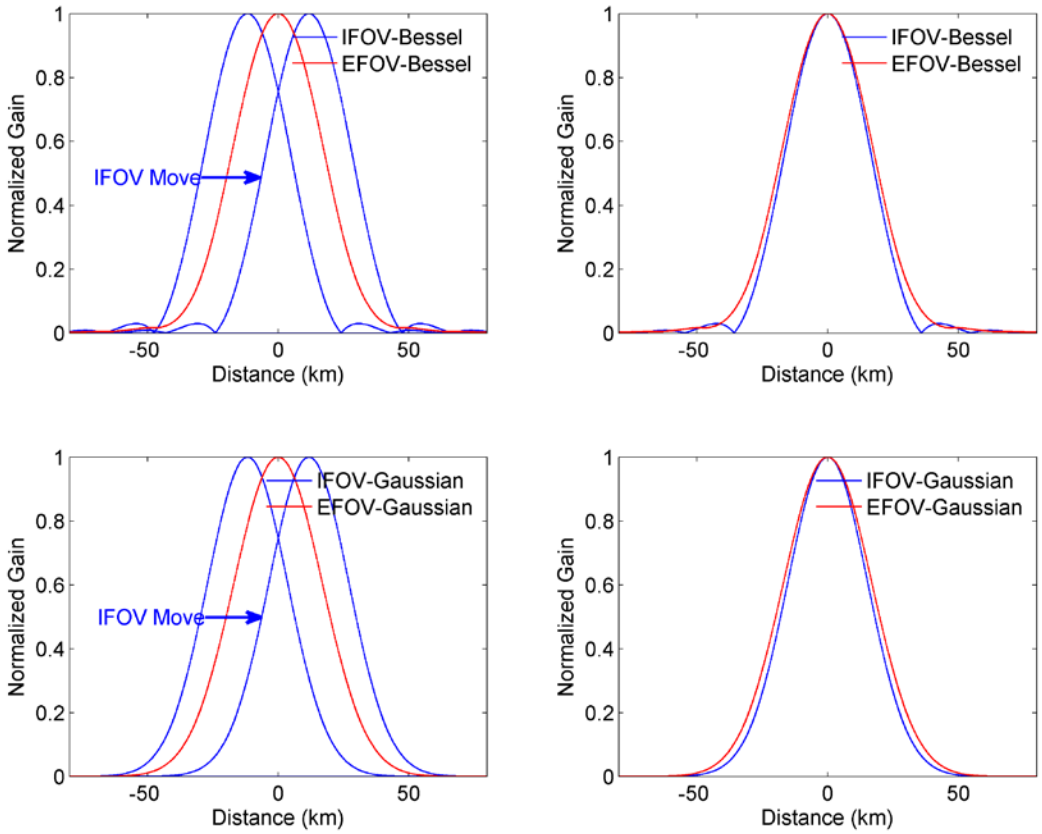

Figure 6.5: The formation of EFOV from IFOV convolution from Bessel and Gaussian models, respectively. The diagram corresponds to the cross-track plane for 37 GHz vertical polarization. Panels 1 and 3 in the left column show the movement of IFOV from beginning to end during the integration time. The IFOV convolution forms the EFOV that corresponds to the recorded TB.

Figure 6.5 shows the translation from IFOV to EFOV. The IFOV in the cross-track plane is modeled for 37v channel. The EFOV is broader than the IFOV in the cross-track plane. The Bessel function most closely matches the estimated SSM/I antenna patterns, and as mentioned above the EFOV is the most appropriate field of view for the cross-track plane, thus the Bessel function EFOV is the reference to which the other options are compared. In the along-track direction, IFOV almost

equals EFOV (Hollinger et al. 1990). The differences between Bessel and Gaussian based IFOVs/EFOVs are shown in Figure 6.6.

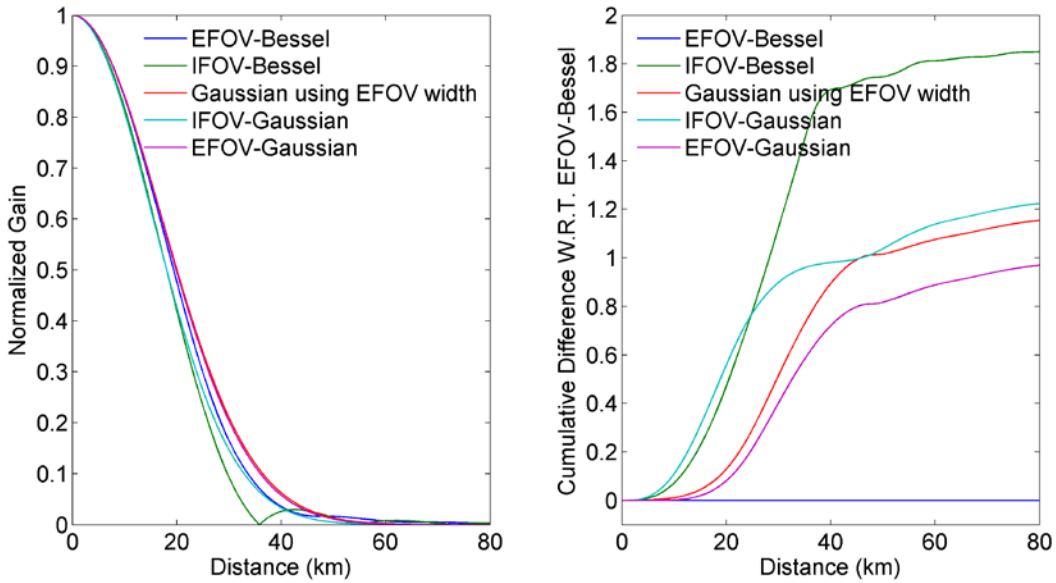

Figure 6.6: Antenna pattern in the cross-track plane at 37v GHz from different IFOV/EFOV assumptions. Left panel shows the antenna pattern for IFOV/EFOV from Bessel and Gaussian function including Gaussian pattern using EFOV width. Right panel shows their cumulative difference with respect to EFOV Bessel pattern. Such differences will propagate as biases into calculating land fraction and removing land contamination.

6.4 Removing Land Signal Based on Spatial Correlation

We examine the strengths and limitations of previous approaches. One option is the use of an analytical function for the land contamination correction that assumes the coastline is straight and the footprint track is perpendicular to it (Desportes et al. 2007). This is computationally inexpensive but not as accurate as other methods, such as using a land-water mask convolved with antenna pattern in the Single Pixel Correction (SPC) approach (Bennartz 1999; Desportes et al. 2007;

Maass and Kaleschke 2010). SPC calculates the area fraction of land signals and then applies a correction to each footprint/pixel one by one. TB_{Land} is estimated by selecting TB measurements with very large values for f_{Land}. Then, for each measured TB, TB_{Water} can be solved using Equation 6.1. However, any small error in f_{Land} can result in larger errors in TB_{Water} as described above. Another previous approach is to use multiple measurements to solve for the two unknowns TB_{Land} and TB_{Water}. The two unknowns can be solved using an overconstrained system of equations of the form of (6.1). For example, Bellerby (Bellerby et al. 1998) used nine pixels of TBs to solve for TB_{Water}. This approach has several advantages: a) it is not necessary to directly estimate TB_{Land}; b) The correction is not sensitive to the uncertainty of a single pixel and reduces the impact of measured TB variability; c) it makes use of the spatial correlation between adjacent pixels since either land or water TBs within a small area are relatively homogeneous such that pixels of relatively small f_{Land} can be used to help solve adjacent pixels of large f_{Land}.

Two factors need to be investigated when using the multiple pixel technique. The first is homogeneity and spatial correlation. It is necessary to assure that TB_{Land} and TB_{Water} do not vary significantly, otherwise it is difficult to solve for them. The second involves choosing an adequate number and combination of pixels, which is, in turn, related to the first factor. Using too few pixels makes the solution similar to

that of the SPC method and reduces its advantages. On the other hand, the homogeneity condition cannot be met when using too many pixels. In particular, the number of land pixels is important because land is more heterogeneous and can introduce larger errors.

We adopt the multiple pixel technique in our approach and improve it. The first thing is defining a single footprint. For a single IFOV footprint, more than 99% of the received power from Earth is within an ellipse of 3 times the 3dB beamwidth. We examined the impact of varying the size of the footprint by computing the land fraction for more than one hundred thousand samples over the Lakes Ontario in March 2006 for multiple footprints. Using 3 times the 3dB beamwidth, the mean land fraction over these samples is 0.7353, 0.7353, 0.7345, 0.7326 and 0.7326 for 19v, 19h, 22v, 37v, 37h, respectively. Modeling the antenna pattern out to 3.5 times the 3dB beamwidth yields mean land fractions of 0.7355, 0.7355, 0.7347, 0.7327, 0.7327, respectively. Given a typical land TB of 280 K and a typical lake TB of 220 K at 37v, this translates to difference of 0.056 K between the two size assumptions for a single pixel respectively, which is negligible. Thus 3 times 3dB beamwidth is adequate for a single footprint size for our land contamination correction purposes.

We combine pixels within a circle with a diameter of 3 times 3dB beamwidth with respect to the center pixel to remove land contamination. This is the area from

which a single footprint receives Earth radiation. We have done both case studies and statistical analysis to examine the impact of using different sizes and numbers of pixels, which are presented in Section 6.5.

A least-squares minimization method is used to estimate the two unknown parameters, TB_{Water} and TB_{Land}, in the multiple-pixel approach. Using (6.1), each TB measurement can be expressed as

$$TB = TB_{Water} + f_{Land}(TB_{Land} - TB_{Water}) \tag{6.5}$$

Given n>2 measurements of TB with varying levels of land contamination, and assuming the same values for TB_{Water} and TB_{Land} in each case, (6.5) can be rewritten as an overconstrained system of equations given by

$$\vec{y} = F\vec{x} \tag{6.6}$$

where

$$\vec{y} = \begin{bmatrix} TB_1 \\ \vdots \\ TB_n \end{bmatrix}, F = \begin{bmatrix} (1 - f_{Land})_1 & (f_{Land})_1 \\ \vdots & \vdots \\ (1 - f_{Land})_n & (f_{Land})_n \end{bmatrix}, \text{and } \vec{x} = \begin{bmatrix} TB_{Water} \\ TB_{Land} \end{bmatrix} \tag{6.7}$$

The ordinary least squares (OLS) estimate for $\vec{x}$ given $\vec{y}$ minimizes the cost function $\|\vec{y} - F\vec{x}\|^2$, with the solution

$$\vec{x}_{OLS} = (F^{\mathrm{T}}F)^{-1}F^{\mathrm{T}}\vec{y} \tag{6.8}$$

The OLS solution can be overly sensitive to the presence of outliers in the measurement vector, $\vec{y}$. In our case, significant outliers are introduced by the presence of rain, clouds, and heterogeneous ground surfaces in the measurements. Alternative regression methods, which reduce the sensitivity to outliers, have been proposed such as the Generalized Linear Model (Meissner and Wentz 2004) and Robust Regression (Elsaesser 2006; Huber and Ronchetti 2009). A regression based on the maximum likelihood estimator (MLE) was introduced by Huber (Huber and Ronchetti 2009) and has been developed as a form of robust regression (Elsaesser 2006; Huber and Ronchetti 2009; Street et al. 1988). One efficient computational algorithm to implement such a regression is the iteratively reweighted least squares (IRLS) method (Jorgensen 2006; Street et al. 1988). We adopt the MLE regression and implement it using the IRLS approach. Our computational method is summarized as follows.

The MLE cost function to be minimized is a weighted version of the OLS cost function given by $\|W(\vec{y} - F\vec{x})\|^2$, with the solution

$$\vec{x}_{MLE} = (F^{\mathrm{T}}WF)^{-1}F^{\mathrm{T}}W\vec{y} \tag{6.9}$$

where W is a diagonal matrix of weights. The weights are given by

$$w_i = \frac{\psi(r_i)}{r_i} \tag{6.10}$$

where r_i is the adjusted residual given by $r_i = (\vec{y} - F\vec{x})_i/\sigma$ and σ is a scale parameter. Different forms of ψ have been proposed. In this study, we use the bisquare functional form (Elsaesser 2006)

$$\psi(r) = \begin{cases} r(1-\frac{r^2}{k^2})^2, |\, r\,| \le k \\ 0, |\, r\,| > k \end{cases} \tag{6.11}$$

where k is the bounded range (Elsaesser 2006; Jorgensen 2006) . The IRLS algorithm is implemented by the following steps: a) an initial estimate is made of $\vec{x}$ using (6.8); b) the weight matrix, W, is computed using (6.10)-(6.11); c) $\vec{x}$ is re-estimated using (6.9); and d) procedures b and c are iterated until convergence is achieved.

In addition to the outlier measurements that are de-weighted by the MLE/IRLS approach, we also filter out data with a large deviation from the mean. This is done by requiring that the residual standard deviation of the linear regression be less than 8 K and the maximum deviation be less than 15 K.

Figure 6.7 shows an example of the signal processing of our method. The left panel shows a 19v TB map over Lake Ontario at 23:09:14 UTC 29 November 2006. Data over Lake Ontario, the smallest of the Great Lakes, contain the most

land contamination. The red dot in the figure denotes a buoy site. The blue circles are centers of nearby pixels within a circle of 190 km diameter. The right panel shows TB as a function of f_{Land}, which has a relationship of $TB = f_{Land}(TB_{Land} - TB_{Water}) + TB_{Water}$. By applying a MLE regression, TB_{Water} is obtained at zero f_{Land}. The linearity between *TB* and f_{Land} is quite good with R^2 of 1.00, 1.00, 1.00, 1.00 and 0.99 for the five channels, respectively. The retrieved values for TB_{Water} are 194.13, 129.36, 221.55, 218.39 and 160.90 K, while RTM simulations (model and ancillary data are the same as those in Chapter 2) give 193.84, 130.73, 222.28, 217.26 and 159.91 K for 19v, 19h, 22v, 37v and 37h, respectively. The differences are 0.29, -1.37, 0.73, 1.13 and 0.99 K, respectively. The minimum f_{Land} is approximately 0.2 for channels of 19v, 19h and 22v, indicating that all TBs over the lake are contaminated. For channels 37v and 37h, the minimum f_{Land} is about 0.015, because higher frequencies have smaller footprints. Nevertheless, the MLE approach is still found to be useful for these two channels for removal of the small amount of land signal still present.

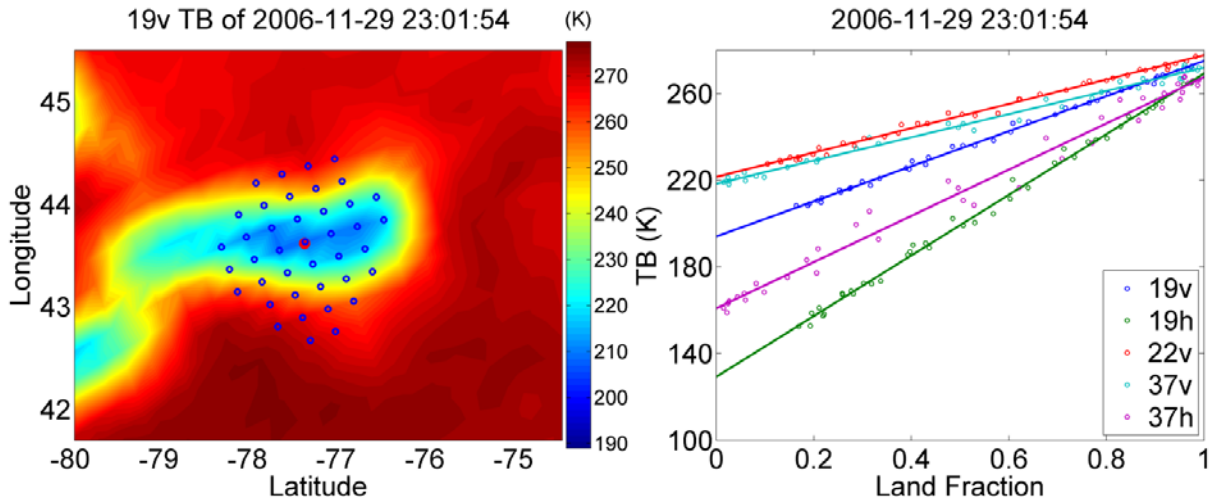

Figure 6.7: An example of solving for TB_{Water} over Lake Ontario. Left panel shows the 19v TB image, with blue circles indicating the centers of samples that are within 95 km of a buoy (location indicated by the red dot). Right panel shows the MLE regression of TB as a function of the land fraction. TB_{Water} is obtained by extrapolation to zero land fraction. The linear regressions have R^2 explained variances of 1.00, 1.00, 1.00, 1.00 and 0.99 at the five SSM/I channels, indicating the robustness of the method. The retrieved TB_{Water} values are 194.13, 129.36, 221.55, 218.39 and 160.90 K, while RTM simulation gives 193.84, 130.73, 222.28, 217.26 and 159.91 K at 19v, 19h, 22v, 37v and 37h, respectively. The retrieval biases with respect to simulation (retrieval - RTM simulation) are 0.29, -1.37, 0.73, 1.13 and 0.99 K, respectively.

The importance of using an appropriate number of pixels to remove land contamination is examined. Examples are illustrated in Figures 6.8 to 6.10. Figure 6.8 maps the locations of pixels that are used to apply the land-contamination correction. In the left panel, only pixels within 40 km of the buoy site are used, while in the right panel, a larger number of pixels within 200 km are used. These two sets of pixels are used to retrieve TB_{Water}.

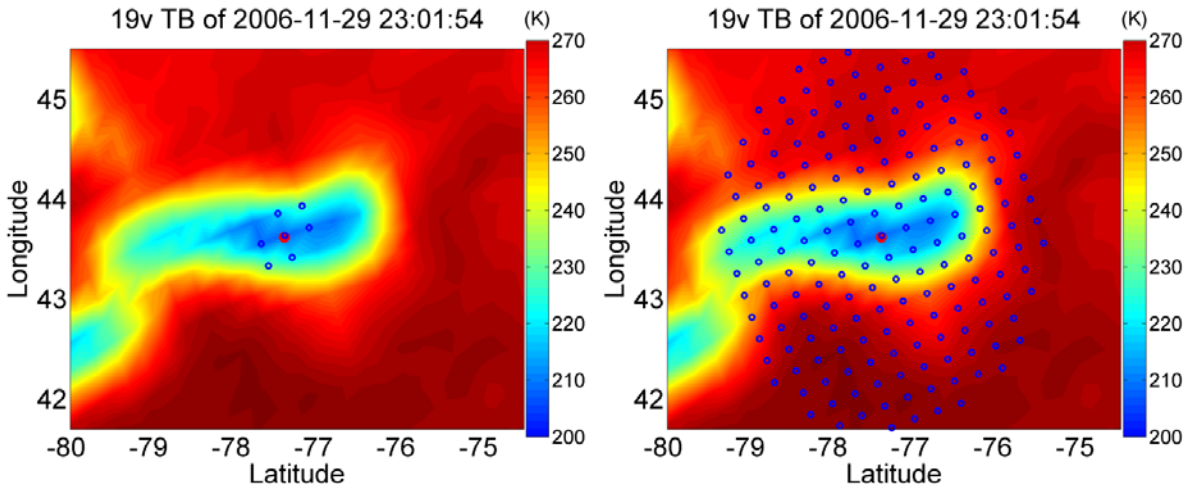

Figure 6.8: The impact of using too few or too many samples on the quality of the land contamination correction. Both panels show the 19v TB map at the same time. The left panel shows all samples within 40 km of the buoy site, while the right panel shows all samples within 200 km. These samples are subsequently used to retrieve TB_{Water}.

Figure 6.9 shows TB_{Water} retrievals using the MLE method. The left panel corresponds to using few pixels, where TBs have land fraction less than 0.6. The right panel corresponds to using many pixels, where the effects of land inhomogeneity become significant such that the variance of warm TBs increases. For example, warm TBs with a land fraction of larger than 0.98 have maximum differences as 4.16, 7.72, 3.22, 3.70 and 5.60 K for the five channels, respectively.

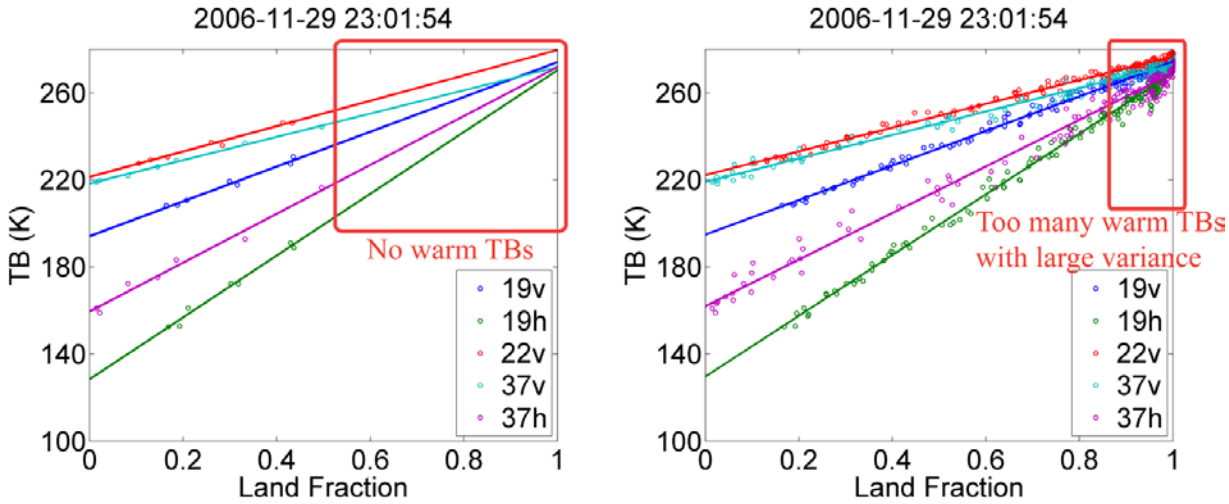

Figure 6.9: Retrieving TB_{Water} using different numbers of TBs. The left panel uses too few TBs, with no warm TBs. As a result, all TBs have corresponding land fractions less than 0.6. The right panel uses too many TBs, in particular too many warm TBs with land fraction close to 1 (the corresponding spatial distribution of TBs can be seen in Figure 6.8). In both cases, the resulting TB_{Water} has large biases relative to the RTM simulations (shown in Figure 6.10).

Figure 6.10 shows the retrieved TB_{Water} compared with simulations. In the left panel, using few pixels has differences of 0.34, -2.33, -0.94, 1.14 and -0.40 K for the five channels, respectively. In the right panel, the differences are 1.02, 1.15, 0.08, 1.79 and 2.03 K, respectively. Both cases produce worse results than if the appropriate number of pixels is used (as in Figure 6.7), where TB differences are 0.29, -1.37, 0.73, 1.13 and 0.99 K, respectively. This reduction in TB differences demonstrates the importance of using an appropriate number of pixels.

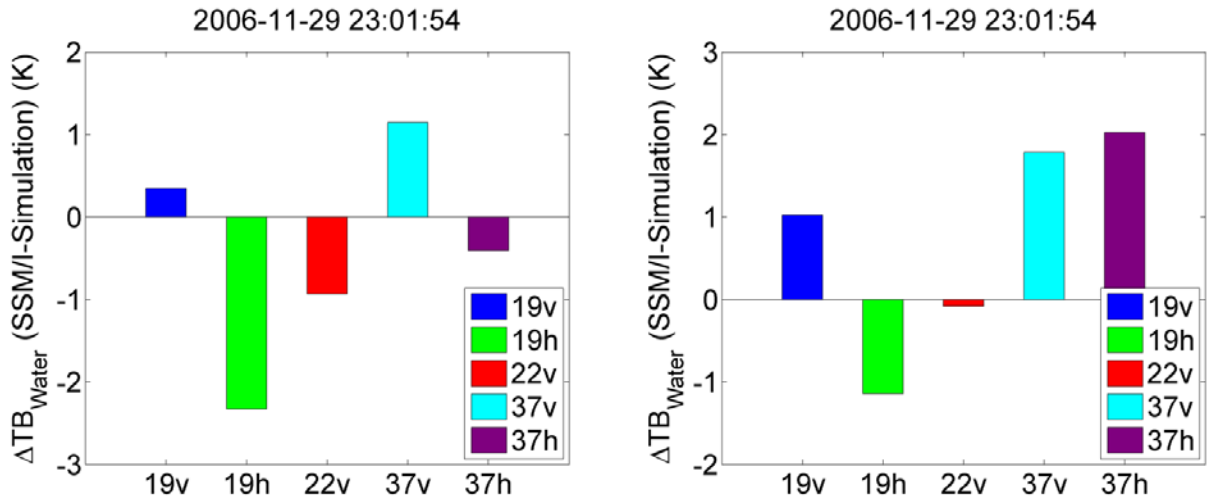

Figure 6.10: The land contamination correction error (estimated TB_{Water} – RTM simulated TB), using different numbers of pixels. The left panel shows results when using too few pixels, with no warm TBs, with biases relative to simulation of 0.34, -2.33, -0.94, 1.14 and -0.40 K for the five channels, respectively. The right panel shows results when using too many pixels, with biases of 1.02, -1.15, -0.08, 1.79 and 2.03 K, respectively. Both cases produce worse results compared to results using the appropriate number of pixels (Figure 6.7).

The importance of using a robust regression algorithm is next considered. Figure 6.11 shows the difference between the OLS and MLE approaches. Panel 1 shows a 19v TB map; Panel 2 shows the OLS minus MLE regressions. Compared to the MLE regression, the OLS regression overestimates TB_{Water} by 0.96, 1.40, 0.80, 0.70 and 0.67 K for 19v, 19h, 22v, 37v and 37h, respectively. Their differences with respect to the RTM simulations are 3.50, 5.18, 1.01, 1.02 and 5.85 K (OLS), and 2.54, 3.78, 0.21, 0.31 and 5.18 K (MLE) for the five channels, respectively. Measured TBs often have large deviations in the presence of clouds and rain. The MLE approach reduces the impact of outliers and makes the results more consistent between channels.

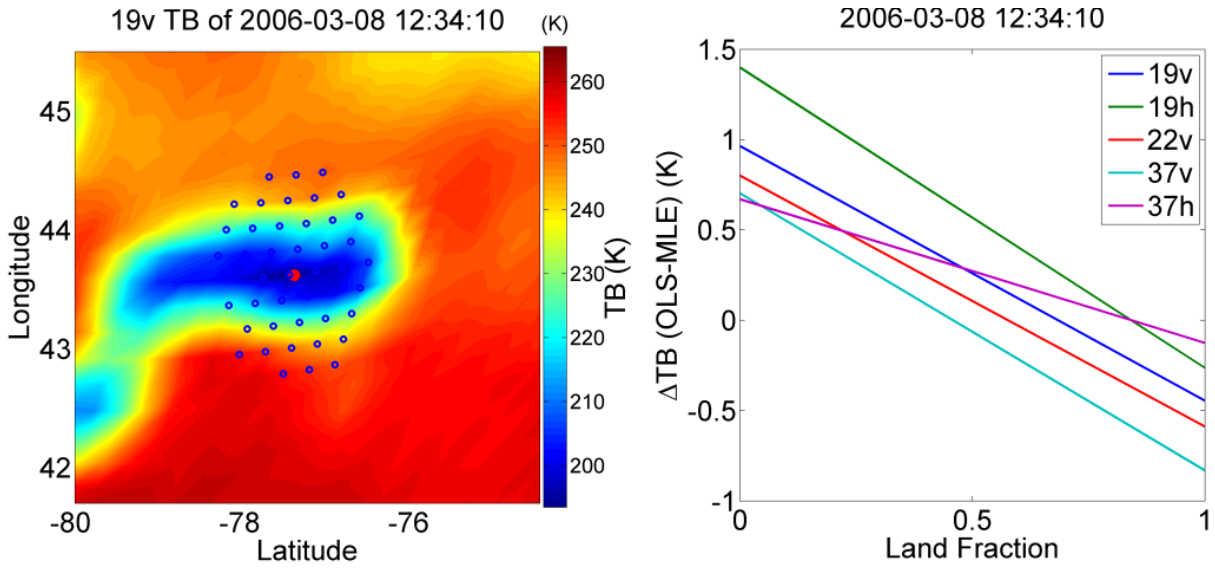

Figure 6.11: Example of difference between MLE and OLS regressions. Left panel shows 19v TB map; Right panel shows the fitting-line differences of OLS minus MLE. OLS overestimates TB_{Water} by 0.96, 1.40, 0.80, 0.70 and 0.67 K for 19v, 19h, 22v, 37v, and 37h, respectively. The differences in retrieved TB_{Water}, compared to RTM simulation, are 3.50, 5.18, 1.01, 1.02 and 5.85 K (OLS), and 2.54, 3.78, 0.21, 0.31 and 5.18 K (MLE) for 19v, 19h, 22v, 37v, and 37h, respectively.

Our method is compared with the SPC method in Figure 6.12. The data on 29 November 2006 were used. The SPC method estimates TB_{Land} from the TB of highest f_{Land} and then calculates TB_{Water} for each pixel. In the left panel, TB_{Water} from the SPC method shows inconsistency, i.e., TB_{Water} varies significantly with f_{Land}, with estimates at high f_{Land} as much as 100 Kelvins higher than estimates from the MLE method. Even when f_{Land} is less than 0.5, TB_{Water} varies more than 50 K. With respect to the RTM simulation, the mean TB_{Water} has differences of -4.03, -8.45, -2.82, 0.22 and -0.78 K for the five channels, respectively. In contrast, the MLE method has differences of 0.29, -1.37, 0.73, 1.13 and 0.99 K compared to the

simulations (as in Figure 6.7). Therefore, the SPC method is not practical for removing land contamination.

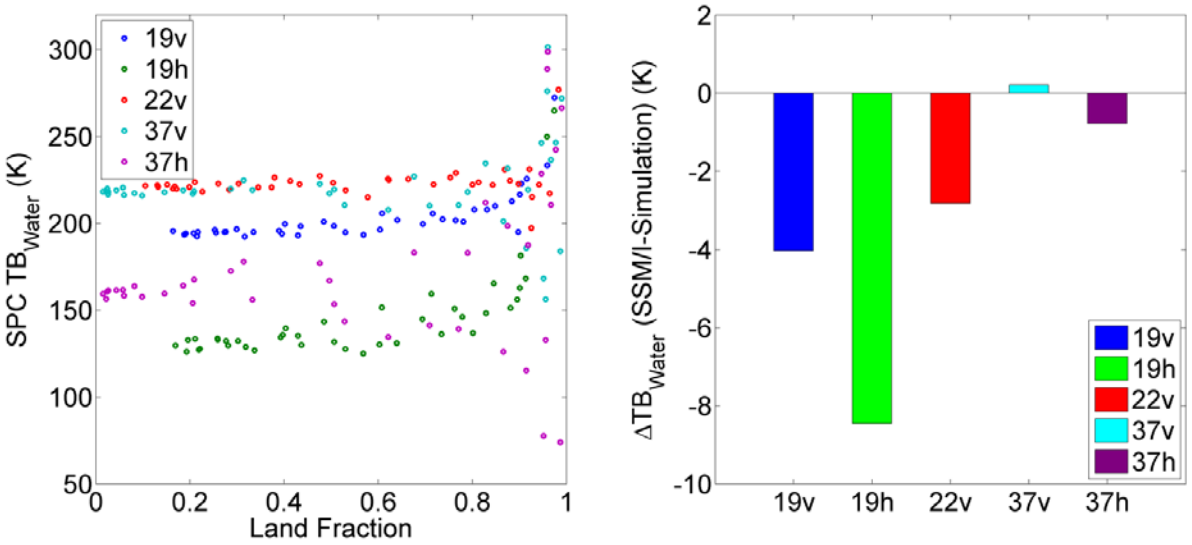

Figure 6.12: Comparison between our method and the SPC method. The left panel shows TB_{Water} as a function of land fraction. The data are from 29 November 2006. TB_{Water} varies significantly with land fraction. Differences from the MLE method can exceed 100 K with land fraction larger than 0.8. Even for land fraction less than 0.5, TB_{Water} can vary more than 50 K. The right panel shows the difference with respect to simulation, where the mean TB_{Water} values have differences of -4.03, -8.45, -2.82, 0.22 and -0.78 K, while the regression based method has differences of 0.29, -1.37, 0.73, 1.13 and 0.99 K for the five channels, respectively.

Figure 6.13 shows the difference between using the Gaussian and Bessel antenna patterns. The data are from 29 November 2006. Panel 1 shows the fitting-line differences of Gaussian minus Bessel. Panel 2 shows the TB_{Water} differences between Gaussian and Bessel of -4.32, -7.07, -2.10, -0.90, -1.77 K for the five channels, respectively. With respect to RTM simulation, using the Gaussian pattern shows differences of -4.03, -8.44, -1.37, 0.23 and -0.78 K, while the Bessel pattern shows differences of 0.29, -1.37, 0.73, 1.13 and 0.99 K for the five channels,

respectively. The Gaussian pattern attributes more weight to edge signals and thus removes more signals and does not approximate the antenna pattern as well.

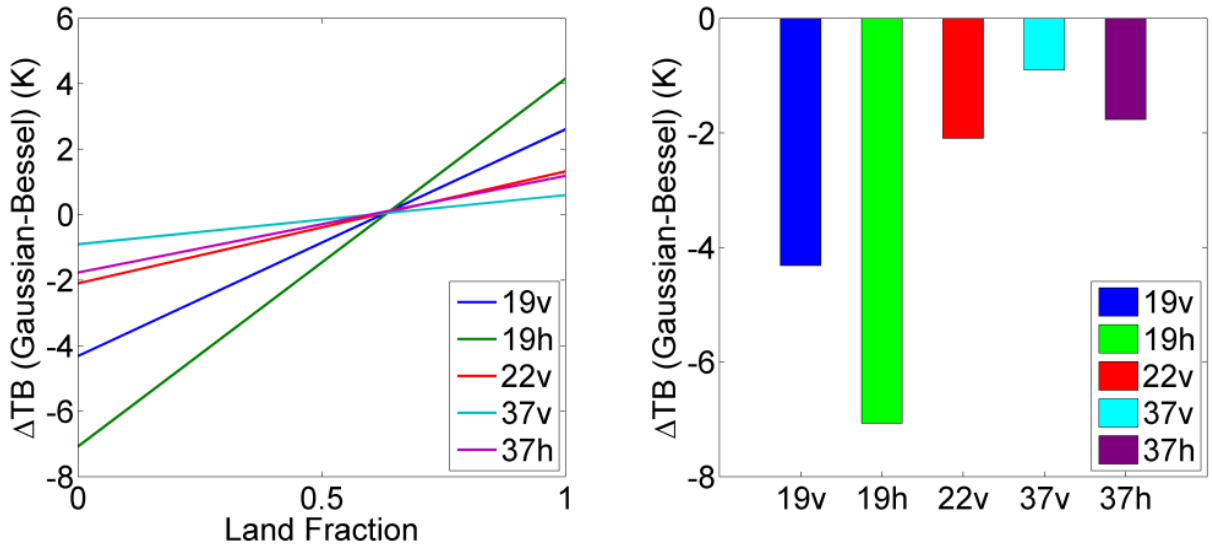

Figure 6.13: Comparison between using Bessel and Gaussian antenna pattern. The data are from 29 November 2006. Left panel shows the difference between using Bessel and Gaussian patterns. Right panel shows the TB_{Water} differences, which are -4.32, -7.07, -2.10, -0.90, -1.77 K for the five channels, respectively. With respect to the RTM simulation, using the Gaussian pattern results in differences of -4.03, -8.44, -1.37, 0.23 and -0.78 K, while using the Bessel pattern produces differences of 0.29, -1.37, 0.73, 1.13 and 0.99 K for the five channels, respectively. The Gaussian pattern attributes more weight to sidelobe signals and thus removes more of the land contamination.

6.5 Validation by TB Simulation and Wind Retrieval

After obtaining corrected TBs, existing over-water retrieval algorithms can be applied to retrieve physical parameters. In this study, we use data from SSM/I F13 from 2006. The version used is provided by the recent SSM/I Fundamental Climate Data Records (FCDR) processed by Colorado State University (Berg et al. 2012).

The FCDR products are intercalibrated for SSM/I sensors F08, F10, F11, F13, F14 and F15 from 1987 to 2009. Each radiometer is intercalibrated with respect to F13. The geolocation and spacecraft attitude have been improved mainly based on examining the coastline shift as aforementioned. No resampling technique is applied between different channels. A land-water mask with a resolution of about 250 m (0.002′×0.002′) has been used (Carroll et al. 2009). Because using a high resolution mask increases computational expense, we degrade this to 1 km (0.008′×0.008′) by averaging the mask. Based on sensitivity studies using both original and degraded masks to compute land fraction, the difference of degrading the land-mask resolution on the computed TBs is of order 0.2‰.

One concern is that lake fresh water is different from oceanic salt water and that may affect the simulation. Figure 9 shows the impact of salinity on TB using the emissivity model we use. It shows that salinity impact is negligible above 5 GHz and thus does not affect modeling SSM/I TBs (lowest frequency of 19.35 GHz). The input geophysical parameters for the simulation come from the surface properties and atmosphere profiles from NCEP-FNL.

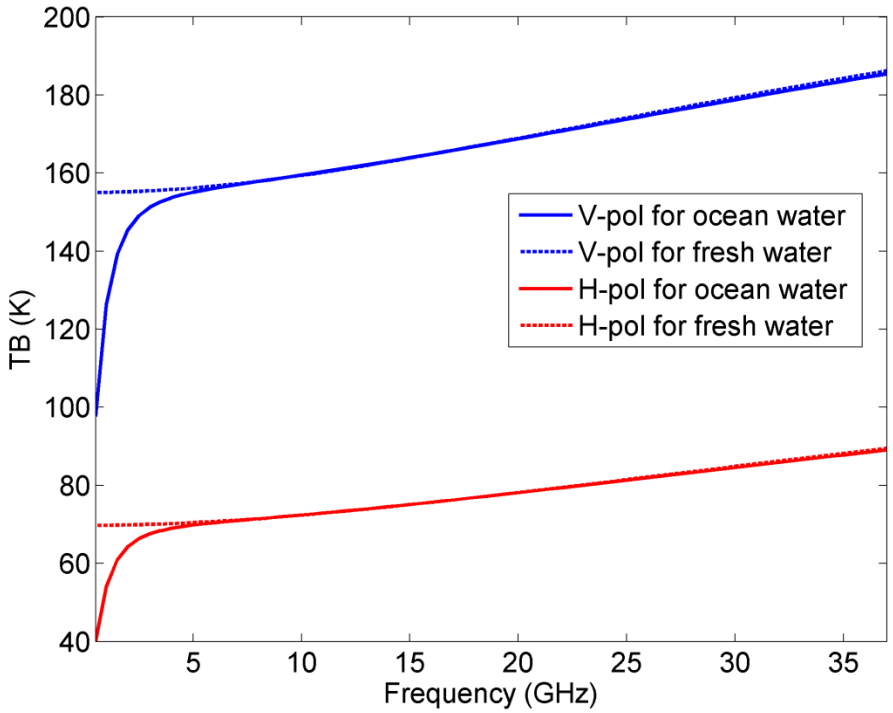

Figure 6.14: Modeled SSM/I TB emitted from the surface for ocean and fresh water, respectively. The impact of salinity becomes negligible for frequencies higher than about 5 GHz. In this model (Elsaesser 2006; Meissner and Wentz 2004), we set parameters as: salinity is 34 PPT for sea water and zero for fresh water; EIA is 53 degrees; water temperature 17 Celsius; wind speed is 6 m/s.

A regression based wind retrieval method for the open ocean was used (Goodberlet et al. 1989). No parameters are tuned in the wind retrieval algorithm, because tuning the retrieval algorithm compromises its utility for validating the robustness of the land correction algorithm. Rain contamination was removed using a rain filter (Stogryn et al. 1994). The retrieved wind was validated using surface buoy measurements provided by the National Data Buoy Center (NDBC) (Meindl and Hamilton 1992. Available: http://www.ndbc.noaa.gov). The buoy data have a temporal resolution of 1 hour. A buoy site in the center of Lake Ontario is used (43.619°, -77.405°). Because Lake Ontario has the smallest surface area

among the five lakes and thus is the worst lake in terms of land contaminated TBs, we choose it to examine the capability of our method. This buoy site has a mean wind speed of 5.96 m/s, a maximum of 21 m/s and a variance of 9.93 m/s in 2006. The SSM/I pixel closest to the buoy site during each overpass is used to compare with buoy wind, and their time difference is within 1 hour.

The corrected TB_{Water} is compared with simulated TBs to test for physical reasonableness. Figure 6.15 shows the comparison between simulated and observed TBs for data over Lake Ontario. There are 10936 samples for each channel. Measured raw TBs are overall warmer than the simulated values before correction (left side). After correction (right side), simulated and measured TBs are well aligned to the 1 to 1 solid line (top plot). Both bias (middle) and variance (bottom) are reduced. Before correction, TBs are warmer with respect to the simulation by 47.88, 82.99, 34.69, 31.80 and 67.16 K, while after correction differences are 0.47, 0.20, -1.16, -0.10 and 3.02 K for the five channels, respectively. The standard deviations are 18.05, 31.09, 16.37, 18.78 and 37.19 K before correction versus 3.19, 5.81, 4.16, 4.15 and 8.69 K after correction. The 37h channel shows considerably larger differences than the other channels; the reason for this is not known. The residual differences are about 4 K. However, it should be pointed out that the residual error in our correction method is much less, because part of the difference comes from uncertainties in the simulated TBs. The

error analysis shown in the following section, based on comparisons between wind retrievals and ground truth winds, shows much smaller residual errors.

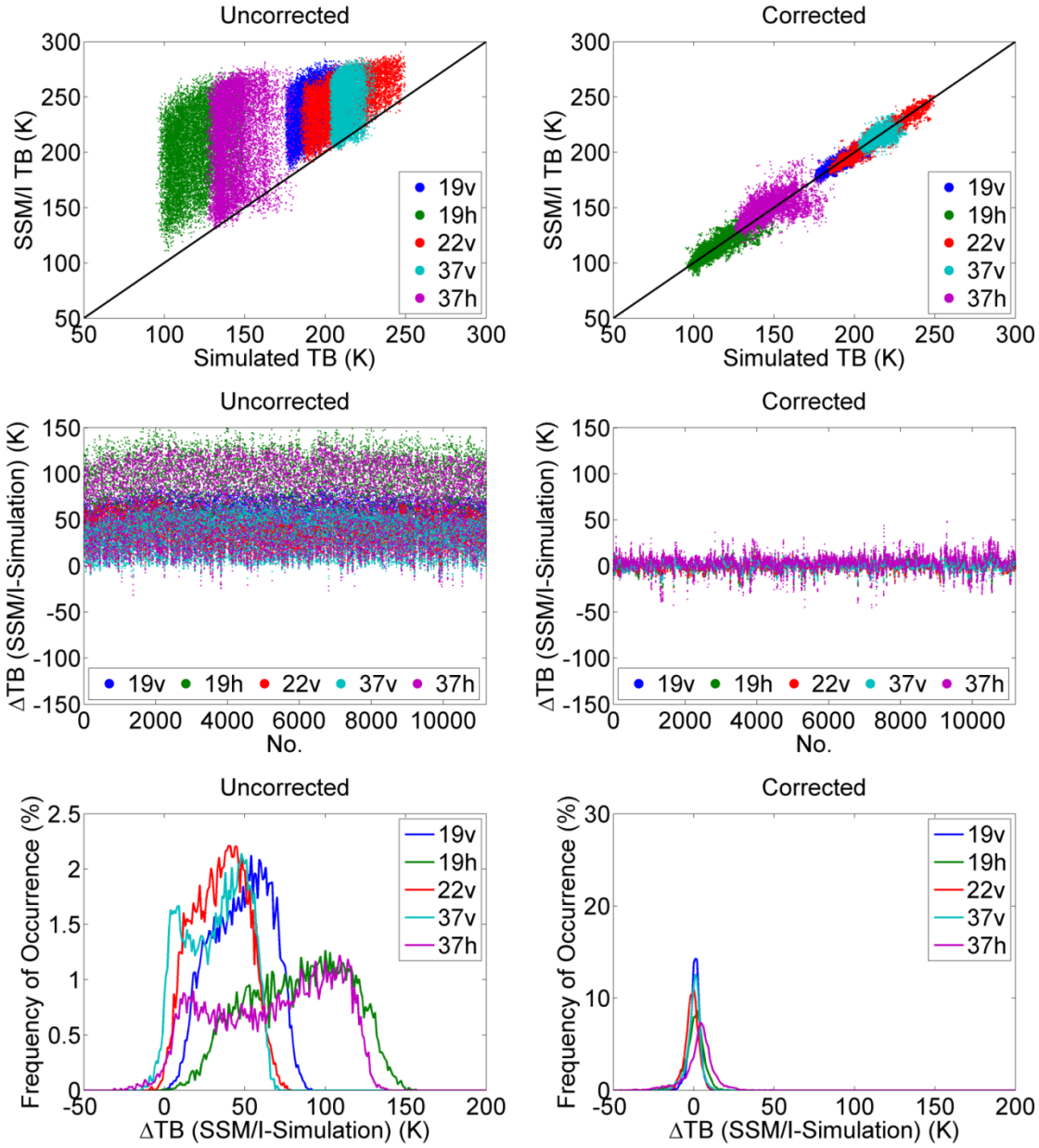

Figure 6.15: Comparison between simulated and observed TBs with and without land contamination correction, respectively. The left panels use uncorrected TBs and the right panels use corrected TBs. The three rows show the scatterplot, bias and histogram, respectively. After correction, observed TBs show much better agreement with simulations, with reduced bias and variance. Before correction, the mean differences between observation and simulation are 47.88, 82.99, 34.69,

31.80 and 67.16 K, while after correction they are 0.47, 0.20, -1.16, -0.10 and 3.02 K for the five channels, respectively. The standard deviations are 18.05, 31.09, 16.37, 18.78 and 37.19 K before correction versus 3.19, 5.81, 4.16, 4.15 and 8.69 K after correction.

Figure 6.16 shows TBs as a function of land fraction before and after correction. Before correction, TBs increase with land fraction. The fitted red line from a linear regression shows that TBs increase by 87.05, 149.98, 67.53, 59.04 and 118.06 K for the five channels when land fractions change from 0 to 1. After correction, TBs have only a small dependence on land fraction. The slope becomes 2.34, 2.64, 3.27, 0.44, 0.22 K respectively.

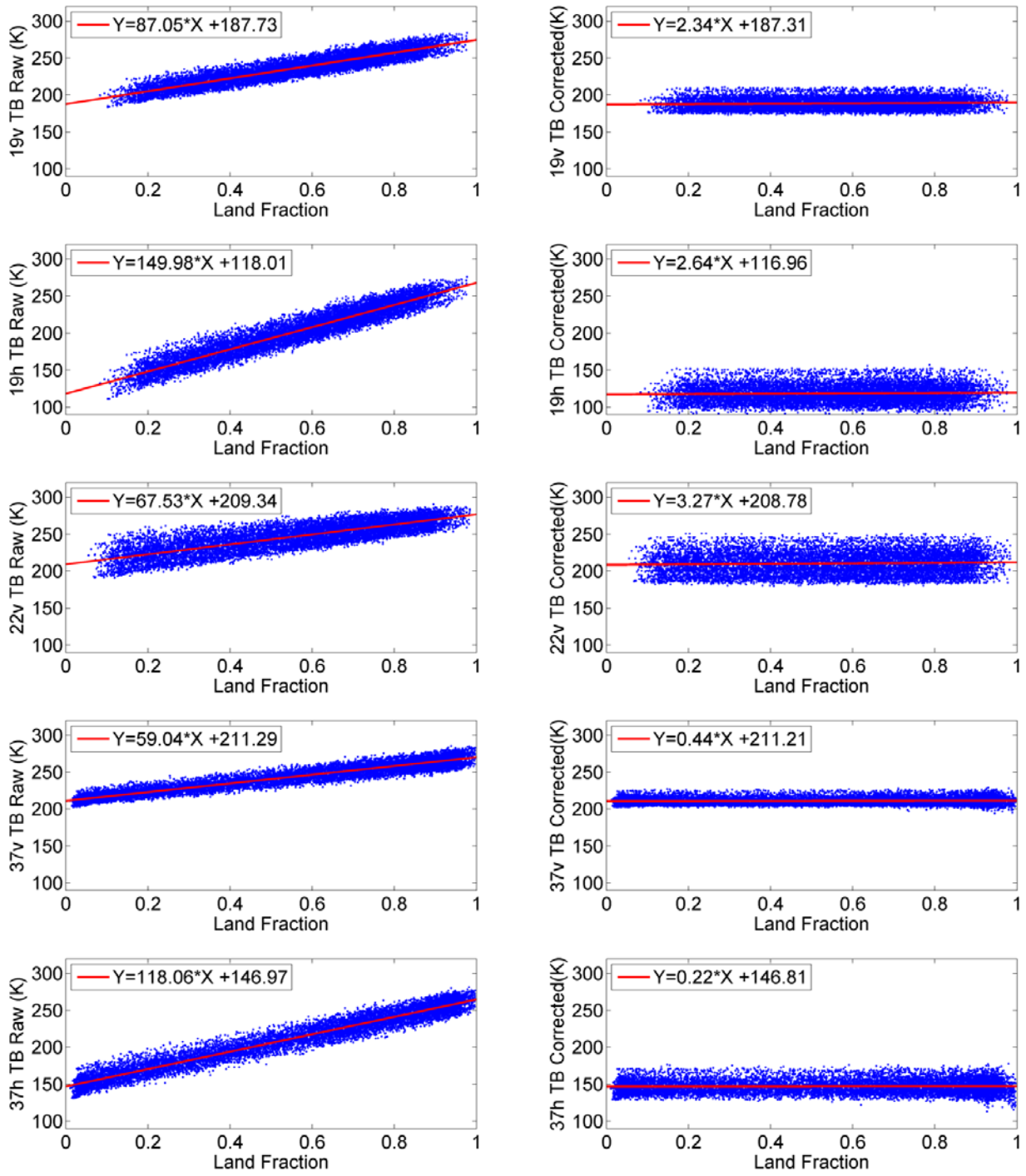

Figure 6.16: TB as a function of land fraction before and after correction. Before correction (left panels), TB increases significantly with land fraction. The red line from linear regression shows that TB increases by 87.05, 149.98, 67.53, 59.04 and 118.06 K for the five channels when land fraction changes from 0 to 1. After correction (right panels), TBs are almost flat as a function of land fraction with slopes of 2.34, 2.64, 3.27, 0.44 and 0.22 K respectively.

It should be noted that simulation is not the absolute benchmark for validation. To characterize the magnitude of any simulation biases, TBs were simulated over land-free ocean using the RTM and NCEP profiles and were compared to observations. The comparison was implemented over latitudes of 40 to 50 degrees in the northern hemisphere; these latitudes are similar to that of the Great Lakes. The simulated and observed data were averaged into 1°×1° grid boxes and compared. Data with cloud liquid water are eliminated to isolate just surface effects, which are the most relevant to the retrieval of wind speeds. It should be noted that the middle of ocean has sparse in-situ observations that limit the accuracy of NCEP atmospheric profiles. Data with large spatial inhomogeneity are filtered out, i.e., TBs in the same 1-by-1 degree grid box with a standard deviation larger than 2 K at each channel. The TB differences (observation minus simulation) are 1.10, 0.47, 0.73, -2.79 and -0.62 K for the five channels, respectively. The standard deviations of TB differences are 2.97, 5.54, 4.93, 3.57 and 7.67 K respectively. These residual differences for the open ocean are of the same order as the land corrected TB observed/simulated differences over Lake Ontario.

The corrected values for TB_{Water} over Lake Ontario were used for wind speed retrievals and were validated against surface buoy measurements. Figure 6.17 shows the comparison between buoy and SSM/I retrieved wind speeds for

uncorrected and land contamination corrected TBs. Hourly buoy wind is compare with SSM/I wind from the closest pixel in space and time to the buoy. By using the corrected TBs, the SSM/I wind speed retrieval is significantly improved, with smaller bias and variance and enhanced correlation. The root mean square error (RMSE) is 1.82 m/s and the correlation is 0.86. Over the open ocean, previous studies reported RMSE of 1.9 m/s and correlation of 0.85 when comparing buoy and SSM/I wind speeds (Goodberlet et al. 1989). Note that the retrieved wind speed still has some residual bias and some negative values. This is partly because the retrieval algorithm used here was specifically tuned for the open ocean.

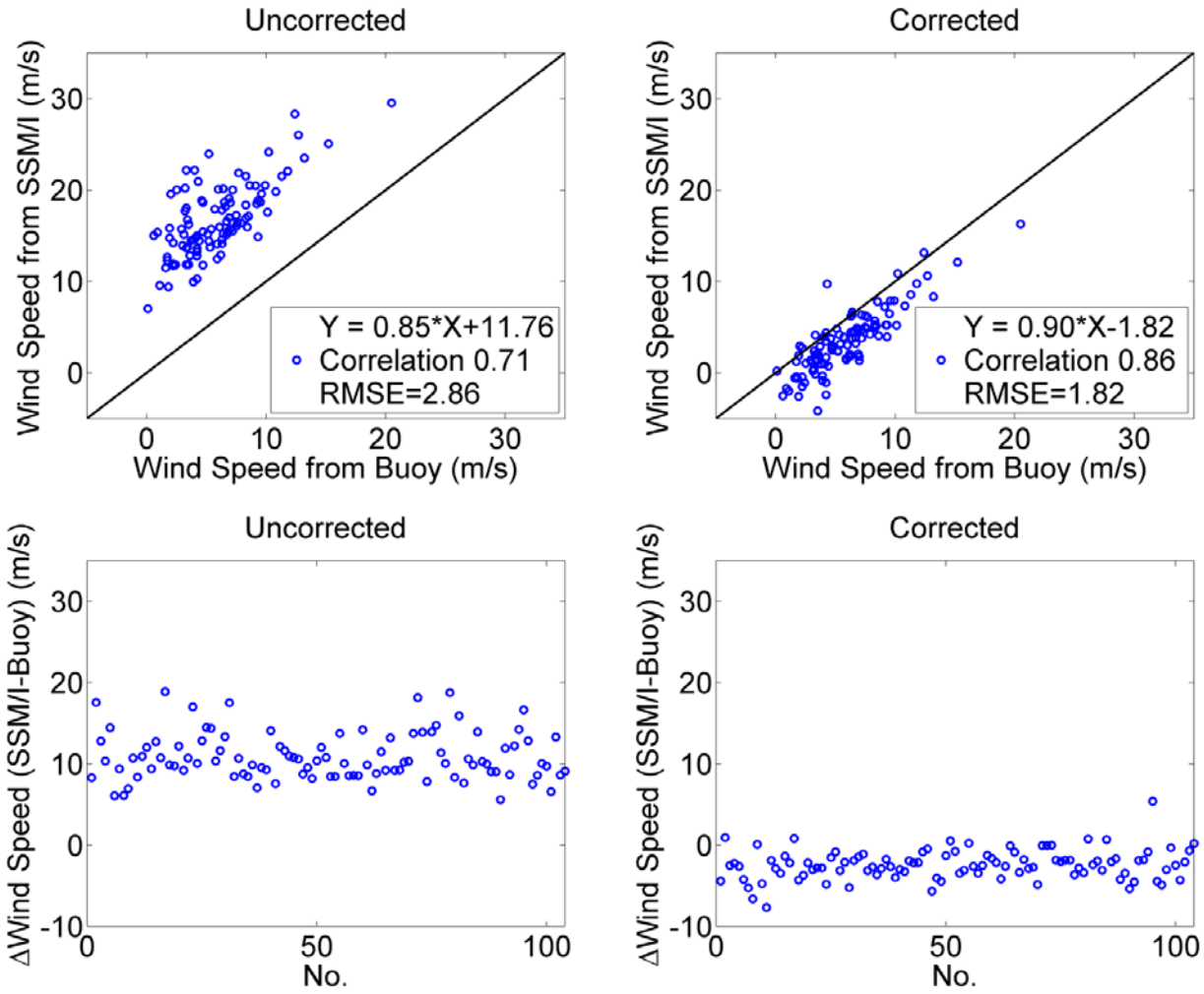

Figure 6.17: Comparison of buoy measured wind speed and SSM/I retrieved wind speed using corrected and uncorrected TBs. The wind speed from corrected TBs show better agreement with the buoy measurements, with an RMSE of 1.82 m/s and a correlation of 0.86. In comparison, previous studies over the open ocean show RMS difference of 1.9 m/s and R of 0.85 (Goodberlet et al. 1989).

We use the residual error in the wind retrievals to estimate the error in the corrected TBs. As an approximation to bound the TB uncertainties, it is assumed that standard deviation of the TB residual error is equivalent at each channel and that the covariance of any two channels is zero. Then the standard deviation of the TB residual error can be derived from the standard deviation of the wind residual

error as:

$$\sigma_{Wind}^2 = \sum_i a_i^2 \sigma^2_{TBi} = \sigma^2_{TB} \sum_i a_i^2 \tag{6.12}$$

where a_i are constant parameters in the regression-based wind algorithm. The standard deviation of the wind-speed residual error is $\sigma_{Wind} = 1.86$ m/s, and therefore the corresponding standard deviation of TB is obtained as $\sigma_{TB} = 0.80$ K for each channel.

The comparisons between using different antenna patterns are presented in Tables 6.1 and 6.2. The two tables come from analyzing the same data in 2006 using different antenna patterns. Table 6.1 presents the comparison between raw/corrected TBs and simulated TBs, using Bessel/Gaussian based IFOV and EFOV antenna patterns. The bias is the mean residual of raw/corrected TB minus simulated TB, and the standard deviation (STD) of the residual is also shown. Overall, using the Bessel based EFOV antenna pattern produces best results with smallest bias and standard deviation. Table 6.2 shows the retrieved wind speed against buoy. Again, the proposed method provides the best wind retrieval against buoy measurements with high correlation and small RMSE.

TB	Raw		G-IFOV		G-EFOV		B-IFOV		B-EFOV		Open Ocean	
	Bias	STD	Bias	STD	Bias	STD	Bias	STD	Bias	STD	Bias	STD
19v	47.88	18.05	-0.51	3.20	-1.05	3.23	1.01	3.15	0.47	3.19	1.10	2.97

19h	82.99	31.09	-1.53	5.76	-2.42	5.85	1.17	5.70	0.20	5.81	0.47	5.54
22v	34.69	16.37	-1.56	4.20	-2.02	4.23	-0.68	4.12	-1.16	4.16	0.73	4.93
37v	31.80	18.78	0.25	4.08	-0.32	4.14	0.51	4.10	-0.10	4.15	-2.79	3.57
37h	67.16	37.19	3.74	8.51	2.57	8.68	4.26	8.54	3.02	8.69	-0.62	7.67

Table 6.1: Comparison of corrected TB against simulation using different antenna patterns. Bias is raw/corrected TB minus simulated TB; G-IFOV is using Gaussian function based IFOV antenna pattern where SSM/I EFOV widths are the input parameters; G-EFOV is using Gaussian function based EFOV; B-IFOV is using Bessel function based IFOV antenna pattern; B-EFOV is using Bessel function based EFOV; Method B-EFOV gives results with the smallest bias and standard deviation.

Raw		G-IFOV		G-EFOV		B-IFOV		B-EFOV		Open Ocean	
R	RMSE	R	RMSE	R	RMSE	R	RMSE	R	RMSE	R	RMSE
0.71	2.86	0.83	1.97	0.84	1.93	0.85	1.86	0.86	1.82	0.85	1.90

Table 6.2: Comparison of wind speed retrieval against buoy using different antenna patterns. Acronym is the same as in Table 6.1, except R for correlation coefficient and RMSE for root mean square error from a liner regression. B-EFOV gives overall best results with large correlation and small RMSE. The numbers for the open ocean are from (Goodberlet et al. 1989).

The comparisons between different correction techniques are shown in Tables 6.3 and 6.4. The same Bessel based antenna pattern is used, but different correction techniques in the aforementioned case study are used to examine all data in 2006 and then results are compared. These different techniques include SPC compared to multiple-pixel, OLS compared to MLE, and using a small number of pixels in the retrieval method compared to using a moderate and large number of pixels. Table 6.3 shows the comparison of corrected TB against simulation, and Table 6.4

presents wind retrieval against buoy. Overall, our proposed method (i.e., Bessel based EFOV antenna pattern, multi pixel method with moderate/adequate number of pixels combination and MLE regression) produces TBs and wind speeds with the lowest bias and standard deviation/RMSE with respect to simulated TBs and buoy winds, respectively.

TB	Raw		SPC		B&S&MLE		B&L&MLE		B&M&OLS		B&M& MLE		Open Ocean	
	Bias	STD	Bias	STD	Bias	STD	Bias	STD	Bias	STD	Bias	STD	Bias	STD
19v	47.88	18.05	8.40	12.70	0.59	4.53	0.65	3.08	0.32	3.17	0.47	3.19	1.10	2.97
19h	82.99	31.09	10.08	17.52	0.62	7.82	-0.16	5.63	0.18	5.80	0.20	5.81	0.47	5.54
22v	34.69	16.37	7.06	13.38	-1.17	5.02	-0.73	4.17	-1.15	4.16	-1.16	4.16	0.73	4.93
37v	31.80	18.78	5.29	33.53	-0.20	5.39	-0.17	3.70	-0.05	4.13	-0.10	4.15	-2.79	3.57
37h	67.16	37.19	10.17	40.98	2.62	11.54	2.82	7.96	3.18	8.61	3.02	8.69	-0.62	7.67

Table 6.3: Comparison of corrected TB against simulation from using different techniques. The same Bessel based EFOV antenna pattern is used as with Table 6.1, but correction techniques are varied: SPC is the single pixel correction method; B is using Bessel antenna pattern; S is using too small area for multiple-pixel (within 40 km to the center pixel); M is using medium adequate area for multiple-pixel (with 3 times 3dB major axis of beamwidth); L is using too large area for multiple-pixel (within 200km to the center pixel); OLS is ordinary least square regression; MLE is maximum likelihood estimation regression. Using the proposed method, B&M&MLE, produces overall best results with small bias and standard deviation.

Raw		SPC		B&S&MLE		B&L&MLE		B&M&OLS		B&M&MLE		Open Ocean	
R	RMSE	R	RMSE	R	RMSE	R	RMSE	R	RMSE	R	RMSE	R	RMSE
0.71	2.86	0.62	3.56	0.86	1.92	0.80	1.86	0.85	1.83	0.86	1.82	0.85	1.90

Table 6.4: Comparison of wind speed retrieval against buoy using different techniques. Acronym is the same as in Table 6.3, except R for correlation coefficient and RMSE for root mean square error from a liner regression. Using the proposed method, B&M&MLE, produces overall best results with high correlation

and small RMSE. The numbers for the open ocean are from (Goodberlet et al. 1989).

6.6 Conclusions

We have developed methods for correcting land contamination and extracting coastal and inland lake information. The method significantly reduces the land contamination, and the corrected TBs show agreement with simulations. The corrected data are used for wind retrieval over the Great Lakes. The retrieved wind speeds are as good as open-ocean winds. This method can also be applied for general retrieval purposes.

Our land contamination algorithm uses a Bessel function based representation of the EFOV antenna pattern. Compared to previous IFOV Gaussian antenna patterns, our new antenna pattern much better represents the real one, as validated by SSM/I measured antenna patterns. This significantly reduces error in calculating land fraction. We use multiple pixels and their spatial correlation to back out land-free signals, where the optimal criteria including number and areas of pixels are found. The maximum likelihood estimator (MLE) regression further reduces the impact of outliers.

We compare our method with previous approaches and examine the differences between various implementation details. It is found that using an

appropriate antenna pattern is important for removing land contamination, and that the Bessel function pattern outperforms the Gaussian pattern. The results are much better compared to techniques based on a single pixel correction. However, it should be noted that resolution is degraded with this multi-pixel approach. Also, the buoy sites have limited data where no data are available in winter and SSM/I passes the buoy location only two times per day. The example retrievals show improved wind speed with RMS error of 1.86 m/s relative to buoy wind estimates. By using this method, the current lack of information near coasts in standard SSM/I data products can be addressed. This method can be applied to other radiometers in coastal regions for general retrieval purposes.

CHAPTER 7
Conclusions

7.1 Summary and Contributions

Spaceborne microwave radiometry is one of the most important observation tools in weather and Earth science. This thesis covers the process of calibrating and intercalibrating both radiometer brightness temperature measurements and their science data products (Yang 2015; Yang et al. 2014; Yang et al. 2015a, 2015b; Yang et al. 2015c). A systematic calibration framework has been developed with both cold and warm end calibration to cover the full dynamic range of radiometer-measured brightness temperature. Algorithms have been developed to correct land contamination and explore coastal information.

An improved method for cold calibration is developed (Yang et al. 2015a). This method produces reliable scan dependent information that was not available previously. By diagnosing the scan dependent calibration, instrument performance can be assessed and scan dependent errors can be identified and corrected. This

method also maximizes the calibration sampling enabling more continuous radiometer monitoring. The impact of collocation criteria, including grid resolution and time windowing, is investigated. Optimal criteria are found, allowing accurate characterization of scan dependent performance.

We develop methods for more robust warm calibration (Yang et al. 2015b). Warm calibration is expanded beyond previous sites in tropical rainforests to include worldwide boreal, temperate, and coastal forests, which increases the sampling size by a factor of 30. We develop techniques for mitigating land heterogeneity. A reliable warm-end calibration is developed with significantly reduced uncertainty. Accurate characterization of scan dependent information becomes available. We find regional differences for warm-end calibration. This is particularly significant at the water vapor channel. High and middle latitude regions, including boreal and temperate sites, yield similar calibration, but are different from tropical sites. This is likely due to improper representation of water vapor in the models used for simulated TBs. It indicates using limited sites, such as the Amazon rainforest alone, will result in regional calibration biases.

The cold and warm calibration methods have been applied to the GPM mission and make important contributions in resolving calibration issues and building up reliable and consistent constellation data (Yang et al. 2015c). The GMI along-scan magnetic interference and edge-of-scan biases are revealed at both ends. Our

method can discern extremely small signals such as the GMI ripple with a peak-to-peak amplitude of 0.1 K. By combining the two-end methods, we find a TB dependent calibration issue with GMI and resolve this issue. The along-scan anomaly with GMI is TB dependent, with the original correcting showing no errors at cold-end but significant residual errors at warm-end. This TB dependent issue across the scan position was not identified before due to the lack of reliable calibration methods at the warm-end. Our method identified the issues and corrections have been developed and applied to the latest GMI data. The warm-end method developed at University of Michigan has been adopted by the other teams. The GPM constellation has been intercalibrated using two-end methods. The first calibration table has been delivered to the GPM ground data center, PPS. The table is compiled from all XCAL teams. The table has been applied to GPM level-1 data and impacts all other higher level science data by making retrieved products consistent between the radiometers of the GPM constellation. Congratulations, my dissertation committee, you got this 10-buck Easter egg!

We investigate calibration variability and dependence on geophysical parameters that is of fundamental importance to calibration quality. A ~40-day cycle is discovered at all channels when intercalibrating any radiometer to GMI. We then determine that this signal is due to the spatial variation of geophysical parameters that can vary periodically with the shifting of calibration collocations.

Calibration shows nonlinear and non-monotonic dependence on geophysical parameters. The dependence can result in large discrepancies between model and observation not only with high value of geophysical parameters (e.g., high water vapor) but also with calm weather conditions with low value of geophysical parameters (e.g., low water vapor), of which the latter is often used for calibration. These results reveal calibration variability and nonlinearity and indicate that model biases and improper sampling can result in temporal and spatial variability.

Among the extensive calibrated and intercalibrated radiometer data, the coastal data tend to be ignored due to land contamination. We have developed methods for correcting land contamination to extract useful coastal information (Yang et al. 2014). The land contamination signals are estimated, and then removed, using a representative antenna pattern convolved with a high-resolution land–water mask. A Bessel function based representation of an EFOV antenna pattern is developed, which much better represent the real one than an IFOV Gaussian antenna pattern used in previous studies, as validated with SSM/I measured antenna patterns. It reduces errors in removing land signals. The land-free signals are obtained using multiple correlated pixels with optimized number and area. This method has been applied in the Great Lakes and validated with simulated data and buoy measurements. The corrected TBs show agreement with simulations. Wind speed retrieval is demonstrated, which is as good as open-ocean wind retrievals. This

method can be applied to any radiometer in coastal regions for general retrieval purposes. This method opens the opportunity to explore the extensive calibrated and intercalibrated climatological data for coastal research.

7.2 Future Work

A comprehensive framework has been established for spaceborne microwave radiometer calibration, intercalibration and science application in coastal areas. These methodologies have been applied to the GPM constellation but can be further used for any other radiometers and missions. A number of radiometers are going to be launched in the near future. For the GPM constellation, new members will be launched, including NOAA-NASA JPSS-1, METOP-C, and DMSP-F20. In addition to GPM, more constellations with microwave radiometers as key payloads are being developed. For instance, the Temporal Experiment and Tropical Systems (TEMPEST) satellite mission plans to use high-frequency radiometers onboard small satellites to measure clouds and precipitation. The Radiometer Atmospheric CubeSat Experiment (RACE) will use a compact radiometer and spacecraft to measure liquid water path and precipitable water vapor. The existing satellite systems such as NOAA, DMSP and Metop continue to launch new satellite to maintain consecutive operational weather observations. All these radiometers and constellations need calibration and intercalibration to correct errors and to

reconcile instrument differences. The radiometers also need continuous monitoring to maintain their calibration. All of these offer great opportunities to implement these developed calibration methods.

The revealed calibration variability and dependence on geophysical parameters are to be investigated. The temporal and spatial variability has been characterized at the cold end. The reason leading to the temporal variability has been determined. The warm-end variability should be characterized. The impact of important factors, for example, water vapor, can be further investigated at both cold and warm ends. It is important to more quantitatively characterize and understand how water vapor variability affects calibration through model parameterizations and reanalysis data. Our results should be used toward developing specific algorithms to handle this variability. Possible solutions include improving model parameterizations, revised handling of reanalysis data, and reducing impact of variability through statistical methods.

While these studies focus on imaging channels, they can be extended to sounding channels. The sounding channels are relatively less well calibrated compared to imaging channels. The weighting function of sounding channels peak not on the ground but above the ground at a height that can vary with conditions (e.g., the presence of hydrometeors). Many sounding channels use cross-track scanning with varying EIA rather than constant EIA as with conical scanning. All

these factors make sounding channels more difficult to calibrate. Our methods at both ends can be extended to sounding channels. Although sounding channels are not as sensitive to surface emission as imaging channels, collocating different sounders can reduce scene difference and help intercalibration, for which our collocation methods for imagers would be useful. By building up a preliminary test dataset, modification can be made to develop more advanced methods for sounding channels. The possible calibration variability can also be studied in sounding channels, since sounders are more sensitive to the atmospheric dynamics that are not well represented in model or reanalysis data.

Since the method for dealing with land contamination has been developed, a following step is to build up coastal data and explore coastal science. The developed algorithm can be applied to any radiometer. A useful coastal dataset can be developed by combining a number of radiometers in a long term record. In any coastal areas, land-contamination free TBs can be built up, which can then be used to derive science data such as wind speed and SST. The diurnal, seasonal, and annual variability can be determined. The long-term climatological change in a specific region such as the Great Lakes can be studied. Additional data such as modeling and reanalysis data can be combined to verify observation or to evaluate model output.

BIBLIOGRAPHY

Adler, R. F., and A. J. Negri, 1988: A satellite infrared technique to estimate tropical convective and stratiform rainfall. *Journal of Applied Meteorology*, **27,** 30-51.

Aires, F., and R. Roca, 1998: Atmospheric sounding using satellite microwave observations. *Technical Report, Dynamic Meteorology Laboratory*.

Allison, L. J., E. B. Rodgers, T. T. Wilheit, and R. W. Fett, 1974: Tropical Cyclone Rainfall as Measured By the Nimbus Electrically Scanning Microwave Radiometer. *Bulletin of the American Meteorological Society*, **55,** 1074-1089.

Bellerby, T., M. Taberner, A. Wilmshurst, M. Beaumont, E. Barrett, J. Scott, and C. Durbin, 1998: Retrieval of land and sea brightness temperatures from mixed coastal pixels in passive microwave data. *IEEE Transactions on Geoscience and Remote Sensing*, **36,** 1844-1851.

Bengtsson, L., S. Hagemann, and K. I. Hodges, 2004: Can climate trends be calculated from reanalysis data? *Journal of Geophysical Research-Atmospheres*, **109**.

Bengtsson, L., and Coauthors, 2007: The need for a dynamical climate reanalysis. *Bulletin of the American Meteorological Society*, **88,** 495-501.

Bennartz, R., 1999: On the use of SSM/I measurements in coastal regions. *Journal of Atmospheric and Oceanic Technology*, **16,** 417-431.

Berg, W., R. P. S. Mathew, H. Jennifer, and K. Christian, 2012: Improved Geolocation and Earth Incidence Angle Information for a Fundamental Climate Data Record of the SSM/I Sensors. *IEEE Transactions on Geoscience and Remote Sensing***,** -1688.

Biswas, S. K., K. Gopalan, W. L. Jones, and S. Bilanow, 2010: Correction of Time-Varying Radiometric Errors in TRMM Microwave Imager Calibrated Brightness Temperature Products. *IEEE Geoscience and Remote Sensing Letters*, **7,** 851-855.

Biswas, S. K., S. Farrar, K. Gopalan, A. Santos-Garcia, W. L. Jones, and S. Bilanow, 2013: Intercalibration of Microwave Radiometer Brightness Temperatures for the Global Precipitation Measurement Mission. *Ieee Transactions on Geoscience and Remote Sensing*, **51,** 1465-1477.

Brown, S. T., and C. S. Ruf, 2005: Determination of an Amazon hot reference target for the on-orbit calibration of microwave radiometers. *Journal of Atmospheric and Oceanic Technology*, **22,** 1340-1352.

Carroll, M. L., J. R. Townshend, C. M. DiMiceli, P. Noojipady, and R. A. Sohlberga, 2009: A new global raster water mask at 250 m resolution. *International Journal of Digital Earth*, **2**.
Chander, G., T. J. Hewison, N. Fox, X. Wu, X. Xiong, and W. J. Blackwell, 2013: Overview of Intercalibration of Satellite Instruments. *Geoscience and Remote Sensing, IEEE Transactions on*, **51,** 1056-1080.
Colton, M. C., and G. A. Poe, 1999: Intersensor calibration of DMSP SSM/I's: F-8 to F-14, 1987-1997. *IEEE Transactions on Geoscience and Remote Sensing*, **37,** 418-439.
Dee, D. P., and Coauthors, 2011: The ERA-Interim reanalysis: configuration and performance of the data assimilation system. *Quarterly Journal of the Royal Meteorological Society*, **137,** 553-597.
Desportes, C., E. Obligis, and L. Eymard, 2007: On the wet tropospheric correction for altimetry in coastal regions. *IEEE Transactions on Geoscience and Remote Sensing*, **45,** 2139-2149.
Draper, D., 2014a: Calibration Data Book for Global Precipitation Measurement (GPM) Microwave Imager (GMI), Ball Aerospace & Technologies Corp. Ball Aerospace & Technologies Corp, 211.
——, 2014b: Calibration Data Book for Global Precipitation Measurement (GPM) Microwave Imager (GMI). Ball Aerospace & Technologies Corp, 211.
Draper, D., D. Newell, D. McKague, and J. Piepmeier, 2015a: Assessing Calibration Stability Using the Global Precipitation Measurement (GPM) Microwave Imager (GMI) Noise Diodes. *Selected Topics in Applied Earth Observations and Remote Sensing, IEEE Journal of*, **PP,** 1-9.
Draper, D., D. Newell, F. Wentz, S. Krimchansky, and G. Skofronick-Jackson, 2015b: The Global Precipitation Measurement (GPM) Microwave Imager (GMI): Instrument Overview and Early On-Orbit Performance. *Selected Topics in Applied Earth Observations and Remote Sensing, IEEE Journal of*, **PP,** 1-11.
Drusch, M., E. F. Wood, and R. Lindau, 1999: The impact of the SSM/I antenna gain function on land surface parameter retrieval. *Geophysical Research Letters*, **26,** 3481-3484.
Elsaesser, G., 2006: A parametric optimal estimation retrieval of the nonprecipitating parameters over the global oceans, M.S. Thesis, Colorado State Univ., Fort Collins, CO.
Ferraro, R. R., F. H. Weng, N. C. Grody, and L. M. Zhao, 2000: Precipitation characteristics over land from the NOAA-15 AMSU sensor. *Geophysical Research Letters*, **27,** 2669-2672.
Ferrazzoli, P., and L. Guerriero, 1996: Passive microwave remote sensing of forests: A model investigation. *IEEE Transactions on Geoscience and Remote Sensing*, **34,** 433-443.

Gaiser, P. W., and Coauthors, 2004: The WindSat spaceborne polarimetric microwave radiometer: Sensor description and early orbit performance. *IEEE Transactions on Geoscience and Remote Sensing*, **42,** 2347-2361.
Galindo-Israel, V., and R. Mittra, 1977: A new series representation for the radiation integral with application to reflector antennas. *Antennas and Propagation, IEEE Transactions on*, **25,** 631-641.
Geer, A. J., P. Bauer, and N. Bormann, 2010: Solar Biases in Microwave Imager Observations Assimilated at ECMWF. *IEEE Transactions on Geoscience and Remote Sensing*, **48,** 2660-2669.
Goodberlet, M. A., C. T. Swift, and J. C. Wilkerson, 1989: Remote-Sensing of Ocean Surface Winds with the Special Sensor Microwave Imager. *Journal of Geophysical Research-Oceans*, **94,** 14547-14555.
Gopalan, K., W. L. Jones, S. Biswas, S. Bilanow, T. Wilheit, and T. Kasparis, 2009: A Time-Varying Radiometric Bias Correction for the TRMM Microwave Imager. *IEEE Transactions on Geoscience and Remote Sensing*, **47,** 3722-3730.
GPM Intersatellite Calibration Working Group (XCAL), 2015: XCAL Meeting Report (2014 Jul & 2015 Jan).
Griffith, C. G., W. L. Woodley, P. G. Grube, D. W. Martin, J. Stout, and D. N. Sikdar, 1978: Rain estimation from geosynchronous satellite imagery-visible and infrared studies. *Monthly Weather Review*, **106,** 1153-1171.
Hallikainen, M. T., P. A. Jolma, and J. M. Hyyppa, 1988: Satellite microwave radiometry of forest and surface types in Finland. *Geoscience and Remote Sensing, IEEE Transactions on*, **26,** 622-628.
Hollinger, J. P., 1971: Passive microwave measurements of sea surface roughness. *Ieee Transactions on Geoscience Electronics*, **9,** 165-169.
Hollinger, J. P., J. L. Peirce, and G. A. Poe, 1990: SSM/I instrument evaluation. *IEEE Transactions on Geoscience and Remote Sensing*, **28,** 781-790.
Hou, A. Y., and Coauthors, 2013: The Global Precipitation Measurement Mission. *Bulletin of the American Meteorological Society*, **95,** 701-722.
Huber, P. J., and E. M. Ronchetti, 2009: Robust Statistics, 2nd Edition. *New York: John Wiley*.
Huete, A., K. Didan, T. Miura, E. P. Rodriguez, X. Gao, and L. G. Ferreira, 2002: Overview of the radiometric and biophysical performance of the MODIS vegetation indices. *Remote Sens. Environ.*, **83,** 195-213.
Hung, C. C., and R. Mittra, 1983: Secondary pattern and focal region distribution of reflector antennas under wide-angle scanning. *Ieee Transactions on Antennas and Propagation*, **31,** 756-763.
Jones, W. L., J. D. Park, S. Soisuvarn, L. Hong, P. W. Gaiser, and K. M. S. Germain, 2006: Deep-space calibration of the WindSat radiometer. *IEEE Transactions on Geoscience and Remote Sensing*, **44,** 476-495.

Joo, S., J. Eyre, and R. Marriott, 2013: The Impact of MetOp and Other Satellite Data within the Met Office Global NWP System Using an Adjoint-Based Sensitivity Method. *Monthly Weather Review*, **141,** 3331-3342.
Jorgensen, M., 2006: Iteratively Reweighted Least Squares. *Encyclopedia of Environmetrics*, John Wiley & Sons, Ltd.
Kelly, G., and J.-N. Thépaut, 2007: Evaluation of the impact of the space component of the Global Observation System through observing system experiments. *ECMWF Newsletter***,** 16-28.
Kleist, D. T., D. F. Parrish, J. C. Derber, R. Treadon, W. S. Wu, and S. Lord, 2009: Introduction of the GSI into the NCEP Global Data Assimilation System. *Weather and Forecasting*, **24,** 1691-1705.
Kroodsma, R. A., D. S. McKague, and C. S. Ruf, 2012: Inter-Calibration of Microwave Radiometers Using the Vicarious Cold Calibration Double Difference Method. *Ieee Journal of Selected Topics in Applied Earth Observations and Remote Sensing*, **5,** 1006-1013.
Kummerow, C., and L. Giglio, 1994: A passive microwave technique for estimating rainfall and vertical structure information from space. Part I: Algorithm description. *Journal of Applied Meteorology*, **33,** 3-18.
Kummerow, C., W. Barnes, T. Kozu, J. Shiue, and J. Simpson, 1998: The Tropical Rainfall Measuring Mission (TRMM) Sensor Package. *Journal of Atmospheric and Oceanic Technology*, **15,** 809-817.
Kunkee, D. B., S. D. Swadley, G. A. Poe, H. Ye, and M. F. Werner, 2008: Special Sensor Microwave Imager Sounder (SSMIS) Radiometric Calibration Anomalies—Part I: Identification and Characterization. *Geoscience and Remote Sensing, IEEE Transactions on*, **46,** 1017-1033.
Liebe, H. J., G. A. Hufford, and T. Manabe, 1991: A model for the complex permittivity of water at frequencies below 1 THz. *International Journal of Infrared and Millimeter Waves*, **12,** 659-675.
Liebe, H. J., P. W. Rosenkranz, and G. A. Hufford, 1992: Atmospheric 60-GHz oxygen spectrum: New laboratory measurements and line parameters. *Journal of Quantitative Spectroscopy & Radiative Transfer*, **48,** 629-643.
Liou, K. N., 2002: *An Introduction to Atmospheric Radiation.* 2 ed. Academic Press.
Lorenc, A. C., and R. T. Marriott, 2014: Forecast sensitivity to observations in the Met Office Global numerical weather prediction system. *Quarterly Journal of the Royal Meteorological Society*, **140,** 209-224.
Maass, N., and L. Kaleschke, 2010: Improving passive microwave sea ice concentration algorithms for coastal areas: applications to the Baltic Sea. *Tellus Ser. A-Dyn. Meteorol. Oceanol.*, **62,** 393-410.

Macelloni, G., S. Paloscia, P. Pampaloni, and R. Ruisi, 2001: Airborne multifrequency L- to Ka-band radiometric measurements over forests. *IEEE Transactions on Geoscience and Remote Sensing*, **39,** 2507-2513.
McKague, D. S., C. S. Ruf, and J. J. Puckett, 2011: Beam Spoiling Correction for Spaceborne Microwave Radiometers Using the Two-Point Vicarious Calibration Method. *IEEE Transactions on Geoscience and Remote Sensing*, **49,** 21-27.
Meindl, E. A., and G. D. Hamilton, 1992. Available: http://www.ndbc.noaa.gov: Programs of the National Data Buoy Center. *Bulletin of the American Meteorological Society*, **73,** 985-993.
Meissner, T., and F. J. Wentz, 2004: The complex dielectric constant of pure and sea water from microwave satellite observations. *IEEE Transactions on Geoscience and Remote Sensing*, **42,** 1836-1849.
Mittra, R., Y. Rahmat-Samii, V. Galindo-Israel, and R. Norman, 1979: An efficient technique for the computation of vector secondary patterns of offset paraboloid reflectors. *Antennas and Propagation, IEEE Transactions on*, **27,** 294-304.
Mo, T., 2005: A study of the NOAA 16 AMSU-A brightness temperatures observed over Amazon rain forest. *Journal of Geophysical Research-Atmospheres*, **110**.
Njoku, E. G., 2014: *Encyclopedia of Remote Sensing.* Springer-Verlag New York.
NOAA, 2000: NCEP FNL Operational Model Global Tropospheric Analyses, continuing from July 1999. Research Data Archive at the National Center for Atmospheric Research, Computational and Information Systems Laboratory.
Otkin, J. A., 2010: Clear and cloudy sky infrared brightness temperature assimilation using an ensemble Kalman filter. *Journal of Geophysical Research-Atmospheres*, **115**.
Poe, G. A., and R. W. Conway, 1990: A study of the geolocation errors of the special sensor microwave imager (SSM/I). *IEEE Transactions on Geoscience and Remote Sensing*, **28,** 791-799.
Prabhakara, C., D. A. Short, W. Wiscombe, R. S. Fraser, and B. E. Vollmer, 1986: Rainfall over Oceans Inferred from Nimbus 7 SMMR: Application to 1982–83 El Niño. *Journal of Climate and Applied Meteorology*, **25,** 1464-1474.
Rahmatsamii, Y., and V. Galindoisrael, 1980: Shaped reflector antenna analysis using the Jacobi-Bessel series. *Ieee Transactions on Antennas and Propagation*, **28,** 425-435.
Rosenkranz, P. W., 1993: Absorption of microwaves by atmospheric gases. *Atmospheric Remote Sensing by Microwave Radiometry*, M. A. Janssen, Ed., John Wiley, New York, 37-90.
——, 1998: Water vapor microwave continuum absorption: A comparison of measurements and models. *Radio Science*, **33,** 919-928.

Rüdiger, C., and Coauthors, 2014: Toward Vicarious Calibration of Microwave Remote-Sensing Satellites in Arid Environments. *Geoscience and Remote Sensing, IEEE Transactions on,* **52,** 1749-1760.
Ruf, C. S., 2000: Detection of calibration drifts in spaceborne microwave radiometers using a vicarious cold reference. *Geoscience and Remote Sensing, IEEE Transactions on,* **38,** 44-52.
Ruf, C. S., Y. Hu, and S. T. Brown, 2006: Calibration of WindSat polarimetric channels with a vicarious cold reference. *IEEE Transactions on Geoscience and Remote Sensing*, **44,** 470-475.
Sapiano, M. R. P., W. K. Berg, D. S. McKague, and C. D. Kummerow, 2013: Toward an Intercalibrated Fundamental Climate Data Record of the SSM/I Sensors. *IEEE Transactions on Geoscience and Remote Sensing*, **51,** 1492-1503.
Shimada, M., and Coauthors, 2011: Generation of 10m resolution PALSAR and JERS-SAR mosaic and forest/non-forest maps for forest carbon tracking. *2011 Ieee International Geoscience and Remote Sensing Symposium (Igarss),* 3510-3513.
Simpson, J., R. F. Adler, and G. R. North, 1988: A Proposed Tropical Rainfall Measuring Mission (TRMM) Satellite. *Bulletin of the American Meteorological Society,* **69,** 278-295.
Stogryn, A. P., 1972: The emissivity of sea foam at microwave frequencies. *Journal of Geophysical Research,* **77,** 1658-1666.
Stogryn, A. P., C. T. Butler, and T. J. Bartolac, 1994: Ocean surface wind retrievals from special sensor microwave imager data with neural networks. *Journal of Geophysical Research-Oceans*, **99,** 981-984.
Street, J. O., R. J. Carroll, and D. Ruppert, 1988: A note on computing robust regression estimates via iteratively reweighted least-squares. *American Statistician*, **42,** 152-154.
T. Wilheit, R. A., S. Avery, E. Barrett, P. Bauer, W. Berg, A. Chang, J. Ferriday, N. Grody, S. Goodman, C. Kidd, D. Kniveton, C. Kummerow, A. Mugnai, W. Olson, G. Petty, A. Shibata, E. Smith, 1994: Algorithms for the retrieval of rainfall from passive microwave measurements. *Remote Sensing Reviews*, **11,** 163-194.
Ulaby, F. T., and D. G. Long, 2014: *Microwave Radar and Radiometric Remote Sensing.* Univ. of Michigan Press, ISBN 978-0-472-11935-6, 1016 pp.
Ulbrich, C. W., 1983: Natural variations in the analytical form of the raindrop size distribution. *Journal of Climate and Applied Meteorology,* **22,** 1764-1775.
Wentz, F. J., and R. W. Spencer, 1998: SSM/I Rain Retrievals within a Unified All-Weather Ocean Algorithm. *Journal of the Atmospheric Sciences*, **55,** 1613-1627.
Wentz, F. J., P. Ashcroft, and C. Gentemann, 2001: Post-launch calibration of the TRMM microwave imager. *IEEE Transactions on Geoscience and Remote Sensing*, **39,** 415-422.

Wentz, F. J., L. Ricciardulli, K. Hilburn, and C. Mears, 2007: How Much More Rain Will Global Warming Bring? *Science*, **317,** 233-235.
Wilheit, T., W. Berg, H. Ebrahimi, R. Kroodsma, D. McKague, V. Payne, and W. J., 2015: Intercalibrating the GPM constellation using the GPM microwave imager (GMI). *2015 IEEE International Geoscience and Remote Sensing Symposium (IGARSS)*.
Wilheit, T. T., 1979: A model for the microwave emissivity of the ocean's surface as a function of wind speed. *IEEE Transactions on Geoscience and Remote Sensing*, **17,** 244-249.
——, 2013: Comparing Calibrations of Similar Conically Scanning Window-Channel Microwave Radiometers. *Ieee Transactions on Geoscience and Remote Sensing*, **51,** 1453-1464.
Wilheit, T. T., A. T. C. Chang, M. S. V. Rao, E. B. Rodgers, and J. S. Theon, 1977: A Satellite Technique for Quantitatively Mapping Rainfall Rates over the Oceans. *Journal of Applied Meteorology*, **16,** 551-560.
World Meteorological Organization, 2015: Observing Systems Capability Analysis and Review Tool (OSCAR), **http://www.wmo-sat.info/oscar/spacecapabilities**.
Yang, J. X., 2015: Calibrate GPS Signal Simulator using an L-Band Radiometer for the Cyclone Global Navigation Satellite System (CYGNSS) mission. *Technical Report, University of Michigan*.
Yang, J. X., D. S. McKague, and C. S. Ruf, 2014: Land Contamination Correction for Passive Microwave Radiometer Data: Demonstration of Wind Retrieval in the Great Lakes Using SSM/I. *J. Atmos. Ocean. Technol.*, **31,** 2094-2113.
Yang, J. X., D. S. McKague, and C. S. Ruf, 2015a: Boreal, Temperate, and Tropical Forests as Vicarious Calibration Sites for Spaceborne Microwave Radiometry. *IEEE Transactions on Geoscience and Remote Sensing*.
——, 2015b: Boreal, Temperate, and Tropical Forests as Vicarious Calibration Sites for Spaceborne Microwave Radiometry. *IEEE Transactions on Geoscience and Remote Sensing*, **54**.
Yang, J. X., D. S. McKague, and C. S. Ruf, 2015c: Identifying and resolving a calibration issue with GMI. *2015 IEEE International Geoscience and Remote Sensing Symposium (IGARSS)***,** (test finalists in Student Paper Contest, 11 ouf 95, acceptance ratio 11%).
Yang, S., F. Z. Weng, B. H. Yan, N. H. Sun, and M. Goldberg, 2011: Special Sensor Microwave Imager (SSM/I) Intersensor Calibration Using a Simultaneous Conical Overpass Technique. *J. Appl. Meteorol. Climatol.*, **50,** 77-95.